



Copyright Undertaking

This thesis is protected by copyright, with all rights reserved.

By reading and using the thesis, the reader understands and agrees to the following terms:

1. The reader will abide by the rules and legal ordinances governing copyright regarding the use of the thesis.
2. The reader will use the thesis for the purpose of research or private study only and not for distribution or further reproduction or any other purpose.
3. The reader agrees to indemnify and hold the University harmless from and against any loss, damage, cost, liability or expenses arising from copyright infringement or unauthorized usage.

IMPORTANT

If you have reasons to believe that any materials in this thesis are deemed not suitable to be distributed in this form, or a copyright owner having difficulty with the material being included in our database, please contact lbsys@polyu.edu.hk providing details. The Library will look into your claim and consider taking remedial action upon receipt of the written requests.

**REACTIVE NITROGEN OXIDES (HONO, N₂O₅ and
ClNO₂) IN DIFFERENT ATMOSPHERIC
ENVIRONMENT IN CHINA: CONCENTRATIONS,
FORMATION AND THE IMPACT ON
ATMOSPHERIC OXIDATION CAPACITY**

YUN HUI

PhD

The Hong Kong Polytechnic University

2018

The Hong Kong Polytechnic University
Department of Civil and Environmental Engineering

**Reactive nitrogen oxides (HONO, N₂O₅ and ClNO₂) in
different atmospheric environment in China:
Concentrations, formation and the impact on
atmospheric oxidation capacity**

YUN Hui

A thesis submitted in partial fulfillment of the
requirements for the Degree of Doctor of Philosophy

February 2018

CERTIFICATE OF ORIGINALITY

I hereby declare that this thesis is my own work and that, to the best of my knowledge and belief, it reproduces no material previously published or written, nor material that has been accepted for the award of any other degree or diploma, except where due acknowledgement has been made in the text.

Sign:

Name: YUN Hui

Abstract

Reactive nitrogen oxides play an important role in the formation of both $\text{PM}_{2.5}$ and O_3 . HONO photolysis is an important source of OH radical which initializes photochemical reactions and leads to the production of O_3 and other secondary products during the daytime. The heterogeneous uptake of N_2O_5 on aerosol surfaces at night is an important source of aerosol nitrate and simultaneously releases ClNO_2 , which is a dominant source of Cl radical in the early morning via photolysis. Cl radical reacts with volatile organic compounds (VOCs) much faster than OH radical. Therefore, reactive nitrogen chemistry has significant impact on atmospheric oxidation capacity (AOC). There is still limited research about the N_2O_5 and ClNO_2 chemistry in China. For HONO, the daytime missing source has long been a concern for scientists, and its level and impact in severe pollution conditions, like in a street canyon microenvironment and in a typical pollution episode, are still seldomly reported.

For this thesis, datasets observed by our group from four separate field campaigns were analyzed. HONO was measured in a street canyon at Mong Kok in urban Hong Kong and at a semi-rural site at Heshan in the western Pearl River Delta (PRD). N_2O_5 and ClNO_2 were observed at a high-elevation site (Mt. Tai Mo Shan, 957 m a.s.l.) in Hong Kong, at a rural site at Wangdu in North China Plain (NCP), and at Heshan in PRD. An observation-based box model (OBM) built on the Master Chemical Mechanism (MCM v3.3.1) and an updated Cl chemistry module was developed to investigate the contribution of HONO and ClNO_2 to the formation of radicals and secondary products

(e.g. HNO_3 , OVOCs and O_3). An iterative box model was also employed to investigate the contribution of N_2O_5 chemistry to NO_x loss and ClNO_2 accumulation over the entire night in the TMS campaign. At Heshan, the formation processes of N_2O_5 and ClNO_2 and the impact on nitrate formation were also investigated. The two sites for HONO can represent a highly-polluted urban environment (Mong Kok) and a regional polluted environment (Heshan), respectively. And the sites for $\text{N}_2\text{O}_5/\text{ClNO}_2$ can represent the environments in the upper boundary layer (TMS) and in rural areas near ground surface (Wangdu and Heshan). This thesis focuses on the characteristics and impacts of reactive nitrogen chemistry in different ambient environments in China.

At Mong Kok, the average daytime HONO mixing ratio was 3.91 ppbv, which was much higher than that at night. OBM simulations constrained by the observed HONO showed that the maximum concentrations of OH, HO_2 , and RO_2 reached 4.65×10^6 , 4.40×10^6 , and 1.83×10^6 molecules cm^{-3} , which were 7.9, 5.0, and 7.5 times, respectively, the results in the case without HONO constrained. Photolysis of HONO contributed to 86.5% of the total primary radical production rates and led to efficient NO_2 and O_3 production under the condition of weak regional transport of O_3 . The formation of HNO_3 contributed to 98.4% of the total radical termination rates. The results suggest that HONO could significantly increase the atmospheric oxidation capacity (AOC) in a street canyon and enhance the secondary formation of HNO_3 and HCHO, which can damage outdoor building materials and pose health risks to pedestrians. At Heshan, high HONO concentration of 1.1 ppbv around noon time was observed together with high HONO/ NO_2 ratio of 6.5%. HONO photolysis was the dominant primary radical source,

and accounted for 43.7%-64.1% of the total production rates of radicals. HONO also governed the in-situ production of O₃ in this environment. The daytime sources of HONO seemed complex which was probably related to NO₂ heterogeneous reaction with water, photo-enhanced reactions on surfaces and photolysis of adsorbed HNO₃/nitrate. Considering the importance of HONO in both the street canyon environment and the regional polluted environment, more studies about the HONO sources are suggested.

In the previous study of TMS campaign, high ClNO₂ of 4.7 ppbv was observed in an aged air mass from PRD, which caused 16% of O₃ enhancement at the ozone peak and Cl chemistry contributed to 41% of the produced O₃ in the following day. In this study, as the aging of “young” air masses captured just after sunset, the predicted ClNO₂ could increase up to 6 ppbv at sunrise, indicating more frequent ClNO₂ peaks in the downwind open sea. A significant portion of the NO_x in the air masses (70% ± 10%) was removed during the nighttime via N₂O₅ chemistry. At Wangdu, morning peaks of ClNO₂ up to 550 pptv and 2070 pptv were observed in the average case and the highest case, respectively. Cl reactions with VOCs contributed to 3% and 9% of the average daytime RO_x budget, and contributed to 10% and 30% in the morning (8:00-8:30). Integrated ozone concentrations also increased 3.3% (4 ppbv) and 13.3% (10 ppbv) for the average case and the highest case, respectively. At Heshan, the maximum N₂O₅ and ClNO₂ concentrations reached up to 3.4 ppbv and 8.3 ppbv (1 min time resolution) in a severe pollution process. The amount of aerosol nitrate formed during the nighttime was 39.7 to 77.3 μg m⁻³ during the severe haze event, which was comparable to the nitrate formed

through $\text{OH}+\text{NO}_2$ during the daytime. Morning peaks of 3.5 ppbv ClNO_2 led to 7% increase of in-situ O_3 production.

This thesis indicates the importance of N_2O_5 chemistry to aerosol nitrate formation at near-ground level, and to atmospheric oxidation capacity (AOC) in the upper boundary layer, and the significant contribution of HONO to AOC in street canyons and regional pollution episodes in China.

Publications

1. **Hui Yun**, Zhe Wang, Qiaozhi Zha, Weihao Wang, Likun Xue, Li Zhang, Qinyi Li, Long Cui, Shuncheng Lee, Steven C.N. Poon, Tao Wang. 2017. Nitrous acid in a street canyon environment: Sources and contributions to local oxidation capacity. *Atmospheric Environment*, 167, 223-234.
2. **Hui Yun**, Tao Wang, Weihao Wang, Yee Jun Tham, Qinyi Li, Zhe Wang, Steven C. N. Poon. 2018. Nighttime NO_x loss and ClNO_2 formation in the residual layer of a polluted region: Insights from field measurements and an iterative box model. *Science of the total Environment*, 622-623, 727-734.
3. **Hui Yun**, Weihao Wang, Tao Wang, Men Xia, Chuan Yu, Zhe Wang, Steven C.N. Poon, Dingli Yue, and Yan Zhou, 2018. Nitrate formation from heterogeneous uptake of dinitrogen pentoxide during a severe winter haze in southern China. *Atmos. Chem. Phys. Discuss.*, <https://doi.org/10.5194/acp-2018-698>.
4. Yee Jun Tham, Zhe Wang, Qinyi Li, **Hui Yun**, Weihao Wang, Xinfeng Wang, Likun Xue, Keding Lu, Nan Ma, Birger Bohn, Xin Li, Simonas Kecorius, Johannes Größ, Min Shao, Alfred Wiedensohler, Yuanhang Zhang, and Tao Wang. 2016. Significant concentrations of nitryl chloride sustained in the morning: investigations of the causes and impacts on ozone production in a polluted region of northern China, *Atmos. Chem. Phys.*, 16, 14959-14977.

Conference presentations

1. **Hui Yun**, et al. Nitrous acid in a street canyon environment: Sources and contributions to local oxidation capacity. European Geophysical Union General Assembly 2017, Vienna, Austria, April 23-28, 2017. (poster)
2. **Hui Yun**, et al. Nighttime NO_x loss and ClNO_2 formation in the residual layer of a polluted region: Insights from field measurements and an iterative box model. The 5th International Symposium on Regional Air Quality Management in Rapid Developing Economic Regions, Guangzhou, China, Nov. 16-19, 2017. (poster)
3. **Hui Yun**, et al. Significant HONO concentration at a semi-rural site in Pearl River Delta during a severe pollution period and its impact on atmospheric oxidation capacity. American Geophysical Union 2017 fall meeting. New Orleans, United States of America, Dec. 11-15, 2017. (poster)

Acknowledgments

This thesis is not only the outcomes of my research work for three years in Hong Kong Polytechnic University, but also a spiritual training for my life. As a person who gave up a good job position in Beijing and a single female PhD candidate, I suffered a lot during these three years, not only from the work pressure, but more from huge mental stress. It was really a long way for me to go through by myself. Fortunately, I have great supervisors who guided me patiently, accommodating colleagues who helped me a lot, good friends who fought together with me, and my parents and little brother who unconditionally support me at any time. I am quite lucky to have them in my life, and I would like to express my sincere thanks and appreciations here.

First and foremost I would like to express my speechless gratitude to my chief-supervisor, Professor Tao Wang. I think that he also suffered a lot from me during these three years. For several times, I was going to break down and wanted to give up the study. It was him who made me calm down to rethink my research and also my life. He encouraged me to fight for the difficulties and helped me to stick to the end. Sometimes I got really bad temper, but Prof. Wang still patiently communicated with me and discussed with me even when he already had a lot of things to deal with. I know that I am a lucky girl to be his student, and I want to give him my greatest thanks for his financial and spiritual support during the most challenging stage in my life.

I also want to thank my colleagues and friends in Prof. Wang's group. My co-supervisor, Dr Zhe Wang, seems more like a friend. We had lunch and played badminton together

with other group members and talked about research and life. Dr. Yee Jun Tham, Dr. Qinyi Li and Dr. Li Zhang helped me a lot when I met with difficulties in data analyzing and paper writing. Weihao Wang is a nice friend and also like a comrade-in-arms, who fought for the field campaigns and part of modeling work together with me. It is a great treasure for me to experience many memorable moments with them and also with Steven. Poon, Bobo, Dr. Jia Guo, Dr. Qingxin Ma, Dr. Xiao Fu, Men Xia, Yutong Liang, Lan Yao, Chuan Yu, Xue Yang, Naiwen Zhang, and Jianing Dai. I am thankful to them for their cooperation and will remember the countless dinners that we had together.

I appreciate these people who always provide me courage to go forward. Prof. Likun Xue, from Shandong University, helped me a lot when I was developing the model. The most words that he said were that “you did a good job”. That really supported me to finish the model developing work. Prof. Ravishankara, from NOAA, is more like a grandpa, who made me realize that I really did something in the past decades from a child in a small village in Inner Mongolia to a PhD student in HKPolyU. My officemates, Long Cui, Han Gong and Yuan Gao shared happiness and depression with me. My roommates, Yanghong Zhou, Xuting Sun, and Jiage Huo, and my dearest friend, Yi Dou, provided support to me in my everyday life, and we consoled each other when we felt full of pressure and found solutions together when we felt confusion. Many thanks to all of them and other friends not mentioned here. I wish everyone a bright future and a happy life.

For my family, I feel indebted to my parents, K.G. Yun, and X.T. Yu, and my little brother, F. Yun. I went back home only twice every year and spent less than three weeks

together with them. I even had not celebrated the Spring Festival with them for two years. But they always stand behind my back and support me unconditionally. The white hair of my parents is the evidence that they worry about my safety and future, but they seldom mention that to me. My little brother takes the responsibility of taking care of my parents after graduation from China University of Geosciences. I can also feel his pressure from work and life. I hope I can do more for them after the PhD study.

I want to thank myself too. I want to say “You are a great girl, you finally get it done!”.

I would like to acknowledge the financial support from Hong Kong Research Grants Council (PolyU 153026/14P and C5022-14G), PolyU Project of Strategic Importance (1-ZE13), Research Institute for Sustainable Urban Development (HKPolyU-RISUD), and the National Natural Science Foundation of China (41275123 and 91544213) for supporting my research.

Table of Contents

Abstract	I
Publications	V
Conference presentations	VI
Acknowledgments	VII
Table of Contents	X
List of figures	XV
List of tables	XX
Chapter 1. Introduction	1
Chapter 2. Literature review	4
2.1 Atmospheric nitrogen chemistry in the boundary layer	4
2.2 Atmospheric oxidation capacity and O ₃ production.....	6
2.3 HONO concentrations, sources and impacts on AOC.....	9
2.4 Formation of N ₂ O ₅ and ClNO ₂ and the impacts on AOC.....	13
References	19
Chapter 3. Instruments and chemical box model based on Master Chemical Mechanism	26
3.1 LOPAP for HONO	27
3.2 Chemical ionization mass spectrometer for N ₂ O ₅ and ClNO ₂	27
3.3 Master Chemical Mechanism (MCM).....	29
3.3.1 Brief introduction of different chemical mechanisms.....	29

3.3.2 MCM protocol for mechanism development	33
3.3.3 Chlorine chemistry for MCM	38
3.4 A zero-dimensional chemical box model	40
3.4.1 Brief introduction of the box model.....	40
3.4.2 Calculation of ozone production rate and RO _x budget.....	41
3.4.3 Important physical parameters in the model	50
3.4.4 Validation for the model setup.....	53
References	56

Chapter 4. Nitrous acid in a street canyon environment: sources and contributions to local oxidation capacity61

4.1 Introduction	61
4.2 Experiment	63
4.2.1 Measurement sites and instruments	63
4.2.2 Model description	65
4.3 General description of trace gases.....	67
4.4 Vehicle emission of HONO	70
4.5 Role of HONO in local photochemistry	74
4.5.1 Contribution of HONO to radical concentrations	74
4.5.2 Analysis of radical budget.....	76
4.5.3 Formation of HNO ₃ and OVOCs.....	80
4.6 Impact of HONO on local NO ₂ and O ₃ production.....	82
4.7 Summary	85
References	86

Chapter 5. Significant HONO concentration at a semi-rural site in Pearl River Delta during a severe pollution period and its impact on atmospheric oxidation capacity91

5.1 Introduction	91
5.2 Experiment	92
5.2.1 Site description and instruments	92
5.2.2 Model setup.....	95
5.3 Overview of the data	95
5.4 Importance of HONO to atmospheric oxidation capacity.....	99
5.4.1 OH mixing ratio and AOC	99
5.4.2 HONO contribution to RO _x production	102
5.4.3 Radical budget and O ₃ production	103
5.5 HONO formation during nighttime.....	106
5.6 Daytime HONO budget.....	109
5.7 Improvement of HONO simulation in the box model.....	114
5.8 Summary	116
References	117

Chapter 6. Nighttime NO_x loss and ClNO₂ formation in the residual layer of a polluted region: Insights from field measurements and an iterative box model.....121

6.1 Introduction	121
6.2 Methods	122
6.2.1 Measurements in the 2013 campaign.....	122
6.2.2 Iterative box model	123
6.3 N ₂ O ₅ uptake coefficient and ClNO ₂ yield	129

6.4 Nighttime NO_x loss pathways.....	132
6.5 ClNO_2 production over the entire night.....	136
6.6 Sensitivity tests about VOCs' concentrations to the NO_3 loss contribution	138
6.7 Influence of ClNO_2 on O_3 production in the following day	141
6.8 Summary	146
References	147
Chapter 7. ClNO_2 measured at a semi-rural site (Wangdu) in North China Plain and the impact on O_3 production	150
7.1 Introduction	150
7.2 Model Setup.....	151
7.3 Diurnal pattern of ClNO_2 and key species	151
7.4 Cl radical production and Cl reactivity	152
7.5 Cl contribution to primary radical production and O_3 formation	155
7.6 Summary	159
References	159
Chapter 8. N_2O_5 heterogeneous chemistry at a semi-rural site in Pearl River Delta during a severe pollution period and its impact on nitrate formation and O_3 production.....	161
8.1 Introduction	161
8.2 Site description, instruments and model setup	162
8.3 Overview of the observation	163
8.4 N_2O_5 heterogeneous chemistry on the selected nights	167
8.4.1 Production of NO_3 and N_2O_5	167
8.4.2 N_2O_5 uptake coefficient and ClNO_2 yield.....	169

8.5 Nitrate formation potential ($p\text{NO}_3^-$) through N_2O_5 chemistry	174
8.5.1 Nighttime $p(\text{NO}_3^-)$	174
8.5.2 Comparison with daytime production of HNO_3	176
8.6 Impact of ClNO_2 on ozone production.....	179
8.7 Summary	183
References	184
Chapter 9. Summary and future work	186
9.1 Summary of this thesis	186
9.1.1 HONO concentrations, formation and the impact.....	186
9.1.2 $\text{N}_2\text{O}_5/\text{ClNO}_2$ concentrations, formation and the impact	187
9.2 Future work	188

List of figures

Figure 2- 1. Scheme of the nitrogen chemistry in the tropospheric atmosphere. (Figure provided by Prof. Tao Wang)

Figure 2- 2. Relationships between different species in the atmospheric oxidation processes (from Liu et al., (2012) and Xue et al., (2016))

Figure 3- 1. Flow chart of main types of reactions in MCM protocol (from website: <http://mcm.leeds.ac.uk/MCMv3.3.1/project.htm>)

Figure 3- 2. Comparison between modeled results of radical concentrations and production rates with MCM v3.3.1 (left panel) and MCM v3.2 (right panel) based on the data of Tung Chung campaign on Nov. 25, 2011.

Figure 3- 3. Comparison between modeled and measured OH (a) and HO₂(b) for the 6.21 case

Figure 4- 1. Google map showing the sampling site of Mong Kok and the surrounding environment. The figure inset in the lower left corner shows the average diurnal variation of vehicle fleet on Nathan Road and Lai Chi Kok Road in 2014, provided by Hong Kong Transport Department.

Figure 4- 2. Time series of hourly mean values of measured species at the MK site and O₃ at a regional background site, Tap Mun (TM), in Hong Kong from March 28 to May 3, 2015.

Figure 4- 3. Diurnal patterns for HONO and related species with hourly averaged data at the MK site and diurnal pattern of O₃ at the TM site. The lines with circle markers are for the whole period. Solid and dash lines are for the sunshine periods and overcast periods, respectively.

Figure 4- 4. The contribution of vehicle emissions ($=0.010 \times \text{NO}_x$) to total HONO concentration. The lines with circle markers are for the whole period. Solid and dash lines are for the sunshine periods and overcast periods, respectively.

Figure 4- 5. The relationship between HONO/NO_x and RH during the daytime (a) and nighttime (b). The color bar in (a) indicates J_{NO_2} .

Figure 4- 6. Modeled radical concentrations with measured HONO constrained (a) and without constraining HONO (b).

Figure 4- 7. (a) Diurnal pattern of simulated OH reactivity on sunny days and (b) the average contribution of different species to OH reactivity during the daytime (7:00–

17:00). NMHCs were based on simultaneous measurements. Seven OVOC species were measured in a different campaign in May, 2014, and constrained in the model; other OVOCs were based on the simulated concentrations.

Figure 4- 8. Production rates for OH (a), HO₂ (c), and RO₂ (e) and destruction rates for OH (b), HO₂ (d), and RO₂ (f) with HONO constrained in the left panel, whereas (g), (i), (k) and (h), (j), (l) are the production and destruction rates, respectively, of OH, HO₂, and RO₂ without constraining HONO in the right panel.

Figure 4- 9. Diagram of the role of HONO in the atmospheric oxidation process in the NO_x-saturated O₃ production regime. The numbers in bold are daytime average rates when the model is constrained by HONO; the numbers in regular form are for the case without constraining HONO.

Figure 4- 10. Diurnal patterns for modeled gas-phase HNO₃ (a) and diurnal patterns for simulated formaldehyde (b) and acetaldehyde (c) without constraining the measured OVOCs into the model as sensitivity tests. Solid black lines and dotted lines are modeled results with and without constraining the measured HONO, respectively.

Figure 4- 11. Average concentrations of NO_x, NO, NO₂, and O₃ from 7:00–17:00 in cases from S1 to S6 (a), and the variations in scenarios with HONO constrained compared to those without HONO constrained (b). (c) shows the relationship between the daytime NO₂/NO ratio at the MK site and the O₃ concentration at the regional background site TM on sunny days.

Figure 5- 1. Google maps of the location of Pearl River Delta in Guangdong Province and the Hua Guo Shan site (a). ZQ, JM, FS, ZS, ZH, GZ, DG, SZ and HZ represents cities of Zhaoqing, Jiangmen, Foshan, Zhongshan, Zhuhai, Guangzhou, Dongguan, Shenzhen and Huizhou in PRD, respectively. The triangles represent the coal-fired power plants in Guangdong Province in 2010. The inserted figure in (a) shows the dense road network in PRD. (b) is the nearby topography of Hua Guo Shan. (c) shows the fire spots in southern China for Jan 4, 2017, which is captured from the web <https://firms.modaps.eosdis.nasa.gov/firemap/>.

Figure 5- 2. Time series of HONO, J_{HONO} , J_{NO_2} , OH, k_{OH} and related parameters from 18:40 of Jan 2 to 10:00 of Jan 8, 2017.

Figure 5- 3. Mean diurnal pattern of HONO, J_{HONO} , NO, NO₂, NO_x, HONO/NO₂, HONO/NO_x, NO/NO_x at the Hua Guo Shan supersite from Jan 3 to Jan 7, 2017.

Figure 5- 4. Simulated AOC (a), primary radical sources (b) and net O₃ production rates (c) based on the chemical box model with MCM v3.3.1. In (b), HONO photolysis rate was deducted by the formation rate of HONO through OH+NO.

Figure 5- 5. Average daytime (7:00-17:00) contribution of different primary radical sources from Jan 3 to Jan 7, respectively.

Figure 5- 6. Production rates for OH (a), HO₂ (c) and RO₂ (e) in the right panel and loss rates of OH (b), HO₂ (d) and RO₂ (f) from Jan 3 to Jan 7 with measured HONO constrained into the model.

Figure 5- 7. Nighttime relationship between HONO and NO₂ (a), HONO/NO₂ and RH (b), HONO and S_{aw} (c) and HONO/NO₂ and S_{aw} (d). The red line in (b) represents the average for the top 5 of HONO/NO₂ and the blue line represents the median for all HONO/NO₂ ratios in an RH interval of 5%.

Figure 5- 8. (a) Calculated values of the production rate of HONO unknown source R_{unknown}. The blue line was the variation of average R_{unknown} at each hour. (b) presents the variation of average HONO formation and loss rates at each hour. (c) Calculated missing HONO concentrations corresponding to the production of unknown HONO sources.

Figure 5- 9. Simulated and measured HONO concentrations with the box model.

Figure 6- 1. Variations of N₂O₅, ClNO₂, and related parameters on five nights (2013/11/15 17:40-0:00, 11/16 17:40-0:00, 11/30 17:40-0:00, 12/1 17:40-0:00, and 12/4 0:00-6:00). The concentrations of NO in these selected periods were close to zero which are not depicted in this figure.

Figure 6- 2. Distribution of integrated NO₃ production rate from time zero to sunrise as a function of the measured NO₂ mixing ratio (a). The bars are the percentage of data spots in each size bin (interval is 1 ppbv of NO₂) in the histogram of NO₂ mixing ratio. (b) to (e) represent the percentage of NO_x loss through the following reactions: (b) NO₃ + VOCs; (c) N₂O₅ + H₂O; (d) N₂O₅ + Cl⁻; and (e) recycling between NO₃ and N₂O₅. (f) is the percentage of net NO₂ loss compared to the initial NO₂ concentration at time zero. The black lines represent the median in each interval of the NO₂ mixing ratio.

Figure 6- 3. (a) Predicted ClNO₂ and N₂O₅ concentrations at sunrise of the following day. (b) The relationship between predicted ClNO₂ with measured NO₂. The color bar shows the predicted yield.

Figure 6- 4. Correlations of uptake coefficients and yields between the cases with original VOCs and these with 1.5/0.5VOCs.

Figure 6- 5. Contributions of different pathways to NO₃ consumption with 1.5VOCs.

Figure 6- 6. Contributions of different pathways to NO₃ consumption with 0.5VOCs.

Figure 6- 7. Correlations of predicted ClNO₂ concentrations at sunrise between the cases with original k_{NO3} and these with 1.5/0.5VOCs.

Figure 6- 8. Model simulated concentrations/mixing ratios of (a) ClNO₂ and Cl, (b) OH, (c) HO₂, and (d) ozone during the day following plume sampling from the Mt. TMS site,

with and without the ClNO₂ chemistry. The measured photolysis rate constant of NO₂ is shown by the blue shading. The model was initiated with the measured ClNO₂ and other relevant chemical constituents at 04:00 (4.7 ppbv of ClNO₂). (Cited from Wang et al., (2016), and this work was done by Xue L.K. in Shandong University)

Figure 6- 9. Simulated Cl, OH, HO₂, and O₃ with and without ClNO₂ formation based on the derived uptake coefficient and yield in the night of Nov. 30-Dec.1 in section 6.3.

Figure 7- 1. Diurnal pattern for main constrained species in the model; (a) and (b) are the average data for the whole modeled period from 20 June to 9 July, (c) and (d) are the patterns for the highest case of ClNO₂ on 21 June.

Figure 7- 2. Concentrations of Cl radical and its production rate with and without ClNO₂; (a), (c) and (e) are for the average case and (b), (d) and (f) are for the megacity case.

Figure 7- 3. Diurnal pattern of simulated Cl and OH reactivity as (a) and (c), (b) and (d) are the compositions of Cl and OH average reactivity from 5:00 to 18:00 for the 6.21 case.

Figure 7- 4. Primary RO_x radical production rates from different sources at Wangdu in the daytime (a, b). Pie charts represent the contributions of ClNO₂ to the primary RO_x radical production in the morning time (average value for 08:00-08:30).

Figure 7- 5. OH, HO₂ and RO₂ enhancement ratio with inclusion of ClNO₂; (a) for the average case and (b) for the megacity case.

Figure 7- 6. Net ozone production rates for (a) average, (b) the megacity case and (c) the difference in integrated net ozone production rate between the simulation with and without the ClNO₂ input.

Figure 8- 1. Time series of N₂O₅, ClNO₂, components of PM_{2.5}, related trace gases and meteorological parameters from 18:40 of Jan 2 to 11:00 of Jan 15, 2017. The inserted figure shows the variation of the ratio of nitrate to PM_{2.5} with increasing nitrate concentration. The green rectangles in the figure indicate the five days used for detailed analysis.

Figure 8- 2. (a) Surface weather chart at 08:00 LT on Jan 6, 2017 downloaded from the website of the Hong Kong Observatory indicating stagnant conditions. (b) The distribution of PM_{2.5} concentrations in the PRD region at 09:00 LT on Jan 6, 2017. This figure was captured from the website. <http://113.108.142.147:20031/GDPublish/publish.aspx>.

Figure 8- 3. The covariance of aerosol nitrate and ClNO₂ in the early nighttime (in 30 min time resolution) for four nights.

Figure 8- 4. Variation of N_2O_5 , ClNO_2 , NO_3^- , trace gases and meteorological conditions during the nighttime of Jan 4 to 5, 2017 as an example for the five selected nights.

Figure 8- 5. Comparison between the measured NO_3^- increase and the NO_3^- formation potential in the early nighttime (periods in Table 8-2) and in the later nighttime (periods in Table 8-3).

Figure 8- 6. Variation of OH mixing ratio and the rate of $\text{OH}+\text{NO}_2$ from Jan 3 and Jan 7.

Figure 8- 7. Comparison between the daytime (7:00 to 17:00 LT, assuming all gas phase HNO_3 partitioned into particle phase) and nighttime (17:00 to 7:00 LT of the next day) NO_3^- formation potential.

Figure 8- 8. Production rates of chlorine radicals (a), production rates of O_3 (b) with and without constraining ClNO_2 in the model.

Figure 8- 9. Impact of the air mass with the highest ClNO_2 on radical and O_3 concentrations by setting the average concentrations of pollutants free from sunrise to 9:00.

List of tables

Table 3- 1. Characteristics of these chemical mechanisms (Parameters of CB05,SAPRC-99, SAPRC-07 are from Chen et al., (2010)).

Table 3- 2. Groupings of MCM reactions.

Table 3- 3. Inorganic reactions incorporated into MCM3.3.1(from Xue et al. (2015)).

Table 3- 4. Examples of reactions of Cl with organics (from Xue et al. (2015)).

Table 4- 1. Average mixing ratios (ppbv) from 7:00 to 17:00 for sunny days. OVOCs were obtained from Cui et al. (2016).

Table 4- 2. Emission ratios (HONO/NO_x) in 16 fresh air masses and other parameters.

Table 4- 3. Scenarios for sensitivity tests.

Table 5- 1. Correlations between R_{unknown} and various parameters.

Table 6- 1. Plume age, time zero, NO_y, and k_{NO_3} used in the simulations in each of the air masses.

Table 6- 2. Average measured data, derived $\gamma_{\text{N}_2\text{O}_5}$ and ϕ_{ClNO_2} , and initial O₃ and NO₂ concentrations at time zero, the net NO₂ loss percentage and predicted ClNO₂ at sunrise for each sample.

Table 6- 3. Uptake coefficients and yields from ambient datasets in previous studies.

Table 6- 4. Initial conditions for the measured case of 4.7 ppbv ClNO₂, and the simulated case for the air mass with 6.0 ppbv ClNO₂ at sunrise.

Table 8- 1. Average concentrations (ppbv) of NMHCs species during the daytime (7:00-17:00 LT) and nighttime (17:00-7:00 LT of the next day) from Jan 3 to Jan 7.

Table 8- 2. Average values of N₂O₅ concentrations, N₂O₅ uptake coefficients, ClNO₂ yields and other related parameters and maximum values of ClNO₂ concentrations in the early nighttime for five selected nights.

Table 8- 3. Average values of N₂O₅ loss rate and related parameters for selected periods in the later nighttime.

Table 8- 4. Average OH mixing ratio and rate of OH + NO₂ during the daytime (7:00 to 17:00 LT) from Jan 3 to Jan 7, 2017.

Chapter 1. Introduction

Particulate matter ($PM_{2.5}$) and ozone (O_3) are two significant air pollution problems in China. Reactive nitrogen chemistry contributes to both the formation of aerosol nitrate and the production of O_3 . In the nighttime, nitrous acid (HONO) and nitryl chloride ($ClNO_2$) are both reservoirs for nitrogen oxides (NO_x). The production of $ClNO_2$ through the heterogeneous uptake of N_2O_5 on aerosol surfaces produce aerosol nitrate simultaneously which is an important removal pathway of NO_x . In the daytime, photolysis of HONO and photolysis of $ClNO_2$ are important sources of free radicals (hydroxyl radical OH and chlorine radical Cl) which initiate the photochemical reactions, remove gas-phase pollutants (eg. SO_2 , CO, NO, NO_2 , and volatile organic compounds (VOCs)) and lead to the formation of nitric acid (HNO_3) and ozone (O_3).

Extensive observations of HONO have been conducted in different ambient environments, and high daytime concentrations were found in most polluted areas. However, significant knowledge gaps exist regarding the characteristics, sources and impacts of HONO in some special environments such as in street canyon and in winter pollution. This thesis analyses the data of HONO and related chemical species observed by our group at a typical street canyon at Mong Kok in Hong Kong, and at a semi-rural station at Heshan in the western Pearl River Delta. A chemical box model based on Master Chemical Mechanism v3.3.1 and a newly-updated Cl chemistry module was developed by me to analyze the impacts of HONO on the production of radicals and secondary products (eg. HNO_3 , OVOCs, and O_3). These two studies provide new

information on concentrations, sources and impacts of HONO in these two special environments.

The impact of N_2O_5 heterogeneous chemistry on NO_x loss, aerosol nitrate formation and radical and O_3 production in different ambient environments was still not well quantified in previous studies. This thesis analyzes the data of N_2O_5 , ClNO_2 and related chemical species observed by our group at the top of Tai Mo Shan (TMS) in Hong Kong, at a rural site at Wangdu in North China Plain, and at the semi-rural site at Heshan in the western Pearl River Delta. The TMS site is 957 m a.s.l which is situated in the upper boundary layer, and the sites of Wangdu and Heshan are located near the ground surface (~10 m and 60 m above ground surface, respectively). The characteristics and the impacts of N_2O_5 and ClNO_2 are expected to be different in these different environments. The chemical box model was utilized to reveal the contribution of chlorine chemistry to daytime photochemistry.

Overall, the present thesis aims to investigate (1) concentrations and sources of HONO in a street canyon environment and in winter pollution and its impact on atmospheric oxidation capacity, (2) concentrations and formation of N_2O_5 and ClNO_2 , and their impacts on nighttime NO_x removal, aerosol nitrate formation, and O_3 production in the upper boundary layer and near ground surface in China.

This thesis has nine chapters. Chapter 1 is this introduction. In Chapter 2, literatures of relevant research are reviewed. In Chapter 3, the instruments for HONO and $\text{N}_2\text{O}_5/\text{ClNO}_2$ measurements and the development of a chemical box model to simulate

radical and O₃ production are described. The concentrations, sources and impact of HONO in a street canyon environment and in a severe winter pollution episode are presented in Chapter 4 and Chapter 5, respectively. In Chapter 6, a modeling study of the TMS data with an iterative box model is presented to reveal the NO_x loss and ClNO₂ formation processes in N₂O₅/ClNO₂-laden air masses. In Chapter 7, the effects of ClNO₂ and Cl chemistry on atmospheric oxidation capacity are discussed based on the Wangdu campaign. In Chapter 8, the latest measurement of N₂O₅/ClNO₂ at Heshan in Pearl River Delta is analyzed and their impact on nitrate and O₃ production is presented. Summary of this thesis and the future work is given in Chapter 9.

Chapter 2. Literature review

2.1 Atmospheric nitrogen chemistry in the boundary layer

Particulate Matter (PM_{2.5}) and ozone (O₃) are two critical air pollution problems in China at present. These pollution problems are described as atmospheric combined pollution which contains gas phase pollutants, including sulfur dioxide (SO₂), nitrogen oxides (NO_x, including NO and NO₂), carbon monoxide (CO), O₃ and volatile organic pollutants (VOCs), and particle phase pollutants, including PM_{2.5} and PM₁₀. Some pollutants come from primary emissions from vehicles, industrial plants, power plants, and burning activities, etc, while other pollutants come from secondary formation of atmospheric chemical reactions. In winter, PM_{2.5} of high concentrations results in severe haze and significantly reduces the visibility in the atmosphere. In summer, O₃ has become the first pollutant in many cities in China (<http://www.mep.gov.cn/hjzl/dqhj/cskqzlkzyb/>). The measured compositions of PM_{2.5} include sulfate (SO₄²⁻), nitrate (NO₃⁻), ammonium (NH₄⁺), chloride (Cl⁻), organic matters (OM), elemental carbon (EC) and metal elements, etc. O₃ is the secondary product of photochemical smog with NO_x and VOCs as precursors. NO_x is the precursor of both PM_{2.5} and O₃, so that more and more attentions are paid on the chemical processes of atmospheric nitrogen species.

As shown in Fig. 2-1, there are many nitrogen species in the atmosphere besides NO and NO₂ and complex chemical reactions exist between these species. In the daytime, NO is

oxidized by O_3 to form NO_2 , but NO_2 fast photolyzes to form NO and O_3 again. So this is a null circle for O_3 formation. Actually O_3 is formed through NO oxidation by peroxy radicals (RO_2 and HO_2), which can be generated by hydroxyl radical (OH) reactions with VOCs and will be described in detail in the next section. OH is an important radical that initializes the daytime photochemistry, and photolysis of nitrous acid ($HONO$) is one of the OH sources. $HONO$ can be generated from direct emission, heterogeneous reactions of NO_2 on ground or aerosol surfaces, and photolysis of adsorbed nitric acid (HNO_3). In the nighttime, NO_2 is oxidized by O_3 to form nitrate radical (NO_3) which fast photolyzes in the day. Therefore, the formation of NO_3 radical is generally only important at night. The reversible reaction between NO_3 and NO_2 then forms N_2O_5 , which can react with aerosol water or aerosol chloride to form aerosol nitrate and nitryl chloride ($ClNO_2$). The photolysis of $ClNO_2$ in the following day provides chlorine radical (Cl) which acts similarly as OH radical but is more reactive than OH radical when reacting with some VOCs.

$HONO$ and $ClNO_2$ both provide oxidants in the atmosphere and then pose impact on atmospheric oxidation capacity and O_3 production, therefore, more and more studies are conducted to know more about their concentrations, sources, formation processes and their impacts. As the daytime and nighttime nitrogen chemistry produce nitric acid and aerosol nitrate, these reactions also contributes to the removal of NO_x and formation of $PM_{2.5}$. In China, North China Plain (NCP) and Pearl River Delta (including Hong Kong) are two regions with severe $PM_{2.5}$ and O_3 pollution problems. The emissions of NO_x in

these regions are also significant. For these reasons, this thesis focuses on the research of reactive nitrogen species ($\text{HONO}/\text{N}_2\text{O}_5/\text{ClNO}_2$) in NCP and PRD-HK.

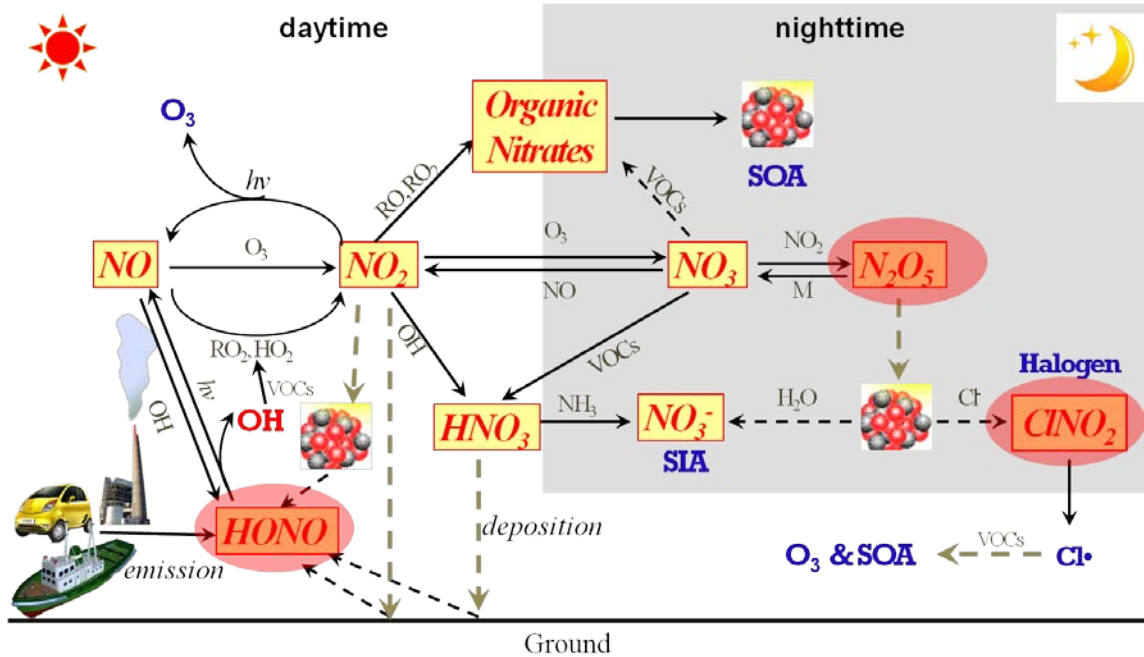


Figure 2- 1. Scheme of the nitrogen chemistry in the tropospheric atmosphere. (Figure provided by Prof. Tao Wang)

2.2 Atmospheric oxidation capacity and O_3 production

Oxidation reactions exist in nearly every corner in the boundary layer and play a role as removal pathways of primary pollutants and formation pathways of secondary pollutants in the atmosphere. The dominant oxidants in the ambient air are O_3 and free radicals, including hydroxyl radical (OH), chlorine radical (Cl) and nitrate radical (NO_3). NO_3 is generally only important during the nighttime due to its fast photolysis in the day. For daytime photochemical reactions, atmospheric oxidation capacity (AOC) is defined as

the total removal rates of VOCs and CO by principal oxidants, including OH, Cl, and O₃ (Elshorbany et al., 2010; Xue et al., 2016).

The most important chemical process in photochemistry is the recycling of RO_x radicals, including OH, hydroperoxy radicals (HO₂), organic peroxy radicals (RO₂) and RO. The photolysis of HONO, O₃, and oxygenated volatile organic compounds (OVOCs) and the ozonolysis of unsaturated VOCs primarily generate OH radicals, which can oxidize VOCs or CO to form RO₂ and HO₂. These peroxy radicals then oxidize nitrogen monoxide (NO) to form nitrogen dioxide (NO₂). The photolysis of NO₂ finally leads to the formation of O₃. The reaction between RO₂ and NO generates RO radicals, which further react with oxygen (O₂) or decompose and form HO₂ and secondary oxygenated volatile organic compounds (OVOCs). OH, HO₂, and RO₂ are three critical radicals in daytime oxidation processes. For HO₂ radicals, photolysis of formaldehyde, and other OVOCs, and the ozonolysis of unsaturated VOCs are primary radical sources, and for RO₂ radicals, the primary sources include photolysis of OVOCs, the ozonolysis of unsaturated VOCs and VOCs oxidation by NO₃ and Cl radicals (Emmerson et al., 2005; Michoud et al., 2012; Xue et al., 2016). Some main secondary products for the photochemistry include nitric acid (HNO₃) from reaction between OH and NO₂, OVOCs, and peroxyacetyl nitrate (PAN). The whole photochemistry is described in Fig. 2-2.

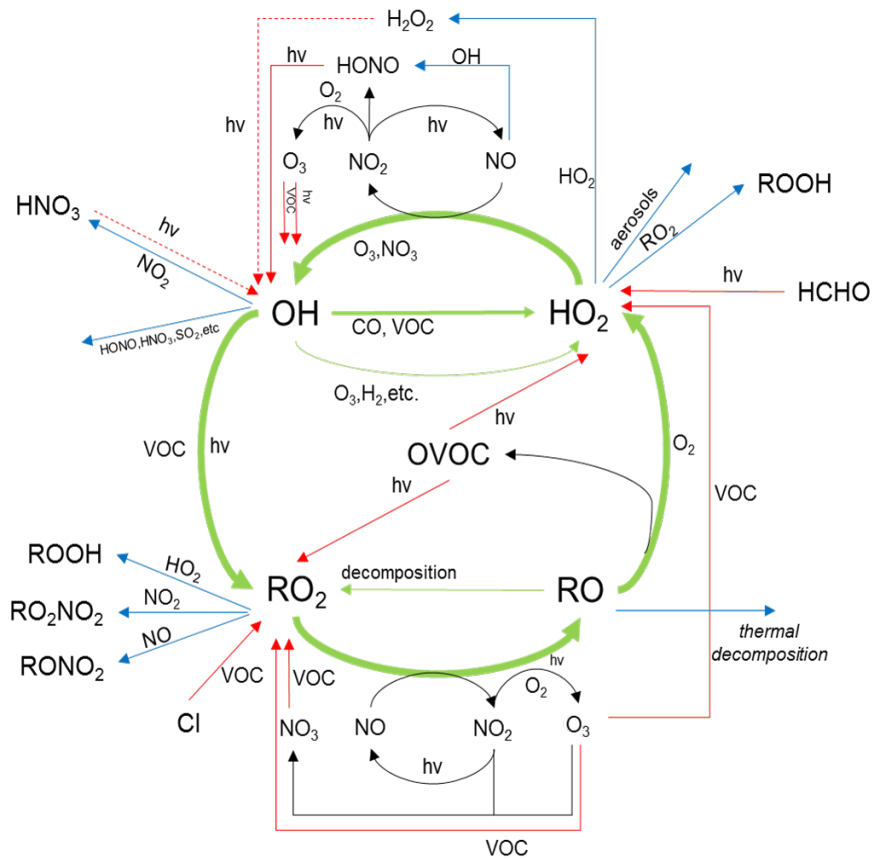


Figure 2- 2. Relationships between different species in the atmospheric oxidation processes (from Liu et al., (2012) and Xue et al., (2016))

Extensive studies have been conducted to understand the relative importance of radical sources and to identify the formation pathway of secondary pollutants based on calculations with chemical box models, due to the difficulty for the direct measurement of radicals and the complexity of the photochemical reactions. A chemical box model assumes the simulated atmospheric boundary layer as a big box and is proper to simulate species with short lifetime, like OH and HO₂, and quick reactions with local emitted species (Perner et al., 1987;Poppe et al., 1994). The model is constrained with the

observed concentrations of long-lived species and then simulates the atmospheric processes with the actual concentration in the environment to reproduce the processes properly. Details about the chemical box model will be described in Chapter 3.

The dominant daytime radical source in the boundary layer was found to be HONO photolysis in New York City (Ren et al., 2006; Ren et al., 2003), urban Santiago, Chile (Elshorbany et al., 2010; Elshorbany et al., 2009b), suburban Paris (Michoud et al., 2012), and Xinken (Su et al., 2008) and Baoding (Tham et al., 2016), China; OVOC photolysis in urban Beijing (Liu et al., 2012), central Tokyo (Kanaya et al., 2007), Mexico City (Volkamer et al., 2010), suburban Hong Kong (Xue et al., 2016), and rural Guangzhou (Lu et al., 2012); and O₃ photolysis at the top of Tai Mo Shan in Hong Kong (Ling et al., 2014) and in rural Nashville, Tennessee (Martinez et al., 2003). These studies mainly focused on general urban, suburban, or rural polluted environments in summer. Radical sources in street canyons and in severe winter pollution conditions have not been thoroughly investigated.

2.3 HONO concentrations, sources and impacts on AOC

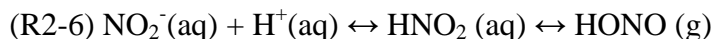
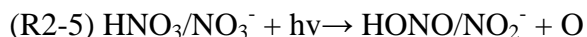
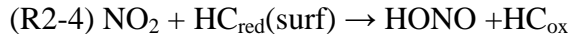
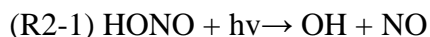
Nitrous acid (HONO) plays an important role in the atmospheric oxidation processes in the boundary layer. The photolysis of HONO (R2-1) is a daytime source of OH which initiates the photochemical reactions, remove gas-phase pollutants and lead to ozone (O₃) formation (Kleffmann, 2007; Pitts and Pitts, 2000). The measurement of HONO in the ambient air has been conducted in many studies, and the concentrations varied from a few pptv in remote or relatively clean areas to several ppbv in polluted urban and

suburban areas (Kleffmann, 2007; Spataro and Ianniello, 2014). The highest ever reported HONO was up to 15 ppbv in Santiago, Chile (Elshorbany et al., 2009), 9.7 ppbv in urban Beijing (Spataro et al., 2013), 8.4 ppbv in Guangzhou city (Qin et al., 2009), and 7.1 ppbv in urban Shanghai (Wang et al., 2013). HONO tended to accumulate during the first half of night and reached to balance in the second half of night. The fast photolysis of HONO in the day led to lower daytime concentrations than that at night.

The sources of HONO were complex, and as the result, the budget of HONO was still not well understood, especially during the daytime. The homogeneous reaction between OH and NO (R2-2) was a long-known pathway for HONO formation. Direct emission from vehicles was also investigated with the reported HONO/NO_x emission ratios from 0.3% to 2.3% (Gutzwiller et al., 2002; Kirchstetter et al., 1996; Kurtenbach et al., 2001), and the latest HONO/NO_x from a tunnel study in Hong Kong was 1.24% (Liang et al., 2017). Much higher HONO/NO_x ratio in ambient air than in direct emissions was an indicator for secondary HONO sources. NO₂ heterogeneous conversion on humid surfaces (aerosol/ground surfaces, R2-3) (Finlayson-Pitts et al., 2003) was considered to be a dominant source of HONO especially during the nighttime. Most lab studies suggested that this conversion is first order in NO₂, and the reactive uptake coefficient on surfaces was around 10⁻⁶ under dark conditions (Arens et al., 2001; Aumont et al., 2003; Kleffmann et al., 1998; Kleffmann et al., 1999). The NO₂ conversion on fresh soot decreased fast in the first several minutes, but slowed down later due to the deactivation of reaction points in darkness (Arens et al., 2001). During the daytime, NO₂

heterogeneous conversion was proposed to be photo-enhanced on soot (Monge et al., 2010), humic acid (Stemmler et al., 2006) and dust surfaces (Ndour et al., 2008), and the $\text{NO}_2 \rightarrow \text{HONO}$ uptake coefficients were suggested to be 10^{-8} - 10^{-7} , 10^{-6} - 10^{-5} and 10^{-6} , respectively. The mechanism was considered to be the oxidation of reductive organics by NO_2 with HONO as a product (R2-4). To simulate the NO_2 conversion on humid surfaces in models, the uptake coefficient of 1×10^{-6} was used as the nighttime uptake coefficient, and a value of 2×10^{-5} multiplied by a factor related to light intensity was used in daytime (Li et al., 2010; Zhang et al., 2016). Photolysis of adsorbed nitric acid (HNO_3) and nitrate (NO_3^-) (R2-5) was found to be a HONO source in both field and lab studies (Ye et al., 2016; Zhou, 2003; Zhou et al., 2007; Zhou et al., 2011), and the suggested photolysis frequency ranged in the order of magnitude of 10^{-6} to 10^{-4} s^{-1} . Su et al. (2011) illustrated that soil nitrite (NO_2^-) can release HONO which was attributed to the biological nitrification and denitrification processes (R2-6). This process depends on the characteristics of soil surfaces, including pH values, water content and temperature. More recently, Meusel et al. (2017) found that the soil HONO emission was also related to the biological species, covered vegetations and the level of nitrite and nitrate in soil. Oswald et al. (2013) showed that ammonia-oxidizing bacteria could directly release HONO. VandenBoer et al. (2015) illustrated that acid replacement was another mechanism for soil HONO emission. Soil can react as a reservoir of HONO at night through HONO reaction with carbonates or other weak acids, but reacts as a source of HONO in the day through air-to-soil transfer of hydrogen chloride (HCl) and HNO_3 produced via photochemical reactions. Some other proposed HONO sources include the

gas phase reaction of NO₂, water and NH₃ (R2-7) (Zhang and Tao, 2010), which was not yet tested by lab or field studies, and the reaction between photolytically excited NO₂ with H₂O, which was considered not important in the boundary layer (Li et al., 2014). The loss pathways of HONO are clear. In addition to photolysis, HONO can also be removed by OH (R2-8). During night, HONO is mainly removed through dry deposition on ground surfaces with a reported deposition velocity of 0.077 to 3 cm s⁻¹ (Li et al., 2012).



The daytime HONO contributed a lot to the atmospheric oxidation capacity (AOC), including radical production and O₃ formation. HONO photolysis was the dominant daytime radical source in New York City (~56%) (Ren et al., 2003, 2006), urban Santiago, Chile (~81% for winter and ~52% for summer) (Elshorbany et al., 2009, 2010),

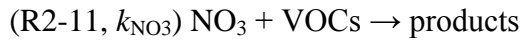
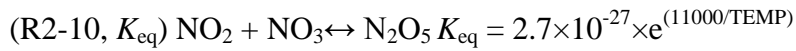
suburban Paris (~35%) (Michoud et al., 2012), and Xinken (Su et al., 2008b) and Baoding (~40%) (Tham et al., 2016), China.

HONO has been extensively observed in urban, suburban, rural and remote areas, and the impact of HONO on radical formation and O₃ production was also investigated in these areas mostly in summer season. However, the observation of HONO in a street canyon environment and in a severe winter pollution environment was seldomly reported and the role of HONO playing in the atmospheric oxidation processes in these environments needs to be further investigated. Different mechanisms for daytime HONO sources were proposed but still had controversies for their relative importance in different environments. This thesis will fill these knowledge gaps based on two latest campaigns. Concentrations, sources and impacts of HONO in these two special environments are presented via basic data analysis and the simulation based on a chemical box model.

2.4 Formation of N₂O₅ and ClNO₂ and the impacts on AOC

The heterogeneous uptake of dinitrogen pentoxide (N₂O₅) on chlorine-containing aerosols is an important nighttime loss pathway of nitrogen oxides (NO_x) and leads to the production of nitryl chloride (ClNO₂) (Brown et al., 2006b; Osthoff et al., 2008). ClNO₂ is a major source of chlorine radical (Cl) in the morning air and affects atmospheric oxidation capacity in the boundary layer (Phillips et al., 2012; Riedel et al., 2014; Sarwar et al., 2014; Thornton et al., 2010; Young et al., 2012). The chemical removal of nighttime NO_x is initialized by the production of nitrate radicals (NO₃) via

the oxidation of nitrogen dioxide (NO₂) by ozone (O₃) (see R2-9). The reaction between NO₂ and NO₃ radicals is reversible and quickly reaches equilibrium with N₂O₅ (see R2-10). NO₃ is an efficient nighttime oxidant of volatile organic compounds (VOCs, see R2-11), especially anthropogenic alkenes and biogenic VOCs (Brown and Stutz, 2012; Ng et al., 2017). N₂O₅ further reacts with aerosol water and chloride to form nitrate and ClNO₂ after accommodation into the aerosol.



The heterogeneous uptake of N₂O₅ can, in general, be described as R2-12_a and R2-12_b, with $k_{\text{N}_2\text{O}_5}$ as the rate coefficient and ϕ as the yield of ClNO₂. The rate coefficient can be calculated with the uptake coefficient of N₂O₅ ($\gamma_{\text{N}_2\text{O}_5}$), the mean molecular speed of N₂O₅ ($C_{\text{N}_2\text{O}_5}$), and aerosol surface area density (S_a), as shown in E2-1, when the gas-phase diffusive effect is negligible (Tang et al., 2014).

$$(E2-1) \quad k_{\text{N}_2\text{O}_5} = \frac{1}{4} \gamma_{\text{N}_2\text{O}_5} C_{\text{N}_2\text{O}_5} S_a$$

The heterogeneous reactions of N_2O_5 are influenced by both the composition of the aerosols and meteorological conditions (Brown and Stutz, 2012; Chang et al., 2011; Phillips et al., 2016), and considerable uncertainties exist in constraining different pathways of the nighttime loss of NO_3 and NO_x . To better understand the nighttime chemistry, field observations of N_2O_5 and ClNO_2 have been extensively conducted. The first simultaneous observation of N_2O_5 and ClNO_2 was conducted along the coastline near Houston, Texas, with maximum concentrations of 0.7 and 1.2 ppbv, respectively (Osthoff et al., 2008). After that, extensive field studies have been carried out in North America and Europe, for example, in the polluted Los Angeles Basin (Mielke et al., 2013; Riedel et al., 2012; Wagner et al., 2012), Boulder, Colorado (Riedel et al., 2013; Thornton et al., 2010), urban Calgary, Canada (Mielke et al., 2015; Mielke et al., 2011), and urban London (Bannan et al., 2015), and at a mountaintop site in Germany (Phillips et al., 2012; Phillips et al., 2016). In China, observations have also been conducted recently at Mt. Tai Mo Shan (TMS) in Hong Kong (Brown et al., 2016; Wang et al., 2016), at a suburban site, Wangdu, in North China Plain (NCP) (Tham et al., 2016), at Mt. Tai (Wang Z et al., 2017), in urban Ji'nan (Wang X et al., 2017), and in urban Beijing (Wang H et al., 2017). The highest levels ever reported for N_2O_5 and ClNO_2 were 7.7 ppbv and 4.7 ppbv, respectively, which were found in one well-processed air mass from the inland PRD region in the TMS campaign (Brown et al., 2016; Wang et al., 2016). This indicates that PRD region may foster active N_2O_5 chemistry.

The N_2O_5 uptake and ClNO_2 production has long been investigated to get insights into the nighttime nitrogen chemistry. Several experimental and calculation methods have

been developed to derive the $\gamma_{\text{N}_2\text{O}_5}$ in the ambient air based on field measurements of key chemical species, including NO_x , O_3 , N_2O_5 , ClNO_2 and aerosol nitrate. Bertram et al. (2009) developed a flow tube to directly measure the uptake coefficient on real ambient aerosols. Three calculation methods of $\gamma_{\text{N}_2\text{O}_5}$ have been proposed utilizing ambient measurements, as recently summarized by Phillips et al. (2016). The first one is to calculate the production rates of ClNO_2 ($p\text{ClNO}_2$) and aerosol nitrate ($p\text{NO}_3^-$) with E2-2 when N_2O_5 concentrations and meteorological conditions are relatively stable, which can also derive the yield of ClNO_2 (Mielke et al., 2013; Phillips et al., 2016; Riedel et al., 2013). The second one is to analyze the correlation between NO_3 or N_2O_5 steady-state lifetime (τ_{NO_3} or $\tau_{\text{N}_2\text{O}_5}$) and NO_2 concentrations according to E2-3 (Brown et al., 2006b; Brown et al., 2009; Brown et al., 2003), which assumed the balance between the NO_3 radical production and loss of both NO_3 and N_2O_5 . The concentrations of N_2O_5 should approximately achieve stability to keep the variation rate to be nearly zero in this situation. The third one is to use an iterative box model (Wagner et al., 2013). The iterative box model tracks back to the time of sunset or the time of emission to derive the initial NO_2 and O_3 concentrations and then derive proper $k_{\text{N}_2\text{O}_5}$ to make the modeled results match the measured N_2O_5 concentrations. The uptake coefficient was derived according to E2-1. The yield of ClNO_2 was calculated by the ratio of measured ClNO_2 concentrations to the integrated N_2O_5 loss. Similar box models through trying different uptake coefficients and yields to match with measured data were also used in other studies (Mielke et al., 2011; Osthoff et al., 2008; Riedel et al., 2013; Thornton et al., 2010; Wagner et al., 2012).

$$(E2-2) \gamma_{N_2O_5} = 2 \frac{pClNO_2 + pNO_3^-}{C_{N_2O_5} S_a [N_2O_5]}, \phi = 2 \left(\frac{pNO_3^-}{pClNO_2} + 1 \right)^{-1}$$

$$(E2-3) \tau_{NO_3}^{-1} = \tau_{N_2O_5}^{-1} K_{eq} [NO_2] = k_{NO_3+} \frac{1}{4} \gamma_{N_2O_5} C_{N_2O_5} S_a K_{eq} [NO_2]$$

The contributions of different pathways to the nighttime loss of NO_3 and NO_x have been quantified by combining the measured data with numerical modeling. The loss of NO_3 was dominated by reactions with anthropogenic alkenes (>70%) in Houston, Texas, where large petrochemical industries were located (Stutz et al., 2010), and by nitrate formation through N_2O_5 uptake in Los Angeles (~90%) (Tsai et al., 2014) and in Boulder, Colorado (~80%) (Wagner et al., 2013). The nighttime loss of NO_x was responsible for up to 60% of the total NO_x loss in a 24 h period in the lower atmosphere (Tsai et al., 2014; Wagner et al., 2013). These studies suggested that the relative importance of each NO_3 and NO_x loss pathway could differ from place to place due to different chemical and meteorological conditions.

Nitrate has been identified to be an important part of secondary inorganic aerosol (SIA) in $PM_{2.5}$ in severe haze pollution events in China (Huang et al., 2014). Pathak et al. (2009) reported that the nitrate in ammonium-poor conditions was most probably formed via the heterogeneous hydrolysis of N_2O_5 in Beijing and Shanghai. Wang H et al. (2017) recently found that N_2O_5 heterogeneous loss during the nighttime was a comparable way to form aerosol nitrate to the daytime partitioning of gas-phase nitric acid (HNO_3) in urban Beijing based on measurements of N_2O_5 and assumption of $ClNO_2$ yield to be 1.0.

ClNO_2 is a major source of chlorine radical (Cl) in the morning air and affects O_3 formation in the boundary layer (Riedel et al., 2014; Sarwar et al., 2014; Thornton et al., 2010; Young et al., 2012). Sustained ClNO_2 concentrations were observed after sunrise under conditions of weak photolysis, i.e., at Pasadena, California (~800 pptv) (Mielke et al., 2013), in urban London (~150 pptv) (Bannan et al., 2015), in Houston, Texas (~40 pptv) (Faxon et al., 2015) and also in Wangdu, NCP, China (~2000 pptv) (Tham et al., 2016). Cl radical reacts much faster than OH with VOCs and results in the formation of RO_2 , which is treated as one of the primary radical source and contributed to ~9-13% of the daily primary radical production (Edwards et al., 2013; Young et al., 2014). O_3 production was then enhanced through the much faster RO_x radical recycling. For example, Osthoff et al. (2008) added 650 pptv and 1500 pptv of ClNO_2 at sunrise into a typical polluted air mass and resulted in ozone enhancement of 6 and 9 ppbv in midday, respectively. Riedel et al. (2014) reported that ClNO_2 of 1.5 ppbv formed in the outflow of continental polluted air mass led to daytime maximum Cl concentration of 1×10^5 atoms cm^{-3} , 2.2 times more RO_x radicals produced in the morning, and an enhancement in integrated ozone production of 15%. Sarwar et al. (2014) modeled the impact of heterogeneous ClNO_2 formation over the Northern Hemisphere, and suggested that this heterogeneous chemistry enhanced monthly mean daily maximum 8 h ozone by up to 7.0 ppbv, and the largest ClNO_2 concentrations and impacts occurred over China and Western Europe.

For N_2O_5 and ClNO_2 , there are still few measurements conducted in China (Brown et al., 2016; Wang et al., 2016; Tham et al., 2016; Wang Z et al., 2017; Wang X et al., 2017;

Wang H et al., 2017). In the campaign conducted at the top of Tai Mao Shan (957 m a.s.l.) in Hong Kong in 2013 (Brown et al., 2016; Wang et al., 2016), the highest ever-reported N_2O_5 (~7.7 ppbv) and ClNO_2 (~4.7 ppbv) were observed in one aged air mass and made significant contribution to radical and O_3 formation when the air mass transported to downwind locations in the open sea. It is interesting to investigate more $\text{N}_2\text{O}_5/\text{ClNO}_2$ -laden air masses observed just after sunset to see if the high ClNO_2 and its impact occurred frequently. The measurement of N_2O_5 and ClNO_2 at TMS in Hong Kong was the first report of these species in the upper boundary layer in China. Two other campaigns in rural or semi-rural areas were conducted at Wangdu in North China Plain and at Heshan in Pearl River Delta, respectively. These two sites were near ground surface, which can be treated as a comparison with the TMS site in the upper boundary layer. This thesis presents the concentrations, formation and impacts of $\text{N}_2\text{O}_5/\text{ClNO}_2$ in different regions and different altitudes in China. These are all new information for us to know more about the nighttime nitrogen chemistry in China.

References

- Arens F, Gutzwiller L, Baltensperger U, Gaggeler HW, Ammann M. Heterogeneous Reaction of NO_2 on Diesel Soot Particles. *Environmental Science & Technology* 2001; 35: 2191-2199.
- Aumont B, Chervier F, Laval S. Contribution of HONO sources to the $\text{NO}_x/\text{HO}_x/\text{O}_3$ chemistry in the polluted boundary layer. *Atmospheric Environment* 2003; 37: 487-498.
- Bannan TJ, Booth AM, Bacak A, Muller J, Leather KE, Le Breton M, et al. The first UK measurements of nitryl chloride using a chemical ionisation mass spectrometer in central London in the summer of 2012, and an investigation of the role of Cl atom oxidation. *Journal of Geophysical Research: Atmospheres* 2015; 120, 5638–5657, doi:10.1002/2014JD022629.

- Bertram TH, Thornton JA, Riedel TP. An experimental technique for the direct measurement of N_2O_5 reactivity on ambient particles. *Atmospheric Measurement Techniques* 2009; 2: 231-242.
- Brown S, Ryerson T, Wollny A, Brock C, Peltier R, Sullivan A, et al. Variability in nocturnal nitrogen oxide processing and its role in regional air quality. *Science* 2006; 311: 67-70.
- Brown SS, Dube WP, Fuchs H, Ryerson TB, Wollny AG, Brock CA, et al. Reactive uptake coefficients for N_2O_5 determined from aircraft measurements during the Second Texas Air Quality Study: Comparison to current model parameterizations. *Journal of Geophysical Research-Atmospheres* 2009; 114, D00F10, doi:10.1029/2008JD011679.
- Brown SS, Dubé WP, Tham YJ, Zha Q, Xue L, Poon S, et al. Nighttime Chemistry at a High Altitude Site Above Hong Kong. *Journal of Geophysical Research: Atmospheres* 2016; 121, doi:10.1002/2015JD024566.
- Brown SS, Stark H, Ravishankara AR. Applicability of the steady state approximation to the interpretation of atmospheric observations of NO_3 and N_2O_5 . *Journal of Geophysical Research-Atmospheres* 2003; 108(D17), 4539, doi:10.1029/2003JD003407.
- Brown SS, Stutz J. Nighttime radical observations and chemistry. *Chemical Society Reviews* 2012; 41: 6405-6447.
- Chang WL, Bhave PV, Brown SS, Riemer N, Stutz J, Dabdub D. Heterogeneous Atmospheric Chemistry, Ambient Measurements, and Model Calculations of N_2O_5 : A Review. *Aerosol Science and Technology* 2011; 45: 665-695.
- Edwards PM, Young CJ, Aikin K, deGouw J, Dube WP, Geiger F, et al. Ozone photochemistry in an oil and natural gas extraction region during winter: simulations of a snow-free season in the Uintah Basin, Utah. *Atmospheric Chemistry and Physics* 2013; 13: 8955-8971.
- Elshorbany YF, Kleffmann J, Kurtenbach R, Lissi E, Rubio M, Villena G, et al. Seasonal dependence of the oxidation capacity of the city of Santiago de Chile. *Atmospheric Environment* 2010; 44: 5383-5394.
- Elshorbany YF, Kurtenbach R, Wiesen P, Lissi E, Rubio M, Villena G, et al. Oxidation capacity of the city air of Santiago, Chile. *Atmospheric Chemistry and Physics* 2009; 9: 2257-2273.
- Emmerson K, Carslaw N, Carpenter L, Heard D, Lee J, Pilling M. Urban atmospheric chemistry during the PUMA campaign 1: Comparison of modelled OH and HO_2 concentrations with measurements. *Journal of Atmospheric Chemistry* 2005; 52: 143-164.
- Faxon C, Bean J, Ruiz L. Inland Concentrations of Cl_2 and ClNO_2 in Southeast Texas Suggest Chlorine Chemistry Significantly Contributes to Atmospheric Reactivity. *Atmosphere* 2015; 6: 1487-1506.
- Finlayson-Pitts B, Wingen L, Sumner A, Syomin D, Ramazan K. The heterogeneous hydrolysis of NO_2 in laboratory systems and in outdoor and indoor atmospheres: An integrated mechanism. *Physical Chemistry Chemical Physics* 2003; 5: 223-242.

- Gutzwiller L, Arens F, Baltensperger U, Gäggeler HW, Ammann M. Significance of semivolatile diesel exhaust organics for secondary HONO formation. *Environmental science & technology* 2002; 36: 677-682.
- Huang R-J, Zhang Y, Bozzetti C, Ho K-F, Cao J-J, Han Y, et al. High secondary aerosol contribution to particulate pollution during haze events in China. *Nature* 2014; 514: 218.
- Kanaya Y, Cao R, Akimoto H, Fukuda M, Komazaki Y, Yokouchi Y, et al. Urban photochemistry in central Tokyo: 1. Observed and modeled OH and HO₂ radical concentrations during the winter and summer of 2004. *Journal of Geophysical Research: Atmospheres* 2007; 112, D21312, doi:10.1029/2007JD008670.
- Kirchstetter TW, Harley RA, Littlejohn D. Measurement of nitrous acid in motor vehicle exhaust. *Environmental science & technology* 1996; 30: 2843-2849.
- Kleffmann J. Daytime Sources of Nitrous Acid (HONO) in the Atmospheric Boundary Layer. *Chem. Phys. Chem.* 2007; 8: 1137-1144.
- Kleffmann J, Becker K, Wiesen P. Heterogeneous NO₂ conversion processes on acid surfaces: possible atmospheric implications. *Atmospheric Environment* 1998; 32: 2721-2729.
- Kleffmann J, Becker KH, Lackhoff M, Wiesen P. Heterogeneous conversion of NO₂ on carbonaceous surfaces. *Physical Chemistry Chemical Physics* 1999; 1: 5443-5450.
- Kurtenbach R, Becker K, Gomes J, Kleffmann J, Lörzer J, Spittler M, et al. Investigations of emissions and heterogeneous formation of HONO in a road traffic tunnel. *Atmospheric Environment* 2001; 35: 3385-3394.
- Li G, Lei W, Zavala M, Volkamer R, Dusanter S, Stevens P, et al. Impacts of HONO sources on the photochemistry in Mexico City during the MCMA-2006/MILAGO Campaign. *Atmos. Chem. Phys.* 2010; 10: 6551-6567.
- Li X, Brauers T, Häsel R, Bohn B, Fuchs H, Hofzumahaus A, et al. Exploring the atmospheric chemistry of nitrous acid (HONO) at a rural site in Southern China. *Atmos. Chem. Phys.* 2012; 12: 1497-1513.
- Li X, Rohrer F, Hofzumahaus A, Brauers T, Haseler R, Bohn B, et al. Missing Gas-Phase Source of HONO Inferred from Zeppelin Measurements in the Troposphere. *Science* 2014; 344: 292-296.
- Liang Y, Zha Q, Wang W, Cui L, Lui KH, Ho KF, et al. Revisiting Nitrous Acid (HONO) Emission from On-road Vehicles: A Tunnel Study with a Mixed Fleet. *Journal of the Air & Waste Management Association* 2017. 67(7), 797-805. <http://dx.doi.org/10.1080/10962247.2017.1293573>.
- Ling ZH, Guo H, Lam SHM, Saunders SM, Wang T. Atmospheric photochemical reactivity and ozone production at two sites in Hong Kong: Application of a Master Chemical Mechanism-photochemical box model. *Journal of Geophysical Research-Atmospheres* 2014; 119, 10567e10582. <http://dx.doi.org/10.1002/2014JD021794>.

- Liu Z, Wang Y, Gu D, Zhao C, Huey L, Stickel R, et al. Summertime photochemistry during CAREBeijing-2007: ROx budgets and O₃ formation. *Atmospheric Chemistry and Physics* 2012; 12: 7737-7752.
- Lu KD, Rohrer F, Holland F, Fuchs H, Bohn B, Brauers T, et al. Observation and modelling of OH and HO₂ concentrations in the Pearl River Delta 2006: a missing OH source in a VOC rich atmosphere. *Atmos. Chem. Phys.* 2012; 12: 1541-1569.
- Martinez M, Harder H, Kovacs TA, Simpas JB, Bassis J, Leshner R, et al. OH and HO₂ concentrations, sources, and loss rates during the Southern Oxidants Study in Nashville, Tennessee, summer 1999. *Journal of Geophysical Research: Atmospheres* 2003; 108, 4617. <http://dx.doi.org/10.1029/2003JD003551>. D19.
- Meusel H, Tamm A, Kuhn U, Wu D, Leifke AL, Fiedler S, et al. Emission of nitrous acid from soil and biological soil crusts represents a dominant source of HONO in the remote atmosphere in Cyprus. *Atmos. Chem. Phys. Discuss.* 2017; 2017: 1-21.
- Michoud V, Kukui A, Camredon M, Colomb A, Borbon A, Miet K, et al. Radical budget analysis in a suburban European site during the MEGAPOLI summer field campaign. *Atmospheric Chemistry and Physics* 2012; 12: 11951-11974.
- Mielke L, Stutz J, Tsai C, Hurlock S, Roberts J, Veres P, et al. Heterogeneous formation of nitryl chloride and its role as a nocturnal NO_x reservoir species during CalNex-LA 2010. *Journal of Geophysical Research: Atmospheres* 2013; 118: 10,638-10,652.
- Mielke LH, Furgeson A, Odame-Ankrah CA, Osthoff HD. Ubiquity of ClNO₂ in the urban boundary layer of Calgary, AB, Canada. *Canadian Journal of Chemistry* 2015; 94(4).
- Mielke LH, Furgeson A, Osthoff HD. Observation of ClNO₂ in a mid-continental urban environment. *Environmental science & technology* 2011; 45: 8889-8896.
- Monge ME, D'Anna B, Mazri L, Giroir-Fendler A, Ammann M, Donaldson D, et al. Light changes the atmospheric reactivity of soot. *Proceedings of the National Academy of Sciences* 2010; 107: 6605-6609.
- Ndour M, D'Anna B, George C, Ka O, Balkanski Y, Kleffmann J, et al. Photoenhanced uptake of NO₂ on mineral dust: Laboratory experiments and model simulations. *Geophysical Research Letters* 2008; 35,L05812, doi:10.1029/2007GL032006.
- Ng NL, Brown SS, Archibald AT, Atlas E, Cohen RC, Crowley JN, et al. Nitrate radicals and biogenic volatile organic compounds: oxidation, mechanisms, and organic aerosol. *Atmospheric Chemistry and Physics* 2017; 17: 2103-2162.
- Osthoff HD, Roberts JM, Ravishankara AR, Williams EJ, Lerner BM, Sommariva R, et al. High levels of nitryl chloride in the polluted subtropical marine boundary layer. *Nature Geoscience* 2008; 1: 324-328.
- Oswald R, Behrendt T, Ermel M, Wu D, Su H, Cheng Y, et al. HONO Emissions from Soil Bacteria as a Major Source of Atmospheric Reactive Nitrogen. *Science* 2013; 341: 1233-1235.

- Pathak RK, Wu WS, Wang T. Summertime PM_{2.5} ionic species in four major cities of China: Nitrate formation in an ammonia-deficient atmosphere. *Atmospheric Chemistry and Physics* 2009; 9: 1711-1722.
- Perner D, Platt U, Trainer M, Hübler G, Drummond J, Junkermann W, et al. Measurements of tropospheric OH concentrations: A comparison of field data with model predictions. *Journal of atmospheric chemistry* 1987; 5: 185-216.
- Phillips GJ, Tang MJ, Thieser J, Brickwedde B, Schuster G, Bohn B, et al. Significant concentrations of nitryl chloride observed in rural continental Europe associated with the influence of sea salt chloride and anthropogenic emissions. *Geophysical Research Letters* 2012; 39, L10811, doi:10.1029/2012GL051912..
- Phillips GJ, Thieser J, Tang M, Sobanski N, Schuster G, Fachinger J, et al. Estimating N₂O₅ uptake coefficients using ambient measurements of NO₃, N₂O₅, ClNO₂ and particle-phase nitrate. *Atmospheric Chemistry and Physics* 2016; 16: 13231-13249.
- Pitts BF, Pitts J. *Chemistry of the upper and lower atmosphere: Theory, experiments and applications*. Academic, US 2000.
- Poppe D, Zimmermann J, Bauer R, Brauers T, Brüning D, Callies J, et al. Comparison of measured OH concentrations with model calculations. *Journal of Geophysical Research: Atmospheres* 1994; 99: 16633-16642.
- Qin M, Xie P, Su H, Gu J, Peng F, Li S, et al. An observational study of the HONO-NO₂ coupling at an urban site in Guangzhou City, South China. *Atmospheric Environment* 2009; 43: 5731-5742.
- Ren X, Brune WH, Mao J, Mitchell MJ, Leshner RL, Simpas JB, et al. Behavior of OH and HO₂ in the winter atmosphere in New York City. *Atmospheric Environment* 2006; 40, Supplement 2: 252-263.
- Ren X, Harder H, Martinez M, Leshner RL, Olinger A, Simpas JB, et al. OH and HO₂ Chemistry in the urban atmosphere of New York City. *Atmospheric Environment* 2003; 37: 3639-3651.
- Riedel TP, Bertram TH, Crisp TA, Williams EJ, Lerner BM, Vlasenko A, et al. Nitryl Chloride and Molecular Chlorine in the Coastal Marine Boundary Layer. *Environmental Science & Technology* 2012; 46: 10463-10470.
- Riedel TP, Wagner NL, Dube WP, Middlebrook AM, Young CJ, Ozturk F, et al. Chlorine activation within urban or power plant plumes: Vertically resolved ClNO₂ and Cl₂ measurements from a tall tower in a polluted continental setting. *Journal of Geophysical Research-Atmospheres* 2013; 118: 8702-8715.
- Riedel TP, Wolfe GM, Danas KT, Gilman JB, Kuster WC, Bon DM, et al. An MCM modeling study of nitryl chloride (ClNO₂) impacts on oxidation, ozone production and nitrogen oxide partitioning in polluted continental outflow. *Atmospheric Chemistry and Physics* 2014; 14: 3789-3800.
- Sarwar G, Simon H, Xing J, Mathur R. Importance of tropospheric ClNO₂ chemistry across the Northern Hemisphere. *Geophysical Research Letters* 2014; 41: 4050-4058.

- Spataro F, Ianniello A. Sources of atmospheric nitrous acid: State of the science, current research needs, and future prospects. *Journal of the Air & Waste Management Association* 2014; 64: 1232-1250.
- Spataro F, Ianniello A, Esposito G, Allegrini I, Zhu T, Hu M. Occurrence of atmospheric nitrous acid in the urban area of Beijing (China). *Science of The Total Environment* 2013; 447: 210-224.
- Stemmler K, Ammann M, Donders C, Kleffmann J, George C. Photosensitized reduction of nitrogen dioxide on humic acid as a source of nitrous acid. *Nature* 2006; 440: 195-198.
- Stutz J, Wong KW, Lawrence L, Ziemba L, Flynn JH, Rappenglück B, et al. Nocturnal NO₃ radical chemistry in Houston, TX. *Atmospheric Environment* 2010; 44: 4099-4106.
- Su H, Cheng YF, Oswald R, Behrendt T, Trebs I, Meixner FX, et al. Soil Nitrite as a Source of Atmospheric HONO and OH Radicals. *Science* 2011; 333: 1616-1618.
- Su H, Cheng YF, Shao M, Gao DF, Yu ZY, Zeng LM, et al. Nitrous acid (HONO) and its daytime sources at a rural site during the 2004 PRIDE-PRD experiment in China. *Journal of Geophysical Research-Atmospheres* 2008; 113, D14312, doi:10.1029/2007JD009060.
- Tham YJ, Wang Z, Li Q, Yun H, Wang W, Wang X, et al. Significant concentrations of nitryl chloride sustained in the morning: investigations of the causes and impacts on ozone production in a polluted region of northern China. *Atmos. Chem. Phys.* 2016; 16: 14959-14977.
- Thornton JA, Kercher JP, Riedel TP, Wagner NL, Cozic J, Holloway JS, et al. A large atomic chlorine source inferred from mid-continental reactive nitrogen chemistry. *Nature* 2010; 464: 271-274.
- Tsai C, Wong C, Hurlock S, Pikelnaya O, Mielke LH, Osthoff HD, et al. Nocturnal loss of NO_x during the 2010 CalNex-LA study in the Los Angeles Basin. *Journal of Geophysical Research: Atmospheres* 2014; 119, 13,004–13,025, doi:10.1002/2014JD022171.
- VandenBoer TC, Young CJ, Talukdar RK, Markovic MZ, Brown SS, Roberts JM, et al. Nocturnal loss and daytime source of nitrous acid through reactive uptake and displacement. *Nature Geoscience* 2015; 8: 55-60.
- Volkamer R, Sheehy P, Molina LT, Molina MJ. Oxidative capacity of the Mexico City atmosphere – Part 1: A radical source perspective. *Atmos. Chem. Phys.* 2010; 10: 6969-6991.
- Wagner NL, Riedel TP, Roberts JM, Thornton JA, Angevine WM, Williams EJ, et al. The sea breeze/land breeze circulation in Los Angeles and its influence on nitryl chloride production in this region. *Journal of Geophysical Research-Atmospheres* 2012; 117, D00V24, doi:10.1029/2012JD017810.
- Wagner NL, Riedel TP, Young CJ, Bahreini R, Brock CA, Dubé WP, et al. N₂O₅ uptake coefficients and nocturnal NO₂ removal rates determined from ambient wintertime measurements. *Journal of Geophysical Research: Atmospheres* 2013; 118: 9331-9350.
- Wang H, Lu K, Chen X, Zhu Q, Chen Q, Guo S, et al. High N₂O₅ Concentrations Observed in Urban Beijing: Implications of a Large Nitrate Formation Pathway. 2017. *Environ. Sci. Technol. Lett.* DOI: 10.1021/acs.estlett.7b00341.

- Wang SS, Zhou R, Zhao H, Wang ZR, Chen LM, Zhou B. Long-term observation of atmospheric nitrous acid (HONO) and its implication to local NO₂ levels in Shanghai, China. *Atmospheric Environment* 2013; 77: 718-724.
- Wang T, Tham YJ, Xue L, Li Q, Zha Q, Wang Z, et al. Observations of nitryl chloride and modeling its source and effect on ozone in the planetary boundary layer of southern China. *Journal of Geophysical Research: Atmospheres* 2016; 121, doi:10.1002/2015JD024556.
- Wang X, Wang H, Xue L, Wang T, Wang L, Gu R, et al. Observations of N₂O₅ and ClNO₂ at a polluted urban surface site in North China: High N₂O₅ uptake coefficients and low ClNO₂ product yields. *Atmospheric Environment* 2017; 156: 125-134.
- Wang Z, Wang W, Tham YJ, Li Q, Wang H, Wen L, et al. Fast heterogeneous N₂O₅ uptake and ClNO₂ production in power plant and industrial plumes observed in the nocturnal residual layer over the North China Plain. *Atmos. Chem. Phys.* 2017; 17: 12361-12378.
- Xue L, Gu R, Wang T, Wang X, Saunders S, Blake D, et al. Oxidative capacity and radical chemistry in the polluted atmosphere of Hong Kong and Pearl River Delta region: analysis of a severe photochemical smog episode. *Atmos. Chem. Phys.* 2016; 16: 9891-9903.
- Ye C, Gao H, Zhang N, Zhou X. Photolysis of Nitric Acid and Nitrate on Natural and Artificial Surfaces. *Environmental Science & Technology* 2016; 50: 3530-3536.
- Young CJ, Washenfelder RA, Edwards PM, Parrish DD, Gilman JB, Kuster WC, et al. Chlorine as a primary radical: evaluation of methods to understand its role in initiation of oxidative cycles. *Atmospheric Chemistry and Physics* 2014; 14: 3427-3440.
- Young CJ, Washenfelder RA, Roberts JM, Mielke LH, Osthoff HD, Tsai C, et al. Vertically resolved measurements of nighttime radical reservoirs in Los Angeles and their contribution to the urban radical budget. *Environmental science & technology* 2012; 46: 10965-10973.
- Zhang B, Tao F-M. Direct homogeneous nucleation of NO₂, H₂O, and NH₃ for the production of ammonium nitrate particles and HONO gas. *Chemical Physics Letters* 2010; 489: 143-147.
- Zhang L, Wang T, Zhang Q, Zheng J, Xu Z, Lv M. Potential Sources of Nitrous Acid (HONO) and Their Impacts on Ozone: A WRF - Chem study in a Polluted Subtropical Region. *Journal of Geophysical Research: Atmospheres* 2016; 121, 3645–3662, doi:10.1002/2015JD024468.
- Zhou X. Nitric acid photolysis on surfaces in low-NO_x environments: Significant atmospheric implications. *Geophysical Research Letters* 2003; 30(23),2217, doi:10.1029/2003GL018620.
- Zhou XL, Huang G, Civerolo K, Roychowdhury U, Demerjian KL. Summertime observations of HONO, HCHO, and O₃ at the summit of Whiteface Mountain, New York. *Journal of Geophysical Research-Atmospheres* 2007; 112: 2156-2202.
- Zhou XL, Zhang N, TerAvest M, Tang D, Hou J, Bertman S, et al. Nitric acid photolysis on forest canopy surface as a source for tropospheric nitrous acid. *Nature Geoscience* 2011; 4: 440-443.

Chapter 3. Instruments and chemical box model based on Master Chemical Mechanism

This chapter first introduces two important instruments applied in the campaigns to measure HONO, and $\text{N}_2\text{O}_5/\text{ClNO}_2$, respectively. The Master Chemical Mechanism is then introduced and compared with other chemical mechanisms. Then the development of a chemical box model, the grouping of large amount of reactions and the calculation principle of radical and O_3 production and loss are described in detail. Validation of the model simulation results by comparing with previous modeling results and radical measurements at Wangdu is put at the last section of this chapter.

At Mong Kok site, the instrument of HONO was setup and conducted by Weihao Wang and Qiaozhi Zha in the campaign. Other data at this site were provided by Hong Kong Environmental Protection Department (HKEPD). The instrument of $\text{N}_2\text{O}_5/\text{ClNO}_2$ was setup and conducted by Yee Jun Tham at TMS site in Hong Kong and at Wangdu site in North China Plain, and by Weihao Wang at Heshan site in Pearl River Delta. At Heshan site, HONO was measured by Chuan Yu and Naiwen Zhang. My work focuses on the development of the chemical box model to analyze radical and O_3 production and the data analysis of these campaigns combined with the chemical box model. In Heshan campaign, I was also responsible for the measurement of VOCs with on-line GC/FID/MS.

3.1 LOPAP for HONO

HONO was continuously measured using a commercial Long-Path Absorption Photometer (QUMA, Model LOPAP-03). A detailed description of the LOPAP system can be found elsewhere (Liang et al., 2017). In brief, ambient air samples first pass through R1 (10 g/L sulfanilamide in 1 M HCl) in a temperature-controlled stripping coil where HONO and a small fraction of the interfering species are absorbed into solution (Channel 1). Then, the air passes through an identical stripping coil in which it is assumed that the same amount of interfering substances is absorbed (Channel 2). The two separate channels of solutions then pass through R2, i.e., a 0.178g/L n-(1-Naphthyl) ethylenediamine-dihydrochloride solution, to form a colored azo dye, which is subsequently detected by long-path absorption. The difference between the two channels is the signal of HONO in the air sampled. Before the field study, an HONO-source generator (QUMA, Model QS-03) was used to check the sampling efficiency of HONO to ensure a sampling efficiency near 100%. Automatic zero checks with synthetic air were performed three times per day, and manual calibrations were conducted every three days. The effective time resolution of this instrument was 10 min.

3.2 Chemical ionization mass spectrometer for N₂O₅ and ClNO₂

N₂O₅ and ClNO₂ were concurrently measured with a quadrupole chemical ionization mass spectrometer (THS Instruments, Atlanta) through converting N₂O₅ and ClNO₂ to ion clusters of I(N₂O₅)⁻ and I(ClNO₂)⁻. Briefly, an alpha radioactive source, 210-Po (NRD, P-2031-2000), was used to generate iodide ions (I⁻) from mixture of CH₃I/N₂

(0.3% v/v). Then, I^- combined with the N_2O_5 and $ClNO_2$ as $I(N_2O_5)^-$ and $I(ClNO_2)^-$, which were detected at 235 and 208 m/z, respectively. The time resolution for the measurement was ~ 7 s, and the derived data were later averaged to time resolution of 1 min for further analysis. To determine the instrument background, the sampling flow was diverted through a filter fully packed with activated carbons. Offline calibrations of N_2O_5 and $ClNO_2$ were performed every afternoon on the site, while standard addition of N_2O_5 into the ambient air was performed every 3 h to monitor the sensitivity changes due to ambient conditions. More detailed principle and calibration method of the CIMS have been described in (Wang et al., 2016). The detection limits were 7 pptv for N_2O_5 and 6 pptv for $ClNO_2$ (3σ , 1 min-averaged data). The average sensitivity of the system was 1.32 ± 0.35 and 1.40 ± 0.28 pptv Hz^{-1} for N_2O_5 and $ClNO_2$, respectively.

The inlet of the CIMS instrument was set at ~ 1.5 m above the roof and 15 m from ground level with a 6 m long PFA-Teflon tubing (1/4 in. outer diameter) as the sampling line. The inlet configuration was like a virtual impactor to remove large particles. The total sampling flow was 11 standard liters per minute (SLPM), and 4 SLPM was diverted into the CIMS, ozone and NO_x analyzer, while the rest was dumped. The total residence time in the sampling system was less than 1 s. The orifice, tubing and fittings were replaced and washed in an ultrasonic bath every day to minimize the effect of the particles deposited on the surface of the sampling inlet (Wang et al., 2016). The uncertainty of the measurement is estimated to be ± 25 %, with a precision of 3%.

3.3 Master Chemical Mechanism (MCM)

3.3.1 Brief introduction of different chemical mechanisms

The tropospheric pollution processes could be very complex when the chemical species like NO, NO₂ and VOCs emitted into the ambient air from natural or anthropogenic sources. These abundant reactions lead to the formation and recycling of reactive radicals including hydroxyl (OH) and hydroperoxy (HO₂) radicals (collectively HO_x), organic peroxy radicals (RO₂) and the formation of O₃ and other secondary pollutants. Thus, chemical mechanisms are developed to describe these processes mathematically. Due to the limited measurement technologies of VOCs and OVOCs and the incomplete knowledge of organic reactions, organic compounds are lumped in most of the chemical mechanisms, which can shorten the computing time. There are four kinds of chemical mechanisms which are extensively used in box models and 3-D chemical transport model, including Carbon Bond Mechanism (CB), Regional Atmospheric Chemical Mechanism (RACM), Statewide Air Pollution Research Center mechanism (SAPRC), and Master Chemical Mechanism (MCM). Characteristics of these chemical mechanisms are listed in Table 3-1.

The earliest Carbon Bond Mechanism was developed by Whitten et al. (1980), after that, Carbon Bond IV (CB IV) and Carbon Bond 05 (CB05) were developed by Gery et al. (1989) and Yarwood et al. (2005) respectively. Organic compounds are lumped based on four types of carbon bond: single-bonded carbon atoms (PAR), “fast” or relatively reactive double bonds (OLE), slow double bonds (ARO), and carbonyl groups (CAR)

(Whitten et al., 1980). CB IV has 33 species and 81 reactions, while CB05 has 51 species and 156 reactions in the core mechanism. CB05 has two mechanism extensions: one includes 33 explicit reactions of precursors of secondary organic aerosol (SOA), and the other one includes 20 reactions for reactive chlorine chemistry. This condensed mechanism can be used to study ozone, particulate matter (PM), visibility, acid deposition and air toxics issues from urban to remote tropospheric conditions (Yarwood et al., 2005). Whitten et al. (2010) updated CB's toluene chemistry in CB05-TU which includes 172 reactions involving 60 chemical species.

Regional Atmospheric Chemical Mechanism (RACM1.0) was developed by Stockwell et al. (1997) based on the earlier Regional Acid Deposition Model, version 2 (RADM2.0) mechanism (Stockwell et al., 1990) which is developed from the original RADM mechanism (Stockwell, 1986). Goliff et al. (2013) updated this mechanism to RACM2 to simulate the atmospheric gas-phase chemistry on a regional scale. Organic species are aggregated into the model species based on their similarity in functional groups and reactivity toward OH radical. The RACM1 includes 77 species and 237 reactions, while the RACM2 mechanism includes 119 species and 363 reactions. Reactions about aromatics, alcohols and acetone were specified to more accurately reflect the processes in the remote and upper troposphere in RACM2.

Statewide Air Pollution Research Center mechanism (SAPRC) was developed in 1988 by Carter (Carter, 1988a,b). Based on this version which was designated as SAPRC-90 (Carter, 1990), several updated versions were developed, such as SAPRC-99 (Carter, 2000a,b) and SAPRC-07 (Carter, 2007; Carter, 2010a; Carter, 2010b). Both of them

were specially designed to evaluate the relative impacts of different types of VOCs on ozone formation through calculating the reactivity scales by Maximum Incremental Reactivity (Carter, 1994). These two mechanisms have different modules in structure for different application, including base mechanism for inorganic species, the common organic products and the intermediate radicals, individual or lumped mechanisms for other VOCs and newly added chlorine mechanisms in SAPRC-07 (Carter, 2010b). Condensed version of SAPRC-99 and SAPRC-07 were developed for use in regional models. Organics are lumped according to the method similar with that of the RACM. SAPRC-99 has 79 species and 211 reactions, while SAPRC-07 has 110 species and 291 reactions only for the base and lumped VOCs mechanisms.

Master Chemical Mechanism (MCM) is a near-explicit chemical mechanism which describes the detailed gas-phase chemical processes and contains 142 non-methane VOCs, 6700 primary, secondary and radical species, and more than 17000 reactions. The mechanism is developed using the protocol for the tropospheric degradation of VOCs by Jenkin et al. (1997). The latest version is MCM v3.3.1 with detailed information from this website, <http://mcm.leeds.ac.uk/MCMv3.3.1/home.htm>. Several previous versions include MCM v1 (Derwent et al., 1998), MCM v2 (Jenkin and Hayman, 1999), MCM v3 (Jenkin et al., 2003; Saunders et al., 2003), MCM v3.1 (Bloss et al., 2005) and MCM v3.2 (released in 2011). MCM v3.3.1 mainly updated the isoprene degradation chemistry and ozonolysis rate constants for alpha-pinene, beta-pinene, limonene, and beta-caryophyllene, which have significant impact on HO_x (OH+HO₂) and NO_x (NO+NO₂) recycling (Jenkin et al., 2015). Unknown VOCs

chemistry is assumed similar with the studied reactions of chemical species with similar structure and reactivity. Acting as a reference benchmark mechanism, MCM can be used to evaluate other condensed mechanisms and the Common Representative Intermediates (CRI) mechanism which is a reduced mechanism based on full MCM (Jenkin et al., 2008; Watson et al., 2008). MCM is another mechanism to assess the contribution of different VOCs to O₃ formation as SAPRC.

Table 3- 1. Characteristics of these chemical mechanisms (Parameters of CB05,SAPRC-99, SAPRC-07 are from Chen et al., (2010)).

Mechanisms	CB05	RACM2.0	SAPRC-99 ^a	SAPRC-07 ^a	MCM3.3.1
Lumped type	structure	molecule	molecule	molecule	Near-explicit
# of reactions	156	363	211	291	17242
Photolysis	23	33	30	34	~2600
Inorganic	44	37	45	55	37
Organic	89	293	136	202 ^b	~14600
Other	-	-	-	-	3
# of species	51	119	79	110	5833
Stable inorganic	12	17	17	17	17
Short-lived inorganic	4	4	4	9^c	4
Stable organic	26	55	42	42	(142)^d
Alkanes	3	5	6	6	(22)
Alkenes	3	4	3	3	(17)
Biogenics	2	3	2	2	(5)
Aromatics	3	7	3	4	(18)
Carbonyls	5	15	13 ^e	13	(19)
Organic nitrates	3	6	5	5	~366
Organic peroxides	2	4	2	2	~1391
Organic acids	3	3	5	5	~90(3)
other	2	8	3	2	(58)
Short-lived organic	9	43	16	42^f	~939^g

a. With extended mechanism for lumped VOCs. b. 72 of these are reactions of steady-state peroxy radical operators. c. Including four steady-state inorganic operators, such as OH. d. Numbers of primary emitted VOCs are shown within parentheses. e. Including aromatic aldehydes. f. Including 29 steady-state organic operators, such as HCHO. g. Number of the organic peroxy radicals.

3.3.2 MCM protocol for mechanism development

MCM v3.3.1 describes the degradation of 18 alcohols and glycols, 9 aldehydes, 22 alkanes, 16 alkenes, 2 dialkenes, 3 monoterpenes, 1 alkyne, 18 aromatics, 16 chloro and hydrochlorocarbons, 8 esters, 10 ethers and glycol ethers, 2 hydrobromocarbons, 10 ketones, 1 sesquiterpenes, 3 organic acids and 4 unclassified compounds. In addition to the organic chemistry, MCM v3.3.1 contains 48 inorganic reactions comprised by 37 thermal gas-phase reactions, 3 gas-particle reactions and 8 photolysis reactions.

Two steps are used to construct the MCM: firstly, the development of a protocol to guide the reaction processes from initiation, propagation to termination; secondly, the development of mechanism for different emitted VOCs based on the protocol. Recent protocol was created to describe the degradation of non-aromatics by Saunders et al. (2003) and aromatics by Jenkin et al. (2003) based on the original protocol developed in 1997 by the University of Leeds. The kinetic and mechanistic data based on the protocol were initially used in a model to simulate the tropospheric oxidation of VOCs and to assess the formation of ozone in the boundary layer over Europe (Jenkin et al., 1997).

The degradation of emitted VOCs and OVOCs were initiated by reactions with OH, O₃, NO₃ and photolysis. All the non-methane hydrocarbons (NMCH) react with OH radical to form organic peroxy radicals (RO₂) through H-extraction and addition of O₂. O₃ reacts with alkenes, dienes and unsaturated oxygenated products to form Criegee biradicals and oxygenated products. NO₃ mainly reacts with double carbon bond to form RO₂. OH and O₃ are the main oxidizing agents during the daytime, and the primary

sources of OH are photolysis of OVOCs, HONO and O₃. O₃ is oxidation product in daytime, while NO₃ daytime lifetime is short due to fast photolysis. Photolysis of OVOCs can also lead to HO₂ and RO₂ formation.

The propagation means reactions of intermediates, including RO₂, excited Criegee biradicals, oxy radical (RO). RO mainly reacts with O₂ to form HO₂ and oxygenated products while it leads to OH and HO₂ formation through decomposition and isomerisation. RO₂ react with NO to form RO or RONO₂ and RO₂ react with NO₂ to form RO₂NO₂ or peroxyacyl nitrates (PANs). RO₂ react with NO₃ to form RO, react with HO₂ to form ROOH and react with R'O₂ to form oxygenated products. Excited Criegee biradicals are stabilized through loss of energy to form stabilized Criegee biradicals which react with H₂O, NO, NO₂, CO and SO₂. Excited Criegee biradicals can decompose to form OH, HO₂ or RO₂.

Oxygenated products are a variety of carbonyl compounds, RONO₂, acyl peroxy nitrates (RC(O)OONO₂), hydroperoxides (ROOH), percarboxylic acids (RC(O)OOH), carboxylic acids (RC(O)OH), alcohols (ROH), and multifunctional compounds containing two or more of these functionalities (Jenkin et al., 1997). All these oxygenated products are called “first generation products” which further degrade within the same framework. This process continued until the chemistry either yields CO₂, or until an organic product or radical is generated for which the subsequent chemistry is already represented in the mechanism (Jenkin et al., 1997). The flow chart in Fig. 3-1 shows the process of the formation of the first generation products.

Simplification is required in this so-called explicit mechanism to limit the total amount of reactions in the system. Firstly, for OH initialized reactions, the chemistry is simplified by limiting the product channels as \leq four channels and disregarding “minor” channels. This method is used to simplify the degradation of first and subsequent generation products (Jenkin et al., 1997). Secondly, degradation of minor products is significantly simplified to maintain proper lifetimes of the products, to keep the carbon and nitrogen balance and to reflect radical propagation and termination processes adequately. The organic nitrates, acyl peroxy nitrates, hydroperoxides, percarboxylic acids, carboxylic acids and alcohols are regarded as minor products (Saunders et al., 2003). Thirdly, reactions between two peroxy radicals are substantially reduced by treating ~1000 peroxy radicals as one representation item which is the sum of all the organic peroxy radicals. Each peroxy radical reacts with this summed item.

Rate coefficients in MCM mainly come from the reviews of laboratory determinations by Atkinson (Atkinson, 1986; Atkinson, 1990; Atkinson, 1997; Atkinson, 2007; Atkinson and Arey, 2003) and Calvert (Calvert et al., 2000). Where no experimental data exist, rate coefficients appropriate to 298K are estimated by a number of reported methods, such as the structure-activity relationship (SAR) method for alkanes, carbonyls and chlorinated hydrocarbons, alkenes and dienes, and the group reactivity (GR) method for alcohols, glycols, esters and glycol ethers (Saunders et al., 2003 and references therein).

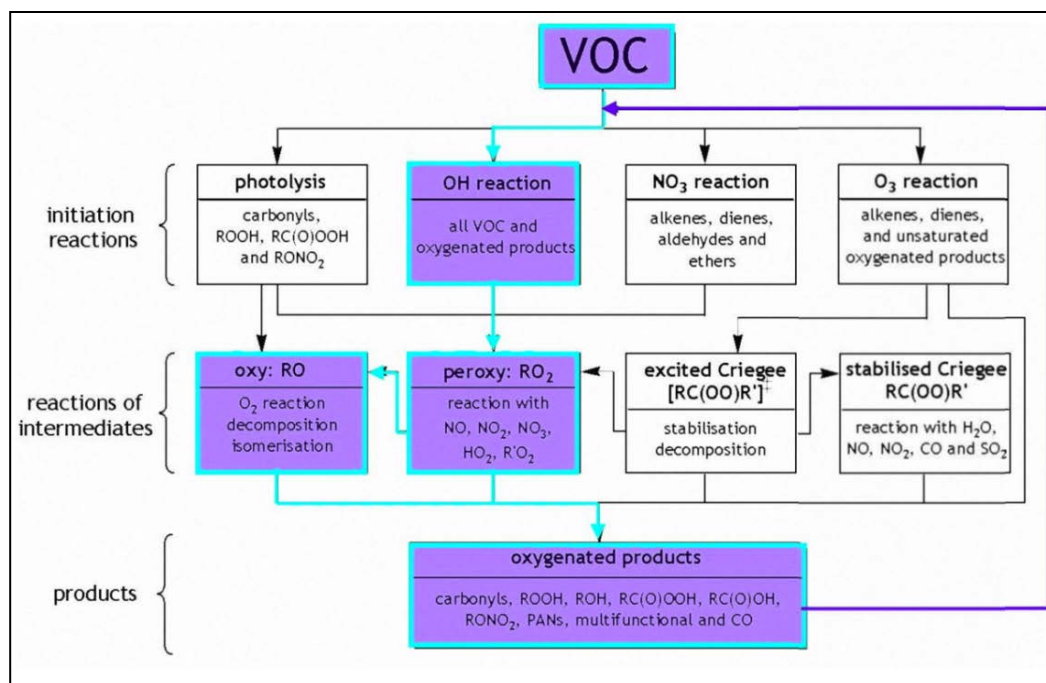


Figure 3- 1. Flow chart of main types of reactions in MCM protocol (from website: <http://mcm.leeds.ac.uk/MCMv3.3.1/project.htm>)

According to the protocol, MCM reactions can be grouped into several categories. Inorganic reactions are treated individually, but it is necessary to group organic reactions for production analysis of radicals or certain compound. RO_x budget is treated as production and loss rates of OH, HO_2 and RO_2 . HCHO as the main source of HO_2 is also treated explicitly, but the production of HO_2 from the photolysis of other aldehyde species is considered as a group (Emmerson et al., 2005b). A complete list of the groupings is given in Table 3-2.

Table 3- 2. Groupings of MCM reactions.

Group of reactions	Products	Name of rate constant
Photolysis reactions		
ROOH/ROOOH/ RCO2H/RCO3H + hv	$\underline{RO}/\underline{RO}_2/\underline{RCO}_3^3 + \underline{OH}/\underline{HO}_2$	
OVOCs+hv	$\underline{HO}_2 + \underline{RO}_2/\underline{RCO}_3/\underline{RO}/\underline{OVOC}$	
OVOCs+hv	$\underline{RO}_2/\underline{RCO}_3$	
OH+VOCs		
OH+CH ₄	$\underline{CH}_3\text{O}_2$	
OH+ primary NMCHs	\underline{RO}_2	
OH+ primary OVOCs	$\underline{HO}_2 + \text{aldehydes/ketones}$	
OH+ secondary VOCs	$\underline{RO}/\underline{RO}_2/\underline{RCO}_3$	
OH+ R~OH ^b	$\underline{HO}_2 + \text{aldehydes/ketones}, \underline{RO}_2/\underline{RCO}_3$	
O₃+alkenes/unsaturated OVOCs		
O ₃ +alkenes/unsaturated OVOCs	CB+aldehydes	
CB decomposition	$\underline{OH}/\underline{HO}_2/\underline{RO}_2/\underline{RCO}_3$	
NO₃ reactions		
NO ₃ +aldehydes/minor OVOCs	$\underline{RCO}_3 + \text{HNO}_3$, few exceptions	
NO ₃ +other VOCs	$\underline{RO}_2/\underline{RCO}_3 + \text{HNO}_3$, few exceptions	
RO₂ degradation		
RO ₂ +NO	RONO ₂ $\underline{RO} + \text{NO}_2$	KRO2NO* α KRO2NO* β
RO ₂ +NO ₃	$\underline{RO} + \text{NO}_2 + (\underline{HO}_2)$	KRO2NO3
RO ₂ +HO ₂	ROOH	KRO2HO2
RO ₂ +R'O ₂	RCHO ROH R'O	α β γ
RCO₃ degradation		
RCO ₃ +NO	$\underline{RO}_2/\underline{R}'\underline{CO}_3 + \text{NO}_2 + (\underline{HO}_2)$	KRO2NO
RCO ₃ +NO ₂	PANs	KFPAN
RCO ₃ +NO ₃	$\underline{RO}_2/\underline{R}'\underline{CO}_3 + \text{NO}_2 + (\underline{HO}_2)$	KRO2NO3
RCO ₃ +HO ₂	RCO2H/ROOH+O ₃ $\underline{RO}_2 + \underline{OH}, \text{RNO}_3^{\text{d}} + \underline{HO}_2 + \underline{OH}$ RCO3H	KAPHO2* α^c KAPHO2* β KAPHO2* γ
RCO ₃ +RO ₂	ROOH/Acids $\underline{R}'\underline{O}_2, \text{ROH} + \underline{R}'\underline{CO}_3$ aldehydes/ketones+($\underline{HO}_2 + \text{NO}_2$),	α β γ
PAN degradation		
PAN decomposition	$\underline{RCO}_3 + \text{NO}_2$	KBPAN
OH+PAN	aldehydes/ketones/ROOH/ROH/PANs /difunctional OVOCs/RNO ₃ / / $\underline{RCO}_3/\underline{RO}_2/ + \text{NO}_2 + (\text{CO} + \underline{HO}_2 + \text{NO}_3)$	
PAN+hv	$\underline{RCO}_3 + \text{NO}_2$	
RONO₂ degradation		
OH+RONO ₂	Aldehydes+NO ₂ , complex products	
RONO ₂ +hv	$\underline{RO} + \text{NO}_2, \underline{HO}_2 + \text{OVOC}, \underline{RCO}_3 + \text{NO}_2$	
RO degradation		
RO+O ₂	aldehydes/ketones + HO ₂	KROPRIM*O ₂
RO+O ₂	aldehydes/ketones + HO ₂	KROSEC*O ₂
RO decomposition	VOCs+ $\underline{HO}_2/\underline{OH}, \underline{RO}_2/\underline{RCO}_3$	KDEC
Isomerization		
Isomerizations	$\underline{OH}/\underline{HO}_2$	KISOM

Statements: a: RCO3 is products from reactions of OH and compounds with C=O bond through H extraction. b: R~OH is ROH,ROOH, ROOOH, RCO2H [RC(O)OH], and RCO3H [RC(O)OOH], with functionalities as C-OH, C-O-OH, HO-C=O, HO-O-C-C=O and HO-O-C=O. c: α,β,γ means branching ratios for products of certain kind of reactions. d: RNO₃ is designated for the difference from RONO₂ which formed from RO₂+NO.

MCM is not developed in conjunction with environmental chamber datasets and does not have the associated in-built validation (Saunders et al., 2003). Methods for testing and validation of MCM can be summarized as two main pathways. Firstly, the mechanism is incorporated into an atmospheric boundary layer model to simulate the chemistry processes in ambient air so that intercomparison with other chamber-validated mechanisms or reproduction of field-observed organic products or radicals. Secondly, comparisons with results from known chamber studies for oxidation of individual or mixture of VOCs species and NO_x are conducted by setting up a special box model with the mechanism.

3.3.3 Chlorine chemistry for MCM

MCM v3.3.1 only considers the 41 chlorine radical (Cl) reactions with alkanes. Xue et al. (2015) developed a chlorine chemistry module with 205 reactions for the MCM based on the previous mechanisms. These reactions include 15 Cl-initiated degradation of aldehydes, 21 reactions for ketones, 42 reactions for alcohols, 5 reactions for organic acids, 5 reactions for organic nitrates, 13 reactions for aromatics, 6 reactions for alkenes (individual reactions for C₂H₄, C₃H₆ and C₅H₈, one lumped reaction for other olefins) and 1 reaction with acetylene, along with 19 inorganic reactions and 5 heterogeneous reactions. This mechanism have been used to assess the importance of ClNO₂ in Chinese atmosphere (Xue et al., 2015;Wang et al., 2016). Table 3-3 shows the inorganic

reactions for the chlorine chemistry module, and Table 3-4 gives examples of reactions of Cl with organics.

Table 3- 3. Inorganic reactions incorporated into MCM3.3.1(from Xue et al. (2015)).

Category	Reaction	k (cm ³ molecules ⁻¹ s ⁻¹ or s ⁻¹) or J (s ⁻¹)	Remarks
Photolysis reactions	Cl ₂ →Cl+Cl	J_{Cl_2}	–
	ClONO ₂ → NO ₂ + Cl	J_{ClONO_2}	–
	ClONO ₂ → NO ₃ + Cl	$0.83 \times J_{ClONO_2}$	a
	ClONO ₂ → NO ₂ + ClO	$0.17 \times J_{ClONO_2}$	a
	HOCl → OH + Cl	J_{HOCl}	–
Cl+X	Cl + O ₃ → ClO + O ₂	$2.8 \times 10^{-11} \times \exp(-250/T)$	b
	Cl + HO ₂ → HCl + O ₂	3.5×10^{-11}	b
	Cl + HO ₂ → ClO + OH	$7.5 \times 10^{-11} \times \exp(-620/T)$	b
	Cl + H ₂ O ₂ → HCl + HO ₂	$1.1 \times 10^{-11} \times \exp(-980/T)$	b
	Cl + NO ₃ → NO ₂ + ClO	2.4×10^{-11}	b
	Cl+ ClONO ₂ → Cl ₂ + O ₃	$6.2 \times 10^{-12} \times \exp(145/T)$	b
OH+X	OH + HCl → Cl + H ₂ O	$1.7 \times 10^{-12} \times \exp(-230/T)$	b
	OH + Cl ₂ → HOCl + Cl	$3.6 \times 10^{-12} \times \exp(-1200/T)$	b
	OH + HOCl → ClO + H ₂ O	5.0×10^{-13}	b
	OH + ClO → HO ₂ + Cl	1.8×10^{-11}	b
	OH + ClO → HCl + O ₂	1.2×10^{-12}	b
ClO+X	ClO + NO ₂ → ClONO ₂	7.0×10^{-11}	b
	ClO + HO ₂ → HOCl + O ₂	$2.2 \times 10^{-12} \times \exp(340/T)$	b
	ClO + NO → Cl + NO ₂	$6.2 \times 10^{-12} \times \exp(295/T)$	b
Hetero. reactions	N ₂ O ₅ → NA + NA	$0.25 \times C_{N_2O_5} \times \gamma_{N_2O_5} \times S_{AERO} \times (1 - \text{ClONO}_2)$	c
	N ₂ O ₅ → NA + ClONO ₂	$0.25 \times C_{N_2O_5} \times \gamma_{N_2O_5} \times S_{AERO} \times \phi_{ClONO_2}$	c
	NO ₃ → products	$0.25 \times C_{NO_3} \times \gamma_{NO_3} \times S_{AERO}$	c
	ClONO ₂ → Cl ₂ + HNO ₃	$0.25 \times C_{ClONO_2} \times \gamma_{ClONO_2} \times S_{AERO}$	c
	HOCl → Cl ₂	$0.25 \times C_{HOCl} \times \gamma_{HOCl} \times S_{AERO}$	c

a: The branching ratio is determined based on the Tropospheric Ultraviolet Visible (TUV) Radiation model calculations (http://cprm.acd.ucar.edu/Models/TUV/Interactive_TUV/). b: The kinetic data are taken from the IUPAC database (<http://iupac.pole-ether.fr/index.html>). c: C_X is the molecular speed of X; γ_X is the uptake coefficient of X on aerosols; S_{AERO} is the aerosol surface area concentration; φ_{ClONO₂} is the product yield of ClONO₂ from the heterogeneous reactions of N₂O₅. NA is nitrate aerosol.

Table 3- 4. Examples of reactions of Cl with organics (from Xue et al. (2015)).

Reactions	Reactions
$\text{Cl} + \text{CH}_4 \rightarrow \text{CH}_3\text{O}_2 + \text{HCl}$	$\text{CH}_3\text{OH} + \text{Cl} \rightarrow \text{HO}_2 + \text{HCHO} + \text{HCl}$
$\text{Cl} + \text{C}_2\text{H}_6 \rightarrow \text{C}_2\text{H}_5\text{O}_2 + \text{HCl}$	$\text{C}_2\text{H}_5\text{OH} + \text{Cl} \rightarrow \text{CH}_3\text{CHO} + \text{HO}_2 + \text{HCl}$
$\text{Cl} + \text{HCHO} \rightarrow \text{HCl} + \text{HO}_2 + \text{CO}$	$\text{C}_2\text{H}_5\text{OH} + \text{Cl} \rightarrow \text{HOCH}_2\text{CH}_2\text{O}_2 + \text{HCl}$
$\text{Cl} + \text{CH}_3\text{CHO} \rightarrow \text{CH}_3\text{CO}_3 + \text{HCl}$	$\text{HCOOH} + \text{Cl} \rightarrow \text{HO}_2 + \text{HCl}$
$\text{Cl} + \text{CH}_3\text{CHO} \rightarrow \text{HCOCH}_2\text{O}_2 + \text{HCl}$	$\text{CH}_3\text{CO}_2\text{H} + \text{Cl} \rightarrow \text{CH}_3\text{O}_2 + \text{HCl}$
$\text{Cl} + \text{GIYOX} \rightarrow \text{CO} + \text{CO} + \text{HO}_2 + \text{HCl}$	$\text{C}_2\text{H}_4 + \text{Cl} \rightarrow \text{CH}_2\text{ClCH}_2\text{O}_2$
$\text{CH}_3\text{COCH}_3 + \text{Cl} \rightarrow \text{CH}_3\text{COCH}_2\text{O}_2 + \text{HCl}$	$\text{C}_3\text{H}_8 + \text{Cl} \rightarrow \text{ISOCIO}_2$
$\text{C}_2\text{H}_2 + \text{Cl} \rightarrow \text{ClCHO} + \text{CO} + \text{HO}_2$	

3.4 A zero-dimensional chemical box model

3.4.1 Brief introduction of the box model

A zero-dimensional box model assumes the simulated atmospheric boundary layer as a big box from the earth surface to the upper boundary layer and neglect the influence from vertical and horizontal turbulence. This kind of model is proper to be applied to simulate species, like OH and HO₂, with short lifetime and quick reactions with local emitted species (Perner et al., 1987; Poppe et al., 1994). The model is observation-based, which means that the concentration of long-lived species which are involved in chemical mechanisms should be measured with quantitative instruments and constrained in the model, thus, the model simulates the tropospheric processes with the actual concentration in the environment to reproduce the processes properly. The main assumptions are the spatial homogeneity for the air parcels passing the experimental site and the quasi-steady state which requires constant precursor concentrations and

meteorological conditions within the parcel over the chemical relaxation time (Poppe et al., 1994). Carslaw et al. (1999) employed MCM v1 into the model to simulate the formation of OH and HO₂, and described the model construction in detail. Here I briefly describe the main parts of this model.

This observation-based model was applied to quantify the in situ O₃ production and RO_x budget. The model was developed based on Master Chemical Mechanism (MCM v3.3.1), which contains 143 VOCs, 5836 species and 17242 reactions. The O₃ production method has been successfully used in our group's published papers which used MCM v3.2 as the chemical part (Xue et al., 2014a; Xue et al., 2014b; Xue et al., 2014c). Here the RO_x budget calculation method was developed by me individually and compared well with the results in the paper of Xue et al. (2016). In order to study the impact of Cl chemistry on atmospheric oxidation capacity, I also added the special Cl module developed by Xue et al. (2015) in addition to the original Cl related reactions in MCM v3.3.1 (eg. Cl reactions with alkanes).

3.4.2 Calculation of ozone production rate and RO_x budget

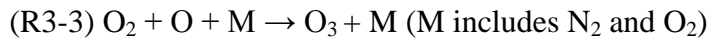
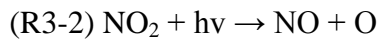
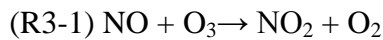
Chemical reactions, physical parameters such as dry deposition and heterogeneous loss must be considered in the model. So the rate of chemical change of species of *i* within the box can be described as follows:

$$(E3-1) \frac{dC_i}{dt} = P_i - L_i C_i - \frac{V_i C_i}{h} - k_{\text{het}} C_i$$

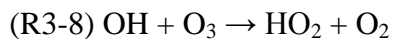
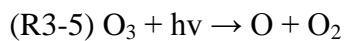
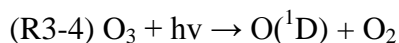
where C_i is the concentration of the species in the box, P_i is the production term, LiC_i describes the loss due to chemical and photolysis reactions, V_i is the deposition velocity of species i over mixing height h , and k_{het} is the rate of loss of the species by heterogeneous processes (Carslaw et al., 1999).

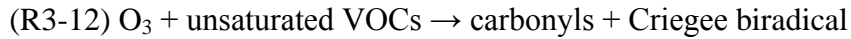
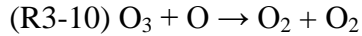
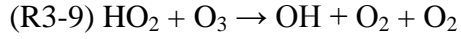
Calculation for ozone production rate

There are two pathways to calculate the ozone production rate: one is for O_3 production and loss, and the other one is for O_x production and loss which treats O_3 and NO_2 as a whole due to the recycling reactions of NO between them (R3-1 to R3-3).



The O_3 production rate relates to R3-3 here. The O_3 loss rate relates to the following reactions:





Thus the O_3 production and loss rates can be calculated as:

$$(E3-2) P(\text{O}_3) = k_1[\text{O}_2][\text{O}][\text{M}(\text{N}_2)] + k_1 [\text{O}_2][\text{O}][\text{M}(\text{O}_2)]$$

$$(E3-3) L(\text{O}_3) = J_{\text{O}_3}[\text{O}_3] + k_3[\text{NO}][\text{O}_3] + k_4[\text{NO}_2][\text{O}_3] + k_5[\text{OH}][\text{O}_3] + k_6[\text{HO}_2][\text{O}_3] + k_7[\text{O}][\text{O}_3] + k_8[\text{Cl}][\text{O}_3] + \sum(k_{9i}[\text{VOC}_i])[\text{O}_3] + \text{dry deposition}$$

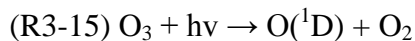
$$(E3-4) \text{net } P(\text{O}_3) = P(\text{O}_3) - L(\text{O}_3)$$

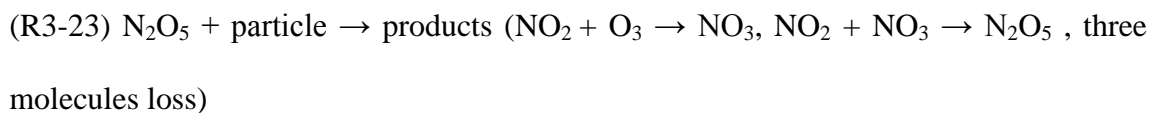
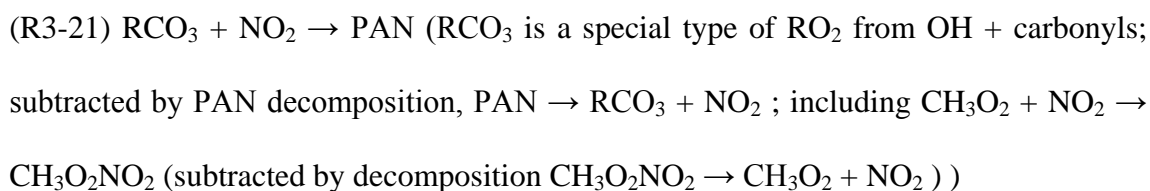
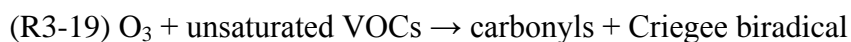
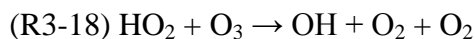
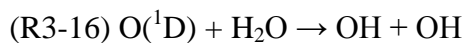
Hereafter, $P(\text{O}_3)$ means net O_3 production rate. This method can be found in Xue et al. (2014b).

The O_x production relates to the following reactions:



The O_x loss rate relates to reactions as follows:





Thus O_x production and loss rate can be calculated as:

(E3-5) $P(O_x) = k_1[HO_2][NO] + \sum(k_{2i}[RO_2]_i[NO])$

(E3-6) $L(O_x) = k_3[O(^1D)][H_2O] + k_4[OH][O_3] + k_5[HO_2][O_3] + \sum(k_{6i}[VOC]_i) [O_3] + k_7[OH][NO_2] + k_8[NO_2][RCO_3] + 2\sum(k_{9i}[VOC]_i) [NO_3] + 3 \text{ Heter. loss}_{N_2O_5} + 2 \text{ Heter. loss}_{NO_3} + \text{dry deposition}$

$$(E3-7) \text{ net } P(O_x) = P(O_x) - L(O_x)$$

This calculation of $P(O_x)$ is extensively applied to represent O_3 production rate in polluted areas for the fast transformation between O_3 and NO_2 (Xue et al., 2014c; Liu et al., 2012; Zhou et al., 2014). Normally, $P(O_3)$ and $P(O_x)$ has good correlation with each other which was shown in Xue et al. (2014b). But the latter method was more widely used.

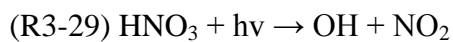
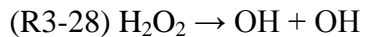
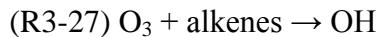
Calculation for RO_x budget

RO_x includes OH, HO_2 , RO and RO_2 , and the budget means the pathways for production and loss. The formation and destruction of these radicals in ambient air are so complex that I summarized the main reaction types here. First, some reactions provide primary OH, HO_2 and RO_2 formation, including reactions as follows:

OH primary sources:

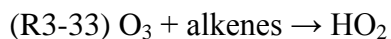
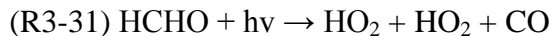


(R3-26) $HONO + hv \rightarrow OH + NO$ (this reaction is gross HONO photolysis, it should be deducted by $OH + NO \rightarrow HONO$ as primary source)

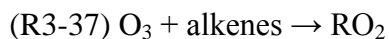




HO₂ primary sources:



RO₂ primary sources:

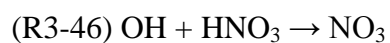
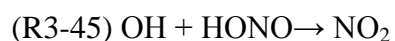
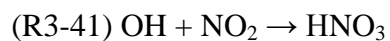
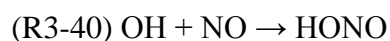


HONO has some sources not well-known in the ambient air, and these reactions are not included in the box model, so measured HONO data are needed for the model to be constrained with these data. ClNO₂ heterogeneous formation is included in the model, but it is difficult to reproduce the measured ClNO₂ with these assumed uptake coefficients and yields due to the high variability of these parameters in the ambient air,

so measured ClNO₂ data are also required as Cl radical source via photolysis. The reaction rates for these reactions are combined together to get the distribution of primary RO_x production rates (Elshorbany et al., 2012;Elshorbany et al., 2010;Elshorbany et al., 2009a;Elshorbany et al., 2009b;Emmerson et al., 2005a;Liu et al., 2012;Michoud et al., 2012).

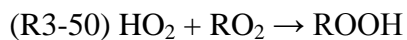
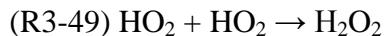
Second, radical termination reactions mean that one radical reacts with another reactant and no radical is formed. This represents radical eliminating processes from the air, which mainly happens when collided into NO_x (Edwards et al., 2014;Edwards et al., 2013). These reactions are listed as follows:

Follows are OH termination reactions:





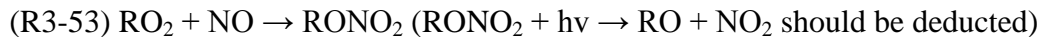
Follows are HO₂ termination reactions:



(R3-51) $\text{HO}_2 + \text{NO}_2 \leftrightarrow \text{HO}_2\text{NO}_2$ (This is a reversible reaction, sometimes it is source of HO₂.)

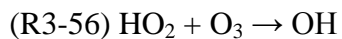
(R3-52) HO₂ heterogeneous loss

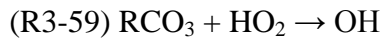
Follows are RO₂ termination reactions:



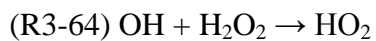
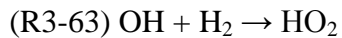
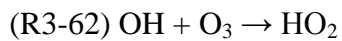
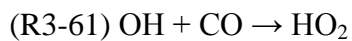
Third, there are some inter-transformation between two of the OH, HO₂, RO and RO₂, as the recycling to maintain the daytime radical concentrations.

Conversions from HO₂ to OH are as follows:





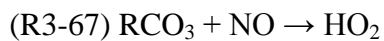
Conversions from OH to HO₂ are as follows:



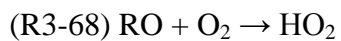
OH converses to RO₂:

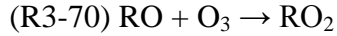


RO₂ converses to HO₂ :



RO is always an intermediate radical. It relates to HO₂ and RO₂ formation as follows:





The main source of RO is



These reactions contain the secondary production and loss for each kind of radical. In the model, the rates for each group of reactions are calculated and output.

3.4.3 Important physical parameters in the model

Solar zenith angle

Here solar zenith angle (θ_z) is needed for the calculation of Local Solar Time (LST) and the rate constants for different photolysis reactions. The zenith angle is the angle between the sun and the vertical.

$$(E3-8) \cos\theta_z = \sin\Phi\sin\delta + \cos\Phi\cos\delta\cosh$$

$$(E3-9) \sec\theta_z = 1/\cos\theta_z$$

$$(E3-10) \delta = \sin^{-1} \left(\sin \left(\frac{23.45}{\text{Radian}} \right) \times \sin \left(\frac{360}{365} (d - 81) \right) \right)$$

These equations are all from the website <http://www.pveducation.org/>. θ_z is the solar zenith angle, Φ is the local altitude, δ is the current declination angle of the sun. h is the hour angle in the local solar time, d is the number of days since the start of the year.

Photolysis reaction coefficient

Photolysis reactions are considered mainly for OVOCs, including aldehydes, ketones, organic peroxides and organic nitrates. Some compounds are not sensitive to wavelengths above 290 nm, so photolysis reactions are neglected for them. The photolysis rates are described with an expression of solar zenith angle.

$$(E3-11) J = I(\cos\theta_z)^m \exp(-n \times \sec\theta_z)$$

l , m , n are three parameters which are optimized according to the absorption cross section and quantum yield data from photolysis experiments (Jenkin et al., 1997; Saunders et al., 2003). And these optimized values are derived at an altitude of 0.5 km on 1 July at the latitude of 45°N for clear sky conditions. So the photolysis data have to be modified with the measured data according to the real data in the campaign, normally with $J(\text{NO}_2)$.

Reaction coefficients for special reactions

MCM contains a lot of RO_2 species, but the reaction coefficients between each RO_2 and NO , HO_2 or NO_3 are not quantified well. Thus, the mechanism treats the reaction coefficient as the same for each RO_2 species, but the branching ratios for the products of each type of reaction can be different for each RO_2 species. The reaction coefficients of these RO_2 -related reactions are denoted as $KRO2NO$, $KRO2HO2$, $KRO2NO3$ in the mechanism and $KAPNO$, $KAPHO2$ are special for RCO_3 reactions. The reaction coefficients of NO_3 reactions with RCHO are treated as $KNO3AL$ similarly. Parameters of $KDEC$, $KROPRIM$ and $KROSEC$ represent RO decomposition, primary RO reactions with O_2 , and secondary RO reactions with O_2 , respectively.

Deposition and dilution

This item in the model is employed to avoid the accumulation of long-lived species. The dry deposition velocity could be set as different values according to the simulated environment. Derwent et al. (1996) recommended the deposition velocities for NO₂ (0.15 cm s⁻¹), HNO₃ (2 cm s⁻¹), O₃ (0.5 cm s⁻¹), SO₂ (0.5 cm s⁻¹), PAN (0.2 cm s⁻¹, assumed the same for all PANs species) and Brasseur et al. (1998) recommended for HCHO (0.33 cm s⁻¹, assumed the same for all aldehydes), H₂O₂ (1.1 cm s⁻¹), methyl- and ethyl-nitrate (1.1 cm s⁻¹, assumed the same for all organic nitrates), and CH₃OOH (0.55 cm s⁻¹ and assumed the same for all organic peroxides). Michoud et al. (2012) applied the highest deposition velocity by function for the multifunctional species. This means the deposition velocity of a species with several functions take the parameter of the function which has the highest deposition velocity. For the remaining MCM species, the dry deposition velocities have been set to a default value of 0.5 cm s⁻¹ and a series of values from 0.0 to 2.0 cm s⁻¹ as sensitivity tests. Other literatures also have other choices for the deposition item.

A representative item was used in some literatures to indicate the lifetime of unconstrained species, which considered the total physical loss due to dry deposition and physical dilution/loss (Edwards et al., 2013, 2014). Most of the time, the physical loss rate coefficient is set as a first order factor of $1.15 \times 10^{-5} \text{ s}^{-1}$ which equals to 24 h lifetime or deposition velocity of 1.15 cm s⁻¹ at the mixing height of 1000 m. For OH reactivity modeling, the dry deposition velocity may need to be increased to 6 h lifetime

at the same mixing height to make the modeled OH reactivity match with the measured data(Tan et al., 2017).

3.4.4 Validation for the model setup

Comparison with radical budget with MCM v3.2

I compared the modeled results of radical concentrations and production rates with MCM v3.3.1 and MCM v3.2 based on the data of Tung Chung campaign on Nov. 25, 2011 as shown in Fig. 3-2. The results with MCM v3.2 were derived by Xue et al., (2016b). The radical concentrations with MCM v3.3.1 were quite close to the results with MCM v3.2. For the radical production rates, the results were also comparable. This indicated that the setup of the calculation of radical budgets with MCM v3.3.1 were applicable for further research.

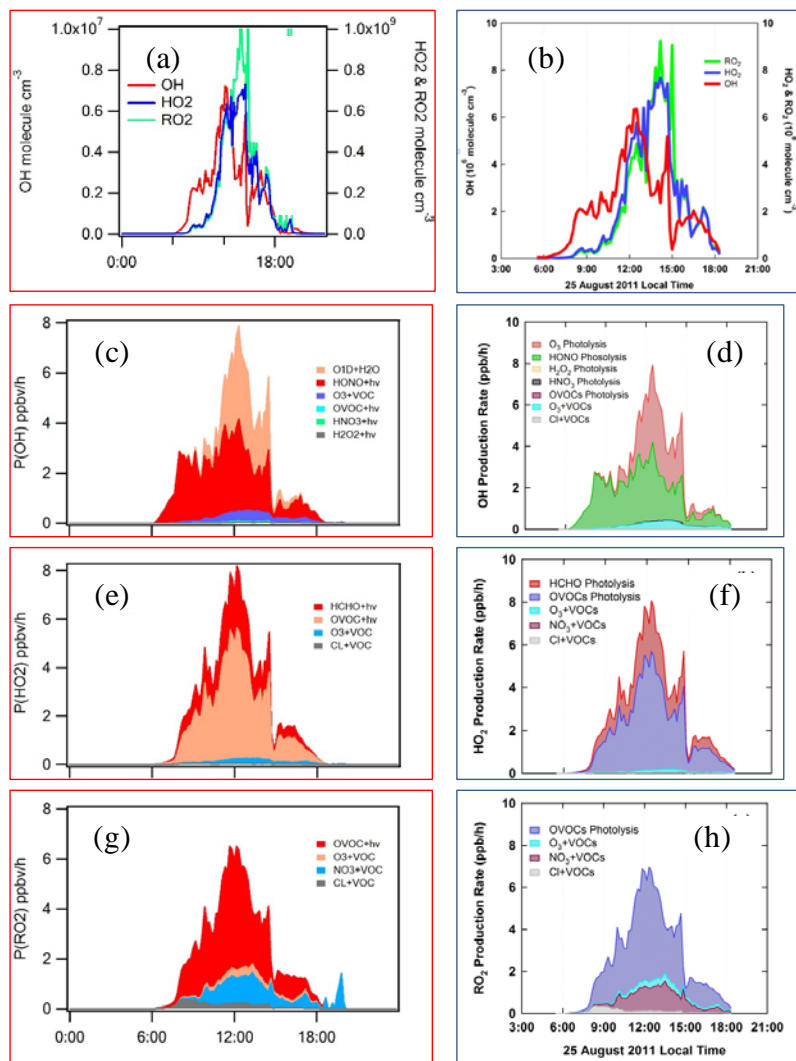


Figure 3- 2. Comparison between modeled results of radical concentrations and production rates with MCM v3.3.1 (left panel) and MCM v3.2 (right panel) based on the data of Tung Chung campaign on Nov. 25, 2011.

Comparison with measured OH and HO₂

I use the simulated and measured results of OH and HO₂ in our Wangdu campaign to validate the model setup. OH, HO₂ and RO₂ concentrations were measured by laser

induced fluorescence (LIF) technique. LIF is a direct method to detect OH radicals, and HO₂ and RO₂ radicals can be detected by fluorescence after chemical conversion to OH (Tan et al., 2017). Generally, the model is setup as following and there could be some differences in the setup according to the research objectives and observed situation.

The observation data of ClNO₂, HCl, HONO, O₃, NO, NO₂, SO₂, CO, CH₄, C₂-C₁₀ NMHCs, OVOCs (methanol, formaldehyde, acetone, acetaldehyde, acetic acid, MEK, MTBE), H₂O, temperature, pressure and aerosol surface area were averaged or interpolated. The model was constrained by the observation data every 10 min. The input of photolysis frequency of NO₂ (J_{NO_2}), HONO (J_{HONO}), O₃ (J_{O_3}) and ClNO₂ (J_{ClNO_2}) were determined from the field measurement. The J_{ClNO_2} here was determined based on the cross section recommended by Sander et al. (2011). Photolysis frequency of other related compounds were predicted following the function of solar zenith angle (Saunders et al., 2003) in the model and were scaled according to the field measured J_{NO_2} . The lifetime of the unmeasured species with respect to physical first order loss rate was set as 6 h which equals to a deposition velocity of 4.63 cm s⁻¹ in a 1000 m deep boundary layer. The model was run for 24 hours period with the starting time as 00:00 local time and was repeatedly run for 6 times to stabilize the unmeasured intermediate species. The data for the last run was used for analysis. As shown in Fig. 3-3, modeled OH and HO₂ match quite well with the measured data, which verify the reliability of the model setup.

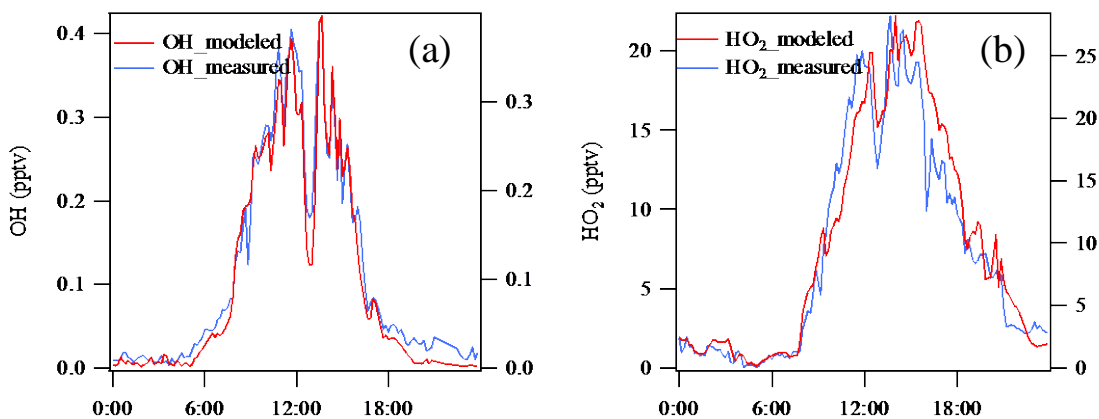


Figure 3- 3. Comparison between modeled and measured OH (a) and HO₂(b) for the 6.21 case

References

- Atkinson R. Kinetics and mechanisms of the gas-phase reactions of the hydroxyl radical with organic compounds under atmospheric conditions. *Chemical Reviews* 1986; 86: 69-201.
- Atkinson R. Gas-phase tropospheric chemistry of organic compounds: a review. *Atmospheric Environment. Part A. General Topics* 1990; 24: 1-41.
- Atkinson R. Gas-phase tropospheric chemistry of volatile organic compounds: 1. Alkanes and alkenes. *Journal of Physical and Chemical Reference Data* 1997; 26: 215-290.
- Atkinson R. Gas-phase tropospheric chemistry of organic compounds: a review. *Atmospheric Environment* 2007; 41: 200-240.
- Atkinson R, Arey J. Gas-phase tropospheric chemistry of biogenic volatile organic compounds: a review. *Atmospheric Environment* 2003; 37: 197-219.
- Bloss C, Wagner V, Jenkin ME, Volkamer R, Bloss WJ, Lee JD, et al. Development of a detailed chemical mechanism (MCMv3.1) for the atmospheric oxidation of aromatic hydrocarbons. *Atmospheric Chemistry and Physics* 2005; 5: 641-664.
- Brasseur G, Hauglustaine D, Walters S, Rasch P, Müller JF, Granier C, et al. MOZART, a global chemical transport model for ozone and related chemical tracers: 1. Model description. *Journal of Geophysical Research: Atmospheres* 1998; 103: 28265-28289.

- Calvert J, Atkinson R, Kerr J, Madronich S, Moortgat G, Wallington T, et al. The mechanisms of atmospheric oxidation of the alkenes. Calvert, Jack G., et al. The mechanisms of atmospheric oxidation of the alkenes. Mechanisms of atmospheric oxidation of the alkanes. Oxford University Press, 2000:401-412.
- Carslaw N, Creasey DJ, Heard DE, Lewis AC, McQuaid JB, Pilling MJ, et al. Modeling OH, HO₂, and RO₂ radicals in the marine boundary layer: 1. Model construction and comparison with field measurements. Journal of Geophysical Research: Atmospheres 1999; 104: 30241-30255.
- Carter WP. Documentation for the SAPRC atmospheric photochemical mechanism preparation and emissions processing programs for implementation in airshed models. Appendix C, California Air Resource Board 1988a.
- Carter WP. Documentation of a gas phase photochemical mechanism for use in airshed modeling. Appendix B to final report on California ARB Contract 1988b.
- Carter WP. A detailed mechanism for the gas-phase atmospheric reactions of organic compounds. Atmospheric Environment. Part A. General Topics 1990; 24: 481-518.
- Carter WP. Development of ozone reactivity scales for volatile organic compounds. Air & Waste 1994; 44: 881-899.
- Carter WP. Documentation of the SAPRC-99 chemical mechanism for VOC reactivity assessment. Contract 2000a; 92: 95-308.
- Carter WP. Implementation of the SAPRC-99 chemical mechanism into the Models-3 framework. Report to the United States Environmental Protection Agency, January 2000b.
- Carter WP. Development of the SAPRC-07 chemical mechanism and updated ozone reactivity scales. field Has A Theoretical Side & An Applied Side the Former Is Part of the 2007.
- Carter WP. Development of a condensed SAPRC-07 chemical mechanism. Atmospheric Environment 2010a; 44: 5336-5345.
- Carter WPL. Development of the SAPRC-07 chemical mechanism. Atmospheric Environment 2010b; 44: 5324-5335.
- Chen S, Ren X, Mao J, Chen Z, Brune WH, Lefer B, et al. A comparison of chemical mechanisms based on TRAMP-2006 field data. Atmospheric Environment 2010; 44: 4116-4125.
- Derwent RG, Jenkin ME, Saunders SM. Photochemical ozone creation potentials for a large number of reactive hydrocarbons under European conditions. Atmospheric Environment 1996; 30: 181-199.
- Derwent RG, Jenkin ME, Saunders SM, Pilling MJ. Photochemical ozone creation potentials for organic compounds in northwest Europe calculated with a master chemical mechanism. Atmospheric Environment 1998; 32: 2429-2441.
- Edwards PM, Brown SS, Roberts JM, Ahmadov R, Banta RM, Dubé WP, et al. High winter ozone pollution from carbonyl photolysis in an oil and gas basin. Nature 2014; 514: 351-354.

- Edwards PM, Young CJ, Aikin K, deGouw J, Dube WP, Geiger F, et al. Ozone photochemistry in an oil and natural gas extraction region during winter: simulations of a snow-free season in the Uintah Basin, Utah. *Atmospheric Chemistry and Physics* 2013; 13: 8955-8971.
- Elshorbany YF, Kleffmann J, Hofzumahaus A, Kurtenbach R, Wiesen P, Brauers T, et al. HOx budgets during HOxComp: A case study of HOx chemistry under NOx-limited conditions. *Journal of Geophysical Research-Atmospheres* 2012; 117, D03307, doi:10.1029/2011JD017008.
- Elshorbany YF, Kleffmann J, Kurtenbach R, Lissi E, Rubio M, Villena G, et al. Seasonal dependence of the oxidation capacity of the city of Santiago de Chile. *Atmospheric Environment* 2010; 44: 5383-5394.
- Elshorbany YF, Kleffmann J, Kurtenbach R, Rubio M, Lissi E, Villena G, et al. Summertime photochemical ozone formation in Santiago, Chile. *Atmospheric Environment* 2009a; 43: 6398-6407.
- Elshorbany YF, Kurtenbach R, Wiesen P, Lissi E, Rubio M, Villena G, et al. Oxidation capacity of the city air of Santiago, Chile. *Atmospheric Chemistry and Physics* 2009b; 9: 2257-2273.
- Emmerson K, Carslaw N, Carpenter L, Heard D, Lee J, Pilling M. Urban atmospheric chemistry during the PUMA campaign 1: Comparison of modelled OH and HO₂ concentrations with measurements. *Journal of Atmospheric Chemistry* 2005a; 52: 143-164.
- Emmerson K, Carslaw N, Pilling M. Urban atmospheric chemistry during the PUMA campaign 2: Radical budgets for OH, HO₂ and RO₂. *Journal of Atmospheric Chemistry* 2005b; 52: 165-183.
- Gery MW, Whitten GZ, Killus JP, Dodge MC. A photochemical kinetics mechanism for urban and regional scale computer modeling. *Journal of Geophysical Research: Atmospheres* 1989; 94: 12925-12956.
- Goliff WS, Stockwell WR, Lawson CV. The regional atmospheric chemistry mechanism, version 2. *Atmospheric Environment* 2013; 68: 174-185.
- Jenkin ME, Hayman GD. Photochemical ozone creation potentials for oxygenated volatile organic compounds: sensitivity to variations in kinetic and mechanistic parameters. *Atmospheric Environment* 1999; 33: 1275-1293.
- Jenkin ME, Saunders SM, Pilling MJ. The tropospheric degradation of volatile organic compounds: A protocol for mechanism development. *Atmospheric Environment* 1997; 31: 81-104.
- Jenkin ME, Saunders SM, Wagner V, Pilling MJ. Protocol for the development of the Master Chemical Mechanism, MCM v3 (Part B): tropospheric degradation of aromatic volatile organic compounds. *Atmospheric Chemistry and Physics* 2003; 3: 181-193.
- Jenkin ME, Watson LA, Utembe SR, Shallcross DE. A Common Representative Intermediates (CRI) mechanism for VOC degradation. Part 1: Gas phase mechanism development. *Atmospheric Environment* 2008; 42: 7185-7195.
- Jenkin ME, Young JC, Rickard AR. The MCM v3.3.1 degradation scheme for isoprene. *Atmospheric Chemistry and Physics* 2015; 15: 11433-11459.

- Liang Y, Zha Q, Wang W, Cui L, Lui KH, Ho KF, et al. Revisiting Nitrous Acid (HONO) Emission from On-road Vehicles: A Tunnel Study with a Mixed Fleet. *Journal of the Air & Waste Management Association* 2017. 67(7), 797-805. <http://dx.doi.org/10.1080/10962247.2017.1293573>.
- Liu Z, Wang Y, Gu D, Zhao C, Huey L, Stickel R, et al. Summertime photochemistry during CAREBeijing-2007: RO_x budgets and O₃ formation. *Atmospheric Chemistry and Physics* 2012; 12: 7737-7752.
- Michoud V, Kukui A, Camredon M, Colomb A, Borbon A, Miet K, et al. Radical budget analysis in a suburban European site during the MEGAPOLI summer field campaign. *Atmospheric Chemistry and Physics* 2012; 12: 11951-11974.
- Perner D, Platt U, Trainer M, Hübler G, Drummond J, Junkermann W, et al. Measurements of tropospheric OH concentrations: A comparison of field data with model predictions. *Journal of atmospheric chemistry* 1987; 5: 185-216.
- Poppe D, Zimmermann J, Bauer R, Brauers T, Brüning D, Callies J, et al. Comparison of measured OH concentrations with model calculations. *Journal of Geophysical Research: Atmospheres* 1994; 99: 16633-16642.
- Sander, S. P., Abbatt, J., Barker, J. R., Burkholder, J. B., Friedl, R. R., Golden, D. M., Huie, R. E., Kolb, C. E., Kurylo, M. J., Moortgat, G. K., Orkin V. L., and Wine, P. H.: Chemical kinetics and photochemical data for use in atmospheric studies, Evaluation No. 17, JPL Publication 10-6, Jet Propulsion Laboratory, Pasadena, available at: <http://jpldataeval.jpl.nasa.gov> (last access: 5 September 2016), 2011.
- Saunders SM, Jenkin ME, Derwent RG, Pilling MJ. Protocol for the development of the Master Chemical Mechanism, MCM v3 (Part A): tropospheric degradation of non-aromatic volatile organic compounds. *Atmospheric Chemistry and Physics* 2003; 3: 161-180.
- Stockwell WR. A homogeneous gas phase mechanism for use in a regional acid deposition model. *Atmospheric Environment* 1986; 20: 1615-1632.
- Stockwell WR, Kirchner F, Kuhn M, Seefeld S. A new mechanism for regional atmospheric chemistry modeling. *Journal of Geophysical Research: Atmospheres* 1997; 102: 25847-25879.
- Stockwell WR, Middleton P, Chang JS, Tang X. The second generation regional acid deposition model chemical mechanism for regional air quality modeling. *Journal of Geophysical Research: Atmospheres* 1990; 95: 16343-16367.
- Tan Z, Fuchs H, Lu K, Hofzumahaus A, Bohn B, Broch S, et al. Radical chemistry at a rural site (Wangdu) in the North China Plain: observation and model calculations of OH, HO₂ and RO₂ radicals. *Atmos. Chem. Phys.* 2017; 17: 663-690.
- Wang T, Tham YJ, Xue L, Li Q, Zha Q, Wang Z, et al. Observations of nitryl chloride and modeling its source and effect on ozone in the planetary boundary layer of southern China. *Journal of Geophysical Research: Atmospheres* 2016; 121, doi:10.1002/2015JD024556.

- Watson LA, Shallcross DE, Utembe SR, Jenkin ME. A Common Representative Intermediates (CRI) mechanism for VOC degradation. Part 2: Gas phase mechanism reduction. *Atmospheric Environment* 2008; 42: 7196-7204.
- Whitten GZ, Heo G, Kimura Y, McDonald-Buller E, Allen DT, Carter WP, et al. A new condensed toluene mechanism for Carbon Bond: CB05-TU. *Atmospheric Environment* 2010; 44: 5346-5355.
- Whitten GZ, Hogo H, Killus JP. The carbon-bond mechanism: A condensed kinetic mechanism for photochemical smog. *Environmental science & technology* 1980; 14: 690-700.
- Xue L, Gu R, Wang T, Wang X, Saunders S, Blake D, et al. Oxidative capacity and radical chemistry in the polluted atmosphere of Hong Kong and Pearl River Delta region: analysis of a severe photochemical smog episode. *Atmos. Chem. Phys.* 2016; 16: 9891-9903.
- Xue L, Wang T, Wang X, Blake DR, Gao J, Nie W, et al. On the use of an explicit chemical mechanism to dissect peroxy acetyl nitrate formation. *Environ Pollut* 2014a; 195: 39-47.
- Xue LK, Saunders SM, Wang T, Gao R, Wang XF, Zhang QZ, et al. Development of a chlorine chemistry module for the Master Chemical Mechanism. *Geoscientific Model Development* 2015; 8: 3151-3162.
- Xue LK, Wang T, Gao J, Ding AJ, Zhou XH, Blake DR, et al. Ground-level ozone in four Chinese cities: precursors, regional transport and heterogeneous processes. *Atmospheric Chemistry and Physics* 2014b; 14: 13175-13188.
- Xue LK, Wang T, Louie PKK, Luk CWY, Blake DR, Xu Z. Increasing External Effects Negate Local Efforts to Control Ozone Air Pollution: A Case Study of Hong Kong and Implications for Other Chinese Cities. *Environmental Science & Technology* 2014c; 48: 10769-10775.
- Yarwood G, Rao S, Yocke M, Whitten G. Updates to the carbon bond chemical mechanism: CB05. Final report to the US EPA, RT-0400675 2005; 8.
- Zhou W, Cohan DS, Henderson BH. Slower ozone production in Houston, Texas following emission reductions: evidence from Texas Air Quality Studies in 2000 and 2006. *Atmospheric Chemistry and Physics* 2014; 14: 2777-2788.

Chapter 4. Nitrous acid in a street canyon environment: sources and contributions to local oxidation capacity

4.1 Introduction

A street canyon is a special urban microenvironment that is formed by parallel high buildings with vehicular roadways in the center (Bright et al., 2013). Poor ventilation conditions and substantial pollutants from vehicle emissions result in serious air pollution problems, posing high health risk to pedestrians, road-users, and surrounding residents (Bright et al., 2011; Bright et al., 2013; Kwak and Baik, 2012). It is well known that street canyons are highly polluted with freshly emitted NO_x and VOCs, but there are few reports of HONO in this microenvironment. In view of direct emissions of HONO from vehicles and secondary formation from NO_2 , elevated concentrations of HONO may be present in heavily trafficked street canyon environments, which can initiate the daytime oxidation processes.

Previous modeling studies of air chemistry in street canyons generally only considered the HONO source through a homogeneous reaction between OH and NO, which may underestimate the HONO concentration and the contribution of HONO to radicals. Bright et al. (2011) simulated the concentration of OH radicals inside and above a street canyon in a Birmingham city center, and their model showed approximately 0.1 pptv of OH within the street canyon and up to 0.8 pptv in the outflow above it. Kwak and Baik (2012) found that the modeled OH and HO_2 concentrations were below 0.3 and 5.0 pptv

inside a street canyon in Austin, Texas, and that OH concentrations increased with the increase of VOC emission but decreased with the increase of NO_x emission. Bright et al. (2013) suggested that the dominant source of OH inside a street canyon was the pathway of HO₂+NO followed by HONO photolysis, and the OH and HO₂ concentrations were below 0.12 and 0.4 pptv, respectively.

Hong Kong is a highly urbanized metropolis with high population density, a large number of vehicles, narrow streets, and congested buildings. Street canyons are widely distributed in downtown areas in this city, and poor air quality in these canyons has been a major concern (Ai et al., 2016; Tian et al., 2011). In the present study, HONO was measured at a roadside station inside a typical street canyon of urban Hong Kong in order to characterize its concentration levels in this special environment. A box model built on MCM v3.3.1 was applied to simulate local oxidation processes and to identify the contribution of HONO to the formation of radicals and secondary products. I first present an overview of the observed data, including HONO diurnal variation, in section 4.3. The vehicle emission ratio of HONO/NO_x is then derived in section 4.4. The contribution of HONO to radical concentration, radical budget, and photochemical secondary products (HNO₃ and OVOCs) are analyzed in section 4.5. The impact of HONO on local NO₂ and O₃ concentrations is discussed in section 4.6. To the best of our knowledge, this is the first assessment of the impact of high daytime HONO concentrations on oxidation chemistry in street canyons.

4.2 Experiment

4.2.1 Measurement sites and instruments

The measurements were conducted from March 28 to May 3, 2015, at a roadside air monitoring station in Mong Kok (MK, 22.32°N, 114.17°E, see Fig. 4-1). The station is part of the air monitoring network of the Hong Kong Environmental Protection Department (HKEPD). It is located at the junction of Nathan Road and Lai Chi Kok Road, whose average daily traffic flow in 2014 was 38,220 and 37,080, respectively (HKTD, 2014). The sampling point was less than 5m from traffic and 2 m above ground level. Vehicles on these roads mainly consist of private cars, taxis, public buses, and light-goods vehicles. Diesel, gasoline, and LPG engines accounted for 26%, 42%, and 32% of the average mix of engine types, respectively, according to the traffic count data from April 14 to 17, 2015. Surrounding the measurement site, restaurants and commercial buildings are distributed to the east and south, residential buildings are to the north, and small shops are to the west (Lee et al., 2015). High-density buildings with an average height of 80m make this area a deep street canyon that can trap traffic pollutants and lead to high NO_x concentrations (Ai et al., 2016).

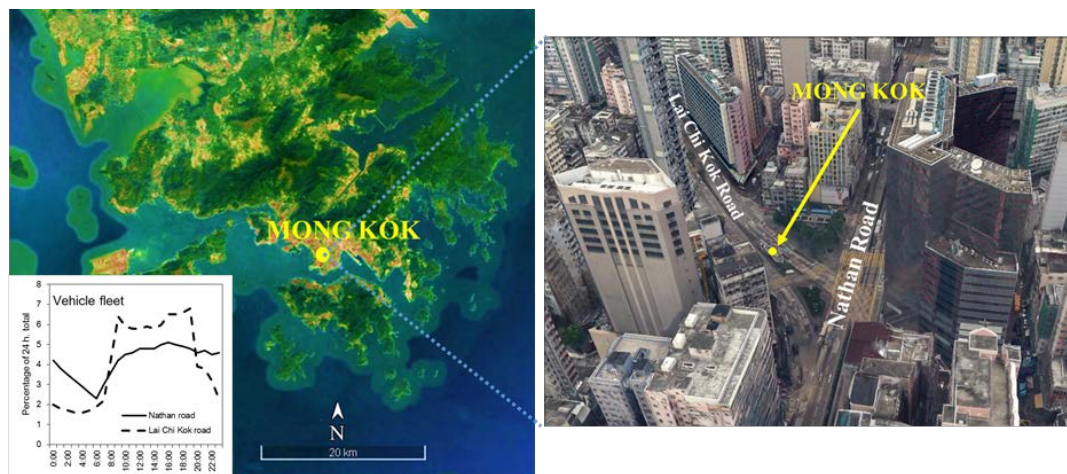


Figure 4- 1. Google map showing the sampling site of Mong Kok and the surrounding environment. The figure inset in the lower left corner shows the average diurnal variation of vehicle fleet on Nathan Road and Lai Chi Kok Road in 2014, provided by Hong Kong Transport Department.

HONO was continuously measured by LOPAP. CO, SO₂, NO, NO₂, O₃, black carbon (BC), and C₂–C₁₀ non-methane hydrocarbons (NMHCs) were also measured by HKEPD at the MK station. CO was measured with nondispersive infrared absorption with gas filter correlation (TECO 48C/API 300). SO₂ was analyzed with an ultraviolet fluorescence analyzer (TECO 43A/API 100E/TECO 43I). NO–NO₂–NO_x was detected using chemiluminescence (API 200A), with NO₂ converted by a molybdenum converter. This thermal catalytic conversion was expected to give reliable NO₂ results due to the dominance of fresh NO_x emission at this site (Xu et al., 2013). O₃ was monitored using the UV absorption method (API 400/API 400A). BC was detected with an AE-51 aethalometer with a time resolution of 10 s. The NMHCs, which included 10 alkanes, 8 alkenes, and 8 aromatics, were analyzed every 30 min with an online analytical system

(Syntech Spectra GC 955, Series 600/800, the Netherlands). The concentrations of OVOCs were not simultaneously measured during this campaign, but formaldehyde, acetaldehyde, methanol, ethanol, acrolein, acetone, and methyl ethyl ketone were measured in May, 2014, at the same station by a proton-transfer-reaction mass spectrometry (PTR-MS) (Cui et al., 2016). The OVOC data was used in the present study for model simulation. Solar radiation was measured at the MK site, and the data were compared with the measurements at King's Park (KP) weather station, which is 1.24 km southeast of the MK station and is operated by the Hong Kong Observatory. At the MK site, the surrounding buildings block the sun in the morning and afternoon, but not at noon. The solar radiation data were used to calculate the photolysis frequency of NO_2 following the method suggested by Trebs et al. (2009). Other meteorological data, including temperature, relative humidity (RH), wind speed, and wind direction were from KP station.

4.2.2 Model description

In order to evaluate the effect of HONO on daytime atmospheric oxidation capacity in the street canyon, a chemical box model with MCM v3.3.1 (Jenkin et al., 2003; Jenkin et al., 2015; Saunders et al., 2003) was applied to calculate the concentrations of OH, HO_2 , and RO_2 radicals and their production and loss rates. Sunny days during the measurement period were selected for model simulations. The daytime (7:00–17:00) average concentrations of NMHCs, OVOCs, and NO_x used for the SUNNY case are listed in Table 4-1. The concentrations of HONO, NO, NO_2 , SO_2 , CO, C2–C10 NMHCs, temperature, RH, and J_{NO_2} were averaged or interpolated every 10 min and constrained

into the model. To account for the direct emission of OVOCs from vehicle exhaust in Hong Kong (Ho et al., 2012), the average profiles of OVOCs in May, 2014, were also constrained in the model. The photolysis frequencies for HONO, O₃, and other species were calculated as a function of solar zenith angle within the model (Saunders et al., 2003) and scaled with the calculated J_{NO_2} values based on measured solar radiation. The first-order physical loss rates of the unconstrained species were set as $4.63 \times 10^{-5} \text{ s}^{-1}$ which is equal to a lifetime of 6 h in a boundary layer of 1000m depth (Tham et al., 2016). The model was run for 24 h starting from 0:00, and this process was repeated six times to stabilize the intermediate species. The output from 7:00–17:00 of the final run was used for further analysis. The original MCM mechanism only considers the formation pathway of HONO from OH+NO, which yields a much lower HONO concentration of 0.14 ppbv on average compared to the measured 3.2 ppbv. We compared cases with and without constraining the measured HONO to evaluate the importance of HONO. To further investigate the HONO impact on the secondary formation of OVOCs, sensitivity tests were conducted without constraining OVOCs. To gain insight into the HONO influence on local NO₂ and O₃ concentrations, sensitivity tests with adjustable NO_x emission rates and an extra O₃ source were also conducted.

Table 4- 1. Average mixing ratios (ppbv) from 7:00 to 17:00 for sunny days. OVOCs were obtained from Cui et al. (2016).

Species	Conc.	Species	Conc.	Species	Conc.
NO	81.0	n-Octane	0.158	m-xylene	0.244
NO ₂	72.3	Ethyne	4.709	o-xylene	0.067
HONO	3.2	Ethene	2.947	1,3,5-trimethylbenzene	0.040
O ₃	11.2	Propene	0.712	1,2,4-trimethylbenzene	0.083
Ethane	1.979	1-Butene	0.140	1,2,3-trimethylbenzene	0.050
Propane	3.394	cis-2-Butene	0.088	Formaldehyde	2.725
i-Butane	2.669	1,3-Butadiene	0.044	Methanol	3.638
n-Butane	4.101	trans-2-Pentene	0.079	Acetaldehyde	2.205
i-Pentane	0.793	1-Pentene	0.063	Ethanol	33.398
n-Pentane	0.265	Isoprene	0.051	Acrolein	1.427
n-Hexane	0.331	Benzene	0.263	Acetone	2.517
2-Methylpentane	0.370	Toluene	1.193	Methyl ethyl ketone	0.453
n-Heptane	0.137	Ethylbenzene	0.087		

4.3 General description of trace gases

The time series of meteorological conditions, O₃, CO, NO, NO₂, total NMHCs, HONO, BC, and J_{NO_2} are shown in Fig. 4-2. The shaded periods represent overcast days with total bright sunshine hours less than five. The hourly concentrations of HONO varied from 0.4 to 13.9 ppbv during the measurement period, with an average of 3.3 ppbv. The average NO and NO₂ concentrations were 74.5 ppbv (1.1–233.5 ppbv) and 55.3 ppbv (9.4–179.7 ppbv), respectively. The level of O₃ ranged from 0.7 to 52.4 ppbv, with an average of 7.6 ppbv. The average NMHC concentration for sunshine days was 87.1 ppbC, as listed in Table 4-1, and the average ratio of NMHC/NO_x was 0.6, which represents a typical NO_x-saturated chemical regime.

The concentrations of HONO varied with the weather conditions. The highest HONO concentrations and the highest HONO/NO_x ratios were observed in the cloudy period from March 30 to April 4. BC and RH were also the highest during this period. During the rainy period from April 8 to 11 (heavy rain on April 11), wet deposition may have accelerated the loss of HONO. The relatively low HONO concentrations from April 24 to 30 could be attributed to fast photolysis.

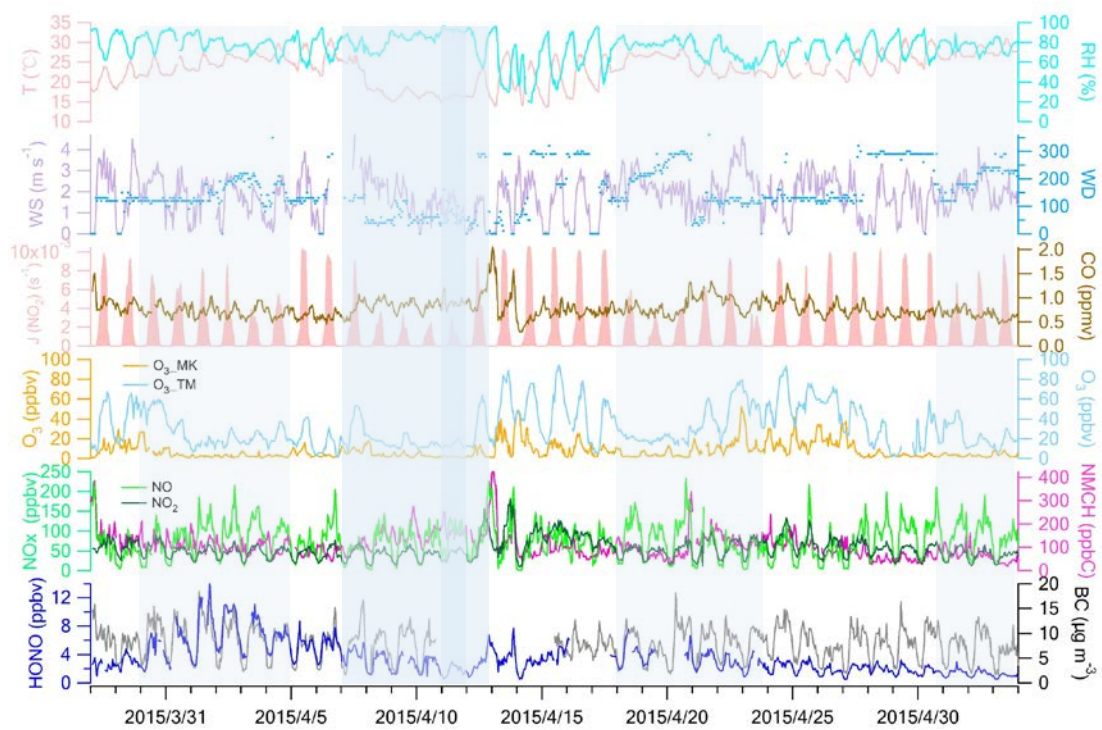


Figure 4- 2. Time series of hourly mean values of measured species at the MK site and O₃ at a regional background site, Tap Mun (TM), in Hong Kong from March 28 to May 3, 2015.

The diurnal variations of HONO and related species are shown in Fig. 4-3 for the whole period, sunny days, and overcast days. The average HONO concentration in the daytime (7:00–17:00) was 3.91 ppbv, which is higher than that of 2.86 ppbv in the nighttime (18:00–6:00). The HONO concentration remained at a relatively high level during the daytime. This pattern was quite different from that previously reported, where HONO was lower during the daytime than during the nighttime in urban and suburban areas (Elshorbany et al., 2009a; Lee et al., 2016; Pusede et al., 2015; Qin et al., 2009; Tong et al., 2015; Wang et al., 2013). Those observation sites were relatively far from the roadside, and there was sufficient sunlight leading to fast HONO photolysis, even in the morning and afternoon. In this study, the similar HONO diurnal pattern to patterns of NO_x , BC, and the local traffic flow (Fig.4-1) suggests that the concentrations of HONO at the MK site were strongly affected by vehicle emissions. The ratio of HONO/ NO_x presented the highest values of 3.9%–4.5% in the period from 1:00 to 5:00, along with relatively high HONO/ NO_2 ratios. The average daytime HONO/ NO_x ratio was 2.6% for the whole period, and 3.0% and 2.2% for the overcast days and sunny days, respectively.

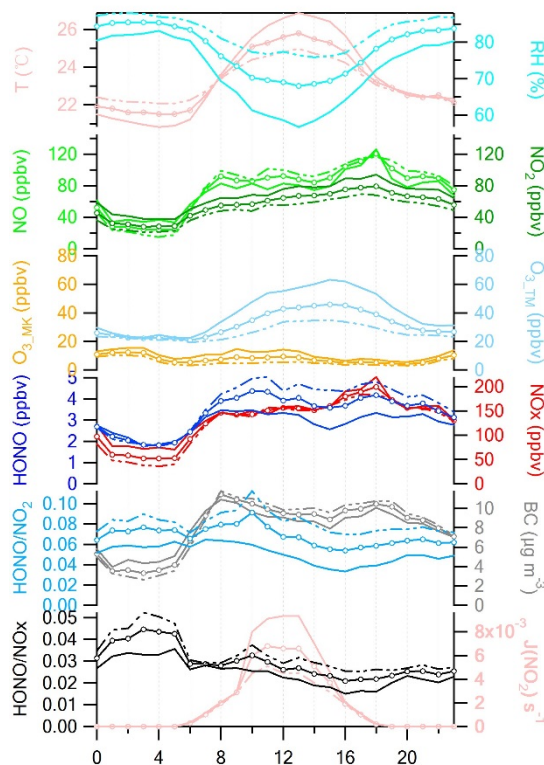


Figure 4- 3. Diurnal patterns for HONO and related species with hourly averaged data at the MK site and diurnal pattern of O₃ at the TM site. The lines with circle markers are for the whole period. Solid and dash lines are for the sunshine periods and overcast periods, respectively.

4.4 Vehicle emission of HONO

The measurement data were analyzed to infer the emission ratios of HONO/NO_x. Sixteen relatively fresh air masses were selected to calculate the emission ratios following the criteria of Xu et al. (2015):

(a) $\Delta\text{NO}/\Delta\text{NO}_x > 0.7$;

(b) Good correlation between HONO and NO_x ($R^2 > 0.65$);

(c) Short duration of an air mass (<1h);

(d) Positive correlation between CO and NO_x;

(e) No precipitation;

(f) $J_{\text{NO}_2} < 0.25 \times 10^{-3} \text{ s}^{-1}$.

A $\Delta\text{NO}/\Delta\text{NO}_x$ ratio of 0.7 was chosen in this study compared to 0.8 in Xu's work considering the increase of NO₂/NO_x ratios in emissions from road vehicles in recent years (HKEPD, 2014). The derived HONO/NO_x emission ratios varied from 0.4% to 1.8%, with an average of 1.0% ($\pm 0.5\%$) as shown in Table 4-2. This value is in the range of reported HONO/NO_x emission ratios from 0.3% to 2.3% (Gutzwiller et al., 2002; Kirchstetter et al., 1996; Kurtenbach et al., 2001), comparable to the results of 0.5%–1.6% from Xu et al. (2015) at Tung Chung, and close to the recent tunnel results of 1.24% in Hong Kong (Liang et al., 2017). The variation of emission ratios in different air masses maybe related to the engine types and the operating conditions. Liang et al. (2017) suggested that vehicles with a diesel particle filter emit larger HONO/NO_x ratios, and diesel engines accounted for 26% of the total vehicle fleet in the present study, which is lower than the 38% in their tunnel study.

Lee et al. (2016) and Qin et al. (2009) estimated the contribution of vehicle emissions to the nighttime measured HONO through multiplying the HONO/NO_x emission ratio by measured NO_x concentrations and assuming that all measured NO_x came from vehicle

emissions. This assumption is applicable in this street canyon environment as NO_x concentration in roadside stations is much higher than that at other urban and rural stations in Hong Kong (HKEPD, 2014). If 1.0% is treated as the HONO/ NO_x emission ratio at MK, the direct emission from vehicles would contribute to 42.5% and 27.9% of the ambient HONO concentrations during 18:00–0:00 and 1:00–5:00, respectively (as shown in Fig. 4-4). During the daytime, the average contribution of vehicle emission to HONO was 38.8%, which should be the upper limit of daytime vehicle emission contributions considering the fast photolysis of HONO (with a lifetime of 10–20 min) after emission. This indicates that there should be other HONO sources in addition to direct vehicle emission to sustain the high HONO concentrations in the street canyon environment.

Table 4- 2. Emission ratios (HONO/ NO_x) in 16 fresh air masses and other parameters.

Date	Time	$\Delta\text{NO}/\Delta\text{NO}_x$	$\Delta\text{HONO}/\Delta\text{NO}_x$	R^2	ΔNO	$\Delta\text{CO}/\Delta\text{NO}_x$
4/3	20:20–20:50	0.73	0.013	0.99	73.6	0.1
4/4	19:10–19:40	0.84	0.018	0.66	34.0	2.9
4/6	21:30–22:00	0.81	0.014	0.95	80.7	3.1
4/8	6:20–6:50	0.72	0.016	0.98	52.8	2.1
4/8	23:40–0:10	0.85	0.006	0.94	48.5	5.6
4/9	6:20–6:50	0.81	0.011	0.85	57.7	1.5
4/9	20:10–20:40	0.88	0.008	0.97	84.4	2.4
4/9	23:10–23:40	0.86	0.005	0.86	82.5	1.3
4/12	6:00–6:30	0.89	0.008	0.84	53.0	1.0
4/15	5:30–6:00	0.79	0.012	0.94	66.3	0.4
4/15	6:20–6:50	0.79	0.013	0.98	86.5	1.9
4/19	5:50–6:20	0.80	0.018	0.90	44.3	0.8
4/22	6:20–6:50	0.81	0.005	0.70	55.9	1.4
4/27	21:40–22:10	0.84	0.005	0.80	141.4	0.1
4/30	20:30–21:10	0.74	0.004	0.72	65.0	1.6
5/1	5:40–6:20	0.79	0.007	0.76	46.4	2.1

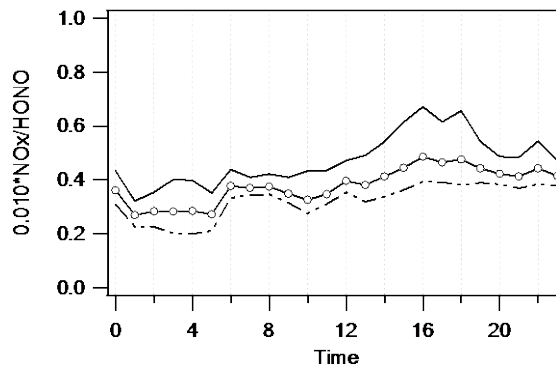


Figure 4- 4. The contribution of vehicle emissions ($=0.010 \times \text{NO}_x$) to total HONO concentration. The lines with circle markers are for the whole period. Solid and dash lines are for the sunshine periods and overcast periods, respectively.

The much larger daytime HONO/NO_x ratios than the vehicle emitted values also indicate that additional sources are present to contribute to the observed high daytime concentrations of HONO at the MK site. One plausible source is the heterogeneous conversion of NO₂ on the ground and building surfaces. A previous study showed that RH affects the NO₂ conversion efficiency on surfaces (Finlayson-Pitts et al., 2003). The relationship between HONO/NO_x and RH during daytime and nighttime is illustrated in Figs. 4-5(a) and (b), respectively. Hourly averaged data were used, and the data for April 11 were excluded in order to avoid the interference from rainfall. As can be seen, the HONO/NO_x ratios were the lowest when the RH was below 60%, with a mean value of 0.02. For RH from 60% to 100%, the average HONO/NO_x ratios were calculated in RH intervals of 5%. The HONO/NO_x ratios appeared to increase with increasing RH in both the daytime and the nighttime. Similar phenomenon has also been found at nighttime in Shanghai and Guangzhou (Qin et al., 2009; Wang et al., 2013). This may be

a result of the stronger heterogeneous conversion of NO_2 and/or the reduced boundary layer height and solar radiation under cloudy conditions.

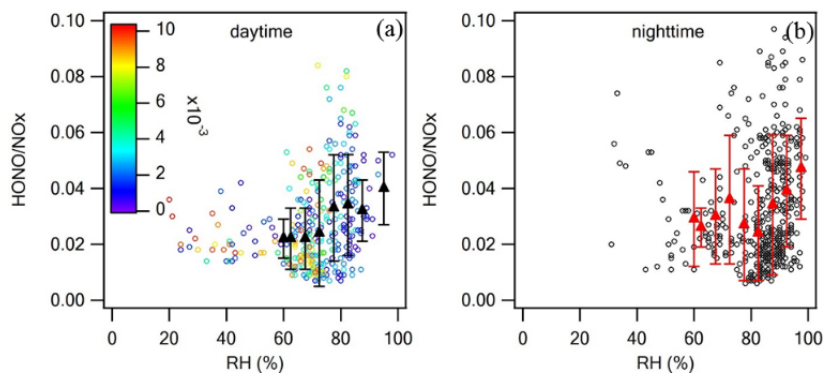


Figure 4- 5. The relationship between HONO/NO_x and RH during the daytime (a) and nighttime (b). The color bar in (a) indicates J_{NO_2} .

4.5 Role of HONO in local photochemistry

4.5.1 Contribution of HONO to radical concentrations

As shown above in Fig. 4-3, an average of 3.2 ppbv of HONO was observed at the MK site for the sunny days. The photolysis of HONO may generate large amounts of OH and cause high atmospheric oxidation capacity in this microenvironment. Atmospheric oxidation capacity (AOC) is defined as the total removal rates of VOCs and CO by principal oxidants, including OH, O_3 , and NO_3 (Elshorbany et al., 2010; Xue et al., 2016). In this roadside environment, high NO concentrations can quickly titrate O_3 and inhibit NO_3 formation. Thus, the oxidation rates of VOCs by O_3 and NO_3 can be negligible compared to OH during the daytime. By employing the above-mentioned OBM model, the concentrations of OH, HO_2 , and RO_2 radicals were simulated for two

cases, i.e., with and without constraining the model with the measured HONO. As shown in Fig. 4-6(a), the simulated OH, HO₂, and RO₂ concentrations when HONO was constrained reached 4.65×10^6 , 4.40×10^6 , and 1.83×10^6 molecule cm⁻³ at the peak, which was 7.9, 5.0, and 7.5 times, respectively, the results without constraining HONO in Fig. 4-6(b).

It is noticed that the modeled concentrations of OH are slightly higher than those of HO₂ in Fig. 4-6(a), which is different from the commonly observed/modeled results in previous studies in urban and rural areas (Liu et al., 2012; Ren et al., 2006; Zhang et al., 2008), where the HO₂ concentration is higher than that of OH. At the MK site, the total daytime OH reactivity was 51.2 s^{-1} , 77.2% of which was due to reactions with NO_x, 5.5% with NMHCs, and 9.6% with OVOCs (Fig. 4-7). The ratio of $k_{\text{VOCs+OH}}[\text{VOCs}]/k_{\text{NO}_x+\text{OH}}[\text{NO}_x]$ was only 0.3 (<1.0), indicating a typical NO_x-saturated O₃ production regime (Kirchner et al., 2001; Wang et al., 2010). In this high-NO_x environment, peroxy radicals can be quickly recycled back to OH and concentrations of VOCs are critical factors for RO₂ and HO₂ production.

The simulated OH concentrations were similar to those modeled in urban Guangzhou ($\sim 1.5 \times 10^7 \text{ cm}^{-3}$) (Zhang et al., 2008) and Beijing ($\sim 9.0 \times 10^6 \text{ cm}^{-3}$) (Liu et al., 2012) and to those measured in New York City ($\sim 1.4 \times 10^6 \text{ cm}^{-3}$) (Ren et al., 2006). The HO₂ concentrations in this work were comparable to the simulated results ($\sim 0.3 \text{ pptv}$) under high NO conditions (around 40 ppbv) in New York City (Ren et al., 2006), but much lower than the up to $6.8 \times 10^8 \text{ cm}^{-3}$ in urban Beijing (Liu et al., 2012).

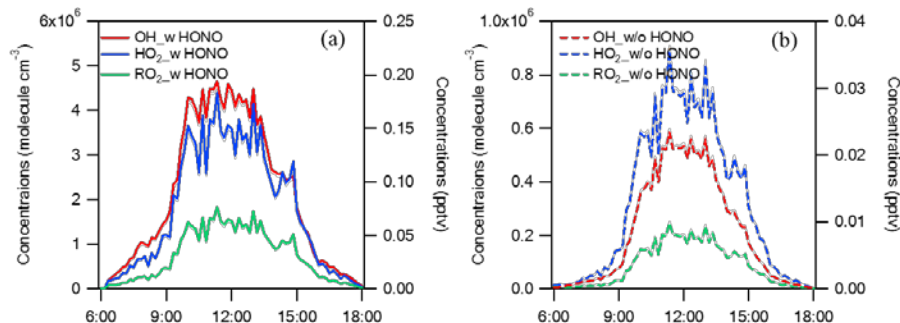


Figure 4- 6. Modeled radical concentrations with measured HONO constrained (a) and without constraining HONO (b).

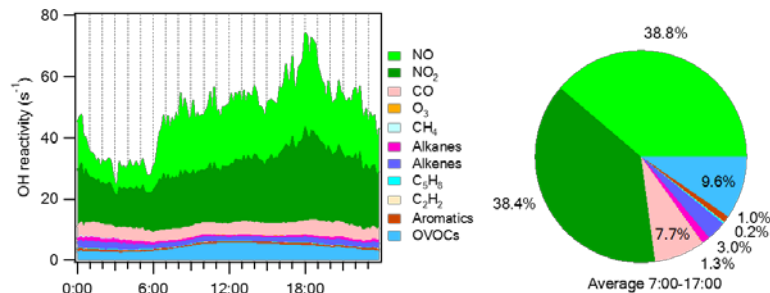


Figure 4- 7. (a) Diurnal pattern of simulated OH reactivity on sunny days and (b) the average contribution of different species to OH reactivity during the daytime (7:00–17:00). NMHCs were based on simultaneous measurements. Seven OVOC species were measured in a different campaign in May, 2014, and constrained in the model; other OVOCs were based on the simulated concentrations.

4.5.2 Analysis of radical budget

A radical budget analysis was carried out to investigate the key processes driving the radical initiation, propagation, and termination in the local atmosphere at the MK site.

Figure 4-8 presents the fractions of different processes involved in the production and destruction of OH, HO₂, and RO₂. High daytime HONO in the street canyon environment significantly enhanced the production and destruction rates of OH, HO₂, and RO₂, accelerating the oxidation processes there. The primary formation of OH was dominated by HONO photolysis, with a net average daytime rate of 6.4 ppbv h⁻¹ (7:00–17:00, deducted by the HONO formation rate of 7.0 ppbv h⁻¹ through OH+NO). The secondary source of OH was the reaction between HO₂ and NO, with an average daytime rate of 5.1 ppbv h⁻¹. The main loss pathways of OH were reactions with NO₂, VOCs (CH₄, NMHCs, and OVOCs in the model), and CO, and the average loss rates were 7.1, 2.9, and 1.4 ppbv h⁻¹, respectively.

The production of HO₂ was dominated by the OH reactions with VOCs and CO, followed by reactions of RO with O₂ and RO decomposition, and the average rates were 1.2, 1.4, 0.79, and 0.86 ppbv h⁻¹, respectively. The photolysis of HCHO and other OVOCs was the primary source of HO₂, with average rates of 0.39 and 0.19 ppbv h⁻¹, which are very small compared to the secondary sources. Nearly all of the HO₂ was cycled back to OH by reactions with high NO in roadside air. The formation of RO₂ was mainly from the OH reactions with VOCs and the average rate was 1.7 ppbv h⁻¹, whereas the destruction of RO₂ was dominated by reactions with NO to form RO and NO₂.

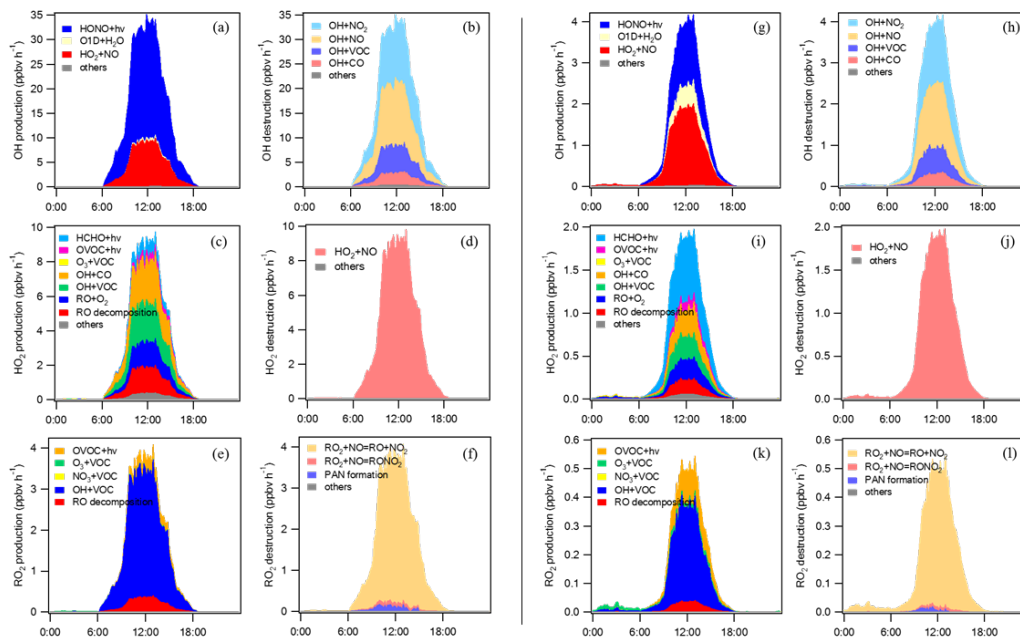


Figure 4- 8. Production rates for OH (a), HO₂ (c), and RO₂ (e) and destruction rates for OH (b), HO₂ (d), and RO₂ (f) with HONO constrained in the left panel, whereas (g), (i), (k) and (h), (j), (l) are the production and destruction rates, respectively, of OH, HO₂, and RO₂ without constraining HONO in the right panel.

Figure 4-9 shows a diagram summarizing the role of HONO in the atmospheric oxidation processes in this NO_x-saturated O₃ regime. If only the primary sources of OH, HO₂, and RO₂ are considered, HONO contributes 86.5% to the total primary production rates. The photolysis of HCHO and other OVOCs accounts for 5.2% and 4.9%, respectively, whereas O₃ photolysis accounts for only 3.0%. The formation of HNO₃, PANs, and RONO₂ contributes to 98.4%, 0.8%, and 0.8%, respectively, of the radical termination rates. Thus, in this street canyon environment, the initial reaction for oxidation of VOC and NO_x is HONO photolysis. The propagation reactions are the OH

reactions with VOCs and CO to form HO₂ and RO₂ and the cycling reactions of these peroxy radicals with NO. The radical termination reactions are mainly the formation of HNO₃.

Previous studies have shown that the dominant primary radical source varies in different urban environments, including OVOC photolysis in urban Beijing (Liu et al., 2012), central Tokyo (Kanaya et al., 2007), and Mexico City (Volkamer et al., 2010) and HONO photolysis in New York City (Ren et al., 2006; Ren et al., 2003) and urban Santiago, Chile (Elshorbany et al., 2010; Elshorbany et al., 2009b). Compared to these studies, our results in a heavily trafficked street canyon reveal the predominant radical source from HONO in such an environment.

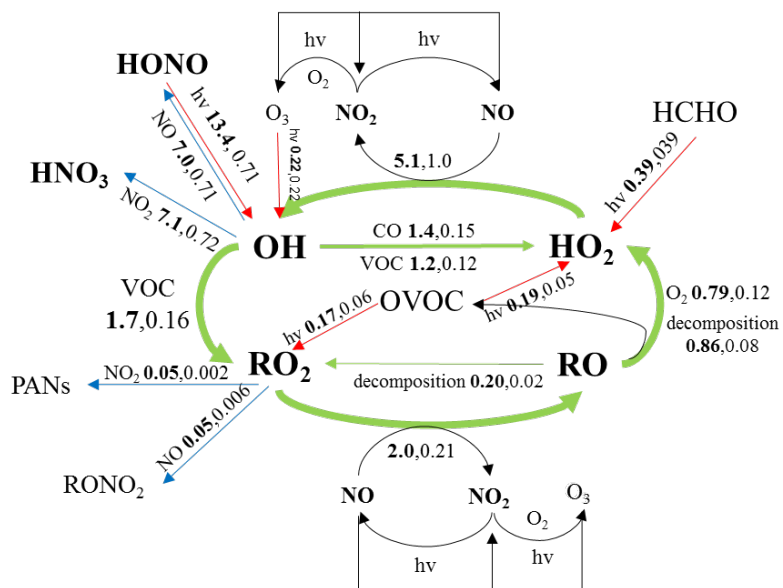


Figure 4- 9. Diagram of the role of HONO in the atmospheric oxidation process in the NO_x-saturated O₃ production regime. The numbers in bold are daytime average rates

when the model is constrained by HONO; the numbers in regular form are for the case without constraining HONO.

4.5.3 Formation of HNO₃ and OVOCs

The reaction between OH and NO₂ is the main radical termination pathway in this high-NO_x environment. The reaction rate of OH+NO₂ was 7.1 ppbv h⁻¹ (4.8×10⁷ molecule cm⁻³ s⁻¹, 98.4% of the total radical termination rates) with HONO constrained, which was much faster than the 1.7 ppbv h⁻¹ (50%) in urban Beijing (Liu et al., 2012), 2.5×10⁶ molecule cm⁻³ s⁻¹ (50%) in suburban Paris (Michoud et al., 2012), and 1.0×10⁷ molecule cm⁻³ s⁻¹ (95%) in New York City (Ren et al., 2006). As shown in Fig. 4-10(a), the average daytime concentration of gas-phase HNO₃ in the model was 21.8 ppbv (~55.8 μg m⁻³ at STP), which is nearly 8.4 times that in the case without constraining HONO. The reported concentrations of nitrate in PM₁₀ was approximately 5.0 μg m⁻³ in Hong Kong (Ho et al., 2003). The measured nitrate at the MK station was 2.4 μg m⁻³ in PM_{2.5} (So et al., 2007) and 1.5 μg m⁻³ in non-refractory fine particulate matter (NR-PM_{1.0}) (Lee et al., 2015; Sun et al., 2016). The low concentrations of aerosol nitrate suggest that most of the gas-phase HNO₃ from the OH+NO₂ reaction either stayed in the gas phase in the air, or probably deposited to ground/building surfaces. This may lead to the damage of outdoor building materials (Gibeaux et al., 2016; Livingston, 2016; Vazquez et al., 2016).

The oxidization of NMHCs by OH can lead to the formation of OVOCs. To evaluate the HONO impact on the secondary formation of OVOCs, sensitivity tests were conducted

without constraining the OVOCs. The OVOCs in these sensitivity tests were formed through OH reactions with primary VOCs, and background and direct emissions were not considered. Figures 4-10(b) and (c) present the modeled results of two typical OVOCs, formaldehyde and acetaldehyde, respectively, with and without constraining HONO. The daytime average concentrations for formaldehyde and acetaldehyde modeled with HONO constrained are 1.78 and 0.87 ppbv, compared to 0.12 and 0.11 ppbv, respectively, without constraining HONO, indicating a significant underestimation of the OVOC concentrations when HONO concentrations are not constrained. The U.S. Environmental Protection Agency suggests that long-term exposure to formaldehyde, even at a low concentration of $1 \mu\text{g m}^{-3}$ ($\sim 0.7\text{ppbat STP}$), can cause health risks (USEPA, 2015). Our study shows that HONO serves as the critical source of OH to oxidize VOCs to produce substantial HCHO, which together with HCHO from direct emission and regional transport, may pose serious health risks to pedestrians and residents in Hong Kong.

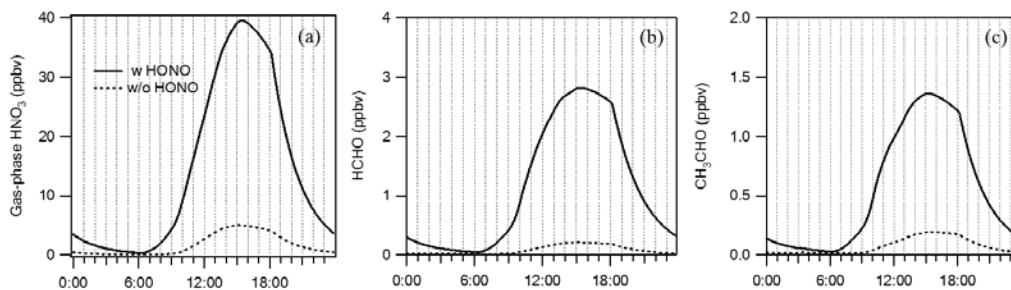


Figure 4- 10. Diurnal patterns for modeled gas-phase HNO_3 (a) and diurnal patterns for simulated formaldehyde (b) and acetaldehyde (c) without constraining the measured

OVOCs into the model as sensitivity tests. Solid black lines and dotted lines are modeled results with and without constraining the measured HONO, respectively.

4.6 Impact of HONO on local NO₂ and O₃ production

Elevated roadside NO₂ pollution is an urgent problem for Hong Kong (HKEPD, 2014). The sustained daytime HONO in the street canyon may be one reason for the elevated NO₂, which needs to be investigated. Several factors can affect the daytime NO₂ (and O₃) concentrations in a street canyon, including local emission of NO_x, local photochemical chemistry, and regional transport of NO_x and O₃ (e.g., Takekawa et al., 2013). Regarding the local photochemistry, the photolysis of NO₂ leads to the formation of O₃, but high NO at the roadside station can titrate O₃ to form NO₂. This is a null cycle and does not lead to the net production of O₃. The oxidation of NO by HO₂ and RO₂ can also generate NO₂ without consuming O₃, which leads to the net production of NO₂ and O₃. The OH radicals from abundant HONO can oxidize VOCs and CO, generating more RO₂ and HO₂; at the same time, they can also remove NO₂ from the system. Thus, the impact of HONO on the net production of O_x (=NO₂+O₃) could be complex in this environment. In addition to local emission and chemistry, regional O₃ (and to a lesser extent, NO₂) could have affected the NO₂ and O₃ at the MK site. The regional O₃ affected the partition of NO and NO₂ at the MK site through the fast titration of NO to form NO₂. As shown in Fig. 4-11(c), the daytime NO₂/NO ratios during sunny days at the MK site increased with increasing background O₃ at TM. The relative contribution of the

HONO-initialized photochemistry to NO₂ and O₃ at the MK site is expected to vary with the strength of regional O₃ transport.

To quantify the HONO impact on local concentrations of NO₂ and O₃ at the MK site under different regional O₃ conditions, six sensitivity tests from S1 to S6, as listed in Table 4-3, were carried out based on the SUNNY case. In these simulations, the initial concentrations of NO and NO₂ are set to the observed values at 0:00. The emission flux of NO_x was allowed to vary until the simulated NO_x matched the observed values. The emission ratio of NO to NO₂ was fixed at 0.81:0.18, derived from section 4.4.

S1 and S2 aimed to evaluate the contribution of HONO to local O_x under average sunny conditions. In S1, a regional O₃ source was introduced into the model and adjusted to transform enough NO to NO₂ to make the simulated concentrations match the observed NO and NO₂ values. HONO was constrained with the measured data in S1. S2 adopted the regional O₃ determined in S1 and repeated the calculation without constraining HONO. The difference in simulated concentrations is the impact of HONO. S3 and S4 assumed that the regional ozone determined in S1 was halved with and without constraining HONO; S5 and S6 assumed that there was no regional transport of O₃ with and without constraining HONO.

Table 4- 3. Scenarios for sensitivity tests.

Scenario number	Description
S1,S2	Match with measured concentrations of NO and NO ₂ , respectively, with average regional O ₃ source, with (S1) and without (S2) HONO constrained
S3,S4	Match with measured total concentrations of NO _x , with 50% regional O ₃ source, with (S3) and without (S4) HONO constrained
S5,S6	Match with measured total concentrations of NO _x , without regional O ₃ source, with (S5) and without (S6) HONO constrained

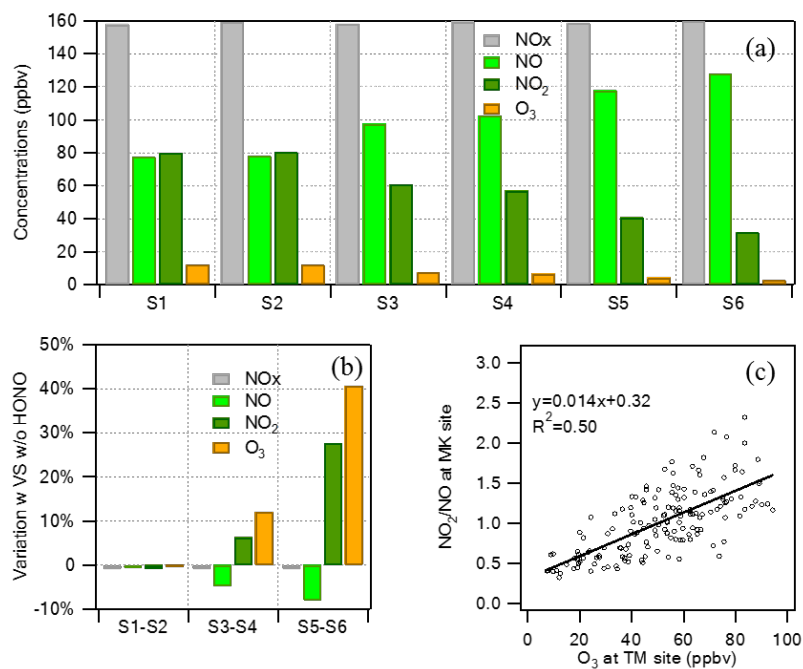


Figure 4- 11. Average concentrations of NO_x, NO, NO₂, and O₃ from 7:00–17:00 in cases from S1 to S6 (a), and the variations in scenarios with HONO constrained compared to those without HONO constrained (b). (c) shows the relationship between the daytime NO₂/NO ratio at the MK site and the O₃ concentration at the regional background site TM on sunny days.

Figure 4-11(a) presents the daytime average concentrations of NO_x , NO, NO_2 , and O_3 in different scenarios. Figure 4-11(b) shows the difference between the cases with and without constraining HONO. It shows that for average conditions encountered in the field study, the impact of HONO on NO_2 and O_3 production was nearly zero, as indicated by the negligible difference in the calculated concentrations in S1 and S2. If regional O_3 strength is reduced to half (S3–S4), HONO can result in a 6% and 12% increase of NO_2 and O_3 , respectively, which is applicable to the days of April 6, 28, 29, and 30 with low regional O_3 concentrations, as shown in Fig. 4-2. The observed NO_2/NO ratio of these days ranged from 0.47 to 0.52, with average daytime NO and NO_2 concentrations of 112.3 and 57.2 ppbv, respectively, which compared well with the simulated values for the scenario of S3 and S4. For the extreme scenario of no regional O_3 (S5–S6), HONO led to increases of NO_2 and O_3 concentrations by 27% and 41%, respectively. These conditions were not encountered during the present field study but they are theoretically possible under extreme calm conditions or when regional ozone is extremely low, thus representing the upper limit of HONO impact on O_x .

4.7 Summary

HONO concentrations ranging from 0.4 to 13.9 ppbv were observed at a roadside station inside a street canyon in Hong Kong. The diurnal variation of HONO in this environment was quite different from the typical patterns observed in other urban ambient environments. Daytime HONO concentrations were significantly higher than those at nighttime, suggesting a predominant source from vehicles, including direct

emission of HONO and conversion of NO₂ to HONO. In this street canyon microenvironment, HONO photolysis was the dominant primary source of radicals, contributing 86.5% of the total production rates of radicals. HONO may enhance the production of NO₂ and O₃ under calm conditions or with low O₃ in background air. The high levels of HONO accelerated the removal of NO_x through the formation of HNO₃ and increased the secondary formation of OVOCs, especially HCHO. The deposition or adsorption of HNO₃ on surfaces may cause damage to building materials, and more HCHO will result in a higher health risk to pedestrians and surrounding residents.

References

- Ai Z, Mak C, Lee H. Roadside air quality and implications for control measures: A case study of Hong Kong. *Atmospheric Environment* 2016; 137: 6-16.
- Bright V, Bloss W, Cai X. Modelling atmospheric composition in urban street canyons. *Weather* 2011; 66: 106-110.
- Bright VB, Bloss WJ, Cai X. Urban street canyons: Coupling dynamics, chemistry and within-canyon chemical processing of emissions. *Atmospheric Environment* 2013; 68: 127-142.
- Cui L, Zhang Z, Huang Y, Lee SC, Blake DR, Ho KF, et al. Measuring OVOCs and VOCs by PTR-MS in an urban roadside microenvironment of Hong Kong: relative humidity and temperature dependence, and field intercomparisons. *Atmospheric Measurement Techniques* 2016; 9: 5763-5779.
- Elshorbany YF, Kleffmann J, Kurtenbach R, Lissi E, Rubio M, Villena G, et al. Seasonal dependence of the oxidation capacity of the city of Santiago de Chile. *Atmospheric Environment* 2010; 44: 5383-5394.
- Elshorbany YF, Kleffmann J, Kurtenbach R, Rubio M, Lissi E, Villena G, et al. Summertime photochemical ozone formation in Santiago, Chile. *Atmospheric Environment* 2009a; 43: 6398-6407.
- Elshorbany YF, Kurtenbach R, Wiesen P, Lissi E, Rubio M, Villena G, et al. Oxidation capacity of the city air of Santiago, Chile. *Atmospheric Chemistry and Physics* 2009b; 9: 2257-2273.
- Finlayson-Pitts B, Wingen L, Sumner A, Syomin D, Ramazan K. The heterogeneous hydrolysis of NO₂ in laboratory systems and in outdoor and indoor atmospheres: An integrated mechanism. *Physical Chemistry Chemical Physics* 2003; 5: 223-242.

- Gibeaux S, Thomachot-Schneider C, Schneider A, Cnudde V, De Kock T, Barbin V, et al. Experimental study of the ageing of building stones exposed to sulfurous and nitric acid atmospheres. 13th International congress on the Deterioration and Conservation of Stone. University of the West of Scotland, 2016, pp. 99-106.
- Gutzwiller L, Arens F, Baltensperger U, Gäggeler HW, Ammann M. Significance of semivolatile diesel exhaust organics for secondary HONO formation. *Environmental science & technology* 2002; 36: 677-682.
- HKEPD, 2014. Air Quality in Hong Kong 2014. Air Science Group. Environmental Protection Department, Hong Kong.
- HKTD, 2014. The Annual Traffic Census-2014. Traffic and Transport Survey Division. Transport Department, Hong Kong.
- Ho K, Lee S, Chan CK, Jimmy CY, Chow JC, Yao X. Characterization of chemical species in PM_{2.5} and PM₁₀ aerosols in Hong Kong. *Atmospheric Environment* 2003; 37: 31-39.
- Ho SSH, Ho KF, Lee SC, Cheng Y, Yu JZ, Lam KM, et al. Carbonyl emissions from vehicular exhausts sources in Hong Kong. *Journal of the Air & Waste Management Association* 2012; 62: 221-234.
- Jenkin ME, Saunders SM, Wagner V, Pilling MJ. Protocol for the development of the Master Chemical Mechanism, MCM v3 (Part B): tropospheric degradation of aromatic volatile organic compounds. *Atmospheric Chemistry and Physics* 2003; 3: 181-193.
- Jenkin ME, Young JC, Rickard AR. The MCM v3.3.1 degradation scheme for isoprene. *Atmospheric Chemistry and Physics* 2015; 15: 11433-11459.
- Kanaya Y, Cao R, Akimoto H, Fukuda M, Komazaki Y, Yokouchi Y, et al. Urban photochemistry in central Tokyo: 1. Observed and modeled OH and HO₂ radical concentrations during the winter and summer of 2004. *Journal of Geophysical Research: Atmospheres* 2007; 112. 112, D21312. <http://dx.doi.org/10.1029/2007JD008670>.
- Kirchner F, Jeanneret F, Clappier A, Krüger B, van den Bergh H, Calpini B. Total VOC reactivity in the planetary boundary layer: 2. A new indicator for determining the sensitivity of the ozone production to VOC and NO_x. *Journal of Geophysical Research: Atmospheres* 2001; 106: 3095-3110.
- Kirchstetter TW, Harley RA, Littlejohn D. Measurement of nitrous acid in motor vehicle exhaust. *Environmental science & technology* 1996; 30: 2843-2849.
- Kurtenbach R, Becker K, Gomes J, Kleffmann J, Lörzer J, Spittler M, et al. Investigations of emissions and heterogeneous formation of HONO in a road traffic tunnel. *Atmospheric Environment* 2001; 35: 3385-3394.
- Kwak K-H, Baik J-J. A CFD modeling study of the impacts of NO_x and VOC emissions on reactive pollutant dispersion in and above a street canyon. *Atmospheric Environment* 2012; 46: 71-80.
- Lee BP, Li YJ, Yu JZ, Louie PK, Chan CK. Characteristics of submicron particulate matter at the urban roadside in downtown Hong Kong-Overview of 4 months of continuous high-resolution

- aerosol mass spectrometer measurements. *Journal of Geophysical Research: Atmospheres* 2015; 120: 7040-7058.
- Lee JD, Whalley LK, Heard DE, Stone D, Dunmore RE, Hamilton JF, et al. Detailed budget analysis of HONO in central London reveals a missing daytime source. *Atmospheric Chemistry and Physics* 2016; 16: 2747-2764.
- Liang Y, Zha Q, Wang W, Cui L, Lui KH, Ho KF, et al. Revisiting Nitrous Acid (HONO) Emission from On-road Vehicles: A Tunnel Study with a Mixed Fleet. *Journal of the Air & Waste Management Association* 2017. 67(7), 797-805. <http://dx.doi.org/10.1080/10962247.2017.1293573>.
- Liu Z, Wang Y, Gu D, Zhao C, Huey L, Stickel R, et al. Summertime photochemistry during CAREBeijing-2007: ROx budgets and O₃ formation. *Atmospheric Chemistry and Physics* 2012; 12: 7737-7752.
- Livingston RA. Acid rain attack on outdoor sculpture in perspective. *Atmospheric Environment* 2016; 146: 332-345.
- Michoud V, Kukui A, Camredon M, Colomb A, Borbon A, Miet K, et al. Radical budget analysis in a suburban European site during the MEGAPOLI summer field campaign. *Atmospheric Chemistry and Physics* 2012; 12: 11951-11974.
- Pusede SE, VandenBoer TC, Murphy JG, Markovic MZ, Young CJ, Veres PR, et al. An atmospheric constraint on the NO₂ dependence of daytime near-surface nitrous acid (HONO). *Environmental Science & Technology* 2015; 49: 12774-12781.
- Qin M, Xie P, Su H, Gu J, Peng F, Li S, et al. An observational study of the HONO-NO₂ coupling at an urban site in Guangzhou City, South China. *Atmospheric Environment* 2009; 43: 5731-5742.
- Ren X, Brune WH, Mao J, Mitchell MJ, Leshner RL, Simpás JB, et al. Behavior of OH and HO₂ in the winter atmosphere in New York City. *Atmospheric Environment* 2006; 40, Supplement 2: 252-263.
- Ren X, Harder H, Martinez M, Leshner RL, Oliger A, Simpás JB, et al. OH and HO₂ Chemistry in the urban atmosphere of New York City. *Atmospheric Environment* 2003; 37: 3639-3651.
- Saunders SM, Jenkin ME, Derwent RG, Pilling MJ. Protocol for the development of the Master Chemical Mechanism, MCM v3 (Part A): tropospheric degradation of non-aromatic volatile organic compounds. *Atmospheric Chemistry and Physics* 2003; 3: 161-180.
- So KL, Guo H, Li YS. Long-term variation of PM_{2.5} levels and composition at rural, urban, and roadside sites in Hong Kong: Increasing impact of regional air pollution. *Atmospheric Environment* 2007; 41: 9427-9434.
- Sun C, Lee B, Huang D, Jie Li Y, Schurman MI, Louie PKK, et al. Continuous measurements at the urban roadside in an Asian megacity by Aerosol Chemical Speciation Monitor (ACSM): particulate matter characteristics during fall and winter seasons in Hong Kong. *Atmospheric Chemistry and Physics* 2016; 16: 1713-1728.

- Takekawa H, Chatani S, Ito A. A new approach for estimation of the effect of NO_x emission reduction on roadside NO₂ concentration in Tokyo. *Atmospheric Environment* 2013; 68: 92-102.
- Tham YJ, Wang Z, Li Q, Yun H, Wang W, Wang X, et al. Significant concentrations of nitryl chloride sustained in the morning: investigations of the causes and impacts on ozone production in a polluted region of northern China. *Atmos. Chem. Phys.* 2016; 16: 14959-14977.
- Tian L, Hossain SR, Lin H, Ho KF, Lee SC, Yu ITS. Increasing trend of primary NO₂ exhaust emission fraction in Hong Kong. *Environmental Geochemistry and Health* 2011; 33: 623-630.
- Tong S, Hou S, Zhang Y, Chu B, Liu Y, He H, et al. Comparisons of measured nitrous acid (HONO) concentrations in a pollution period at urban and suburban Beijing, in autumn of 2014. *Science China Chemistry* 2015; 58: 1393-1402.
- Trebs I, Bohn B, Ammann C, Rummel U, Blumthaler M, Königstedt R, et al. Relationship between the NO₂ photolysis frequency and the solar global irradiance. *Atmospheric Measurement Techniques* 2009; 2: 725-739.
- USEPA, 2015. Technical Support Document EPA's 2011 National-scale Air Toxics Assessment, 2011 NATA TSD. United States Environmental Protection Agency, United States. <https://www.epa.gov/sites/production/files/2015-12/documents/2011-nata-tds.pdf>.
- Vazquez P, Carrizo L, Thomachot-Schneider C, Gibeaux S, Alonso FJ. Influence of surface finish and composition on the deterioration of building stones exposed to acid atmospheres. *Construction and Building Materials* 2016; 106: 392-403.
- Volkamer R, Sheehy P, Molina LT, Molina MJ. Oxidative capacity of the Mexico City atmosphere - Part 1: A radical source perspective. *Atmos. Chem. Phys.* 2010; 10: 6969-6991.
- Wang SS, Zhou R, Zhao H, Wang ZR, Chen LM, Zhou B. Long-term observation of atmospheric nitrous acid (HONO) and its implication to local NO₂ levels in Shanghai, China. *Atmospheric Environment* 2013; 77: 718-724.
- Wang ZQ, Chen YS, Qi B, Yang B. Ozone production during the field campaign RISEFEX 2003 in the sea of Japan: analysis of sensitivity and behaviour based on an improved indicator. *Atmos. Chem. Phys.* 2010; 10: 9579-9591.
- Xu Z, Wang T, Wu J, Xue L, Chan J, Zha Q, et al. Nitrous acid (HONO) in a polluted subtropical atmosphere: Seasonal variability, direct vehicle emissions and heterogeneous production at ground surface. *Atmospheric Environment* 2015; 106: 100-109.
- Xu Z, Wang T, Xue LK, Louie PKK, Luk CWY, Gao J, et al. Evaluating the uncertainties of thermal catalytic conversion in measuring atmospheric nitrogen dioxide at four differently polluted sites in China. *Atmospheric Environment* 2013; 76: 221-226.
- Xue L, Gu R, Wang T, Wang X, Saunders S, Blake D, et al. Oxidative capacity and radical chemistry in the polluted atmosphere of Hong Kong and Pearl River Delta region: analysis of a severe photochemical smog episode. *Atmos. Chem. Phys.* 2016; 16: 9891-9903.

Zhang Y, Su H, Zhong L, Cheng Y, Zeng L, Wang X, et al. Regional ozone pollution and observation-based approach for analyzing ozone-precursor relationship during the PRIDE-PRD2004 campaign. *Atmospheric Environment* 2008; 42: 6203-6218.

Chapter 5. Significant HONO concentration at a semi-rural site in Pearl River Delta during a severe pollution period and its impact on atmospheric oxidation capacity

5.1 Introduction

The Pearl River Delta region suffers severe photochemical problem with high NO_2 and O_3 for long (Wang et al., 2009; Wang et al., 2017). HONO, as an important source of OH radical, has been of much concern in this region. Su et al. (2008a,b) conducted the first HONO measurement in Xinken (rural) in the PRD. Nighttime HONO of 0.4 to 3.5 ppbv was observed, while surprisingly high daytime HONO was also observed with an average of 1.2 ppbv. Soil emission due to the biological nitrification and denitrification processes was later considered to explain the daytime missing HONO source (Su et al., 2011). Li et al. (2012) observed HONO of 1-5 ppbv in Back Garden in suburban Guangzhou. HONO of 0.2 ppbv was observed at noon time, and the analysis provided evidence for the photolysis of $\text{HNO}_3/\text{NO}_3^-$ as a probable daytime HONO source.

Intensive observations of HONO and related chemical species were conducted by our group from Jan 2 to Jan 8, 2017, on the top of Hua Guo Shan (60 m a.s.l.) located in the city of Heshan in the western PRD. A severe pollution event was captured during the first week of the observation. This chapter first gives an overview of the measurement data and diurnal profiles, and a box model built on the Master Chemical Mechanism (MCM v3.3.1) was then applied to simulate local oxidation processes and to identify the

contribution of HONO to the formation of radicals and O₃. The nocturnal formation and daytime HONO budget was then investigated and possible daytime HONO sources were suggested.

5.2 Experiment

5.2.1 Site description and instruments

The observation was conducted at a semi-rural site called Hua Guo Shan (HGS, 22.71°N, 112.92° E), in the city of Heshan, which is affiliated to Jiangmen (JM) in Pearl River Delta. The Guangdong Atmospheric Supersite, which is part of Guangdong-Hong Kong-Macau Regional Air Quality Monitoring Network, is situated here. As shown in Fig. 5-1(a), there are totally 11 cities in Pearl River Delta, and Jiangmen locates in the western PRD. Coal-fired power plants (triangles) densely distributed in central PRD area, including the cities of Guangzhou (GZ), Foshan (FS), Zhongshan (ZS), Zhuhai (ZH), Dongguan (DG) and Shenzhen (SZ). Dense road network also distributes in central PRD area. Hua Guo Shan is a hill with a height of 60 m above sea level in the southwest of the town called Tao Yuan (see Fig. 5-1(b)), which locates at the boundary between the central PRD area and western mountainous area. There are five main roads near the HGS site, including three national roads (G325, G94 and G15), and two provincial roads (S272 and S270). The hill is surrounded by similar hills within close range, and few residents lived at the foot of the hill, where there were some farmlands being harvested. Fig. 5-1(c) shows the fire spots from MODIS NRT C6 on Jan 4, 2017. The observation period was just the period for winter harvest in southern China, so

biomass burning occurred frequently in Guang Dong and surrounding provinces, including Guang Xi, Hu Nan, Jiang Xi and Fu Jian.

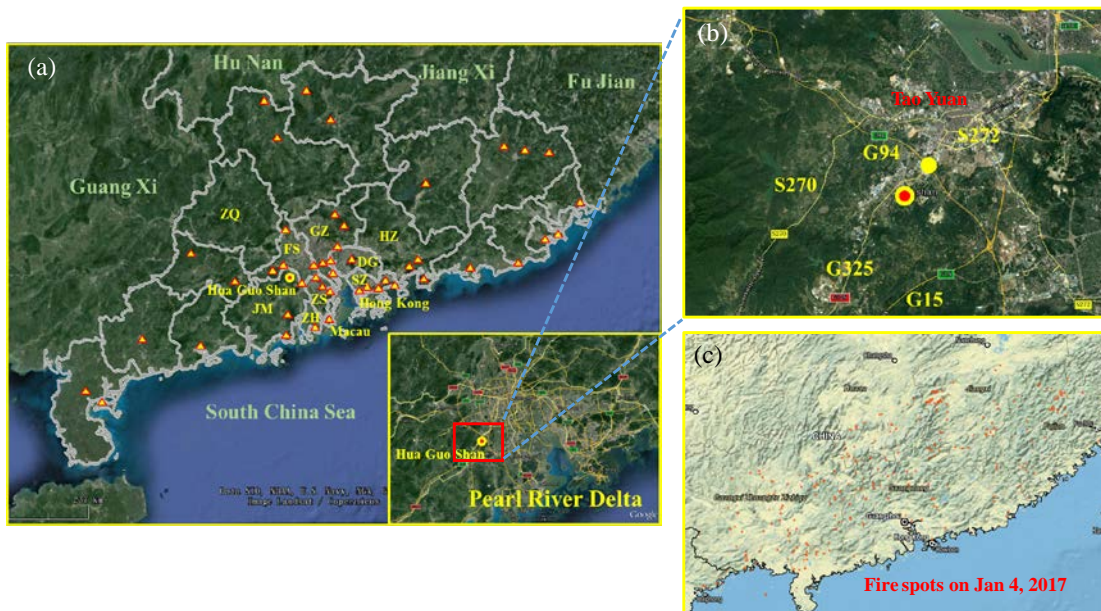


Figure 5- 1. Google maps of the location of Pearl River Delta in Guangdong Province and the Hua Guo Shan site (a). ZQ, JM, FS, ZS, ZH, GZ, DG, SZ and HZ represents cities of Zhaoqing, Jiangmen, Foshan, Zhongshan, Zhuhai, Guangzhou, Dongguan, Shenzhen and Huizhou in PRD, respectively. The triangles represent the coal-fired power plants in Guangdong Province in 2010. The inserted figure in (a) shows the dense road network in PRD. (b) is the nearby topography of Hua Guo Shan. (c) shows the fire spots in southern China for Jan 4, 2017, which is captured from the web <https://firms.modaps.eosdis.nasa.gov/firemap/>.

HONO was continuously measured using LOPAP. N_2O_5 and $ClNO_2$ were concurrently measured with CIMS. Trace gases of carbon monoxide(CO), sulfur dioxide (SO_2),

ozone (O₃), nitrogen oxides (NO and NO₂), total reactive nitrogen (NO_y) were simultaneously measured. C₂–C₁₀ non-methane hydrocarbons (NMHCs) were measured with an online gas chromatograph (GC) equipped with a flame ionization detector (FID) and a mass spectrometer (MS). Oxygenated hydrocarbons (OVOCs), including formaldehyde, acetaldehyde, acetone, methyl ethyl ketone (MEK) and others were sampled with 2,4-dinitrophenyl- hydrazine cartridges every 3 hours and then were analyzed with a HPLC system. Concentrations of PM_{2.5} were measured using a Multi Angle Absorption Photometer (MAAP, Thermo Model 5012). The ionic compositions of PM_{2.5}, including NH₄⁺, K⁺, Na⁺, NO₃⁻, SO₄²⁻, and Cl⁻, together with gas-phase HNO₃ and HCl, were determined by a gas and aerosol collector coupled with ion chromatography (GAC-IC) system (Dong et al., 2012). BC was detected with an AE-51 aethalometer with a time resolution of 10 s. The dry-state particle number size distribution was determined by a Scanning Mobility Particle Sizer (SMPS Model 3936L75, TSI), covering the size ranges from 16.5 to 1000 nm. The ambient (wet) particle number size distributions varied with the relative humidity, and were calculated based on a size-resolved kappa-Köhler function (Hennig et al., 2005; Liu et al., 2014). Ambient particle surface area concentrations (S_a) were finally calculated with the (wet) ambient particle number size distribution assuming spherical particles.

Meteorological parameters including wind direction, wind speed, relative humidity (RH), pressure and temperature were measured with an ultrasonic anemometer and a weather station. Solar radiation was measured by a spectro-radiometer (StellarNetInc). The solar

radiation data were used to calculate the photolysis frequency of NO₂ following the method suggested by Trebs et al. (2009).

5.2.2 Model setup

In order to evaluate the importance of HONO to radical and O₃ production, the chemical box model based on MCM v3.3.1 (Jenkin et al., 2003; Jenkin et al., 2015; Saunders et al., 2003) and an updated chlorine (Cl) chemistry (Xue et al., 2015) was constrained with observation data of N₂O₅, ClNO₂, HCl, HONO, O₃, NO, NO₂, SO₂, CO, C₂-C₁₀ NMHCs, OVOCs (formaldehyde, acetaldehyde, acetone, and MEK), temperature, aerosol surface area, and J_{NO_2} every 10 min. The photolysis frequencies for HONO, O₃, and other species were calculated as a function of solar zenith angle within the model (Saunders et al., 2003) and scaled with the calculated J_{NO_2} values based on measured solar radiation. The first-order physical loss rates of the unconstrained species were set as $3.47 \times 10^{-5} \text{ s}^{-1}$ which is equal to a lifetime of 8 h in a boundary layer of 1000m depth. The model was run from 0:00 on Jan 3 to 11:00 on Jan 8, and the simulation for the first 24 h was repeated three times to stabilize the intermediate species. The production and loss rates of radicals, HONO and O₃ were simultaneously output from the model. Cases with and without constraining the measured HONO were compared to evaluate the importance of HONO.

5.3 Overview of the data

In this campaign, the meteorological conditions presented characteristics with high RH and low wind speed during the pollution episode. Temperature ranged from 16 to 27 °C

during the observation period. The average RH was 90% with a range from 54% to 100% during the nighttime, and was 73% with a range from 46% to 100% in the day. RH sustained at a high level in the early morning until 10:00. Solar radiation was relatively weak on Jan 5 and Jan 7, but O₃ could still reach 120 ppbv on Jan 5 which indicated strong atmospheric oxidation capacity on this episode day (see Fig. 5-2). The air was stagnant during the episode days with slow wind speed of 0.8 m s⁻¹ as average. The measured dry aerosol surface density reached 7×10³ μm² cm⁻³, and had consistent variation with that of PM_{2.5}. Due to the high RH during the nighttime and early morning, the wet aerosol surface density was as high as 5×10⁴ μm² cm⁻³, which may provide large surface for heterogeneous reactions on aerosols.

HONO was continuously measured from 18:40 of Jan 2 to 10:00 of Jan 8, 2017 as shown in Fig. 5-2. The concentration of HONO presented large variation from day to day. The highest HONO concentration was 9.0 ppbv (time resolution of 10 min) which occurred at 8:40 on Jan 5 and at 10:00 on Jan 6. Jan 5 and Jan 6 were two episode days, with PM_{2.5} up to 395 μg m⁻³ and O₃ up to 163 ppbv. The average HONO mixing ratio was 2.7±1.9 ppbv, with 3.1±1.6 ppbv at night and 2.3±2.2 ppbv in the day. The average nighttime and daytime HONO concentrations were comparable to these in Guangzhou, China (Qin et al., 2009) and Santiago, Chile (Elshorbany et al., 2009), but higher than two previous studies in Xinken and Backgarden in PRD (Li et al., 2012; Su et al., 2008a; Su et al., 2008b). As shown in Fig. 5-3, HONO started to increase after sunset until the early morning. From 8:00 to 10:00, with the increase of solar radiation, HONO slowly decreased, but after 10:00 it decreased much faster until 13:00. From 13:00 to 18:00,

HONO sustained at an average level of 1.1 ppbv, but with large variability from day to day.

Figure 5-2 also presents the concurrently measured NO, NO₂, the calculated ratios of HONO/NO₂ and HONO/NO_x. Fresh NO was observed from late night to early morning every day, with an average of 9.0±11.7 ppbv. NO₂ ranged from 6.0 to 70.0 ppbv with an average of 26.2±12.7 ppbv. The average HONO/NO₂ was 10.7%±6.6% for the whole period with 8.9%±6.7% in the day and 11.6±5.6% at night. The average daytime and nighttime ratios of HONO/NO₂ were also comparable to these in Guangzhou, China (7% and 13%) (Qin et al., 2009) and Santiago, Chile (7.5% and 10%) (Elshorbany et al., 2009), but higher than two previous studies in Xinken (4.3% at night) and Backgarden (5.3% and 5.7%) in PRD (Li et al., 2012; Su et al., 2008a; Su et al., 2008b). From the diurnal patterns in Fig. 5-3, HONO had similar diurnal pattern with NO₂ and NO_x, which indicated that they had common sources or NO₂ was the precursor of HONO. The ratios of HONO/NO_{2/x} increased from 18:00 to 21:00 and then sustained at a relatively high level until sunrise. After sunrise, with the fast photolysis of HONO, HONO/NO_{2/x} decreased. From 11:00 to 18:00, the ratio sustained at around 6.5% and presented a small peak of 7.9% at 13:00, which indicated that even during the daytime, HONO still had high conversion rate from NO₂, or there were other HONO sources or precursors other than NO₂.

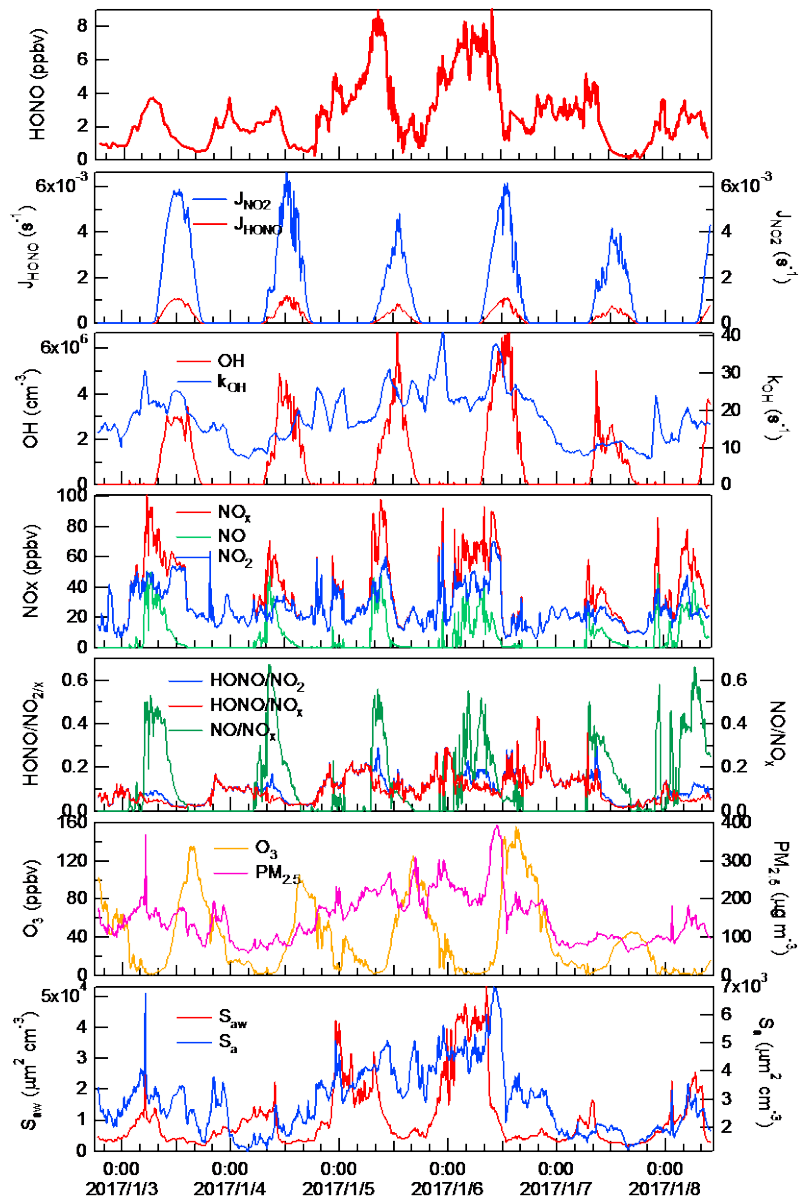


Figure 5- 2. Time series of HONO, J_{HONO} , J_{NO_2} , OH, k_{OH} and related parameters from 18:40 of Jan 2 to 10:00 of Jan 8, 2017.

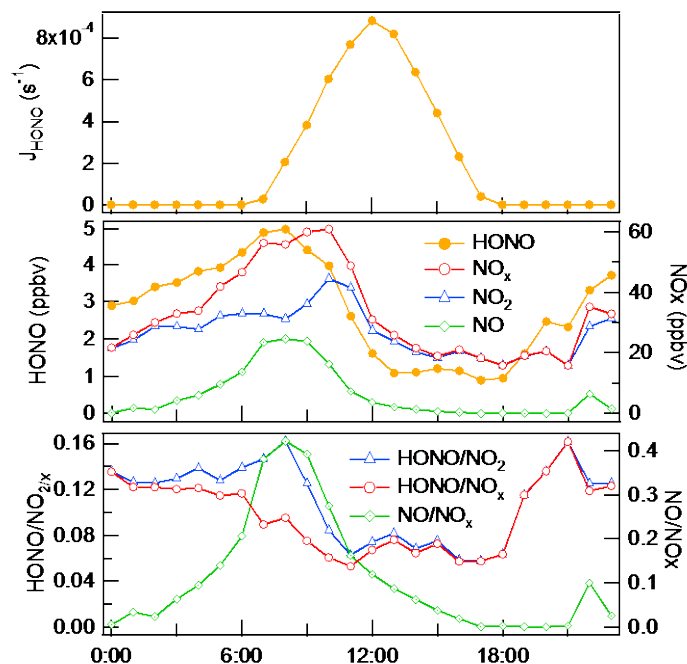


Figure 5- 3. Mean diurnal pattern of HONO, J_{HONO} , NO, NO₂, NO_x, HONO/NO₂, HONO/NO_x, NO/NO_x at the Hua Guo Shan supersite from Jan 3 to Jan 7, 2017.

5.4 Importance of HONO to atmospheric oxidation capacity

5.4.1 OH mixing ratio and AOC

HONO is an important source of OH radicals in the boundary layer. With measured HONO constraining in the chemical box model, maximum OH mixing ratios at noon time ranged from 3.0 to 6.7×10^6 molecule cm^{-3} , and daytime OH reactivity (k_{OH}) ranged from 8 to 40 s^{-1} (see Fig. 5-2). These OH mixing ratios were close to the winter OH levels of $\sim 2.7 \times 10^6$ molecule cm^{-3} in Boulder, Colorado (Kim et al., 2014), and of 1.4×10^6 molecule cm^{-3} in New York City (Ren et al., 2006). They were also close to 6.0×10^6 molecule cm^{-3} (simulated results) at a suburban site, Tung Chung, in Hong

Kong during a severe summertime episode (O_3 peak of ~ 150 ppbv and $\text{PM}_{2.5}$ peak of $\sim 110 \mu\text{g m}^{-3}$) (Xue et al., 2016). Compared to the measured summertime OH mixing ratio of $15\text{-}26 \times 10^6 \text{ molecule cm}^{-3}$ at Backgarden, Guangzhou in the year of 2006 (Lu et al., 2012), the OH mixing ratios in this winter campaign were much lower. The weaker solar radiation might be one of the reasons with maximum J_{NO_2} of $6 \times 10^{-3} \text{ s}^{-1}$ in this campaign compared to $10 \times 10^{-3} \text{ s}^{-1}$ in Lu's work. It seemed that the OH mixing ratios were relatively low in more polluted environments partly due to the reduced solar radiation. If the measured HONO was not constrained into the model, the simulated HONO concentrations could only reach 0.2 ppbv in the model, and the daytime maximum OH mixing ratios also reduced to 2.0 to $3.8 \times 10^6 \text{ molecule cm}^{-3}$ (equivalent to 30%-45% decrease), which indicated that HONO was an important source of OH. In this campaign, it is surprising that OH mixing ratios during the hazy days (Jan 5 and Jan 6) were higher than those during the relatively clean days (Jan 3 and Jan 4). This is an indicator for the strong atmospheric oxidation capacity on hazy days, which may be related to the high HONO during the episode days.

Atmospheric oxidation capacity is defined as the total removal rates of VOCs and CO by principal oxidants, including OH, O_3 , NO_3 , and Cl (Elshorbany et al., 2010; Xue et al., 2016). The calculated AOC for each day from Jan 3 to Jan 7 is presented in Fig. 5-4(a). It was only up to 7.80×10^7 and $6.51 \times 10^7 \text{ molecule cm}^{-3} \text{ s}^{-1}$ on Jan 3 and Jan 4, while it reached 1.63×10^8 and $2.28 \times 10^8 \text{ molecule cm}^{-3} \text{ s}^{-1}$ on Jan 5 and Jan 6. On one hand, concentrations of pollutants like CO and VOCs during these two episode days were higher than these during the less-polluted days. On the other hand, OH mixing

ratios were also higher. These calculated AOC values on Jan 5 and Jan 6 were comparable to 2.04×10^8 and 1.27×10^8 molecule $\text{cm}^{-3} \text{s}^{-1}$ derived in the severe summertime photochemical smog episode in Hong Kong (Xue et al., 2016). OH reactions contributed to 96% of total AOC on average in this winter campaign and to 89% and 93% in the summertime episode in Hong Kong (Xue et al., 2016). This indicated that OH was the predominant oxidant during both the summer and winter pollution episodes in the PRD-HK region.

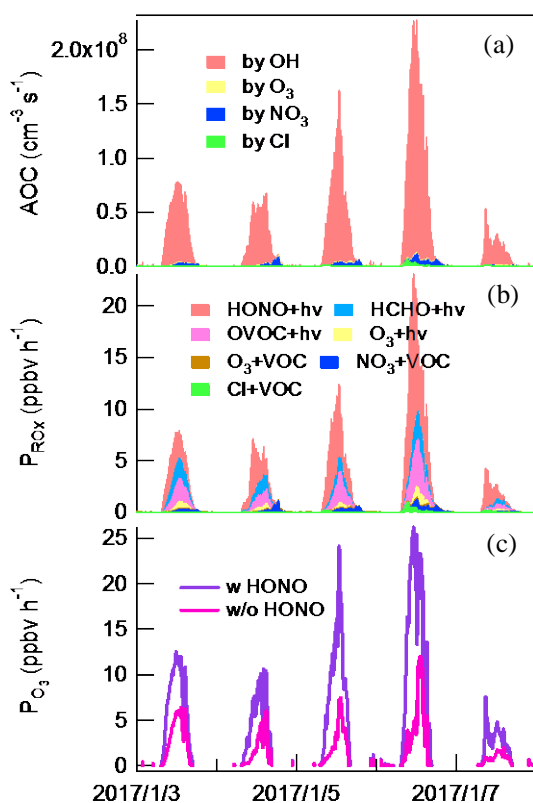


Figure 5- 4. Simulated AOC (a), primary radical sources (b) and net O_3 production rates (c) based on the chemical box model with MCM v3.3.1. In (b), HONO photolysis rate was deducted by the formation rate of HONO through OH+NO.

5.4.2 HONO contribution to RO_x production

The primary production rates of radicals (P_{RO_x} , $RO_x=OH+HO_2+RO_2$) were used to reveal the atmospheric capacity to provide radicals and initialize the photochemistry (Edwards et al., 2014). As shown in Fig. 5-4(b), the maximum values of P_{RO_x} were 7.27 and 7.16 ppbv h⁻¹ on Jan 3 and Jan 4, while they were 12.4 and 23.1 ppbv h⁻¹ on Jan 5 and Jan 6. The daytime average (7:00-17:00) contribution to P_{RO_x} from photolysis of HONO, HCHO, other OVOCs, O₃ and VOC oxidation by O₃, NO₃ and Cl was shown in Fig. 5-5 with pie charts. HONO photolysis was the dominant primary radical source for each day, and accounted for 43.7%-64.1% of the total production rates. The photolysis of HCHO and other OVOCs were another two important radical sources, and accounted for 9.7%-22.1% and 14.4-23.6%, respectively. The contribution of HONO photolysis seemed more important on Jan 5 and Jan 6 than that on Jan 3 and Jan 4, which could be attributed to much higher HONO concentrations on these two episode days. The reported average percentage of the contribution of HONO photolysis to total radical production in summer was ~56% in New York City (Ren et al., 2006; Ren et al., 2003), ~52% in urban Santiago, Chile (Elshorbany et al., 2010; Elshorbany et al., 2009), ~35% in suburban Paris (Michoud et al., 2012), ~40% at Wangdu (Tham et al., 2016), Beijing, ~15% at Backgarden, Guangzhou (Lu et al., 2012) and ~13% at Tung Chung, Hong Kong (Xue et al., 2016). While in winter it was ~81% in urban Santiago, Chile, and ~48% in New York City (Ren et al., 2006). Compared to these summertime studies, the contribution of HONO photolysis to radical production during the episode days in this work was especially significant. Especially in the morning, the contribution of HONO

photolysis could reach 71.2% taking Jan 6 as an example, and in the afternoon the contribution from photolysis of HCHO, other OVOCs and O₃ increased.

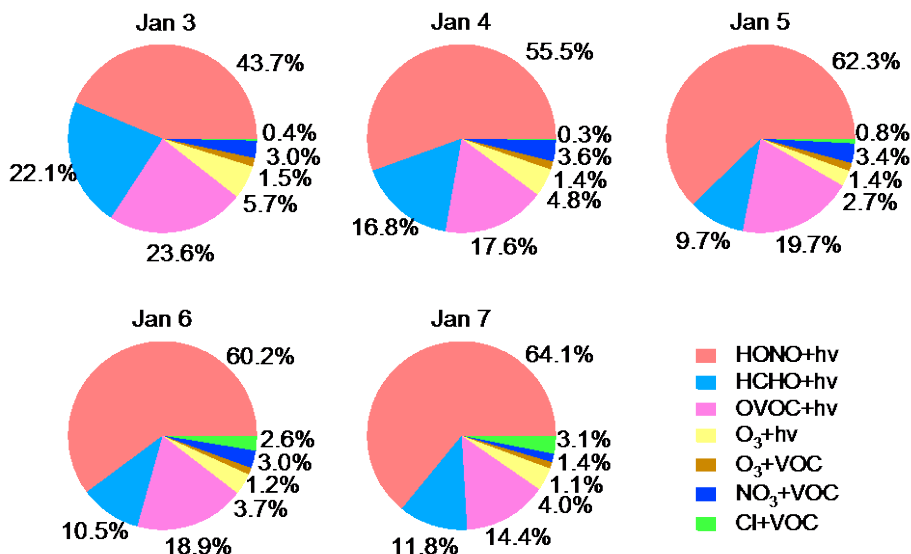


Figure 5- 5. Average daytime (7:00-17:00) contribution of different primary radical sources from Jan 3 to Jan 7, respectively.

5.4.3 Radical budget and O₃ production

Radical budget is used to clearly present the initiation, propagation, and termination processes of radicals (OH, HO₂ and RO₂) which are the main chemical processes during the daytime. As shown in Fig. 5-6, the total OH production and loss rates were 17.0-49.0 ppbv h⁻¹ with measured HONO constrained into the model. If measured HONO was not constrained, the total OH production and loss rates reduced to 7.0- 14.0 ppbv h⁻¹ and the production and loss rates of HO₂ and RO₂ also reduced correspondingly. HONO photolysis (deducted by the HONO formation through OH+NO) was the dominant primary OH source, and accounted for nearly 84%-93% of the primary production of

OH. Photolysis of O_3 (4%-11%), OVOCs and ozonolysis of VOCs were all minor pathways for OH production. The secondary formation of OH was mainly from the reaction between HO_2 and NO. The loss of OH was through reactions with NO_2 , VOCs and CO. During the two episode days, the OH+VOCs reactions accounted for 50%-52% of OH loss, due to the abundance of VOCs, while they accounted for 39%-42% during these two relatively clean days.

For the primary production of HO_2 , photolysis of HCHO was more important than other OVOCs (65% vs 34%) on Jan 3 and Jan 4, while they were half to half on Jan 5 and Jan 6. The secondary formation of HO_2 was through OH reaction with CO, VOCs, RO reaction with O_2 , and RO decomposition. The loss of HO_2 was nearly all through the reaction with NO. For the primary production of RO_2 , photolysis of other OVOCs accounted for 63%-77% of the primary production rates, followed by NO_3 reactions with VOCs (18%-22%), and O_3 photolysis (3%-4%). Cl reactions with VOCs accounted for ~15% of the primary production rates on Jan 6 due to the high $ClNO_2$ peak (~3.5 ppbv) on that morning. The secondary formation of RO_2 was through OH reactions with VOCs and RO decomposition. Overall, the formation of RO_2 was dominated by OH reactions with VOCs. The loss of RO_2 presented two main pathways: one was to react with NO to form RO and NO_2 , and the other one was to react with NO_2 to form PAN, which accounted for 76%-81% and 19%-24%, respectively.

Considering the whole radical recycling processes, the reactions were mainly initialized by HONO photolysis, especially in the morning. The propagation reactions were mainly OH reactions with VOCs and CO. And the termination reactions were OH reaction with

NO₂ to form HNO₃ and PAN formation. The contribution of PAN formation to the termination rates increased from 21%-22% to 30%-36% from clean days to hazy days. Even though the solar radiation was relatively weak in hazy days, high HONO and high VOCs still sustained high photochemical rates and much stronger oxidation capacity than that in relatively clean days.

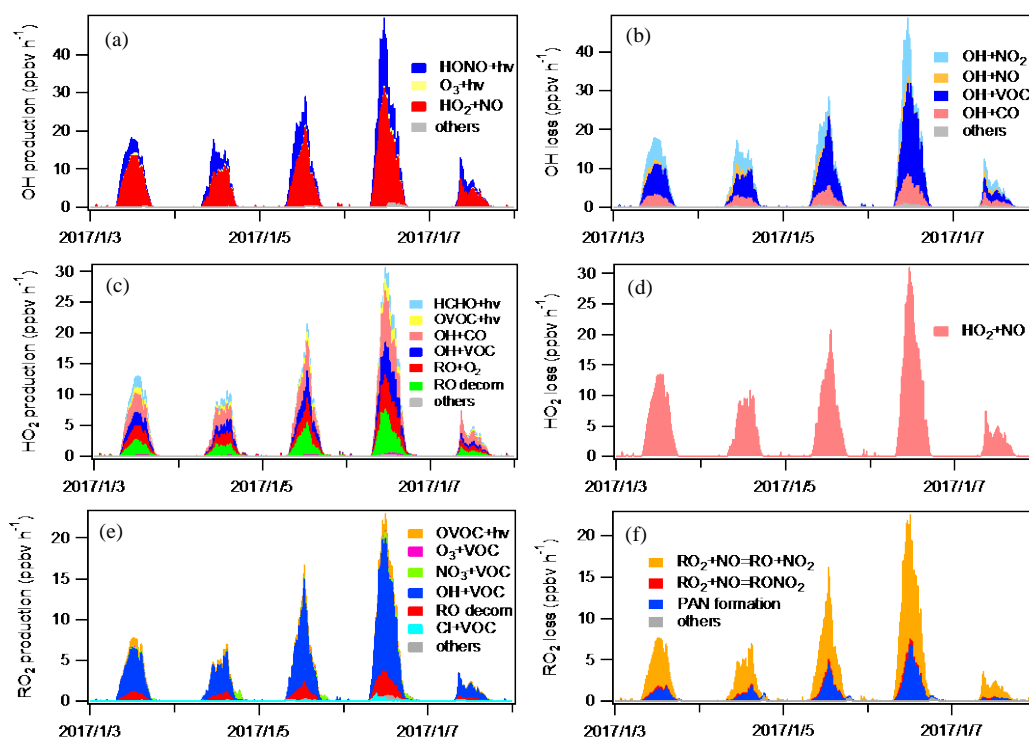


Figure 5- 6. Production rates for OH (a), HO₂ (c) and RO₂ (e) in the right panel and loss rates of OH (b), HO₂ (d) and RO₂ (f) from Jan 3 to Jan 7 with measured HONO constrained into the model.

The recycling of radicals transforms NO to NO₂ and the photolysis of NO₂ lead to O₃ production. The maximum net production rates of O₃ (P_{O₃}) was 11.8 and 9.5 ppbv h⁻¹ on

Jan 3 and Jan 4, and reached up to 24.1 and 26.6 ppbv h⁻¹ on Jan 5 and Jan 6 (see Fig. 5-4), respectively, with measured HONO constrained; while they were only up to 6.0 to 12.0 ppbv h⁻¹ (reduced by 39%-56%) without HONO constrained. Therefore, HONO played a critical role in the production of radical and ozone during this severe pollution episode. Given the importance of HONO during the observation, HONO sources need to be further investigated.

5.5 HONO formation during nighttime

Direct emissions of HONO from vehicles were considered to be negligible due to the high HONO/NO_x ratio during nighttime. The observed lowest HONO/NO_x during nighttime was 2.7% in the selected air masses with NO₂ ≥ 20 ppbv (suggested by Su et al. (2008b), which was higher than the highest HONO/NO_x emission ratio of 2.3% (Gutzwiller et al., 2002; Kirchstetter et al., 1996; Kurtenbach et al., 2001). This indicates the importance of HONO formation through secondary production. Even though high NO was observed at late night and in the early morning, the average ratio of NO/NO_x in the selected air masses was 44% (25%-66%), which was lower than the typical ratio of NO/NO_x ≥ 95% in fresh emission (Kurtenbach et al., 2001). This also suggested that the measured air masses were mixed by freshly emitted and aged air masses. Hence, the ratio of HONO/NO₂ was applied as an indicator for the secondary production of HONO from NO₂.

The conversion frequency of HONO by NO₂ was calculated with E5-1. The average value of C_{HONO} during the nighttime was 0.065 ± 0.076 h⁻¹, with a large variability from

nearly zero to 0.40 h^{-1} . The C_{HONO} in this work was much higher than $0.024 \pm 0.015 \text{ h}^{-1}$ in Backgarden by Li et al. (2012) and $0.016 \pm 0.014 \text{ h}^{-1}$ in Xinken by Su et al. (2008b), which may indicate that HONO conversion from NO_2 was more efficient in the more humid environment.

$$(E5-1)C_{\text{HONO}} = \frac{[\text{HONO}]_{t_2} - [\text{HONO}]_{t_1}}{(t_2 - t_1) \times \overline{\text{NO}_2}}$$

Figure 5-7 illustrates the relationship between HONO, NO_2 , RH, and wet aerosol surface density (S_{aw}) during the nighttime. The nighttime increase of HONO/ NO_2 was accompanied by the simultaneous increase of HONO and NO_2 (see Fig. 5-3), and the covariation between HONO and NO_2 in Fig. 5-7(a) further indicates the heterogeneous conversion from NO_2 to HONO. With the method suggested by Stutz et al. (2004), the average for the top 5 of HONO/ NO_2 (red line) and the median for all HONO/ NO_2 ratios (blue line) in an RH interval of 5% were investigated in Fig. 5-7(b). From RH of 55% to 80%, HONO/ NO_2 increased fast with the increase of RH, whereas the increase of HONO/ NO_2 slowed down after 80% and even dropped. In Li et al. (2012), the HONO/ NO_2 ratio presented an obvious turning point at RH of 70%, which was attributed to the fast dissolution of HONO into water layers formed on surfaces under high RH conditions. In this work, the slowing down of HONO/ NO_2 increase could also be attributed to this reason. At the same time, there may be some other factors to support the conversion from NO_2 to HONO under high RH condition in this work.

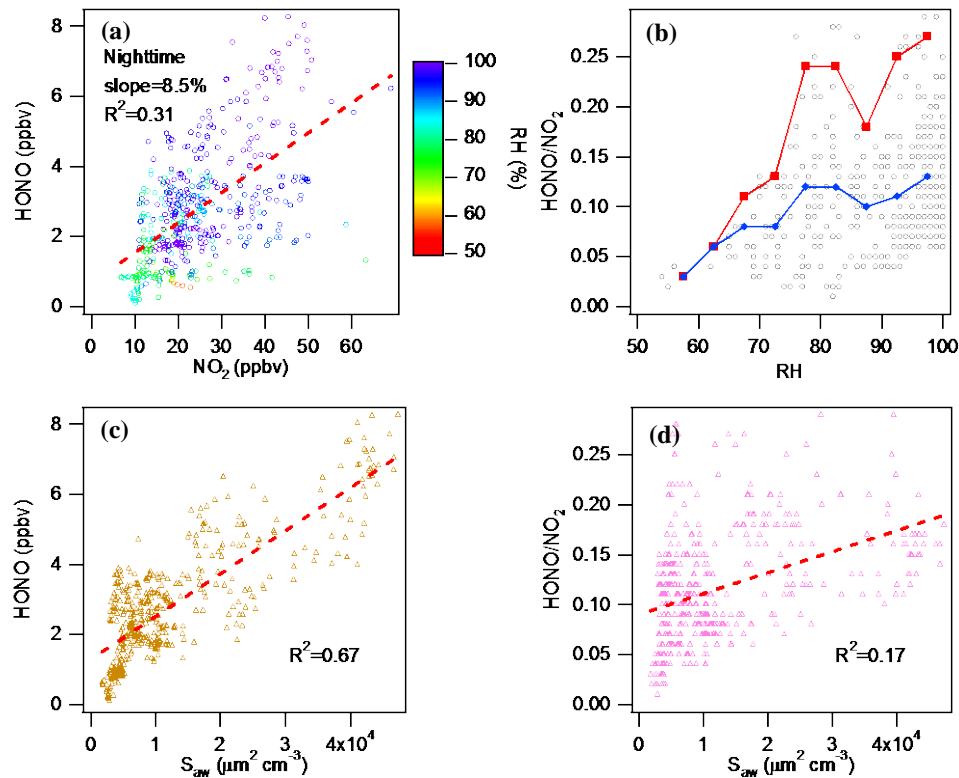


Figure 5- 7. Nighttime relationship between HONO and NO_2 (a), HONO/NO_2 and RH (b), HONO and S_{aw} (c) and HONO/NO_2 and S_{aw} (d). The red line in (b) represents the average for the top 5 of HONO/NO_2 and the blue line represents the median for all HONO/NO_2 ratios in an RH interval of 5%.

Good correlation was shown in Fig. 5-7(c) between HONO and S_{aw} , especially when S_{aw} were more than $1.5 \times 10^4 \mu\text{m}^2 \text{cm}^{-3}$, which mainly happened in the nights of Jan 4-5 and Jan 5-6. But the correlation between HONO/NO_2 and S_{aw} was relatively weak ($R^2=0.17$), even though the correlation was positive. This may indicate that during the nighttime, the NO_2 conversion on aerosol surfaces might be a small pathway to form HONO. The correlation between HONO/NO_2 and black carbon (BC) was much weaker ($R^2=0.13$), which indicated a small role of soot in the nighttime formation of HONO.

5.6 Daytime HONO budget

The conversion of NO₂ on ground surfaces seemed continued in the early morning, because the HONO mixing ratios did not decrease just after sunrise. The HONO lifetime to photolysis could reach up to several hours after sunrise and before sunset, but was approximately 14 min at noon time. The balance between HONO production and loss could be reached more easily around noon, and HONO photolysis was the dominant HONO loss pathway at that time. Due to the short lifetime of HONO around noontime, the influence from vertical or horizontal transport became negligible. So the data in the time period from 9:00 to 15:00 was chosen to analyze the HONO unknown source. The values of $\frac{\Delta\text{HONO}}{\Delta t}$ varied between -0.27 ppbv h⁻¹ and 1.17 ppbv h⁻¹, with nearly zero on average during the selected period. The production rate of the unknown daytime HONO source was calculated as E5-2. R_{unknown} varied from 0.3 to 17.4 ppbv h⁻¹, with an average of 4.3 ± 3.6 ppbv h⁻¹. As shown in Fig. 5-8(a), R_{unknown} was higher in the morning than in the afternoon. R_{unknown} exceeded 10 ppbv h⁻¹ during the period from 9:40 to 12:00 on Jan 6, together with high NO₂ and K⁺, which indicated a possible source of biomass burning. Figure 5-8(b) shows that the unknown HONO source was the dominant daytime HONO source, which is more important than the homogeneous reaction between OH and NO. A HONO concentration without considering the unknown source can also be calculated according to E5-2 if R_{unknown} is assigned as zero. And the discrepancy between this HONO concentration and the measured HONO concentration is just the concentration of HONO from the unknown source as described in E5-3. In

this work, the $\text{HONO}_{\text{missing}}$ was 1.9 ± 1.6 ppbv, ranging from 0.2 to 7.5 ppbv, and it contributed to 45.2% -100% of the measured HONO concentrations (see Fig. 5-8(c)).

$$(E5-2) R_{\text{unknown}} = \frac{\Delta \text{HONO}}{\Delta t} + J_{\text{HONO}}[\text{HONO}] + k_{\text{OH}+\text{HONO}}[\text{OH}][\text{HONO}] - k_{\text{OH}+\text{NO}}[\text{OH}][\text{NO}]$$

$$(E5-3) [\text{HONO}]_{\text{missing}} = [\text{HONO}]_{\text{measured}} - \frac{k_{\text{OH}+\text{NO}}[\text{OH}][\text{NO}] - \frac{\Delta \text{HONO}}{\Delta t}}{J_{\text{HONO}} + k_{\text{OH}+\text{HONO}}[\text{OH}]}$$

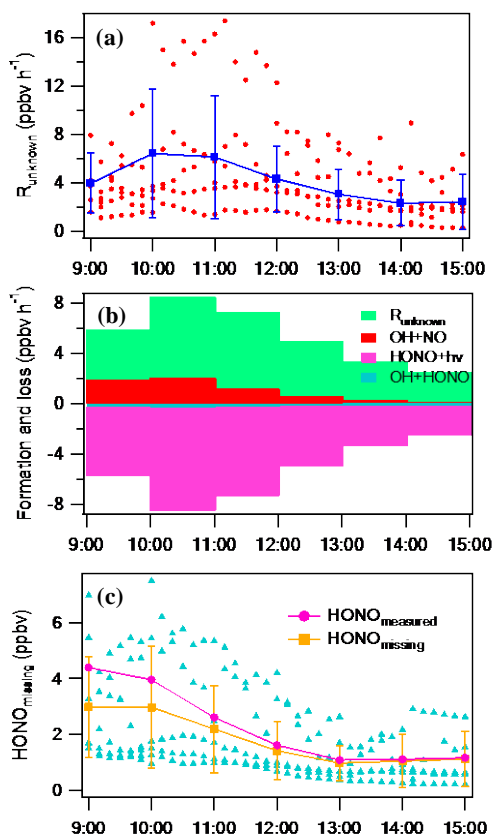


Figure 5- 8. (a) Calculated values of the production rate of HONO unknown source R_{unknown} . The blue line was the variation of average R_{unknown} at each hour. (b) presents the variation of average HONO formation and loss rates at each hour. (c) Calculated

missing HONO concentrations corresponding to the production of unknown HONO sources.

By analyzing the correlation between R_{unknown} and various parameters, possible HONO sources can be speculated. As listed in Table 5-1, correlations for the whole period from 9:00 to 15:00 were presented together with these only in the morning or only in the afternoon. The outliers of R_{unknown} on Jan 6 ($>10 \text{ ppbv h}^{-1}$) were excluded when the correlation was conducted, which would affect the correlation analysis and lead to fake correlation. During the daytime, the correlation between R_{unknown} and NO_2 was good ($R^2=0.38$) in the morning, while it was bad ($R^2=0.03$) in the afternoon, which may indicate that NO_2 was an important precursor of HONO in the morning, but not in the afternoon.

In the morning, the weaker correlation between R_{unknown} and $\text{NO}_2 * S_{\text{aw}}$ ($R^2=0.31$) revealed that the NO_2 conversion was probably not on the aerosol surfaces. However, if the solar radiation represented by J_{NO_2} was considered, the situation seemed different because R_{unknown} had a better correlation with $J_{\text{NO}_2} * \text{NO}_2 * S_{\text{aw}}$ ($R^2=0.42$). R_{unknown} had good correlation with the concentrations of $\text{PM}_{2.5}$, BC, NH_4^+ and total nitrate (THNO_3) ($R^2=0.54, 0.49, 0.58, \text{ and } 0.55$, respectively). And it is obvious that the correlation between BC was significantly improved if considering the J_{NO_2} ($R^2=0.55$). The best correlation existed between R_{unknown} and $\text{NO}_2 * \text{RH} * \text{NH}_3$ with $R^2=0.67$. Homogeneous reactions between NO_2 , H_2O and NH_3 was suggested as a possible source of HONO by Zhang and Tao (2010) through theoretical calculation, but the mechanism was still not

verified. Overall, the sources of HONO seemed complex in the morning with NO₂ as an important precursor.

In the afternoon, the NO₂ related reactions were no longer important. One possible reason was that the concentration of NO₂ was lower in the afternoon than in the morning. NO₂ is an important precursor for O₃ production, and O₃ accumulated fast in the afternoon. Thus, in the afternoon NO₂ probably participated more in the photochemical reactions, but not the HONO formation process. It is noticed that R_{unknown} correlated well with S_{aw}, PM_{2.5}, BC, and NH₄⁺ in the afternoon (R²=0.49, 0.46, 0.62, and 0.51, respectively). This indicated that HONO formation was highly related to aerosols in the afternoon. The best correlation existed between R_{unknown} and J_{NO₂*BC} with R²=0.68. However, previous lab study showed that the photo-enhanced NO₂ conversion on soot surfaces was not an important HONO source due to the low uptake coefficients in the order of 10⁻⁸-10⁻⁷ (Monge et al., 2010), which is much lower than the calculated uptake coefficients of 1.1 ± 1.4×10⁻⁴ based on E5-4. This is contrary to the good correlation between R_{unknown} and J_{NO₂*BC} in this work. Hence, more studies about the reactions on soot are suggested to be conducted with other precursors other than NO₂.

$$(E5-4) P_{\text{hetero}} = \frac{1}{4} \gamma_{\text{NO}_2 \rightarrow \text{HONO}} \times S_{\text{aw}} \times V_{\text{NO}_2} \times \text{NO}_2$$

$$(E5-5) P_{\text{HNO}_3 \rightarrow \text{HONO}} = \frac{f \times [\text{THNO}_3] \times V_{\text{HNO}_3} \times t_d \times j_{\text{HNO}_3 \rightarrow \text{HONO}}}{H}$$

The photolysis of deposited nitrate was possibly another source of HONO in the afternoon, even though the correlation was not as significant as J_{NO₂*BC}. The

production rate of HONO through this mechanism can be calculated through E5-5: Where f is the fraction of noontime full sun to which the surfaces were exposed (0.25), V_{HNO_3} is the dry deposition velocity of HNO_3 (5cm s^{-1}) over t_d period (24 h) within a mixing height H of 250 m, $j_{\text{HNO}_3 \rightarrow \text{HONO}}$ is the photolysis rate constant of HNO_3 via HONO pathway. $j_{\text{HNO}_3 \rightarrow \text{HONO}}$ was $2.25 \times 10^{-5} \text{ s}^{-1}$ with average $P_{\text{HNO}_3 \rightarrow \text{HONO}}$ as 3.19 ppbv h^{-1} and average $[\text{THNO}_3]$ as 9.1 ppbv. This value was comparable to $1.2 \pm 0.2 \times 10^{-5} \text{ s}^{-1}$ (Zhou, 2003) and within the range of $6.0 \times 10^{-6} - 3.7 \times 10^{-4} \text{ s}^{-1}$ on natural and artificial surfaces (Ye et al., 2016).

Table 5- 1. Correlations between R_{unknown} and various parameters.

Parameters	R^2 (9:00-15:00)	R^2 (9:00-12:00)	R^2 (12:00-15:00)
NO_2	0.03	0.38	0.03
J_{NO_2}	0	0.01	0.05
$J_{\text{NO}_2} * \text{NO}_2$	0	0.07	0.02
S_{aw}	0.11	0.01	0.49
$\text{NO}_2 * S_{\text{aw}}$	0.14	0.31	0
$J_{\text{NO}_2} * \text{NO}_2 * S_{\text{aw}}$	0.14	0.42	0
RH	0	0	0.03
$\text{NO}_2 * \text{RH}$	0.07	0.45	0.05
$\text{NO}_2 * \text{RH} * \text{NH}_3$	0.15	0.67	0.01
$\text{PM}_{2.5}$	0.46	0.54	0.46
BC	0.54	0.49	0.62
NH_4^+	0.53	0.58	0.51
THNO_3	0.27	0.55	0.29
$J_{\text{NO}_2} * \text{PM}_{2.5}$	0.26	0.30	0.40
$J_{\text{NO}_2} * \text{BC}$	0.49	0.55	0.68
$J_{\text{NO}_2} * \text{THNO}_3$	0.13	0.22	0.31

Statement: The correlation was conducted excluding the points with R_{unknown} more than 10.0 ppbv h^{-1} . R_{unknown} from 9:40 to 12:00 on Jan 6 were more than 10 ppbv h^{-1} , which were outliers.

It is difficult to speculate the HONO contribution from soil emission based on our current data. Our measurement site located at a height of 60 m above sea level, and on the top of a small hill surrounded by thick woods, which could be treated as the height of upper canopy. Recent research suggested that bare soil had the highest emission efficiency of HONO, while soil covered with vegetations emitted less HONO (Meusel et al., 2017). The contribution of HONO from soil emission at our site needs to be considered carefully.

5.7 Improvement of HONO simulation in the box model

In the original reactions of MCM, HONO has only one source which is the reaction between OH and NO. For the loss of HONO, one pathway is its photolysis and the other way is the reaction between OH and HONO. Later, Xue et al. (2014) added two pathways as HONO sources according to the parameterizations of Li et al. (2010), which were the reactions of NO₂ on aerosol surfaces and ground surfaces, respectively.



$$k_a = 0.25 \times C_{\text{NO}_2} \times \gamma_a \times S_a ;$$

$$k_g = 0.125 \times C_{\text{NO}_2} \times \gamma_g \times S_g ;$$

where C_{NO_2} is the mean molecular speed of NO₂; γ_a and γ_g are the uptake coefficients of NO₂ on the aerosol and ground surfaces; S_g is the effective surface density of the ground,

which is calculated with the ratio of an effective surface area of 1.7 m^2 per geometric ground surface to the mixing height of the boundary layer; S_a is the aerosol surface area concentration. The values of γ_g were set as 1.0×10^{-6} during the nighttime, and increased to 2.0×10^{-5} after sunrise. During the daytime, if the solar radiation exceeded 400 W m^{-2} , a higher γ_g were set as $2.0 \times 10^{-5} \times (\text{solar radiation} / 400)$. As to γ_a , a value of 1.0×10^{-6} during the nighttime and increased it to 5.0×10^{-6} during the day. According to the analysis in section 5.1, the conversion ratio of HONO/NO₂ actually increased with RH during the nighttime. The median ratio of HONO/NO₂ in the RH interval of 75-80% was nearly 5.0 times of that in the RH interval of 50-55%. Hence, we corrected the nighttime γ_a and γ_g as an equation of $1.0 \times 10^{-6} + 0.13 \times 10^{-6} \times (\text{RH} - 50)$ in the RH interval from 50% to 80%; after 80%, γ_a and γ_g were set as 5.0×10^{-6} . During the daytime, the photolysis of aerosol nitrate and deposited nitrate were possible sources of HONO. The deposition rate of HNO₃ was set as $5.0 \times 10^{-5} \text{ s}^{-1}$ (Edwards et al., 2013). The partitioning rate of gas phase HNO₃ to particle phase NO₃⁻ was set as 6.0×10^{-6} , which was the original value used in MCM. The lifetime of aerosol nitrate and the deposited nitrate was set as 24 h which equals to a physical loss rate of $1.15 \times 10^{-5} \text{ s}^{-1}$ in the boundary layer height of 1000 m to avoid the accumulation of nitrate in the system. The photolysis rate of these nitrate was treated as 100 times of that of gas phase HNO₃, and the maximum value was $3 \times 10^{-5} \text{ s}^{-1}$ at noon. The deposition velocity of HONO was set as 0.5 cm s^{-1} in an efficient mixing height of 75 m. As shown in Fig. 8, the original HONO mechanism significantly underestimated both the daytime and the nighttime HONO concentrations. After the nighttime RH-corrected method was used, the nighttime HONO concentrations

increased significantly and matched better with the measured results. If the photolysis of deposited nitrate and aerosol nitrate was considered in the model, the total nitrate concentration was around 20-30 ppbv during the daytime. These pathway increased the daytime HONO concentrations to around 1 ppbv, and matched better with measured daytime HONO except on these two episode days. There are probably other daytime HONO sources in the haze event, which needs to be further investigated. In this work, it is showed that the RH-related conversion from NO_2 to HONO and the photolysis of nitrate could well improve the accuracy of the simulated results of HONO with a box model based on MCM.

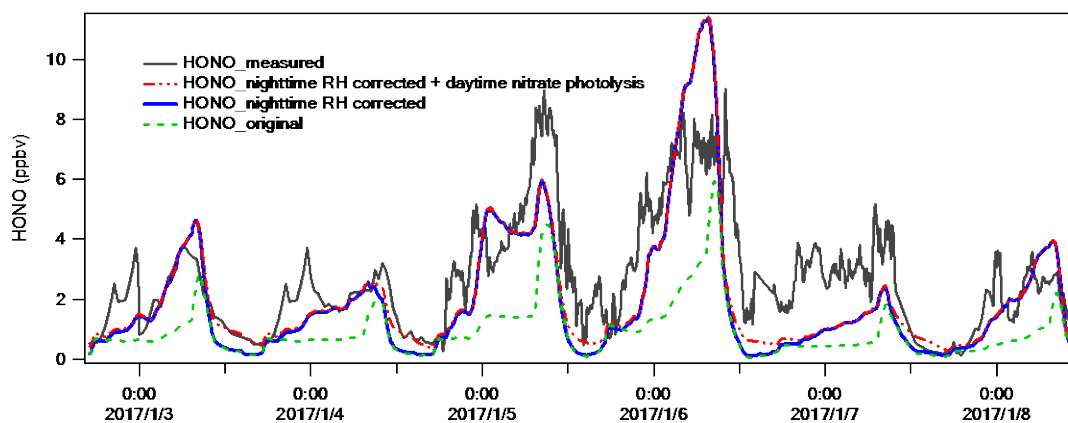


Figure 5- 9. Simulated and measured HONO concentrations with the box model.

5.8 Summary

Extremely high HONO concentrations (up to 9.0 ppbv) were observed in a severe pollution episode at a semi-rural site (Hua Guo Shan) in the western PRD in January, 2017. The concentration of HONO was 2.7 ± 1.9 ppbv on average, and it sustained at a

relatively high level in the morning and had peaks even in the afternoon. High HONO concentration of 1.1 ppbv around noon time was observed together with high HONO/NO₂ ratio of 6.5%. HONO was the dominant source (43.7%-64.1%) of primary radicals (=OH+HO₂+RO₂), and governed the in-situ production of ozone, especially in these two severely-polluted days. Nighttime conversion of NO₂ to HONO was highly related to relative humidity (RH). A large unknown daytime source of HONO with production rate of 4.3 ± 3.6 (0.3-17.4, range) ppbv h⁻¹ was derived which correlated to a NO₂ related source in the morning, and a possible photosensitive source on aerosol surface (e.g. photo-enhanced reactions on surfaces or nitrate photolysis) in the afternoon. Further studies should focus on the quantification of reaction coefficients for reactions which lead to HONO formation, and apply these parameters into a model to identify their relative importance.

References

- Dong H-B, Zeng L-M, Hu M, Wu Y-S, Zhang Y-H, Slanina J, et al. The application of an improved gas and aerosol collector for ambient air pollutants in China. *Atmospheric Chemistry and Physics* 2012; 12: 10519-10533.
- Edwards PM, Brown SS, Roberts JM, Ahmadov R, Banta RM, Dubé WP, et al. High winter ozone pollution from carbonyl photolysis in an oil and gas basin. *Nature* 2014; 514: 351-354.
- Elshorbany YF, Kleffmann J, Kurtenbach R, Lissi E, Rubio M, Villena G, et al. Seasonal dependence of the oxidation capacity of the city of Santiago de Chile. *Atmospheric Environment* 2010; 44: 5383-5394.
- Elshorbany YF, Kurtenbach R, Wiesen P, Lissi E, Rubio M, Villena G, et al. Oxidation capacity of the city air of Santiago, Chile. *Atmospheric Chemistry and Physics* 2009; 9: 2257-2273.

- Gutzwiller L, Arens F, Baltensperger U, Gäggeler HW, Ammann M. Significance of semivolatile diesel exhaust organics for secondary HONO formation. *Environmental science & technology* 2002; 36: 677-682.
- Hennig T, Massling A, Brechtel F, Wiedensohler A. A tandem DMA for highly temperature-stabilized hygroscopic particle growth measurements between 90% and 98% relative humidity. *Journal of aerosol science* 2005; 36: 1210-1223.
- Jenkin ME, Saunders SM, Wagner V, Pilling MJ. Protocol for the development of the Master Chemical Mechanism, MCM v3 (Part B): tropospheric degradation of aromatic volatile organic compounds. *Atmospheric Chemistry and Physics* 2003; 3: 181-193.
- Jenkin ME, Young JC, Rickard AR. The MCM v3.3.1 degradation scheme for isoprene. *Atmospheric Chemistry and Physics* 2015; 15: 11433-11459.
- Kim S, VandenBoer TC, Young CJ, Riedel TP, Thornton JA, Swarthout B, et al. The primary and recycling sources of OH during the NACHTT-2011 campaign: HONO as an important OH primary source in the wintertime. *Journal of Geophysical Research: Atmospheres* 2014; 119: 6886-6896.
- Kirchstetter TW, Harley RA, Littlejohn D. Measurement of nitrous acid in motor vehicle exhaust. *Environmental science & technology* 1996; 30: 2843-2849.
- Kurtenbach R, Becker K, Gomes J, Kleffmann J, Lörzer J, Spittler M, et al. Investigations of emissions and heterogeneous formation of HONO in a road traffic tunnel. *Atmospheric Environment* 2001; 35: 3385-3394.
- Li X, Brauers T, Häsel R, Bohn B, Fuchs H, Hofzumahaus A, et al. Exploring the atmospheric chemistry of nitrous acid (HONO) at a rural site in Southern China. *Atmos. Chem. Phys.* 2012; 12: 1497-1513.
- Liu H, Zhao C, Nekat B, Ma N, Wiedensohler A, Van Pinxteren D, et al. Aerosol hygroscopicity derived from size-segregated chemical composition and its parameterization in the North China Plain. *Atmospheric Chemistry and Physics* 2014; 14: 2525-2539.
- Lu KD, Rohrer F, Holland F, Fuchs H, Bohn B, Brauers T, et al. Observation and modelling of OH and HO₂ concentrations in the Pearl River Delta 2006: a missing OH source in a VOC rich atmosphere. *Atmos. Chem. Phys.* 2012; 12: 1541-1569.
- Meusel H, Tamm A, Kuhn U, Wu D, Leifke AL, Fiedler S, et al. Emission of nitrous acid from soil and biological soil crusts represents a dominant source of HONO in the remote atmosphere in Cyprus. *Atmos. Chem. Phys. Discuss.* 2017; 2017: 1-21.
- Michoud V, Kukui A, Camredon M, Colomb A, Borbon A, Miet K, et al. Radical budget analysis in a suburban European site during the MEGAPOLI summer field campaign. *Atmospheric Chemistry and Physics* 2012; 12: 11951-11974.
- Monge ME, D'Anna B, Mazri L, Giroir-Fendler A, Ammann M, Donaldson D, et al. Light changes the atmospheric reactivity of soot. *Proceedings of the National Academy of Sciences* 2010; 107: 6605-6609.

- Qin M, Xie P, Su H, Gu J, Peng F, Li S, et al. An observational study of the HONO–NO₂ coupling at an urban site in Guangzhou City, South China. *Atmospheric Environment* 2009; 43: 5731-5742.
- Ren X, Brune WH, Mao J, Mitchell MJ, Leshner RL, Simpas JB, et al. Behavior of OH and HO₂ in the winter atmosphere in New York City. *Atmospheric Environment* 2006; 40, Supplement 2: 252-263.
- Ren X, Harder H, Martinez M, Leshner RL, Olliger A, Simpas JB, et al. OH and HO₂ Chemistry in the urban atmosphere of New York City. *Atmospheric Environment* 2003; 37: 3639-3651.
- Saunders SM, Jenkin ME, Derwent RG, Pilling MJ. Protocol for the development of the Master Chemical Mechanism, MCM v3 (Part A): tropospheric degradation of non-aromatic volatile organic compounds. *Atmospheric Chemistry and Physics* 2003; 3: 161-180.
- Stutz J, Alicke B, Ackermann R, Geyer A, Wang S, White AB, et al. Relative humidity dependence of HONO chemistry in urban areas. *Journal of Geophysical Research: Atmospheres* 2004; 109, D03307, doi:10.1029/2003JD004135.
- Su H, Cheng YF, Cheng P, Zhang YH, Dong SF, Zeng LM, et al. Observation of nighttime nitrous acid (HONO) formation at a non-urban site during PRIDE-PRD2004 in China. *Atmospheric Environment* 2008a; 42: 6219-6232.
- Su H, Cheng YF, Shao M, Gao DF, Yu ZY, Zeng LM, et al. Nitrous acid (HONO) and its daytime sources at a rural site during the 2004 PRIDE-PRD experiment in China. *Journal of Geophysical Research-Atmospheres* 2008b; 113, D14312, doi:10.1029/2007JD009060.
- Tham YJ, Wang Z, Li Q, Yun H, Wang W, Wang X, et al. Significant concentrations of nitryl chloride sustained in the morning: investigations of the causes and impacts on ozone production in a polluted region of northern China. *Atmos. Chem. Phys.* 2016; 16: 14959-14977.
- Trebs I, Bohn B, Ammann C, Rummel U, Blumthaler M, Königstedt R, et al. Relationship between the NO₂ photolysis frequency and the solar global irradiance. *Atmospheric Measurement Techniques* 2009; 2: 725-739.
- Wang T, Wei XL, Ding AJ, Poon CN, Lam KS, Li YS, et al. Increasing surface ozone concentrations in the background atmosphere of Southern China, 1994-2007. *Atmospheric Chemistry and Physics* 2009; 9: 6217-6227.
- Wang T, Xue L, Brimblecombe P, Lam YF, Li L, Zhang L. Ozone pollution in China: A review of concentrations, meteorological influences, chemical precursors, and effects. *Science of The Total Environment* 2017; 575: 1582-1596.
- Xue L, Gu R, Wang T, Wang X, Saunders S, Blake D, et al. Oxidative capacity and radical chemistry in the polluted atmosphere of Hong Kong and Pearl River Delta region: analysis of a severe photochemical smog episode. *Atmos. Chem. Phys.* 2016; 16: 9891-9903.
- Xue LK, Saunders SM, Wang T, Gao R, Wang XF, Zhang QZ, et al. Development of a chlorine chemistry module for the Master Chemical Mechanism. *Geoscientific Model Development* 2015; 8: 3151-3162.

Ye C, Gao H, Zhang N, Zhou X. Photolysis of Nitric Acid and Nitrate on Natural and Artificial Surfaces. *Environmental Science & Technology* 2016; 50: 3530-3536.

Zhang B, Tao F-M. Direct homogeneous nucleation of NO_2 , H_2O , and NH_3 for the production of ammonium nitrate particles and HONO gas. *Chemical Physics Letters* 2010; 489: 143-147.

Zhou X. Nitric acid photolysis on surfaces in low-NO environments: Significant atmospheric implications. *Geophysical Research Letters* 2003; 30(23), 2217, doi:10.1029/2003GL018620.

Chapter 6. Nighttime NO_x loss and ClNO_2 formation in the residual layer of a polluted region: Insights from field measurements and an iterative box model

6.1 Introduction

Severe photochemical pollution with high levels of NO_x and O_3 has been of major concern in the Pearl River Delta region (including Hong Kong) (Wang et al., 1998, 2001, 2009, 2017; Zhang et al., 2008a). Hazy days with high aerosol loadings also occur from time to time, especially in winter (Deng et al., 2008; Fan et al., 2014; Huang et al., 2016; Wang X et al., 2016; Zhang et al., 2008b). In a previous field campaign at Mt Tai Mo Shan (TMS, 957 a.s.l) in Hong Kong, the highest levels ever reported for N_2O_5 and ClNO_2 (7.7 ppbv and 4.7 ppbv, respectively) were observed in one well-processed air mass from the inland PRD region (Brown et al., 2016; Wang T et al., 2016). The ClNO_2 of 4.7 ppbv enhanced peak O_3 concentration by 16% when the air mass moved out to the open sea (Wang T et al., 2016). Elevated concentrations of N_2O_5 or ClNO_2 (up to 3.5 ppbv and 1.5 ppbv, respectively) were also observed on several other occasions just after sunset during that study. These $\text{N}_2\text{O}_5/\text{ClNO}_2$ -laden air masses were also brought to the site by northerly winds from the inland PRD region. Similar winds were present at the time when the highest concentrations were observed. As the air masses aged, high concentrations of ClNO_2 may be present in downwind locations and may have significant effects on the O_3 production in the following day (Wang T et al., 2016).

In this follow-up study, an iterative box model was applied to investigate NO_x loss and ClNO_2 formation over the entire night for $\text{N}_2\text{O}_5/\text{ClNO}_2$ -laden air masses in the TMS campaign. The uptake coefficient of N_2O_5 and the yield of ClNO_2 were first estimated, and then the relative importance of NO_x loss pathways in the observed air masses was determined. It is demonstrated that high levels of ClNO_2 can be frequently produced in the locations downwind of TMS. This study adds new insights into the nighttime nitrogen chemistry in the residual layers of polluted regions.

6.2 Methods

6.2.1 Measurements in the 2013 campaign

The 2013 field study was conducted at the highest point of Hong Kong, Mt. Tai Mo Shan (957m a.s.l), from Nov 15 to Dec 6, 2013. Detailed descriptions of the site and the list of measured species and techniques were reported by Brown et al., (2016) and Wang T et al., (2016). Briefly, the N_2O_5 and ClNO_2 were concurrently measured with an iodide-chemical ionization mass spectrometer (CIMS, THS Instruments Inc., Atlanta). Aerosol surface area density was calculated in real-time based on measured particle size distribution and numbers using an Ultra fine Particle Monitor (TSI Model3031). Canisters were sampled for the analysis of NMHCs only during the daytime due to entry restrictions to the observation site at night. The five nights selected for investigation had similar back trajectories from northern PRD areas and relatively high $\text{N}_2\text{O}_5/\text{ClNO}_2$ concentrations observed just after sunset or late at night. Fig. 6-1 shows the variations in

N_2O_5 , ClNO_2 , and related parameters during five selected nights. Details of the measurements and air mass analysis can be found in Wang T et al. (2016).

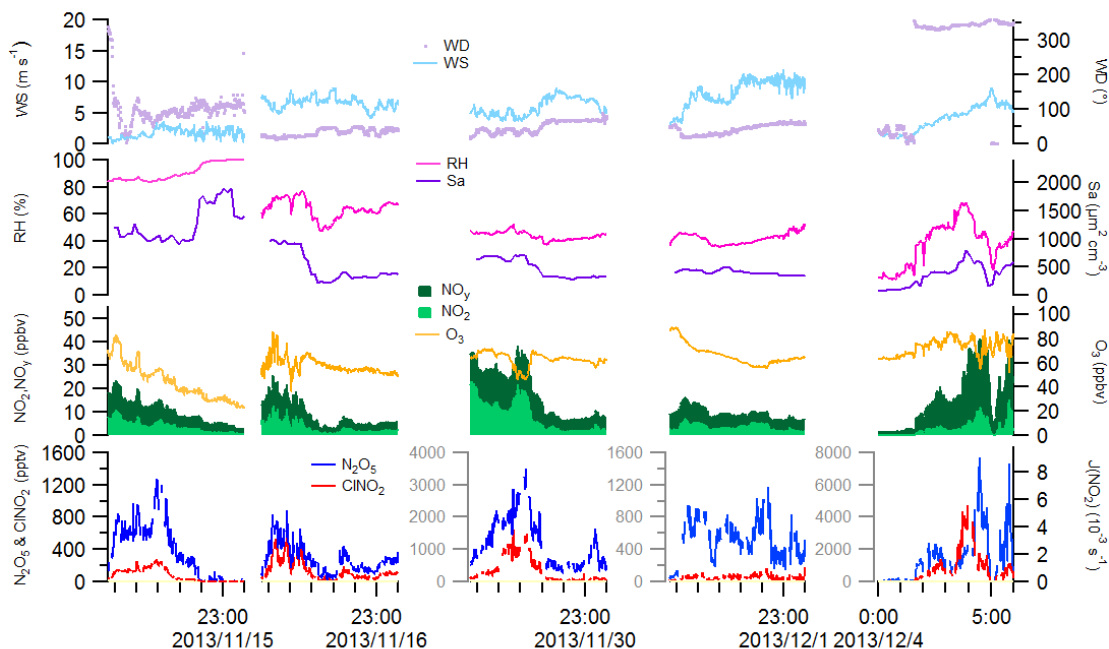


Figure 6- 1. Variations of N_2O_5 , ClNO_2 , and related parameters on five nights (2013/11/15 17:40-0:00, 11/16 17:40-0:00, 11/30 17:40-0:00, 12/1 17:40-0:00, and 12/4 0:00-6:00). The concentrations of NO in these selected periods were close to zero which are not depicted in this figure.

6.2.2 Iterative box model

Calculation process and equations

The iterative box model used in this study was developed by Wagner et al. (2013). It was able to derive the N_2O_5 uptake coefficient and ClNO_2 yield from our data without requiring high-resolution aerosol nitrate concentrations or the steady-state assumption. It

was also able to estimate the integrated N_2O_5 loss and ClNO_2 formation over the entire night. The physical process simulated by the model was the transport of an air mass emitted at time zero (sunset or emission time after sunset) from someplace to the measurement site, and then farther downwind. The simulation stopped at sunrise. The model only considered the chemical reactions from R2-9 to R2-12 and assumed no mixing, dilution, deposition, or interruption during the transport of the air mass. The reaction rates of R2-9 and R2-10 were given as the rates in the Master Chemical Mechanism (<http://mcm.leeds.ac.uk/MCM/>). The first-order rate coefficient for the reaction between NO_3 and VOCs (k_{NO_3}) needed to be assigned, which is discussed later in this Section. Aerosol surface density was assigned as the measured values. The reaction duration was the period from time zero (sunset or emission time) to the measurement time and further to sunrise.

Equations 6-1 to 6-7 were used to calculate the $k_{\text{N}_2\text{O}_5}$ and ϕ_{ClNO_2} . The parameter $s(t_2)$ was an assumed value between 0 and 1. There were two steps in the calculation. In the first step, $s(t_2)$ was set to 1, and the model approximated the initial concentrations of O_3 and NO_2 at time zero based on the measured NO_2 and O_3 , as shown in E6-1 and E6-2, respectively. E6-3 to E6-5 were then used to predict the N_2O_5 concentration from time zero to the measurement time. $k_{\text{N}_2\text{O}_5}$ was iterated until the predicted N_2O_5 concentration matched the measured concentration. In the second step, a new $s(t_2)$ was calculated with E6-6 using the data from the first step. New initial NO_2 and O_3 concentrations were then approximated, and a new $k_{\text{N}_2\text{O}_5}$ value was derived using the same method as in the first step. This process was repeated until the difference between the two $k_{\text{N}_2\text{O}_5}$ was less than

1%. The number of adjustments to $k_{N_2O_5}$ could be no more than 30, and the new $s(t_2)$ could not be calculated more than 10 times. Otherwise, the calculating process would become nonconvergent. The uptake coefficient was derived according to the derived $k_{N_2O_5}$ and E2-1. The yield of $ClNO_2$ was calculated by the ratio of measured $ClNO_2$ concentrations to the integrated N_2O_5 loss, as shown in E6-7. By re-running the cases in a box model using the derived $k_{N_2O_5}$ and ϕ_{ClNO_2} from time zero to sunrise (6:15, Local Time), it was possible to calculate the integrated NO_3 and N_2O_5 loss and $ClNO_2$ production over the entire night for use in the analysis of the nighttime nitrogen chemistry.

$$(E6-1) \quad \frac{d[O_3]}{dt} = -k_1[O_3][NO_2]$$

$$(E6-2) \quad \frac{d[NO_2]}{dt} = -(1+s(t_2))k_1[O_3][NO_2]$$

$$(E6-3) \quad \frac{d[N_2O_5 + NO_3]}{dt} = +k_1[O_3][NO_2] - k_{N_2O_5}[N_2O_5] - k_{NO_3}[NO_3]$$

$$(E6-4) \quad [N_2O_5] = \frac{1}{1 + \frac{1}{K_{eq}[NO_2]}} [N_2O_5 + NO_3]$$

$$(E6-5) \quad [NO_3] = \left(1 - \frac{1}{1 + \frac{1}{K_{eq}[NO_2]}}\right) [N_2O_5 + NO_3]$$

$$(E6-6) \quad s(t_2) = \frac{\int_0^{t_2} k_{N_2O_5}[N_2O_5]dt + [N_2O_5]_{t_2}}{[O_3]_{(0)} - [O_3]_{(t_2)}}$$

$$(E6-7) \phi = \frac{[ClNO_2]}{\int k_{N_2O_5} [N_2O_5] dt}$$

Time zero

Time zero was set as the moment when the nighttime nitrogen reactions began. At this time, N_2O_5 and $ClNO_2$ concentrations were zero. Sunset was selected as time zero, because $N_2O_5/ClNO_2$ -laden air masses formed just after sunset, as shown in Fig. 6-1. The sunset was at 17:15 during the sampling period. I checked the correlation plot of measured O_3 to NO_2 to determine whether there was fresh NO input to the air mass after sunset. If a negative slope was found, indicating the presence of a NO interruption, the plume age was calculated based on E6-8, as suggested by Brown et al. (2006a). Time zero was then reset to the plume age. In the E6-8, S was a constant of either 1 or 2; 1 if NO_3+VOCs was the dominant NO_x loss, and 2 if N_2O_5 uptake was the dominant path. S was assigned as 2 in this study to estimate the plume age. \bar{O}_3 is the average O_3 concentration of the plume, and m is the slope from the correlation plot of O_3 to NO_2 .

$$(E6-8) t_{\text{plume}} = \frac{\ln[1 - S(m + 1)]}{Sk_1\bar{O}_3}$$

As shown in Table 6-1, a negative correlation was found in the air mass between 19:21 and 20:35 on Nov 30, 2013. However, the estimated plume age was even longer than the reaction duration since sunset. Therefore, I still chose sunset as time zero for that date. For the air masses on Dec 4, 2013, plume ages of 5.5 to 6.2 h were derived, so that we assumed that the four air masses on Dec 4 were emitted 5 to 6 hours before the observed

times and selected time zero between 21:00 and 0:00 for the four air masses measured between 2:35 and 6:00.

Table 6- 1. Plume age, time zero, NO_y , and k_{NO_3} used in the simulations in each of the air masses.

Series	Time periods	Plume age	Time zero	NO_y (ppbv)	$\text{NO}_x / \text{NO}_y$	k_{NO_3} (10^{-3} s^{-1})
1	2013/11/15 18:15-21:00	/	sunset	13	0.38	2.20
2	2013/11/16 18:15-19:30	/	sunset	16	0.38	2.65
3	2013/11/30 18:15-19:20	/	sunset	27	0.44	3.26
4	2013/11/30 19:21-20:35	$\approx 3.8\text{h}$	sunset	29	0.48	3.50
5	2013/12/01 18:15-21:00	/	sunset	11	0.36	1.82
6	2013/12/04 02:35-03:16	$\approx 6.2\text{h}$	21:00	16	0.19	1.48
7	2013/12/04 03:17-04:21	/	22:00	24	0.17	1.45
8	2013/12/04 04:22-04:49	$\approx 5.5\text{h}$	23:00	36	0.22	3.27
9	2013/12/04 05:16-06:00	/	00:00	24	0.21	1.45

NO_3 reactivity

NO_3 reactivity is the total loss rate of NO_3 via reactions with VOCs, NO , and species other than NO_2 and via uptake on aerosol surfaces. Canisters for NMHCs analysis were collected only during the daytime due to entry restrictions to the observation site after sunset during the study period. I estimated the concentrations of NMCHs for the calculation of k_{NO_3} in the following way (Wang T et al., 2016). First, I ensured that the NO_y mixing ratios at the times when the canisters were collected were comparable to those in the nighttime air masses to be studied. Second, the concentrations of each NMHC species in the selected canisters were scaled according to the ratio of NO_y . I then regarded the concentrations of the longer-lived alkanes, alkynes, and benzene as their

concentrations in the nighttime air masses. Finally, I reduced the concentrations of alkenes, other aromatics, and DMS to half as their concentrations in the air masses captured just after sunset, and to one fourth as their concentrations in the air masses on Dec 4, which were well-processed when they arrived at the TMS site (Wang T et al., 2016). The NO_3 reactivity calculated based on these estimated VOC concentrations ranged from 1.45×10^{-3} to $3.50 \times 10^{-3} \text{ s}^{-1}$ (Table 6-1). More recently (in November, 2016), another campaign was conducted at the same site, and samples were collected with canisters at 18:00 (Local Time). The calculated k_{NO_3} values with the measured NMHCs from two polluted air masses in 2016 were 1.65×10^{-3} and $4.91 \times 10^{-3} \text{ s}^{-1}$, which were similar to those studied in the 2013 campaign (i.e., $\text{N}_2\text{O}_5/\text{ClNO}_2$ -laden air masses observed soon after sunset). Therefore, the NO_3 reactivity values shown in Table 6-1 are considered to be reasonable.

While the estimated NO_3 reactivity values for the 2013 campaign are believed reasonable, they may have some uncertainty. Sensitivity tests with $1.5k_{\text{NO}_3}$ and $0.5k_{\text{NO}_3}$ were conducted to evaluate the effects of VOCs' concentrations on the NO_3 loss, which are discussed in detail in section 6.6. Here I only illustrate the main results. The resulting changes of uptake coefficients were within the range of $\pm 30\%$, while the deviations of yields were $\pm 35\%$ averagely. The change of contributions to NO_3 loss from different pathways were approximately $\pm 20\%$ for $\text{NO}_3 + \text{VOCs}$ and $\text{N}_2\text{O}_5 + \text{H}_2\text{O}$, and $\pm 5\%$ for $\text{N}_2\text{O}_5 + \text{Cl}$. The change of k_{NO_3} did not affect the predicted ClNO_2 concentrations at sunrise due to the constraint of measured N_2O_5 and ClNO_2 . As to other NO_3 reactions, NO was nearly zero at this site and NO_3 heterogeneous uptake on

aerosols was assumed to be negligible due to the much smaller mixing ratio of NO_3 than that of N_2O_5 and the small uptake coefficient of NO_3 (Brown and Stutz, 2012).

Filtering of the data

Data with a relative humidity (RH) greater than 90% were excluded due to the uncertainty in measurements under high RH conditions and the difficulty in quantifying the aerosol growth factor needed to derive aerosol surface density. The first hour after sunset was not included in the analysis to meet the requirement for the equilibrium between NO_3 and N_2O_5 as suggested by Wagner et al. (2013). The input data included concentrations of measured NO_2 , O_3 , N_2O_5 and ClNO_2 , aerosol surface density, and temperature. The time resolution was 1 min; that is, the air mass passing through the measurement site within a 1 min period was treated as homogeneous.

6.3 N_2O_5 uptake coefficient and ClNO_2 yield

The N_2O_5 uptake coefficients and ClNO_2 yields of $\text{N}_2\text{O}_5/\text{ClNO}_2$ -laden air masses for five nights were derived according to the method described in the preceding section. The uptake coefficients ranged from 0.0005 to 0.016 with an average of 0.004 ± 0.003 , which are within the wide range reported in previous studies (from 0.0005 to 0.1) (Brown and Stutz, 2012; Phillips et al., 2016). The yields ranged from 0.02 to 0.98 with an average of 0.42 ± 0.26 . The average uptake coefficients and yields for each air mass are shown in Table 6-2. For the night of Dec 4, 2013, they were calculated in four separate periods due to contrasting chemical characteristics of the four sampled air masses. Low N_2O_5 and high ClNO_2 were observed from 3:17 to 4:21. In contrast, high

N₂O₅ together with low ClNO₂ were measured from 4:22 to 4:49, which can be explained by the smaller uptake coefficient and yield in this air mass.

Table 6- 2. Average measured data, derived $\gamma_{\text{N}_2\text{O}_5}$ and ϕ_{ClNO_2} , and initial O₃ and NO₂ concentrations at time zero, the net NO₂ loss percentage and predicted ClNO₂ at sunrise for each sample.

Time periods	S _a μm ² cm ⁻³	T °C	RH %	O ₃ ppbv	NO ₂ ppbv	N ₂ O ₅ pptv	ClNO ₂ pptv
2013/11/15 18:15-21:00	1032	15	86	52	5	674	150
2013/11/16 18:15-19:30	926	15	72	61	6	509	349
2013/11/30 18:15-19:20	678	10	46	69	12	1578	444
2013/11/30 19:20-20:35	644	9	47	56	14	2434	1030
2013/12/01 18:15-21:00	438	11	40	69	4	619	55
2013/12/04 2:35-3:16	398	13	50	79	3	1416	830
2013/12/04 3:17-4:21	603	12	60	78	4	1772	2414
2013/12/04 4:22-4:49	501	13	44	68	8	4783	1179
2013/12/04 5:16-6:00	495	13	39	76	5	2437	558

Table 6- 2. Continued.

Time periods	γ	ϕ	O _{3,zero} ppbv	NO _{2,zero} ppbv	NO _{2,loss}	ClNO _{2,sunrise} pptv
2013/11/15 18:15-21:00	0.002±0.002	0.37±0.26	56	9	73%	577
2013/11/16 18:15-19:30	0.007±0.003	0.60±0.23	65	10	72%	1806
2013/11/30 18:15-19:20	0.004±0.022	0.59±0.20	72	17	69%	3057
2013/11/30 19:20-20:35	0.003±0.001	0.58±0.15	58	26	62%	4276
2013/12/01 18:15-21:00	0.004±0.003	0.29±0.20	72	6	79%	282
2013/12/04 2:35-3:16	0.002±0.001	0.59±0.23	83	16	61%	1412
2013/12/04 3:17-4:21	0.003±0.001	0.40±0.26	93	32	67%	3270
2013/12/04 4:22-4:49	0.001±0.001	0.30±0.14	88	38	53%	1491
2013/12/04 5:16-6:00	0.003±0.002	0.17±0.21	91	39	61%	683

Table 6-3 compares the uptake coefficients and yields at TMS with those found in the boundary layers from the United States, Europe, and North China Plain. The uptake coefficients in this study were similar to those derived from aircraft measurements in New England (Brown et al., 2006b) and Texas (Brown et al., 2009) in the United States, but lower than those found in the North China Plain (Tham et al., 2016; Wang H et al.,

2017; Wang X et al., 2017; Wang Z et al., 2017). The uptake coefficients of N_2O_5 are influenced by RH and chemical composition of aerosols. Some previous ambient datasets provided evidence for the suppression of N_2O_5 uptake from aerosol nitrate or organics (Brown et al., 2006b; Wagner et al., 2013), while some others found no dependence on aerosol compositions (Brown et al., 2009; Phillips et al., 2016). It is difficult to pin down the exact reasons for the differences or similarities between our site and others in part because particle composition was not simultaneously measured during the 2013 TMS campaign. It is possible that the chemical conditions at this elevated site (957 m a.s.l) was more similar to the two aircraft measurements, and the pollution levels in the North China Plain were much higher than those in Pearl River Delta. It is noticed that our N_2O_5 uptake coefficients were slightly lower than the values (0.014 ± 0.007) determined with the steady-state approach in the same campaign (Brown et al., 2016). One possible reason is the different periods of data under examination. Brown et al (2016) excluded the data of the first 3 h after sunset in order to meet the condition of steady state assumption, while the present work specifically look into these early periods. The air masses may be different in the two periods. Another reason may be related to different k_{NO_3} adopted in the two studies. The estimated k_{NO_3} for the early evening of this work was 1.45×10^{-3} to $3.50 \times 10^{-3} \text{ s}^{-1}$, which was higher than the average k_{NO_3} of $5.5 \pm 2.5 \times 10^{-4} \text{ s}^{-1}$ for later periods in Brown et al., (2016). For the same total loss rate, if more loss from $\text{NO}_3 + \text{VOC}$, less loss would be from N_2O_5 uptake.

The average yield (0.42) in this study is smaller than that at rural Germany, but larger than that in the US site (Boulder) and at three sites in North China. Current

understanding is that the yield is enhanced by the particulate chloride content (e.g., Bertram and Thornton, 2009). The TMS site is near to the South China Sea, and the relatively large yield at this site compared to the inland sites may be related to abundant oceanic chloride, but more measurements of aerosol composition are needed to pin down the reasons for the difference among the sites.

Table 6- 3. Uptake coefficients and yields from ambient datasets in previous studies.

Site	γ	ϕ	Notes	Reference
Boulder, Colorado	0.002 to 0.1 (0.015 as peak)	less than 0.1 as majority	10-300 m, pollution-boundary layer/residual layer	(Wagner et al., 2013)
TO, Germany (825 m a.s.l)	0.028±0.029 (0.004 to 0.11)	0.49±0.35 (0.035 to 1.38)	Semi-rural mountain site, residual layer	(Phillips et al., 2016)
Mt Tai, (1465ma.s.l)	0.061±0.025 (0.021 to 0.102)	0.27±0.24 (0.02 to 0.90)	High yield in coal-burning power plant plumes	(Wang Z et al., 2017)
Ji'nan, urban ground	0.042 to 0.092	0.014 and 0.082	Low yield with rich chloride in aerosols	(Wang X et al., 2017)
Wangdu, rural ground	0.014, 0.03	0.30, 0.35	Campaign average and highest ClNO ₂ case, respectively	(Tham et al., 2016)
Beijing, urban ground	0.025-0.072	/	Four nights using the steady state lifetime method	(Wang H et al., 2017a)
TMS in 2013 (957m a.s.l)	0.004±0.003 (0.0005-0.016)	0.42±0.26 (0.02-0.98)	Large variability	This work

6.4 Nighttime NO_x loss pathways

To investigate the loss of NO_x, it was necessary to first examine the loss pathways of NO₃ radicals. After the N₂O₅ uptake coefficients and ClNO₂ yields were derived, as described in Section 6.3, the box model was rerun from time zero to sunrise. The derived NO₂ and O₃ concentrations at time zero (NO_{2,zero} and O_{3,zero}), reported in Section

6.3, were treated as initial conditions in the simulation. The produced NO_3 were consumed through NO_3 reactions with VOCs ($\text{NO}_3 + \text{VOCs}$), N_2O_5 hydrolysis ($\text{N}_2\text{O}_5 + \text{H}_2\text{O}$), and ClNO_2 formation ($\text{N}_2\text{O}_5 + \text{Cl}$), whereas a portion of the NO_3 remained as NO_3 and N_2O_5 in the air to sustain the equilibrium. The integrated NO_3 production and loss were calculated when the model was rerun. The same method as in Wagner et al. (2013) was used to evaluate the relative importance of these four pathways to the loss of NO_3 radicals.

Figure 6-2 shows the integrated NO_3 production and the contribution of each NO_3 loss pathway to the consumption of the produced NO_3 . To examine the variation under different NO_2 conditions, the data were plotted as a function of the measured NO_2 mixing ratio. The blue dots in Fig. 6-2 are for individual model calculation, and the black line is the median of each bin of the NO_2 histogram, with 1 ppbv as the interval. Fig. 6-2(a) demonstrates that 64% of the NO_2 mixing ratio lies in the range from 2 to 7 ppbv; the data points with NO_2 values ranging from 7 ppbv to 21 ppbv account for 36%. The integrated NO_3 production increased with the increase in measured NO_2 . The median of the integrated NO_3 production ranged from 3 to 15 ppbv with an average of 10 ppbv. When NO_2 concentrations were less than 7 ppbv, the NO_3 reactions with VOCs were the dominant loss pathway, consuming 65% of the total NO_3 produced. N_2O_5 hydrolysis and ClNO_2 formation accounted for 21% and 11%, respectively. When the NO_2 concentrations were more than 7 ppbv, the NO_3 reactions with VOCs, N_2O_5 hydrolysis, and ClNO_2 formation consumed 37%, 30%, and 30% of the produced NO_3 , respectively. These results were different from those in the winter campaign conducted

in Colorado, in which N_2O_5 hydrolysis was the dominant (~80%) loss pathways for nighttime NO_3 (Wagner et al., 2013). The difference could first be attributed to the lower temperature (typically 0 °C) in the winter study of Wagner et al., (2013), which favored N_2O_5 in the equilibrium between NO_3 and N_2O_5 . In addition, $\gamma_{\text{N}_2\text{O}_5}$ was higher and ϕ_{ClNO_2} was lower in Wagner et al., (2013) compared to those in TMS. As a result, the pathway of N_2O_5 hydrolysis was dominant in Wagner et al., (2013), while the ClNO_2 formation was also important at TMS.

The net NO_2 loss was estimated using the integrated NO_3 production and a multiplier (η), as shown in E6-9 and E6-10 (Wagner et al., 2013). $F(\text{NO}_3 \text{ reactivity})$, $F(\text{N}_2\text{O}_5 \text{ hydrolysis})$, and $F(\text{ClNO}_2 \text{ formation})$ were the fractions of each NO_3 loss pathway in consuming the total NO_3 production. The accumulated ClNO_2 and the residual NO_3 and N_2O_5 all regenerate NO_2 through photolysis at sunrise, so these items were excluded from the net NO_2 loss.

$$(E6-9) \text{ Net } \text{NO}_2 \text{ loss} = \eta \times \int_{\text{time zero}}^{\text{sunrise}} k_1 [\text{O}_3][\text{NO}_2]$$

$$(E6-10) \eta = 1 \times F(\text{NO}_3 \text{ reactivity}) + 2 \times F(\text{N}_2\text{O}_5 \text{ hydrolysis}) + 1 \times F(\text{ClNO}_2 \text{ formation})$$

Figure 6-2(f) shows the percentage of net NO_2 loss compared to the NO_2 concentration at time zero. NO_3 and N_2O_5 chemistry reduced the initial NO_2 , which was on average 17 ± 14 ppbv, by 35% to 89% with an average of $70\% \pm 10\%$ over the entire night. NO_3 reactions with VOCs and the heterogeneous uptake of N_2O_5 contributed to approximately 40% and 60% of the net NO_2 loss, respectively. Some of the initial NO_2

remained in the air masses at sunrise in the form of ClNO_2 (average, $10\% \pm 7\%$), $\text{NO}_3/\text{N}_2\text{O}_5$ (average, $5\% \pm 6\%$), and NO_2 (average, $15\% \pm 5\%$).

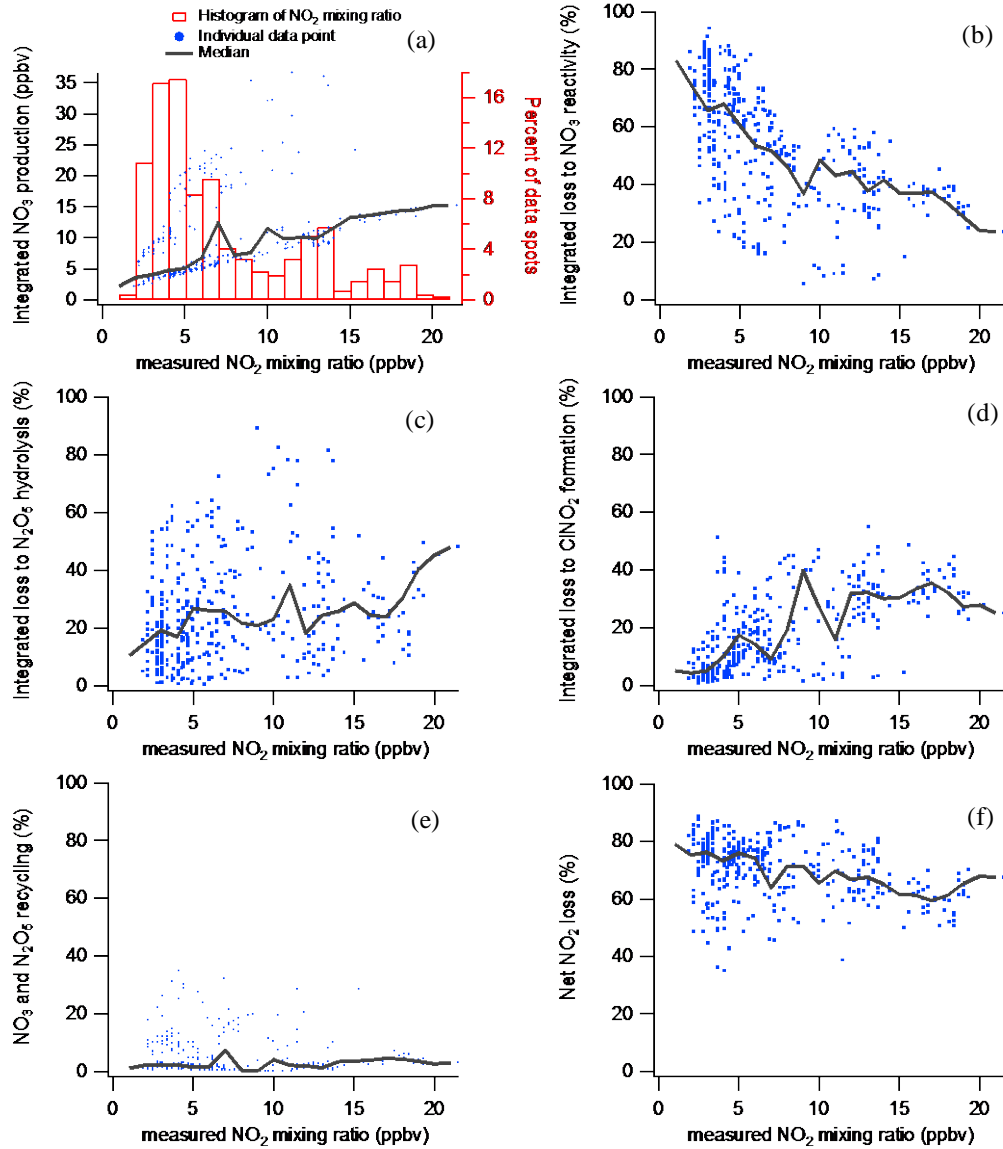


Figure 6- 2. Distribution of integrated NO_3 production rate from time zero to sunrise as a function of the measured NO_2 mixing ratio (a). The bars are the percentage of data spots in each size bin (interval is 1 ppbv of NO_2) in the histogram of NO_2 mixing ratio. (b) to

(e) represent the percentage of NO_x loss through the following reactions: (b) $\text{NO}_3 + \text{VOCs}$; (c) $\text{N}_2\text{O}_5 + \text{H}_2\text{O}$; (d) $\text{N}_2\text{O}_5 + \text{Cl}^-$; and (e) recycling between NO_3 and N_2O_5 . (f) is the percentage of net NO_2 loss compared to the initial NO_2 concentration at time zero. The black lines represent the median in each interval of the NO_2 mixing ratio.

6.5 ClNO_2 production over the entire night

One of the objectives of this study was to determine the amount of ClNO_2 produced over the entire night in the selected cases. Fig. 6-3(a) shows the observed ClNO_2 concentrations at TMS and the corresponding predicted concentrations of ClNO_2 at sunrise in downwind locations. The average predicted ClNO_2 concentrations in each case are listed in Table 6-2. After sufficient ageing of air masses observed just after sunset, the accumulated ClNO_2 concentrations were 3.8 to 6.8 times the ClNO_2 measured at the observation site. The ClNO_2 concentrations for the four periods on Dec 4 also increased at sunrise by 22%-70% of the measured concentrations. On Nov 30, the ClNO_2 was below 2 ppbv in the early evening, but increased to over 6 ppbv at sunrise. The uptake coefficients were modest, but the yields were relatively high on this night (see Table 6-2).

Figure 6-3(b) shows that the predicted ClNO_2 concentrations at sunrise positively correlated to the measured NO_2 concentrations, with R values of 0.77. Higher yields led to greater ClNO_2 production under the same NO_2 level when NO_2 concentrations were more than 7 ppbv. At TMS, the O_3 concentrations were always much higher than the NO_2 concentrations (Wang T et al., 2016), which means that there was sufficient O_3 to

oxidize NO_2 . The accumulation of ClNO_2 was probably limited by nighttime NO_2 concentrations. Overall, the calculations confirmed our previous finding that abundant ClNO_2 is frequently produced in the residual layer of the PRD region, which has a significant impact on the daytime oxidative capacity and photochemistry of the upper boundary layer.

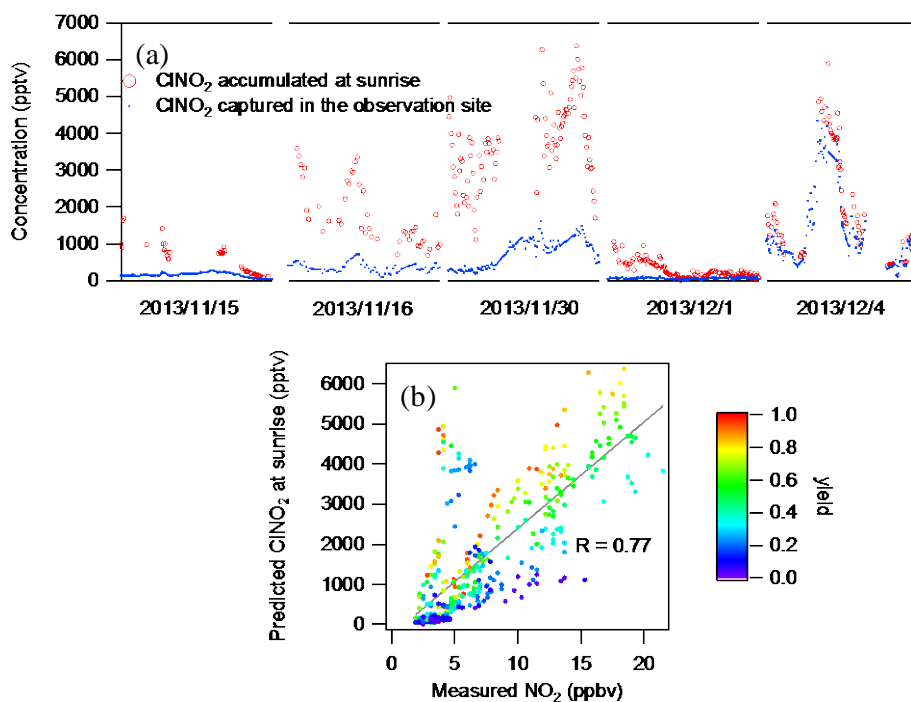


Figure 6- 3. (a) Predicted ClNO_2 and N_2O_5 concentrations at sunrise of the following day. (b) The relationship between predicted ClNO_2 with measured NO_2 . The color bar shows the predicted yield.

6.6 Sensitivity tests about VOCs' concentrations to the NO₃ loss contribution

Sensitivity tests were conducted by multiplying the original estimated VOCs with a factor of 1.5 and 0.5 as suggested in Wang T et al., (2016) in order to evaluate the effects of estimated VOCs' concentrations to the NO₃ loss contribution. The change of NO₃ reactivity first affected the values of N₂O₅ uptake coefficients and ClNO₂ yields, considering the competition for NO₃ radicals between NO₃+VOCs and N₂O₅ heterogeneous reactions. The deviations of uptake coefficients were within the range of ±30% as shown in Fig. 6-4, while the deviations of yields were relatively disperse, and within the range of ±35% averagely. The increase of k_{NO_3} led to decrease of uptake coefficients and increase of yields, and vice versa. This is mainly attributed to the constraint of N₂O₅ and ClNO₂ concentrations during the model calculations.

The change of these parameters could cause effects on the contributions of different pathways to NO₃ consumption as shown in Fig. 6-5 and Fig. 6-6. The patterns of each pathway seem similar with these in Fig. 6-2. However, the increase of k_{NO_3} led to the increase of the contribution of NO₃+VOCs to NO₃ consumption and the decrease of the contribution of N₂O₅ heterogeneous reactions. The average contributions to NO₃ loss were 52%, 23%, and 22% for NO₃+VOCs, N₂O₅+H₂O and N₂O₅+Cl, respectively. For the net NO₂ loss, 69% of NO₂ were removed through NO₃+VOCs and N₂O₅ heterogeneous reactions with contributions of 44% and 56%, respectively. On the contrary, the decrease of k_{NO_3} led to the decrease of the contribution of NO₃+VOCs to

NO₃ consumption, while the contribution of N₂O₅ heterogeneous reactions increased. The average contributions to NO₃ loss were 30%, 41%, and 25% for NO₃+VOCs, N₂O₅+H₂O and N₂O₅+Cl⁻, respectively. For the net NO₂ loss, 69% of NO₂ were removed through NO₃+VOCs and N₂O₅ heterogeneous reactions with contributions of 22% and 78%, respectively. The change of k_{NO_3} did not change the predicted ClNO₂ concentrations at sunrise due to the constraint of measured N₂O₅ and ClNO₂ as shown in Fig. 6-7.

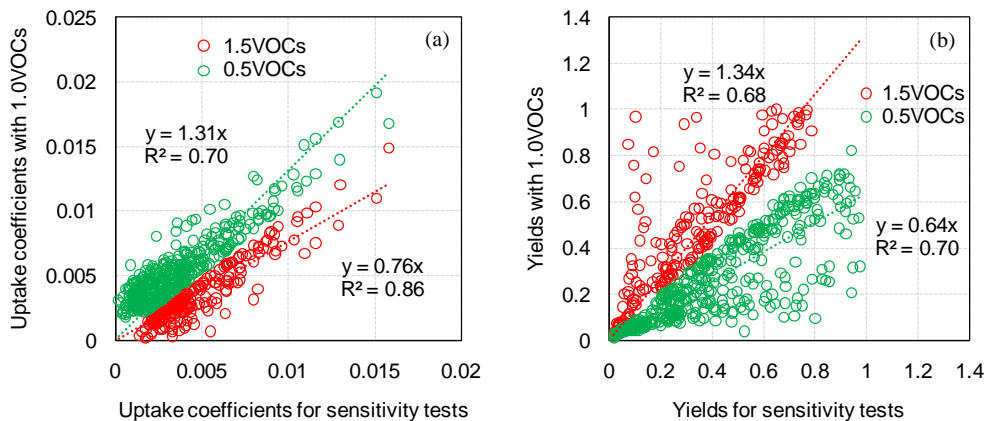


Figure 6- 4. Correlations of uptake coefficients and yields between the cases with original VOCs and these with 1.5/0.5VOCs.

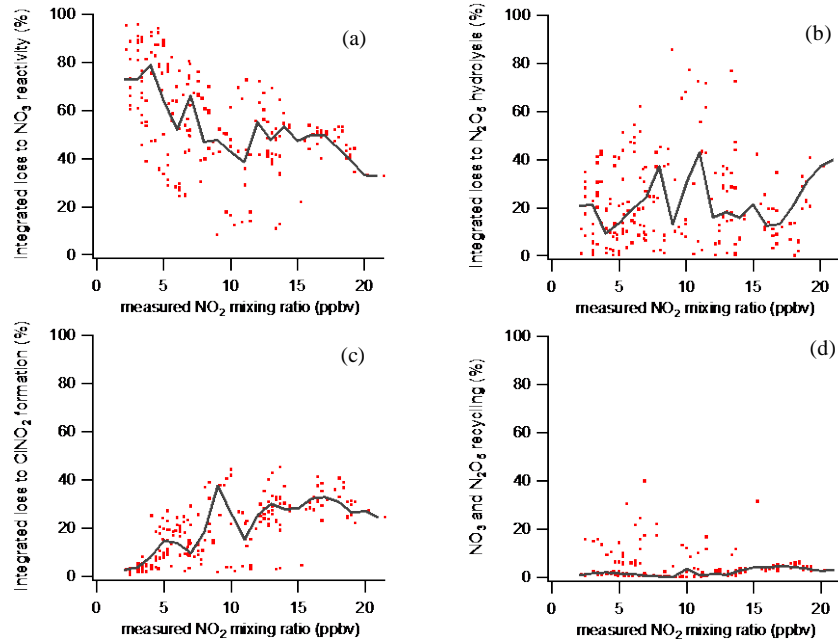


Figure 6- 5. Contributions of different pathways to NO_3 consumption with 1.5VOCs.

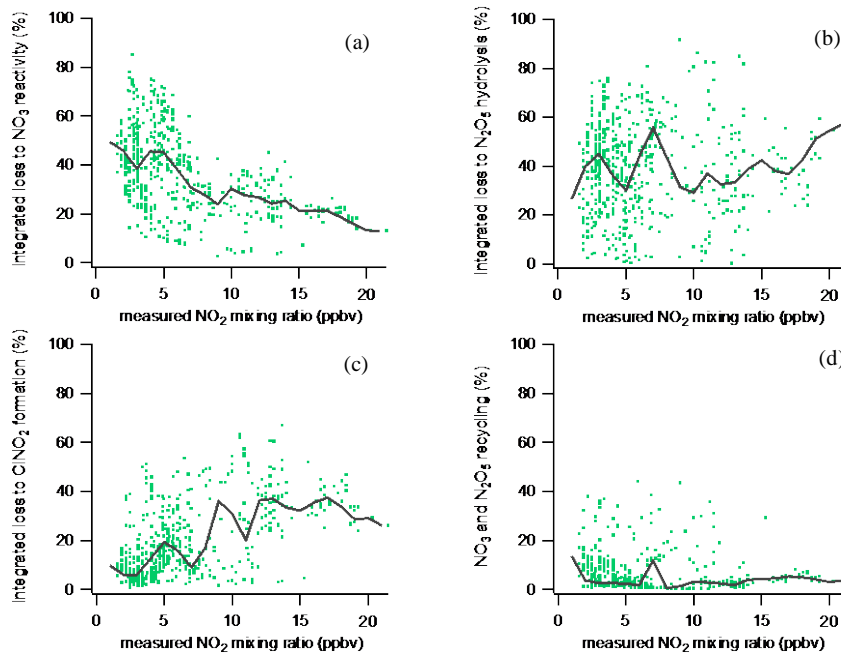


Figure 6- 6. Contributions of different pathways to NO_3 consumption with 0.5VOCs.

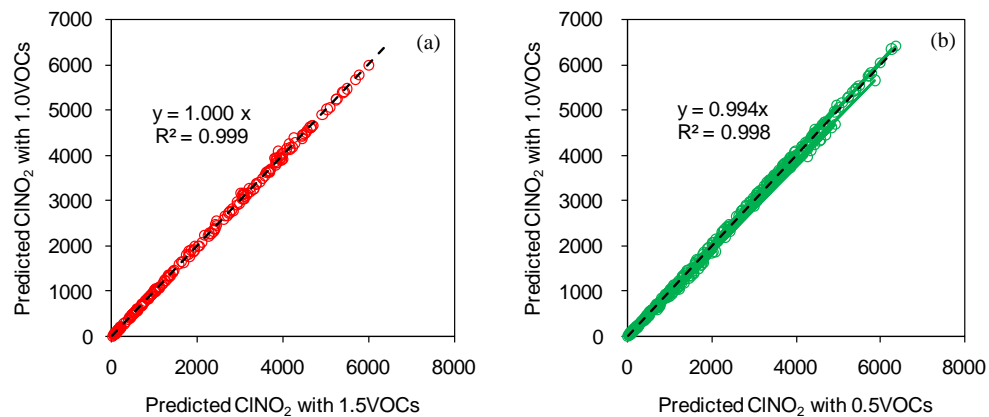


Figure 6- 7. Correlations of predicted ClNO_2 concentrations at sunrise between the cases with original k_{NO_3} and these with 1.5/0.5VOCs.

6.7 Influence of ClNO_2 on O_3 production in the following day

This section focuses on the impact of the high ClNO_2 on the radical and O_3 production in the open sea. The measured highest ClNO_2 was 4.7 ppbv occurred at 4:00 on Dec. 4, 2013, and the modeled highest ClNO_2 was 6.0 ppbv at sunrise. Wang et al. (2016) has already evaluated the impact of the 4.7 ppbv ClNO_2 by releasing the measured air mass free in the box model at sunrise for the following 24 h. The details of the box model were described in Chapter 3. Here, only the lifetime to dry deposition was changed to 24 h due to the high altitude for this campaign. The model was initialized by observed data and run for a 24 h period to track the chemical evolution in the air mass after leaving the TMS site. Scenarios with and without ClNO_2 were compared to see the impact of ClNO_2 . The photolysis frequencies were scaled with measured J_{NO_2} at the TMS site. The model was run 6 times to stabilize the intermediates, and the daytime output of the last run was

subject to further analysis. Detailed description for the model can be found in Wang et al., (2016).

The results for the measured highest ClNO₂ (4.7 ppbv) case are shown in Fig. 6-8 which is cited from Wang et al. (2016). The initial data for this simulation was also listed in Table 6-4. Photolysis of ClNO₂ in the morning led to peak concentrations of Cl of 1.1×10^5 molecules cm⁻³. The concentrations of OH and HO₂ were increased by a maximum of 77% and 106% due to the Cl reactions with VOCs and the recycled NO₂. Daytime peak ozone increased from 95 ppbv to 110 ppbv, or a 15.8% increase (Fig. 6-8). The ozone formation is not sensitive to different concentrations of VOCs used in the simulations, as it is in a NO_x-limited regime indicated by higher ozone levels with increased NO₂ concentrations. The ClNO₂ chemistry accounts for 41% of the total ozone produced (~36 ppbv, see Fig. 6-8(d), which is derived with the discrepancy between 110 ppbv and the lowest point of 74 ppbv for the red line).

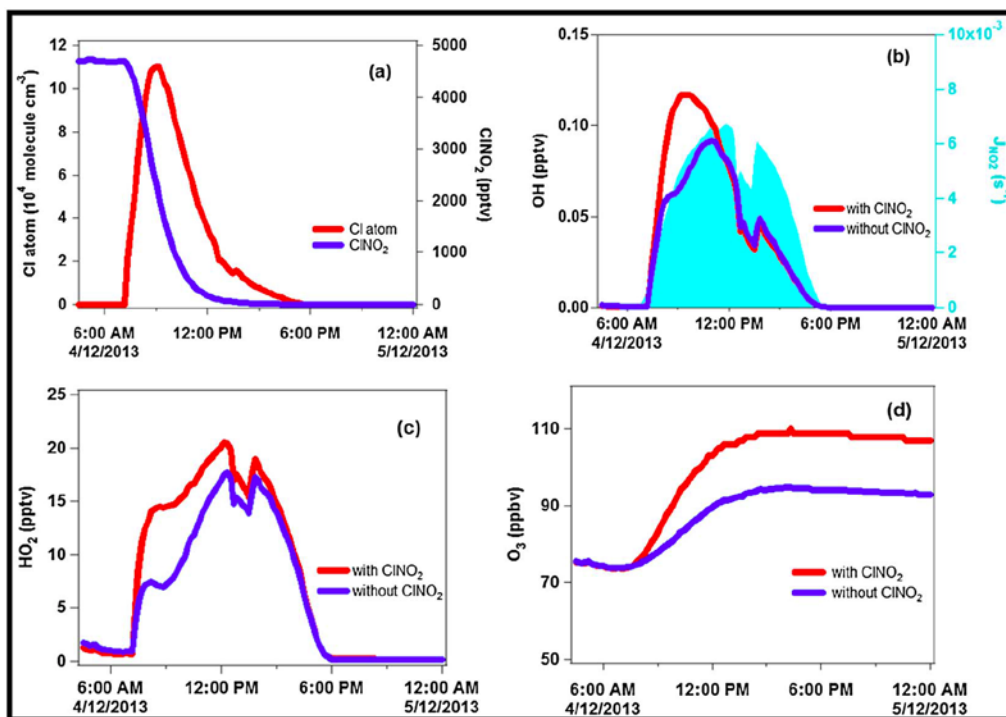


Figure 6- 8. Model simulated concentrations/mixing ratios of (a) ClNO_2 and Cl, (b) OH, (c) HO_2 , and (d) ozone during the day following plume sampling from the Mt. TMS site, with and without the ClNO_2 chemistry. The measured photolysis rate constant of NO_2 is shown by the blue shading. The model was initiated with the measured ClNO_2 and other relevant chemical constituents at 04:00 (4.7 ppbv of ClNO_2). (Cited from Wang et al., (2016), and this work was done by Xue L.K. in Shandong University)

The impact of the simulated ClNO_2 of 6.0 ppbv was also evaluated with the similar method. But I released the air mass measured at 17:30, and applied the derived uptake coefficient of 0.003 and the yield of 0.58 on Nov. 30-Dec. 1. The comparison scenario set the yield as 0 so that all N_2O_5 heterogeneous loss leads to nitrate formation. The initial data for this simulation was also listed in Table 6-4. First, this simulation is

treated as a check for the results from the iterative box model to see if it can form 6.0 ppbv ClNO_2 using the full chemical mechanism of MCM. The simulated ClNO_2 can reach 6.0 ppbv at sunrise as shown in Fig. 6-9(a). The photolysis of ClNO_2 can generate Cl radical as high as 2.4×10^5 molecules cm^{-3} . The average OH and HO_2 in the morning (7:00-12:00) with ClNO_2 formation was 2.9 and 5.9 times these in the case without ClNO_2 formation, respectively. Peak O_3 increased from 61.5 to 82.7 ppbv, that is, $\sim 34.3\%$ increase. Cl chemistry contributed to 56.5% of the total O_3 formation (the ratio of 21.1 ppbv to 37.4 ppbv). Therefore, the ClNO_2 in the upper boundary layer can have significant impact on atmospheric oxidation capacity, including radical formation and O_3 formation.

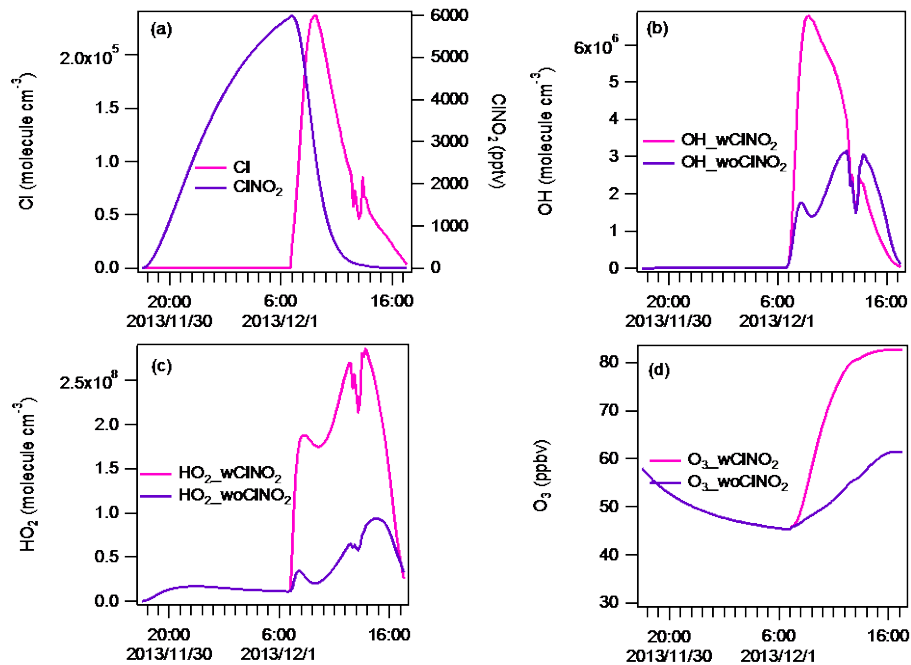


Figure 6- 9. Simulated Cl, OH, HO_2 , and O_3 with and without ClNO_2 formation based on the derived uptake coefficient and yield in the night of Nov. 30-Dec.1 in section 6.3.

Table 6- 4. Initial conditions for the measured case of 4.7 ppbv ClNO₂, and the simulated case for the air mass with 6.0 ppbv ClNO₂ at sunrise.

Species (unit)	Measured case	Simulated case
ClNO ₂ (ppbv)	4.7	0
N ₂ O ₅ (ppbv)	2.15	0
NO (pptv)	20	0
NO ₂ (ppbv)	5	26
O ₃ (ppb)	76	58
HONO (pptv)	634	450
SO ₂ (ppbv)	4.4	0
CO (ppbv)	496	335
CH ₄ (ppmv)	1.944	1.929
Ethane (pptv)	2810	2638
Propane (pptv)	3649	391
n-butane (pptv)	3249	2440
i-butane (ppt)	2436	1733
n-pentane (pptv)	754	1392
i-pentane (pptv)	1062	971
n-hexane (pptv)	766	659
2-methylpentane (pptv)	1066	760
3-methylpentane (pptv)	712	519
2-methylhexane (pptv)	556	0
3-methylhexane (pptv)	610	0
2_3-dimethylbutane (pptv)	199	0
n-heptane (pptv)	378	319
n-octane (pptv)	91	65
n-Nonane (pptv)	84	66
Ethene (pptv)	756	699
Propene (pptv)	119	112
1-butene (pptv)	28.5	27
i-butene (pptv)	51	51
Isoprene (pptv)	41	32
Ethyne (pptv)	2776	2437
Benzene (pptv)	754	740
Toluene (pptv)	3546.5	2979
o-xylene (pptv)	479.5	291
m-xylene (pptv)	1196.5	753
Ethylbenzene (pptv)	790.5	573
n-Propylbenzene (pptv)	79	26
i-Propylbenzene (pptv)	33	12
1,2,3-trimethylbenzene (pptv)	220.5	43

Species (unit)	Measured case	Simulated case
1,2,4-trimethylbenzene (pptv)	213.5	61
1,3,5-trimethylbenzene (pptv)	118.5	18
o-ethyltoluene (pptv)	190	37
m-ethyltoluene (pptv)	102	37
p-ethyltoluene (pptv)	107.5	23
α -pinene (pptv)	27.5	12
β -pinene (pptv)	17	3
cis-butene (pptv)	3.5	3
trans-2-butene (pptv)	3	2
DMS(pptv)	0	23
RH(%)	60	47
Temperature(K)	286	282
S_{aero} (m^{-1})	7.06E-04	6.44E-04
Pressure (mmHg)	665	665

6.8 Summary

An iterative box model was used to derive N_2O_5 uptake coefficients and ClNO_2 yields in $\text{N}_2\text{O}_5/\text{ClNO}_2$ -laden air masses intercepted just after sunset or late at night on top of Tai Mo Shan in Hong Kong. The average uptake coefficient was 0.004 ± 0.003 , with a range of 0.0005 to 0.016. The ClNO_2 yield ranged from 0.02 to 0.98, with an average of 0.42 ± 0.26 . ClNO_2 formation ($\text{N}_2\text{O}_5 + \text{Cl}^-$), N_2O_5 hydrolysis ($\text{N}_2\text{O}_5 + \text{H}_2\text{O}$), and NO_3 reactions with volatile organic compounds ($\text{NO}_3 + \text{VOCs}$) consumed 23%, 27%, and 47% of the NO_3 produced on average, respectively. A significant portion of the NO_x in the air masses ($70\% \pm 10\%$) was removed during the night via NO_3 reactions with VOCs (~40%) and N_2O_5 heterogeneous loss (~60%). Compared to Los Angeles (Tsai et al., 2014) and Colorado (Wagner et al., 2013), a larger fraction of NO_x took the form of ClNO_2 in Hong Kong, especially under high NO_2 conditions. As the “young” air masses

captured just after sunset aged, the predicted ClNO_2 increased up to 6 ppbv at sunrise, indicating strong production of ClNO_2 in the polluted air masses from the PRD region. The high ClNO_2 has been predicted to have significant effects on the atmospheric oxidation capacity in the upper boundary layer in our previous study. The present work indicates that such impact can occur more frequently.

References

- Bertram T, Thornton J. Toward a general parameterization of N_2O_5 reactivity on aqueous particles: the competing effects of particle liquid water, nitrate and chloride. *Atmospheric Chemistry and Physics* 2009; 9: 8351-8363.
- Brown S, Neuman J, Ryerson T, Trainer M, Dube W, Holloway J, et al. Nocturnal odd-oxygen budget and its implications for ozone loss in the lower troposphere. *Geophysical research letters* 2006a; 33, L08801, doi:10.1029/2006GL025900.
- Brown S, Ryerson T, Wollny A, Brock C, Peltier R, Sullivan A, et al. Variability in nocturnal nitrogen oxide processing and its role in regional air quality. *Science* 2006b; 311: 67-70.
- Brown SS, Dube WP, Fuchs H, Ryerson TB, Wollny AG, Brock CA, et al. Reactive uptake coefficients for N_2O_5 determined from aircraft measurements during the Second Texas Air Quality Study: Comparison to current model parameterizations. *Journal of Geophysical Research-Atmospheres* 2009; 114, D00F10, doi:10.1029/2008JD011679.
- Brown SS, Dubé WP, Tham YJ, Zha Q, Xue L, Poon S, et al. Nighttime Chemistry at a High Altitude Site Above Hong Kong. *Journal of Geophysical Research: Atmospheres* 2016; 121, 2457–2475, doi:10.1002/2015JD024566..
- Brown SS, Stutz J. Nighttime radical observations and chemistry. *Chemical Society Reviews* 2012; 41: 6405-6447.
- Deng X, Tie X, Wu D, Zhou X, Bi X, Tan H, et al. Long-term trend of visibility and its characterizations in the Pearl River Delta (PRD) region, China. *Atmospheric Environment* 2008; 42: 1424-1435.
- Fan Q, Yu W, Fan S, Wang X, Lan J, Zou D, et al. Process analysis of a regional air pollution episode over Pearl River Delta Region, China, using the MM5-CMAQ model. *Journal of the Air & Waste Management Association* 2014; 64: 406-418.

- Huang Z, Ou J, Zheng J, Yuan Z, Yin S, Chen D, et al. Process Contributions to Secondary Inorganic Aerosols during Typical Pollution Episodes over the Pearl River Delta Region, China. *Aerosol and Air Quality Research* 2016; 16: 2129-2144.
- Phillips GJ, Thieser J, Tang M, Sobanski N, Schuster G, Fachinger J, et al. Estimating N₂O₅ uptake coefficients using ambient measurements of NO₃, N₂O₅, ClNO₂ and particle-phase nitrate. *Atmospheric Chemistry and Physics* 2016; 16: 13231-13249.
- Tham YJ, Wang Z, Li Q, Yun H, Wang W, Wang X, et al. Significant concentrations of nitryl chloride sustained in the morning: investigations of the causes and impacts on ozone production in a polluted region of northern China. *Atmos. Chem. Phys.* 2016; 16: 14959-14977.
- Tsai C, Wong C, Hurlock S, Pikelnaya O, Mielke LH, Osthoff HD, et al. Nocturnal loss of NO_x during the 2010 CalNex-LA study in the Los Angeles Basin. *Journal of Geophysical Research: Atmospheres* 2014; 119.
- Wagner NL, Riedel TP, Young CJ, Bahreini R, Brock CA, Dubé WP, et al. N₂O₅ uptake coefficients and nocturnal NO₂ removal rates determined from ambient wintertime measurements. *Journal of Geophysical Research: Atmospheres* 2013; 118: 9331-9350.
- Wang H, Lu K, Chen X, Zhu Q, Chen Q, Guo S, et al. High N₂O₅ Concentrations Observed in Urban Beijing: Implications of a Large Nitrate Formation Pathway. *Environ. Sci. Technol. Lett.* 2017a; doi: 10.1021/acs.estlett.7b00341.
- Wang T, Cheung VTF, Anson M, Li YS. Ozone and related gaseous pollutants in the boundary layer of eastern China: Overview of the recent measurements at a rural site. *Geophysical Research Letters* 2001; 28: 2373-2376.
- Wang T, Lam KS, Lee ASY, Pang SW, Tsui WS. Meteorological and chemical characteristics of the photochemical ozone episodes observed at Cape D'Aguilar in Hong Kong. *Journal of Applied Meteorology* 1998; 37: 1167-1178.
- Wang T, Tham YJ, Xue L, Li Q, Zha Q, Wang Z, et al. Observations of nitryl chloride and modeling its source and effect on ozone in the planetary boundary layer of southern China. *Journal of Geophysical Research: Atmospheres* 2016a; 121, 2476-2489, doi:10.1002/2015JD024556.
- Wang T, Wei XL, Ding AJ, Poon CN, Lam KS, Li YS, et al. Increasing surface ozone concentrations in the background atmosphere of Southern China, 1994-2007. *Atmospheric Chemistry and Physics* 2009; 9: 6217-6227.
- Wang T, Xue L, Brimblecombe P, Lam YF, Li L, Zhang L. Ozone pollution in China: A review of concentrations, meteorological influences, chemical precursors, and effects. *Science of The Total Environment* 2017b; 575: 1582-1596.
- Wang X, Chen W, Chen D, Wu Z, Fan Q. Long-term trends of fine particulate matter and chemical composition in the Pearl River Delta Economic Zone (PRDEZ), China. *Frontiers of Environmental Science & Engineering* 2016b; 10: 53-62.
- Wang X, Wang H, Xue L, Wang T, Wang L, Gu R, et al. Observations of N₂O₅ and ClNO₂ at a polluted urban surface site in North China: High N₂O₅ uptake coefficients and low ClNO₂ product yields. *Atmospheric Environment* 2017c; 156: 125-134.

- Wang Z, Wang W, Tham YJ, Li Q, Wang H, Wen L, et al. Fast heterogeneous N_2O_5 uptake and ClNO_2 production in power plant plumes observed in the nocturnal residual layer over the North China Plain. *Atmos. Chem. Phys. Discuss.* 2017d; 2017: 1-26.
- Zhang Y, Su H, Zhong L, Cheng Y, Zeng L, Wang X, et al. Regional ozone pollution and observation-based approach for analyzing ozone-precursor relationship during the PRIDE-PRD2004 campaign. *Atmospheric Environment* 2008a; 42: 6203-6218.
- Zhang YH, Hu M, Zhong LJ, Wiedensohler A, Liu SC, Andreae MO, et al. Regional Integrated Experiments on Air Quality over Pearl River Delta 2004 (PRIDE-PRD2004): Overview. *Atmospheric Environment* 2008b; 42: 6157-6173.

Chapter 7. ClNO₂ measured at a semi-rural site (Wangdu) in North China Plain and the impact on O₃ production

7.1 Introduction

In the summer of 2014, the first field measurement of ClNO₂ in the NCP was conducted by our research group at a semi-rural site (38.665° N, 115.204° E) in Wangdu County of Hebei province. The North China Plain is one of the most polluted regions in China due to intense and fast economic development. Zhang et al. (2014) found both NO_x and total VOCs in Beijing decreased over the study period between 2005 and 2011, with 1.4 ppbv yr⁻¹ and 1.6 ppbv yr⁻¹, respectively, while daytime average O₃ increased rapidly at an annual rate of 2.6 ppbv yr⁻¹, around 5% yr⁻¹, according to ground-based on-line measurements at an urban site.

In this field campaign, surprisingly high morning peaks of ClNO₂ were observed. The peak of ClNO₂ was up to 550 pptv in the average case, while it was up to 2070 pptv in an air mass from the outflow of Tianjin, which was termed as the megacity case. Detailed information about the measurement is given in Tham et al. (2016). My research focuses on evaluating the impact of ClNO₂ on the atmospheric oxidation capacity and O₃ production. In this chapter, the diurnal variation of ClNO₂ and related species is first presented, and then the Cl production is examined and the difference of reactivity between Cl and OH is compared. The impacts of the ClNO₂ on the primary radical productions and ozone formation are finally assessed.

7.2 Model Setup

In order to evaluate the contributions of ClNO₂ to daytime primary radical and O₃ production, an explicit observation-based chemical box model was utilized. The model was developed based on the latest version of Master Chemical Mechanism v3.3.1 (Jenkin et al., 2015) and was updated with a Cl chemistry module (Xue et al., 2015). The setup of the model was described in detail in Chapter 3 when comparing the measured and simulated OH and HO₂. The daytime output from the final run of the model was used for further analysis of the primary radical production and O₃ production/loss processes.

7.3 Diurnal pattern of ClNO₂ and key species

As shown in Fig. 7-1, the diurnal pattern of ClNO₂ shows that the concentrations of ClNO₂ accumulated during the nighttime, maintained at a relatively high level even after sunrise and dropped sharply to nearly zero with the increase of the photolysis rates before the noon time. The concentration of ClNO₂ at sunrise in the megacity case was higher than that in the average case, as 2.1 ppbv vs 0.5 ppbv. HCl, as another Cl radical source in the daytime, was also higher in the megacity case than in the average case. On the contrary, HCHO was nearly 10 ppbv in the average case while it was only 4 ppbv in the megacity case. NMCHs in the average case were also much higher than that in the megacity case, especially for alkanes, isoprene and aromatics. Thus, the average case was characterized with high VOCs and OVOCs, while the NO_x concentrations were similar in these two cases.

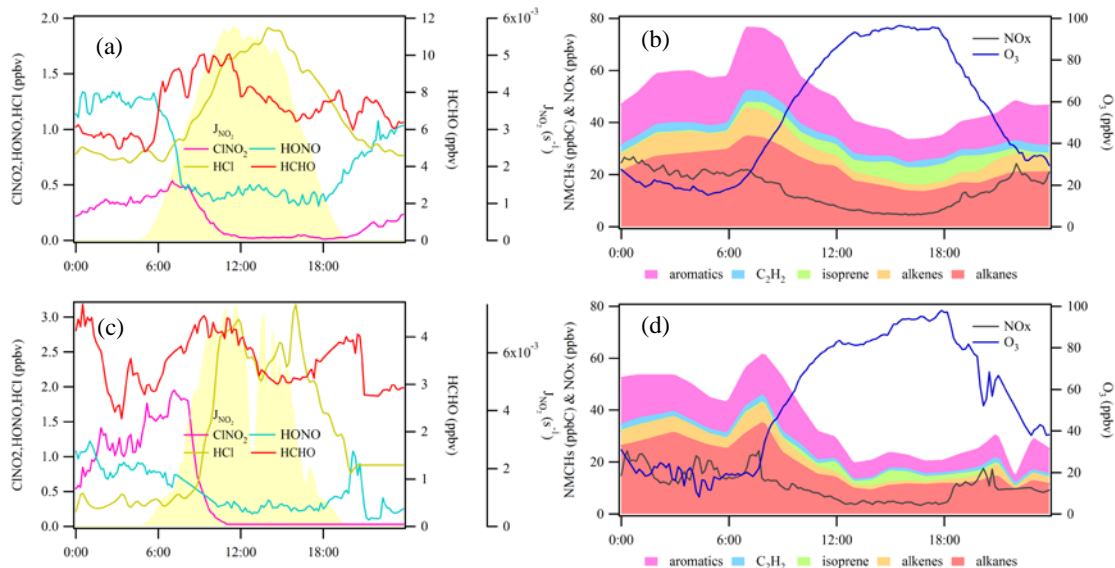


Figure 7- 1. Diurnal pattern for main constrained species in the model; (a) and (b) are the average data for the whole modeled period from 20 June to 9 July, (c) and (d) are the patterns for the highest case of CINO₂ on 21 June.

7.4 Cl radical production and Cl reactivity

According to the simulation results shown in Fig. 7-2, the abundance of Cl radical is in the magnitude of 10^4 atom cm^{-3} and CINO₂ was the major source of Cl from sunrise to the noon time. If there is no CINO₂ in the box model, Cl concentration dropped by one order of the magnitude. As expected, Cl concentration in megacity case is nearly 6 times of that in the average case due to much higher CINO₂ concentration in the morning. The production rates of Cl are in the magnitude of 10^6 atom $\text{cm}^{-3} \text{ s}^{-1}$ which is in the range reported in literatures as $10^5 \sim 10^6$ atom $\text{cm}^{-3} \text{ s}^{-1}$ (Riedel et al., 2012; Riedel et al., 2014). The reaction of HCl and OH also leads to the formation of Cl atom, and it is the main source from noon to sunset, together with the photolysis of Cl₂. The photolysis of

ClONO₂ and HOCl is not a significant Cl radical source due to their low concentrations in the system.

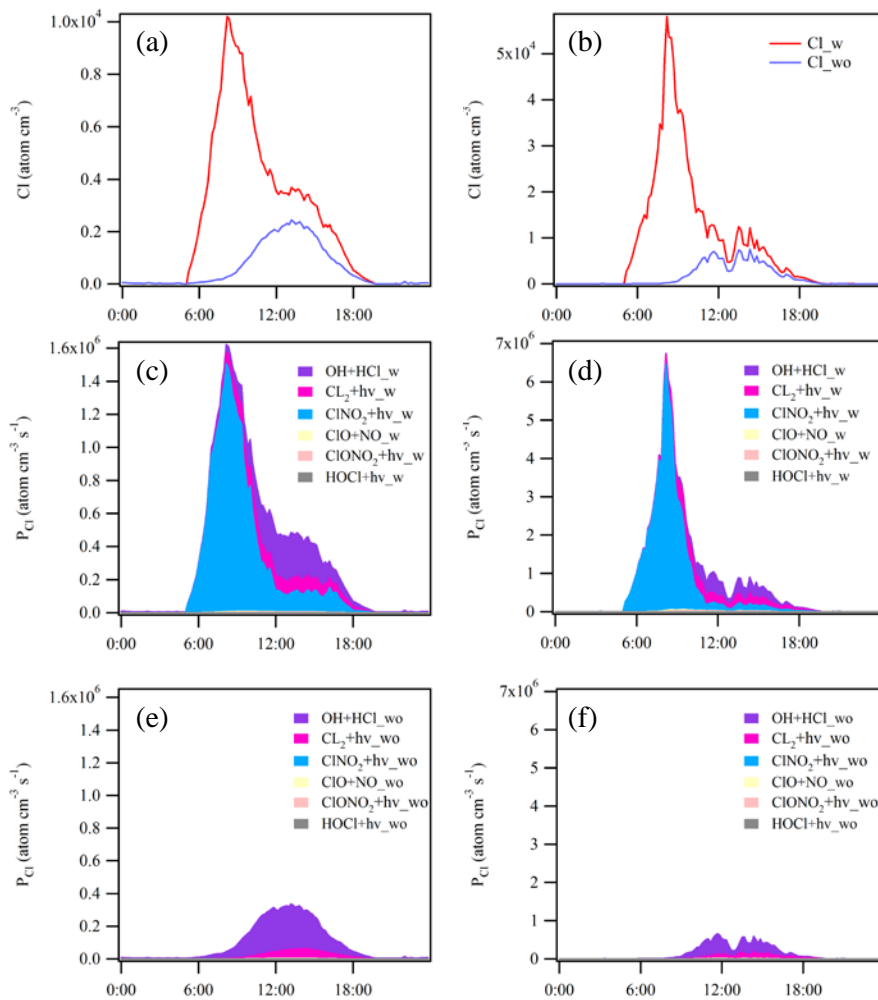


Figure 7- 2. Concentrations of Cl radical and its production rate with and without ClNO₂; (a), (c) and (e) are for the average case and (b), (d) and (f) are for the megacity case.

Cl and OH are two reactive radicals which initialize the oxidation of atmospheric VOCs and consume the pollutants. Reactivity represents the activity of the radical to scavenge

the VOCs and other pollutants, and is treated as the sum of products between reaction constants and the concentrations of pollutants as E7-1 and E7-2.

$$(E7-1)k_{OH} = \sum k_i \times [OH\text{reactants}]_i$$

$$(E7-2)k_{Cl} = \sum k_i \times [Cl\text{ reactants}]_i$$

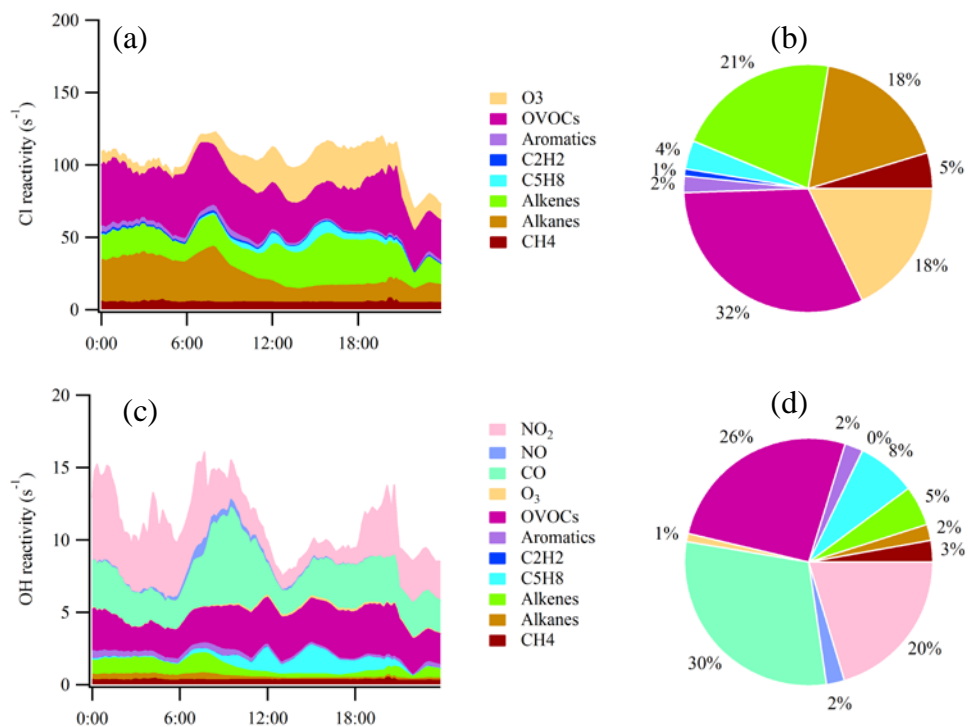


Figure 7- 3. Diurnal pattern of simulated Cl and OH reactivity as (a) and (c), (b) and (d) are the compositions of Cl and OH average reactivity from 5:00 to 18:00 for the 6.21 case.

The reaction constants of Cl radical are several times to tens of times greater than that of OH radical. Fig. 7-3 shows that the Cl reactivity is $100\ s^{-1}$ while OH reactivity is about

15 s⁻¹ by taking the megacity case as an example. If CO, NO, NO₂ are not considered in the OH reactivity, Cl reactivity is nearly 20 times of OH reactivity. Alkanes, alkenes, O₃ and OVOCs are the dominant compositions of Cl reactivity, while CO, OVOCs, NO₂ and isoprene are the dominant compositions of OH reactivity. The results are similar with that of Young et al. (2014). Compared to OH, Cl can consume alkanes much faster and make the relatively inert VOCs become reactive and then contribute to RO₂ formation.

7.5 Cl contribution to primary radical production and O₃ formation

Quantification of the contribution of Cl chemistry to the total RO_x budget is important. Fig. 7-4 illustrates that RO₂ can be formed through oxidation of VOCs by Cl radical, and accounted for 10% and 30% of total primary production rates of radicals during the morning period 8:00-8:30, respectively. The daytime average contributions were 3% and 9% for the average case and the megacity case, respectively. Even though photolysis of HONO, O₃ (O¹D+H₂O), HCHO, and other OVOCs and oxidation of unsaturated VOCs by O₃ are the dominant RO_x sources throughout the whole day, Cl chemistry can be of equal importance as HONO in the early morning. Here, I only consider the Cl chemistry near the ground surface, if the integrated Cl chemistry through the entire boundary layer is considered, it may be more important than the prediction in this work, as suggested by Young et al. (2012). The contribution of Cl chemistry to RO_x budget is limited by two factors, one is the concentration of ClNO₂ itself, and the other is the abundance of other radical sources. Thus, the contribution was relatively low in the average case due to both

the low ClNO₂ concentration and the high level of other radical sources, like HCHO and other OVOCs. Fig. 7-5 illustrates that the mixing ratios of RO₂, HO₂ and OH all increases when the ClNO₂ data were constrained in the box model compared to the scenario without ClNO₂, especially in the early morning. RO₂, HO₂ and OH increase by 10%-18% for the average case, while they increase by 50%-110% for the megacity case. This indicates that Cl chemistry can enhance the atmospheric oxidation capacity efficiently in the morning.

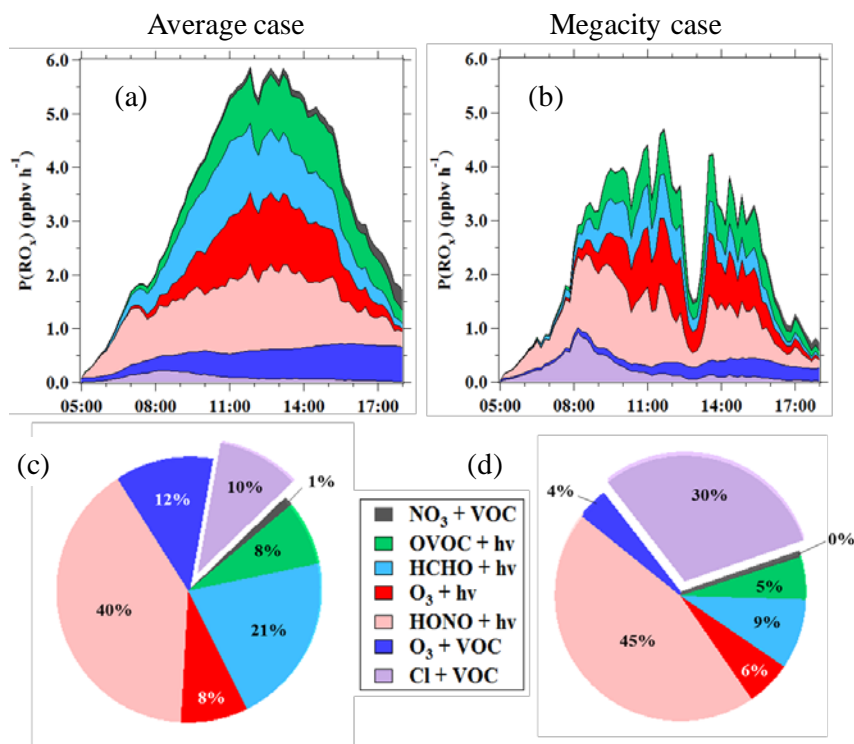


Figure 7- 4. Primary RO_x radical production rates from different sources at Wangdu in the daytime (a, b). Pie charts represent the contributions of ClNO₂ to the primary RO_x radical production in the morning time (average value for 08:00-08:30).

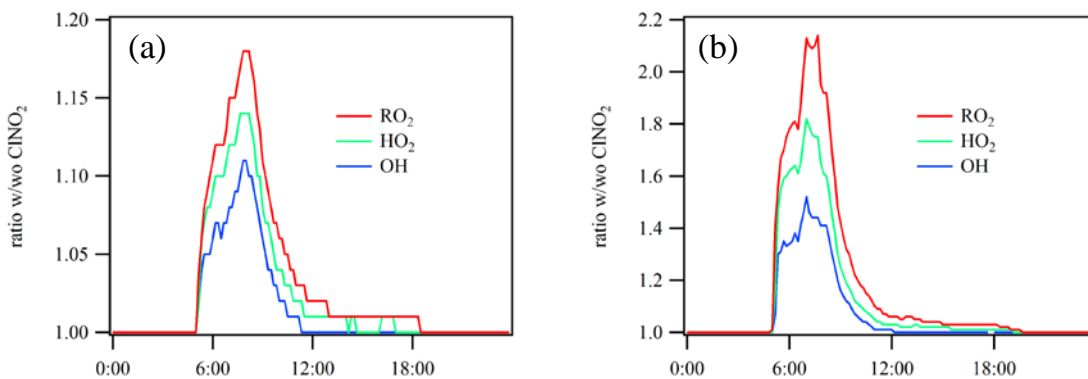


Figure 7- 5. OH, HO₂ and RO₂enhancement ratio with inclusion of ClNO₂; (a) for the average case and (b) for the megacity case.

The effect of ClNO₂ photolysis on in-situ ozone production is also relevant. Fig. 7-6 shows the net ozone production rates ($P(O_3)$) during daytime (from 05:00 to 18:00) and the difference in integrated total ozone production simulated with and without ClNO₂ input. The O₃ production rates were enhanced throughout the day due to the ClNO₂ effect, especially during the morning hours. The increase in net $P(O_3)$ for campaign average reached 0.9 ppbv h⁻¹ or 17% in the morning. For the megacity outflow, much higher increases in $P(O_3)$ can be seen in the entire morning, with a maximum of 3.3 ppbv h⁻¹ (or 76% increase) at ~08:00. Integrating over the entire daytime period, the increase in total ozone production was 4.3 ppbv (3%) and 11 ppbv (13%) for average case and the megacity case, respectively.

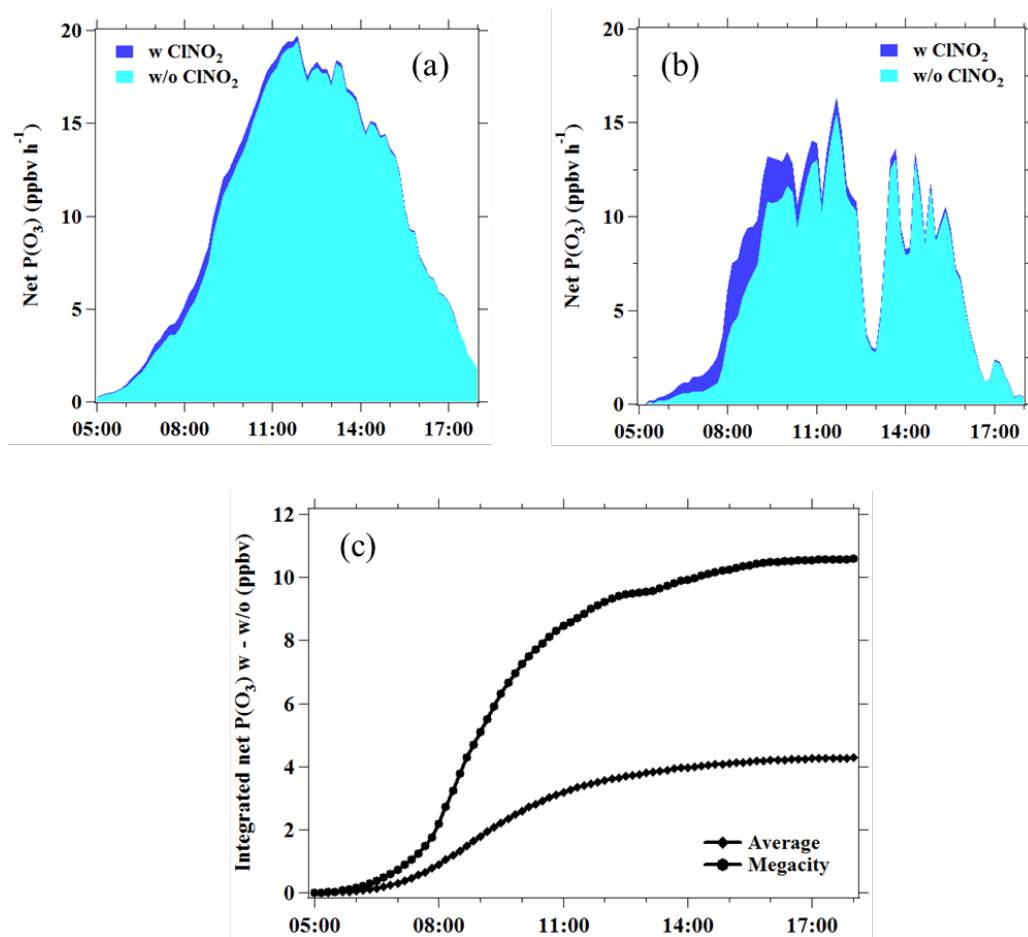


Figure 7- 6. Net ozone production rates for (a) average, (b) the megacity case and (c) the difference in integrated net ozone production rate between the simulation with and without the CINO₂ input.

The reasons for the difference between the average case and the megacity case could result from the concentrations of the CINO₂ and the abundance of other radical sources. First, if the concentrations of CINO₂ in the average case and the megacity case were exchanged, the increased O₃ production due to Cl reactions in the average case increases from 4.3 to 10.9 ppbv, while it drops from 10.6 to 4.5 ppbv for the megacity case. This confirmed the importance of CINO₂ mixing ratios in driving the ozone enhancement.

Second, the higher HCHO and other OVOCs in the average case provided a larger pool of RO_x, weakening the relative effect of chlorine radical.

7.6 Summary

A campaign was conducted at a semi-rural site at Wangdu, a rural site in North China Plain. The average mixing ratios of ClNO₂ were up to 550 pptv, while the highest mixing ratio of ClNO₂ was 2070 pptv. ClNO₂ photolysis and subsequent Cl chemistry enhanced the RO_x concentration by 10-18% for the average case and 50-118% for the megacity case, and Cl reactions with VOCs contributed to 3% and 9% of the average daytime RO_x budget. The contribution to RO_x budget could reach 10% and 30% in the early morning (8:00-8:30). Integrated ozone concentrations also increased 3.3% (4 ppbv) and 13.3% (10 ppbv) for the average case and the megacity case, respectively. Therefore, ClNO₂ is an important radical source in NCP and has considerable impact on air quality.

References

- Jenkin ME, Young JC, Rickard AR. The MCM v3.3.1 degradation scheme for isoprene. *Atmospheric Chemistry and Physics* 2015; 15: 11433-11459.
- Riedel TP, Bertram TH, Crisp TA, Williams EJ, Lerner BM, Vlasenko A, et al. Nitryl Chloride and Molecular Chlorine in the Coastal Marine Boundary Layer. *Environmental Science & Technology* 2012; 46: 10463-10470.
- Riedel TP, Wolfe GM, Danas KT, Gilman JB, Kuster WC, Bon DM, et al. An MCM modeling study of nitryl chloride (ClNO₂) impacts on oxidation, ozone production and nitrogen oxide partitioning in polluted continental outflow. *Atmospheric Chemistry and Physics* 2014; 14: 3789-3800.

- Sander SP, Abbatt J, Barker J, Burkholder JB, Friedl RR, Golden DM, et al. Chemical Kinetics and Photochemical Data for Use in Atmospheric Studies, Evaluation No. 17, 2011.
- Saunders SM, Jenkin ME, Derwent RG, Pilling MJ. Protocol for the development of the Master Chemical Mechanism, MCM v3 (Part A): tropospheric degradation of non-aromatic volatile organic compounds. *Atmospheric Chemistry and Physics* 2003; 3: 161-180.
- Xue LK, Saunders SM, Wang T, Gao R, Wang XF, Zhang QZ, et al. Development of a chlorine chemistry module for the Master Chemical Mechanism. *Geoscientific Model Development* 2015; 8: 3151-3162.
- Young CJ, Washenfelder RA, Edwards PM, Parrish DD, Gilman JB, Kuster WC, et al. Chlorine as a primary radical: evaluation of methods to understand its role in initiation of oxidative cycles. *Atmospheric Chemistry and Physics* 2014; 14: 3427-3440.
- Young CJ, Washenfelder RA, Roberts JM, Mielke LH, Osthoff HD, Tsai C, et al. Vertically resolved measurements of nighttime radical reservoirs in Los Angeles and their contribution to the urban radical budget. *Environmental science & technology* 2012; 46: 10965-10973.
- Zhang Q, Yuan B, Shao M, Wang X, Lu S, Lu K, et al. Variations of ground-level O₃ and its precursors in Beijing in summertime between 2005 and 2011. *Atmospheric Chemistry and Physics* 2014; 14: 6089-6101.

Chapter 8. N₂O₅ heterogeneous chemistry at a semi-rural site in Pearl River Delta during a severe pollution period and its impact on nitrate formation and O₃ production

8.1 Introduction

The PRD region has favorable conditions for the N₂O₅ heterogeneous chemistry due to the frequently high NO_x and O₃ in this region. Li et al. (2016) has predicted that the highest ClNO₂ in PRD region was located in the western parts of the PRD, like Jiangmen and Zhaoqing, and that N₂O₅ chemistry could increase the total nitrate concentration and ozone concentrations by up to 13.45 μg m⁻³ (~57.4 %) and 7.23 ppbv (~16.3%), respectively, in the planetary boundary layer in the PRD region. However, field studies of N₂O₅ and ClNO₂ have not been conducted in other places in PRD other than in Hong Kong. The importance of N₂O₅ chemistry to nitrate formation and O₃ production has not been thoroughly investigated based on measurements in the PRD region.

In the present study, intensive observations of N₂O₅ and ClNO₂ were conducted from Jan 2 to Jan 15, 2017, at a rural site at Heshan in the western PRD, and a severe pollution event was captured during the first week of the observation. An overview of the measurement data on the variation of N₂O₅ and ClNO₂ was first given. The uptake coefficients of N₂O₅ and the yields of ClNO₂ were then estimated based on the measurement. The contribution of N₂O₅ chemistry to nitrate formation was then

investigated with the derived parameters. The impact of ClNO₂ morning peak on O₃ production was then simulated with an observation-based chemical box model. This study investigated the level of N₂O₅ and ClNO₂ in inland PRD region, and evaluated the importance of N₂O₅ chemistry to nitrate and O₃ formation in a severe pollution episode for the first time.

8.2 Site description, instruments and model setup

The observation was conducted at a semi-rural site called Hua Guo Shan (HGS, 22.71°N, 112.92° E), in the city of Heshan, which is affiliated to Jiangmen (JM) in Pearl River Delta. The site has been described in Chapter 5. N₂O₅ and ClNO₂ were concurrently measured with a quadrupole chemical ionization mass spectrometer (THS Instruments, Atlanta). Morning peaks of ClNO₂ were observed during the campaign on Jan 6 and several other days. The day of Jan 6 was taken as an example to investigate the contributions of ClNO₂ to in-situ O₃ production with the model described in Chapter 5. The observation data were constrained into the model every 10 min. The $J(\text{ClNO}_2)$ here was treated the same as Tham et al. (2016). The importance of ClNO₂ was evaluated by comparing cases with and without constraining the measured ClNO₂. OH concentrations and the reaction rate of OH+NO₂ were also derived during the simulation to estimate the formation of aerosol nitrate during the daytime. OH concentrations and the reaction rate of OH+NO₂ were also derived with the modeling method. Average concentrations of species constrained into the box model from Jan 3 to Jan 7 are listed in Table 8-1. The method to simulate the chemical evolution of an air mass as described in

Chapter 6 was used to check the impact of the highest ClNO₂ air mass in this campaign on the radical and O₃ formation in the following day.

Table 8- 1. Average concentrations (ppbv) of NMHCs species during the daytime (7:00-17:00 LT) and nighttime (17:00-7:00 LT of the next day) from Jan 3 to Jan 7.

Species	Daytime	Nighttime	Species	Daytime	Nighttime
Ethane	2.257	2.310	Isoprene	0.092	0.026
Propane	7.032	6.239	Cis-2-Pentene	0.006	0.005
i-Butane	2.561	2.324	1-Hexene	0.032	0.023
n-Butane	4.879	4.588	1,3-Butadiene	0.041	0.067
i-Pentane	2.105	3.435	Benzene	0.767	0.832
n-Pentane	1.666	4.128	Toluene	5.447	6.076
2-Methylpentane	0.980	0.868	Ethylbenzene	1.313	1.812
n-Hexane	0.762	0.706	m-xylene	1.143	1.936
n-Heptane	0.307	0.273	p-xylene	1.143	1.936
n-Octane	0.085	0.068	o-xylene	0.988	1.644
Ethene	2.487	2.684	1,3,5-trimethylbenzene	0.025	0.029
Propene	0.352	0.393	1,2,4-trimethylbenzene	0.022	0.045
Ethyne	2.162	2.054	1,2,3-trimethylbenzene	0.029	0.029
trans-2-Butene	0.021	0.021	i-propbenzene	0.027	0.034
1-Butene	0.063	0.072	propbenzene	0.038	0.034
cis-2-Butene	0.024	0.027	m-ethyltoluene	0.076	0.068
1-Pentene	0.011	0.011	p-ethyltoluene	0.049	0.042
trans-2-Pentene	0.006	0.005	o-ethyltoluene	0.041	0.037

8.3 Overview of the observation

Figure 8-1 shows the time series of N₂O₅, ClNO₂, components of PM_{2.5}, related trace gases and meteorological parameters from 18:40 of Jan 2 to 11:00 of Jan 15, 2017. The average temperature and RH during the measurement period were 17 ± 4°C and 86 ± 14%, respectively. A severe pollution episode occurred on Jan 3 to 7 due to stagnant

meteorological conditions (Fig. 8-2(a)), and the concentrations of most pollutants decreased to very low levels on Jan 9 and Jan 12 to 15, which corresponded to the change in weather conditions. The most polluted days were Jan 5 and 6 with the highest $\text{PM}_{2.5}$ of $400 \mu\text{g m}^{-3}$ and the highest O_3 of 160 ppbv. The $\text{PM}_{2.5}$ data from the PRD regional air quality monitoring network revealed that the HGS site was within the most polluted area during this haze event (Fig. 8-2(b)). This pollution event was characterized by concurrent high levels of $\text{PM}_{2.5}$ and O_3 and is in contrast to the winter haze in north China, which experienced high $\text{PM}_{2.5}$ but low O_3 (e.g., Sun et al., 2016; Wang H et al., 2018a). The mixing ratios of N_2O_5 and ClNO_2 were up to 3358 pptv and 8324 pptv (1 min time resolution), respectively, indicating active N_2O_5 heterogeneous chemistry.

Very high concentrations of aerosol nitrate (up to $108 \mu\text{g m}^{-3}$, 1 h time resolution) were also observed during the multi-day episode. Nitrate contributed to 24% of the total $\text{PM}_{2.5}$ mass concentration on average, which was comparable to that of organic matters ($\text{OM} = 1.7 \cdot \text{OC}$, 28%) and much higher than that of sulfate (16%) and ammonium (11%). The contribution of nitrate to the $\text{PM}_{2.5}$ increased with an increase in nitrate concentration, and reached nearly 40% at its highest nitrate level, indicating that nitrate was a dominant component of the $\text{PM}_{2.5}$ on the most polluted days. The concentration of NO_3^- exhibited a concurrent increase with that of ClNO_2 in the early nighttime on Jan 3 to 4, Jan 4 to 5, Jan 5 to 6 and Jan 9 to 10 (see Fig. 8-3), suggesting that N_2O_5 heterogeneous reactions significantly contributed to the formation of nitrate during the nighttime. The measured increases of the NO_3^- concentration during these four nights were 35.3, 50.9, 43.3 and $32.7 \mu\text{g m}^{-3}$, respectively. A similar increase in ClNO_2 was observed on Jan 6 to 7, but

the composition of the $PM_{2.5}$ was not available due to instrument maintenance. The discussion in the remainder of this manuscript will focus on the detailed analysis of these five nights to investigate the role of N_2O_5 heterogeneous chemistry in nitrate formation.

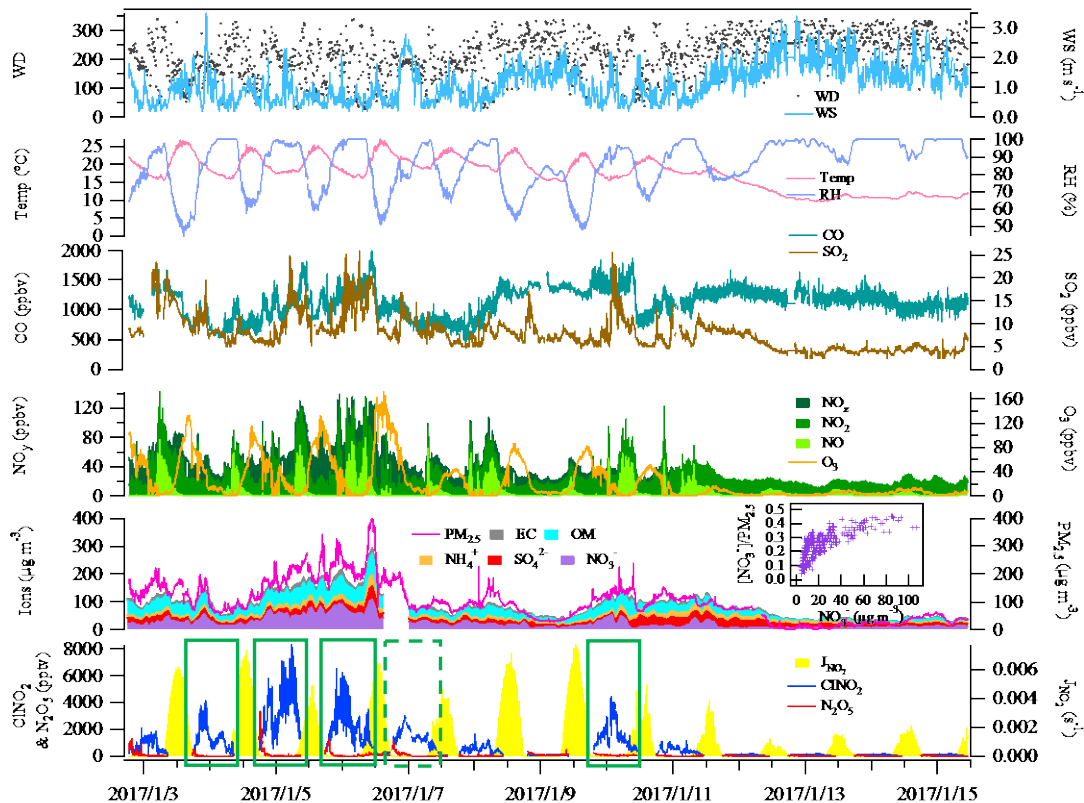


Figure 8- 1. Time series of N_2O_5 , $ClNO_2$, components of $PM_{2.5}$, related trace gases and meteorological parameters from 18:40 of Jan 2 to 11:00 of Jan 15, 2017. The inserted figure shows the variation of the ratio of nitrate to $PM_{2.5}$ with increasing nitrate concentration. The green rectangles in the figure indicate the five days used for detailed analysis.

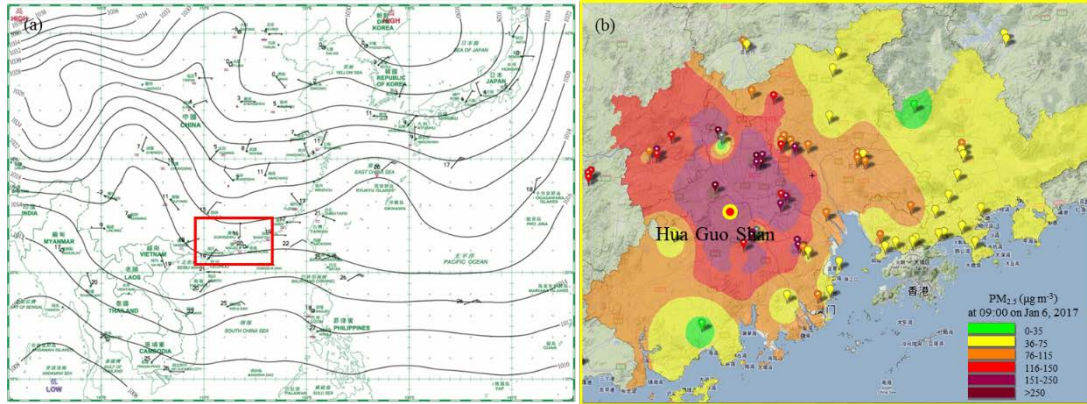


Figure 8- 2. (a) Surface weather chart at 08:00 LT on Jan 6, 2017 downloaded from the website of the Hong Kong Observatory indicating stagnant conditions. (b) The distribution of PM_{2.5} concentrations in the PRD region at 09:00 LT on Jan 6, 2017. This figure was captured from the website. <http://113.108.142.147:20031/GDPublish/publish.aspx>.

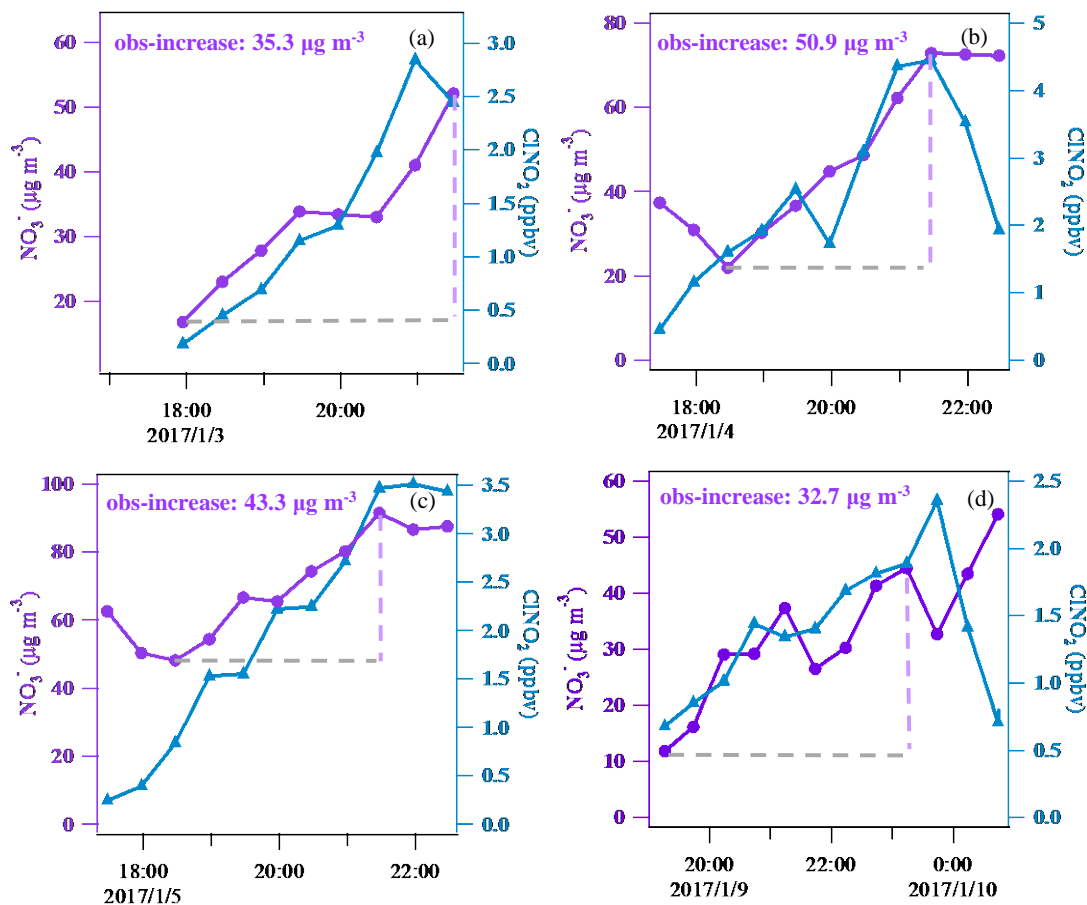


Figure 8- 3. The covariance of aerosol nitrate and ClNO₂ in the early nighttime (in 30 min time resolution) for four nights.

8.4 N₂O₅ heterogeneous chemistry on the selected nights

8.4.1 Production of NO₃ and N₂O₅

The first step in the nighttime nitrate formation via N₂O₅ chemistry is the production of NO₃ and N₂O₅. To get insight into the key factors affecting the NO₃/N₂O₅ chemistry, the variation of N₂O₅ and production rate of NO₃ were examined with some relevant gases and meteorological parameters of the five nights. Fig. 8-4 shows the data of the night of

Jan 4 to 5 as an example. Some common features were identified for all five nights. In general, low wind speed ($< 2.0 \text{ m s}^{-1}$) at night facilitated the accumulation of air pollutants, and high RH was favorable for N_2O_5 heterogeneous uptake. In addition, high aerosol surface density provided interfaces for N_2O_5 heterogeneous reactions.

In the first couple of hours after sunset (Fig. 8-4, red rectangle), N_2O_5 exhibited a peak and quickly dropped to hundreds of pptv, while nitrate and ClNO_2 concurrently increased, which was indicative of the local production and loss of N_2O_5 . NO was below the detection limit during this period. The production rates of NO_3 ($P_{\text{NO}_3} = k_{\text{NO}_2+\text{O}_3}[\text{NO}_2][\text{O}_3]$) were the fastest just after sunset and decreased gradually due to reduced O_3 levels. There was a period later in the night (22:00 to 01:00) when fresh emissions of NO were observed, and the production of NO_3 was suppressed due to the titration of O_3 by NO. In the later nighttime, NO was below the detection limit (Fig. 8-4, blue rectangle). During this period, NO_3 and N_2O_5 were produced at moderate rates, and the very low N_2O_5 concentrations (below the detection limit) suggested a fast loss of N_2O_5 probably leading to the local production of ClNO_2 and nitrate, which was not revealed in the observed variations of ClNO_2 and nitrate. The concentrations of ClNO_2 and nitrate during this period fluctuated due to the change in the air masses indicated by the change in SO_2 concentrations and wind speeds.

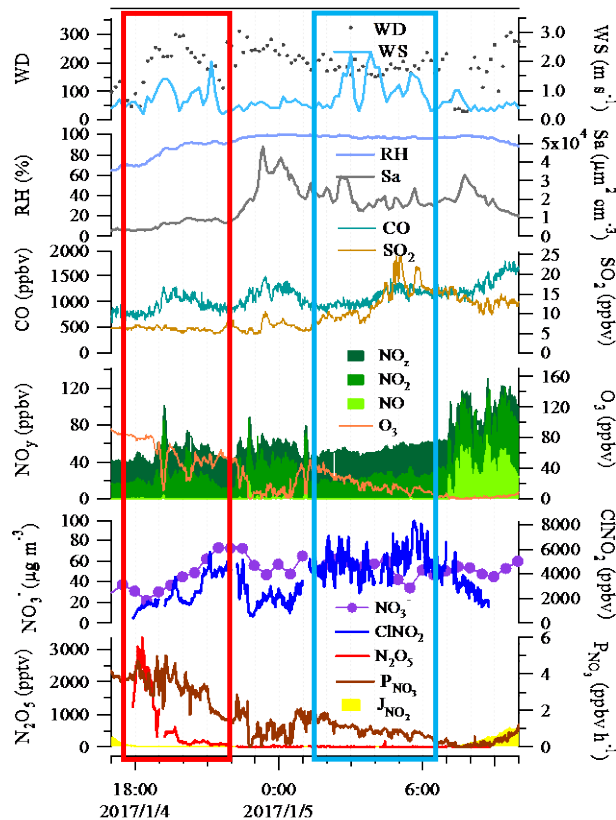


Figure 8- 4. Variation of N_2O_5 , $CINO_2$, NO_3^- , trace gases and meteorological conditions during the nighttime of Jan 4 to 5, 2017 as an example for the five selected nights.

8.4.2 N_2O_5 uptake coefficient and $CINO_2$ yield

The N_2O_5 uptake coefficient and $CINO_2$ yield, together with the reactivity of NO_3 with NO and $VOCs$, determines the loss pathways of NO_3 and N_2O_5 . To derive the uptake coefficient of N_2O_5 , a method suggested by McLaren et al. (2010) was applied by treating NO_3 and N_2O_5 as a whole ($[NO_3] + [N_2O_5]$) without assuming the chemical system was in the steady state. This approach considers that the change of NO_3 and N_2O_5 concentrations is mainly due to NO_3/N_2O_5 chemistry, and thus it requires that the air mass have relatively stable chemical conditions and not be subject to fresh NO

emissions. It also requires that ClNO₂ is produced from the N₂O₅ chemistry and has an increasing trend to derive the yield of ClNO₂. This method is applicable for the early nighttime (red rectangle, section 3.2.1) for these five nights.

The variation rate of [NO₃] + [N₂O₅] can be calculated by deducting the production rate of [NO₃] + [N₂O₅] with its loss rate as E8-1.

$$(E8-1) \frac{d([N_2O_5]+[NO_3])}{dt} = P_{NO_3} - L_{N_2O_5+NO_3}$$

The loss of [NO₃] + [N₂O₅] is through the NO₃ reaction with VOCs and N₂O₅ heterogeneous reactions, which can both be expressed as pseudo first order losses as E8-2:

$$(E8-2) L_{N_2O_5+NO_3} = L_{NO_3} + L_{N_2O_5} = k_{NO_3} [NO_3] + k_{N_2O_5} [N_2O_5]$$

where k_{NO₃} and k_{N₂O₅} represent the total first order rate constants for NO₃ and N₂O₅, respectively. The loss rate of N₂O₅ can then be obtained from E8-3:

$$(E8-3) L_{N_2O_5} = k_{N_2O_5} [N_2O_5] = k_{NO_2+O_3} [NO_2][O_3] - \frac{d[N_2O_5]}{dt} - \frac{d[NO_3]}{dt} - k_{NO_3} [NO_3]$$

Because NO₃ was not measured, it was calculated by assuming an equilibrium of NO₂-NO₃-N₂O₅ as shown in E8-4. High levels of NO would break this equilibrium. Thus, the periods with detected NO were excluded. d[NO₃]/dt and d[N₂O₅]/dt were calculated as the rate of change of NO₃ and N₂O₅ in a time resolution of 10 min. k_{NO₃} was derived with the measured concentrations of NMHCs as E8-5 by interpolating the data of NMHCs to 10 min time resolution. The NO₃ reactivity with VOCs (k_{NO₃}) in the early

nighttime ranged from 0.632 to $1.54 \times 10^{-3} \text{ s}^{-1}$ (Table 8-2), which was higher than those derived at Mt. TMS in winter 2013 (0.17 to $1.1 \times 10^{-3} \text{ s}^{-1}$) (Brown et al., 2016), but lower than those in the North China Plain during the summertime ($2.57 \times 10^{-3} \text{ s}^{-1}$) (Tham et al., 2016; Wang H et al., 2017, 2018b; Wang Z et al., 2017). NMHCs were not measured on Jan 9 to 10, 2017. Therefore, we used the average k_{NO_3} in the early nighttime on Jan 3 to 4 as a replacement because these two periods had similar pollution levels for most pollutants. For the later nighttime (Fig. 8-4, blue rectangle), low levels of N_2O_5 and moderate levels of P_{NO_3} also made E8-3 inapplicable even though NO was not detected.

$$(E8-4) [\text{NO}_3] = \frac{[\text{N}_2\text{O}_5]}{[\text{NO}_2] \times K_{\text{eq}}}$$

$$(E8-5) k_{\text{NO}_3} = \sum k_i [\text{VOC}_i]$$

Finally, the uptake coefficient of N_2O_5 was derived using E8-6 for every 10 min and averaged for the whole selected periods. In E8-6, $C_{\text{N}_2\text{O}_5}$ is the mean molecular speed of N_2O_5 , and S_a is the aerosol surface density. The yield of ClNO_2 was derived from E8-7 by dividing the integrated production of ClNO_2 ($[\text{ClNO}_2]_{\text{max}}$) by the integrated loss of N_2O_5 since sunset.

$$(E8-6) k_{\text{N}_2\text{O}_5} = \frac{L_{\text{N}_2\text{O}_5}}{[\text{N}_2\text{O}_5]} = \frac{1}{4} C_{\text{N}_2\text{O}_5} S_a \gamma_{\text{N}_2\text{O}_5}$$

$$(E8-7) \phi = \frac{[\text{ClNO}_2]_{\text{max}}}{\int L_{\text{N}_2\text{O}_5} dt}$$

The relative importance of NO_3 reactions with VOCs and N_2O_5 heterogeneous reactions can be examined by comparing the values of the loss coefficient of NO_3 reactions

$\left(\frac{k_{\text{NO}_3}}{[\text{NO}_2] \times K_{\text{eq}}}\right)$ and N_2O_5 heterogeneous reactions ($k_{\text{N}_2\text{O}_5}$) (Tham et al., 2016). Based on the calculations, the values of $\frac{k_{\text{NO}_3}}{[\text{NO}_2] \times K_{\text{eq}}}$ were 1.82×10^{-5} to $6.07 \times 10^{-5} \text{ s}^{-1}$ (see Table 8-2), while that of $k_{\text{N}_2\text{O}_5}$ were 3.78×10^{-3} to $20.4 \times 10^{-3} \text{ s}^{-1}$, which was two orders of magnitude higher than that of $\frac{k_{\text{NO}_3}}{[\text{NO}_2] \times K_{\text{eq}}}$, suggesting that N_2O_5 heterogeneous reactions were the dominant loss pathway of NO_3 and N_2O_5 .

The average $\gamma_{\text{N}_2\text{O}_5}$ and ϕ_{CINO_2} derived for the early night of the five cases are listed in Table 8-2. The data show that the uptake coefficient ranged from 0.009 to 0.101, which was comparable to the previous values derived at Mt. Tai Mo Shan (TMS) in Hong Kong (0.004 to 0.022) (Brown et al., 2016) and in the North China Plain (0.006 to 0.102) (Tham et al., 2018; Tham et al., 2016; Wang H et al., 2017, 2018b; Wang X et al., 2017; Wang Z et al., 2017; Zhou et al., 2018). The yield in this study varied from 0.20 to 0.36, which was similar to most studies in China (Tham et al., 2018; Tham et al., 2016; Wang Z et al., 2017; Yun et al., 2018; Zhou et al., 2018).

Table 8- 2. Average values of N₂O₅ concentrations, N₂O₅ uptake coefficients, ClNO₂ yields and other related parameters and maximum values of ClNO₂ concentrations in the early nighttime for five selected nights.

Date	N ₂ O ₅ pptv	Max-ClNO ₂ pptv	NO ₂ ppbv	O ₃ ppbv	RH %	Sa μm ² cm ⁻³	P _{NO3} ppbv h ⁻¹
Jan.3 17:40-20:50	102	3145	22	68	68	3644	4.0
Jan 4 17:00-22:00	700	4608	24	61	82	6452	3.3
Jan 5 17:00-22:00	338	4828	18	73	81	8399	3.4
Jan 6 17:00-22:40	326	2908	13	82	77	5092	2.8
Jan 9 19:00-00:20	121	2553	19	41	85	5173	1.9

Table 8- 2. Continued.

Date	k _{NO3} 10 ⁻³ s ⁻¹	L _{N2O5} ppbv h ⁻¹	k _{NO3} /(K _{eq} [NO ₂]) 10 ⁻⁵ s ⁻¹	k _{N2O5} 10 ⁻³ s ⁻¹	γ _{N2O5}	φ _{ClNO2}
Jan.3 17:40-20:50	0.632	3.9	3.26	20.4	0.101	0.36
Jan 4 17:00-22:00	1.54	3.2	6.07	4.16	0.009	0.32
Jan 5 17:00-22:00	0.790	3.3	4.06	9.00	0.015	0.29
Jan 6 17:00-22:40	0.677	2.6	4.95	3.78	0.013	0.20
Jan 9 19:00-00:20	0.632	1.9	1.82	4.28	0.015	0.28

8.5 Nitrate formation potential (pNO₃⁻) through N₂O₅ chemistry

8.5.1 Nighttime p(NO₃⁻)

The formation potential of NO₃⁻ through N₂O₅ chemistry is the total amount of NO₃⁻ accumulated from N₂O₅ heterogeneous loss. It can be calculated by deducting the integrated loss of N₂O₅ with the integrated production of ClNO₂ as E8-8.

$$(E8-8) \text{ p(NO}_3^-) = (2-\phi) \int L_{\text{N}_2\text{O}_5} dt = 2 \int L_{\text{N}_2\text{O}_5} dt - [\text{ClNO}_2]_{\text{max}}$$

In the early nighttime, the average loss rate of N₂O₅ (L_{N₂O₅}) ranged from 1.9 to 3.9 ppbv h⁻¹ (Table 8-2), which was close to the average P_{NO₃} due to the dominance of the N₂O₅ heterogeneous reactions in NO₃ and N₂O₅ loss. Based on the derived N₂O₅ loss rate and the maximum ClNO₂ concentration, the formation potential of NO₃⁻ was derived and ranged from 39.7 to 77.3 μg m⁻³ as shown in Fig. 8-5. The measured increase of the NO₃⁻ concentration in the early nighttime can be completely explained by the integrated production of NO₃⁻ via the N₂O₅ heterogeneous reactions during the same period.

In the later nighttime, the method described in section 8.4.2 was not valid for calculating the N₂O₅ heterogeneous loss rate as mentioned above. We attempted to estimate the formation potential of nitrate by assuming that the N₂O₅ heterogeneous reactions continued to dominate the loss of NO₃ + N₂O₅ in the later nighttime. The k_{NO₃} in the later nighttime were comparable to those in the early nighttime, and the high RH close to 100% in the later nighttime was favorable for the N₂O₅ heterogeneous reactions. It

was assumed that all NO_3 was quickly consumed by the N_2O_5 heterogeneous reactions, which means that the loss rate of N_2O_5 approximated to the production rate of NO_3 ($L_{\text{N}_2\text{O}_5} \approx P_{\text{NO}_3}$). As listed in Table 8-3, the N_2O_5 loss rates ranged from 0.82 to 1.26 ppbv h^{-1} , which were significantly lower than those derived in the early nighttime. The derived N_2O_5 loss rate here and the yield of ClNO_2 in the early nighttime were used to estimate the formation potential of NO_3^- in the later nighttime. As shown in Fig. 8-5, the nitrate produced during these later periods ranged from 7.3 to 37.7 $\mu\text{g m}^{-3}$, which was significantly lower than those in the early nighttime, indicating that the nighttime nitrate from N_2O_5 chemistry was mainly produced in the early nighttime.

Table 8- 3. Average values of N_2O_5 loss rate and related parameters for selected periods in the later nighttime.

Date	NO_2 ppbv	O_3 ppbv	P_{NO_3} ppbv h^{-1}	k_{NO_3} 10^{-3} s^{-1}	$L_{\text{N}_2\text{O}_5}$ ppbv h^{-1}
Jan 3-4 21:00-05:00	20.8	20.7	1.00	0.684	1.00
Jan 5 01:30-06:50	22.4	19.5	0.96	1.45	0.96
Jan 5-6 23:40-01:10	21.1	25.5	1.26	1.13	1.26
Jan 6-7 23:00-06:00	22.1	14.4	0.82	0.709	0.82
Jan 10 01:50-03:30	24.8	15.6	0.90	/	0.90

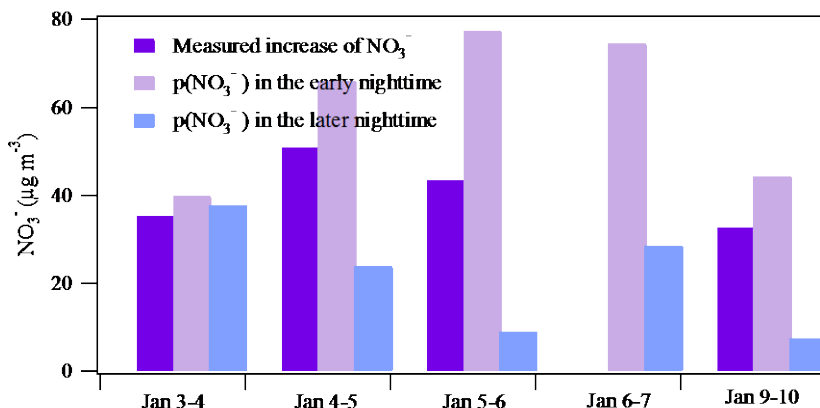


Figure 8- 5. Comparison between the measured NO₃⁻ increase and the NO₃⁻ formation potential in the early nighttime (periods in Table 8-2) and in the later nighttime (periods in Table 8-3).

8.5.2 Comparison with daytime production of HNO₃

During the daytime, the formation of NO₃⁻ is mainly from the gas-particle partitioning of the gas phase HNO₃ formed through the OH + NO₂ reaction. Hence, the daytime formation potential of HNO₃ (p(HNO₃)) can be treated as the upper limit for the locally-produced daytime aerosol nitrate. To calculate the daytime p(HNO₃), a box model based on MCM v3.3.1 was used to derive the mixing ratio of OH and the rates of OH + NO₂. This model was previously used in our study at Wangdu in North China (Tham et al., 2016). The calculated mixing ratios of OH at Wangdu with this model compared well with those observed by the laser-induced fluorescence (LIF) technique (Tan et al., 2017). In the present study, the average daytime OH (7:00 to 17:00) mixing ratios were 1.71 to 3.82×10⁶ cm⁻³ during Jan 3 to 7 as listed in Table 8-4 with the maximum values reaching 3.24 to 6.71×10⁶ cm⁻³. The detailed results for OH can be found in Fig. 8-6.

The average production rates of HNO₃ through the OH + NO₂ reaction were 1.40 to 5.21 ppbv h⁻¹ from Jan 3 to Jan 7, and the integrated formation potential of HNO₃ during the daytime was 35.7 to 131.8 μg m⁻³, which was comparable to the nighttime p(NO₃⁻) ranging from 77.4 to 102.9 μg m⁻³ (Fig. 8-7). Nighttime production of nitrate via the heterogeneous uptake of N₂O₅ accounted for 43.8 to 57.7% of the total nitrate (NO₃⁻ + HNO₃) produced in a 24 h period at the site. These results underscored the important role of N₂O₅ heterogeneous chemistry in nitrate formation in this severe winter haze in southern China.

Table 8- 4. Average OH mixing ratio and rate of OH + NO₂ during the daytime (7:00 to 17:00 LT) from Jan 3 to Jan 7, 2017.

Date	OH (cm ⁻³)	NO ₂ (ppbv)	OH + NO ₂ (ppbv h ⁻¹)
Jan 3	2.18×10 ⁶	36.2	3.49
Jan 4	2.47×10 ⁶	23.6	2.60
Jan 5	2.62×10 ⁶	30.8	3.09
Jan 6	3.82×10 ⁶	31.5	5.21
Jan 7	1.71×10 ⁶	18.4	1.40

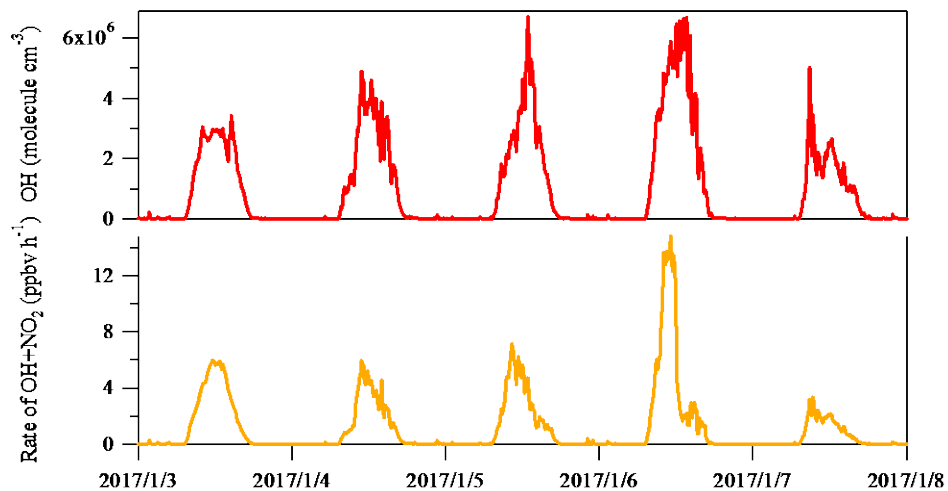


Figure 8- 6. Variation of OH mixing ratio and the rate of OH+NO₂ from Jan 3 and Jan 7.

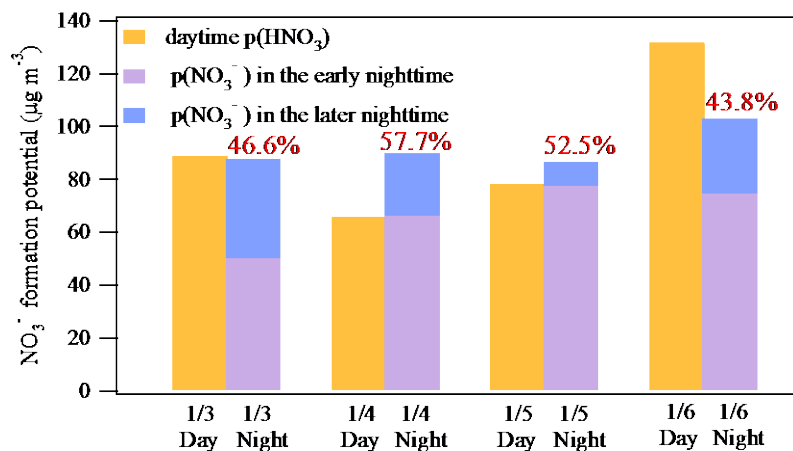


Figure 8- 7. Comparison between the daytime (7:00 to 17:00 LT, assuming all gas phase HNO₃ partitioned into particle phase) and nighttime (17:00 to 7:00 LT of the next day) NO₃⁻ formation potential.

8.6 Impact of ClNO₂ on ozone production

Besides particulate nitrate, ClNO₂ is another product of N₂O₅ heterogeneous reactions on aerosol surfaces. A morning peak of ClNO₂ (up to 3.5 ppbv) was observed from 7:00 to 10:00 on Jan 6. With the photolysis of ClNO₂ after sunrise, chlorine radicals (Cl) were set free to the atmosphere with a rate up to 1.0 ppbv h⁻¹ as presented in Fig. 8-8(a). If there was no ClNO₂ in the morning, the production rate of Cl was only 0.02 ppbv h⁻¹ through the reaction between OH+HCl. Cl radical can react with VOCs to produce RO₂ which will then participate in the recycling of radicals (OH, HO₂ and RO₂) and affect the formation of O₃. By comparing the cases with and without constraining ClNO₂ in the model (see Fig. 8-8(b)), the production of Cl radicals indeed enhanced the production rate of O₃. The integrated O₃ production during the daytime was 8 ppbv higher with ClNO₂ constrained than without ClNO₂, and the ClNO₂ in the morning of Jan 6 could lead to 7% increase of total O₃ production. From the distribution of primary radicals' production, HONO was the dominant radical source during this study, especially in the morning as shown in Chapter 5. Cl chemistry only contributed to 3.3% of total primary radical production rates in this morning, and 6.0% from 8:30 to 10:00.

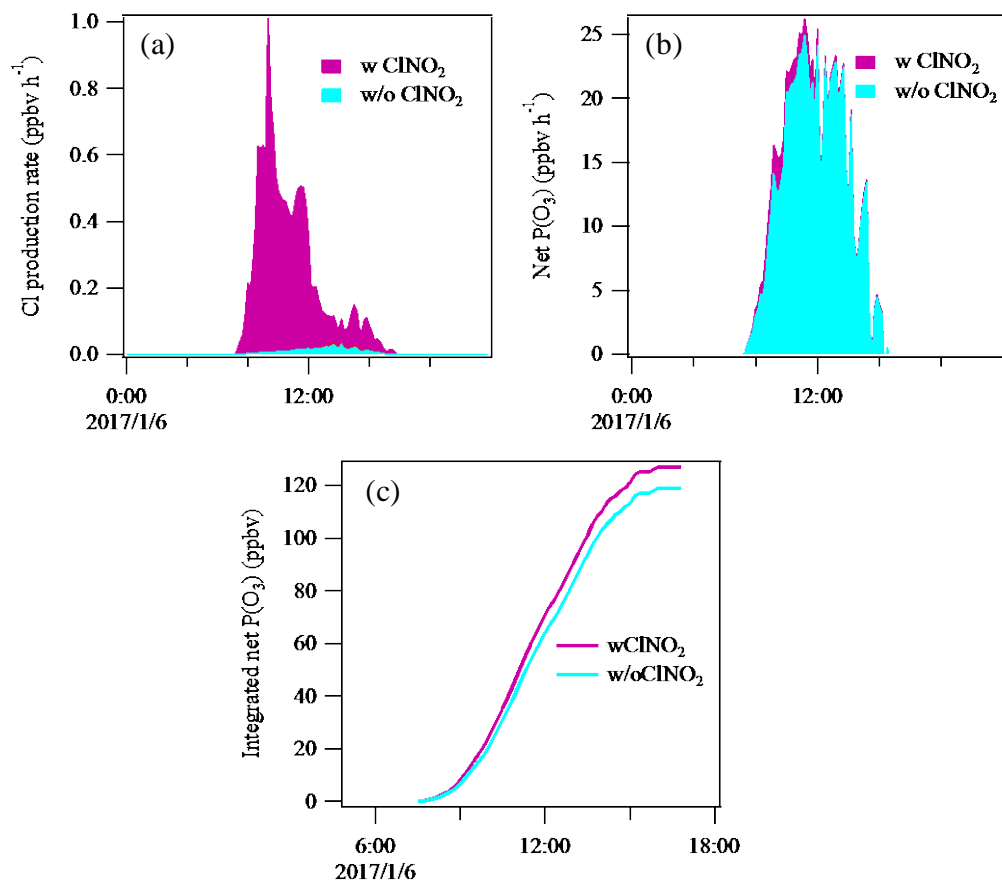


Figure 8- 8. Production rates of chlorine radicals (a), production rates of O₃ (b) with and without constraining CINO₂ in the model.

A CINO₂ peak similar with that on Jan 6 was not measured in the morning on Jan 5 due to the maintenance of the instrument. But a relative stable air mass with high CINO₂ lasting from 1:30 to 6:00 was captured on Jan 5 (see Fig. 8-1). CINO₂ sustained at a high level of averagely 5.0 ppbv, and reached the maximum concentration (~8.3 ppbv) in a period with a SO₂ peak (~25 ppbv). It is interesting to know the impact of this air mass when it transported to the downwind areas. The method of releasing the pollutants in the

air mass with averaged concentrations freely in the following day as described in Chapter 6 was used to evaluate the impact of ClNO_2 in this air mass.

During the period of this observed air mass, the average wind speed was 1.1 m s^{-1} , and it was stable southerly wind without fresh emission. After 6:00, the wind direction changed to northerly wind with an average wind speed of 0.6 m s^{-1} which brought large amount of freshly-emitted NO from north to south. It is speculated that this nighttime stable air mass with the highest ClNO_2 concentration was transported to the inland areas which were as far as $\sim 17.8 \text{ km}$ away from the observation site. This air mass was probably brought back to the observation site together with the freshly-emitted pollutants from northern areas after the change of wind direction. For this air mass near ground surface, fresh emission and the increase of the boundary layer in the morning will both affect the concentrations of pollutants, which are not well-considered in the model. Speculating from the variation of the temperature, the boundary layer height started to increase at 9:00. Thus, only the output data before 9:00 was analyzed to see the impact of ClNO_2 .

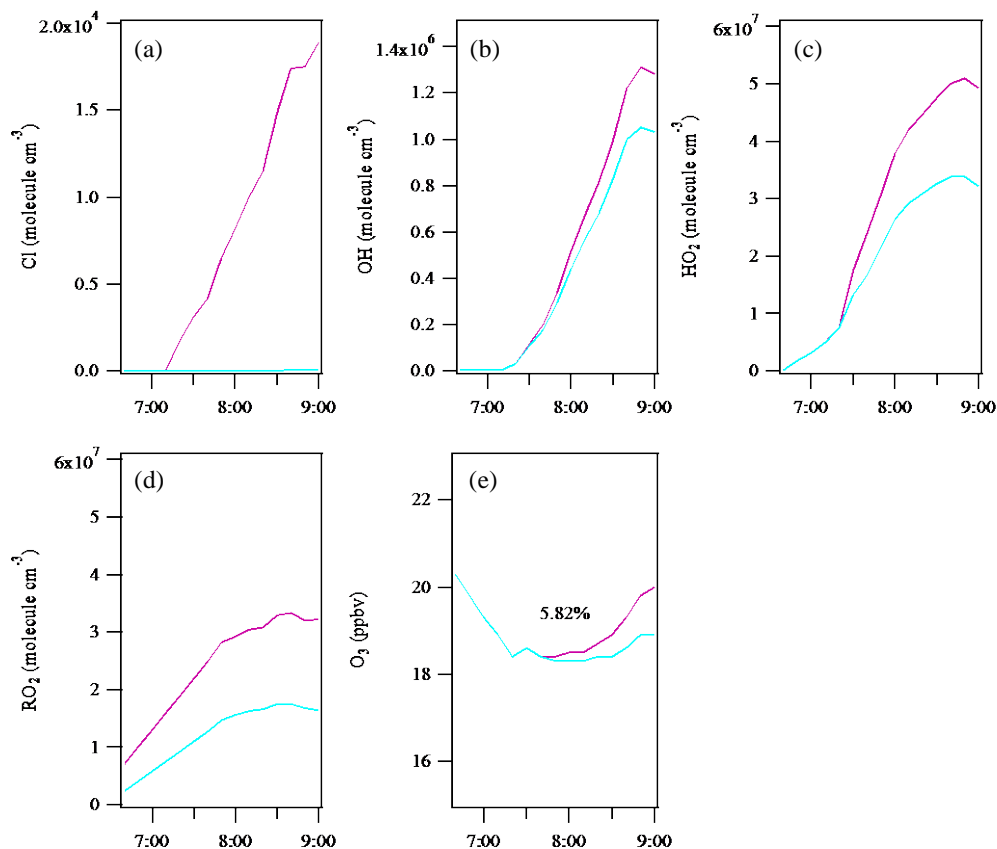


Figure 8- 9. Impact of the air mass with the highest ClNO₂ on radical and O₃ concentrations by setting the average concentrations of pollutants free from sunrise to 9:00.

As shown in Fig. 8-9, Cl radicals were produced in the early morning and led to the increase of OH, HO₂ and RO₂ radicals, and finally resulted in 5.82% increase of O₃ concentration at 9:00. HONO of 4.1 ppbv, O₃ of 20.3 ppbv, and HCHO of 9.6 ppbv were simultaneously set free with ClNO₂ of 5.0 ppbv. HONO was still the dominant radical sources which contributed to 63% of the total radical production rates before

9:00. Thus, the impact of ClNO₂ near ground was limited by the abundance of other radical sources.

8.7 Summary

In January 2017, a severe haze event occurred in the Pearl River Delta (PRD) of southern China during which high levels of PM_{2.5} (~400 μg m⁻³) and O₃ (~160 ppbv) were observed at a semi-rural site (Heshan) in the western PRD. Nitrate concentrations were up to 108 μg m⁻³ (1 h time resolution), and the contribution of nitrate to PM_{2.5} reached nearly 40%. Concurrent increases in NO₃⁻ and ClNO₂ (with a maximum value of 8.3 ppbv in 1 min time resolution) were observed in the first several hours after sunset, indicating an intense N₂O₅ heterogeneous uptake on aerosols. The formation potential of NO₃⁻ via N₂O₅ heterogeneous reactions was estimated to be 39.7 to 77.3 μg m⁻³ in the early hours (3 to 6 h) after sunset based on the measurement data, which could completely explain the measured increase in the NO₃⁻ concentration during the same time period. Daytime production of nitric acid from the gas-phase reaction of OH + NO₂ was calculated with a chemical box model built using the Master Chemical Mechanism (MCM v3.3.1) and constrained by the measurement data. The integrated nocturnal nitrate formed via N₂O₅ chemistry was comparable to or even higher than the nitric acid formed during the daytime. This study confirms that N₂O₅ heterogeneous chemistry was a significant source of aerosol nitrate during hazy days in southern China.

A typical morning peak of ClNO₂ (~3.5 ppbv) led to 7% increase of O₃ production. But the impact of ClNO₂ at this near-ground site was not that considerable compared to the impact of HONO.

References

- Brown SS, Dubé WP, Tham YJ, Zha Q, Xue L, Poon S, et al. Nighttime Chemistry at a High Altitude Site Above Hong Kong. *Journal of Geophysical Research: Atmospheres* 2016; 121, 2457–2475, doi: 10.1002/2015JD024566.
- Li Q, Zhang L, Wang T, Tham YJ, Ahmadov R, Xue L, et al. Impacts of heterogeneous uptake of dinitrogen pentoxide and chlorine activation on ozone and reactive nitrogen partitioning: improvement and application of the WRF-Chem model in southern China. *Atmos. Chem. Phys.* 2016; 16: 14875-14890.
- McLaren R, Wojtal P, Majonis D, McCourt J, Halla JD, Brook J. NO₃ radical measurements in a polluted marine environment: links to ozone formation. *Atmos. Chem. Phys.* 2010; 10: 4187-4206.
- Sun Y, Chen C, Zhang Y, Xu W, Zhou L, Cheng X, et al. Rapid formation and evolution of an extreme haze episode in Northern China during winter 2015. *Scientific reports* 2016; 6: 27151.
- Tan Z, Fuchs H, Lu K, Hofzumahaus A, Bohn B, Broch S, et al. Radical chemistry at a rural site (Wangdu) in the North China Plain: observation and model calculations of OH, HO₂ and RO₂ radicals. *Atmos. Chem. Phys.* 2017; 17: 663-690.
- Tham YJ, Wang Z, Li Q, Wang W, Wang X, Lu K, et al. Heterogeneous N₂O₅ uptake coefficient and production yield of ClNO₂ in polluted northern China: Roles of aerosol water content and chemical composition. *Atmos. Chem. Phys. Discuss.* 2018; 2018: 1-27.
- Tham YJ, Wang Z, Li Q, Yun H, Wang W, Wang X, et al. Significant concentrations of nitryl chloride sustained in the morning: investigations of the causes and impacts on ozone production in a polluted region of northern China. *Atmos. Chem. Phys.* 2016; 16: 14959-14977.
- Wang H, Lu K, Chen X, Zhu Q, Chen Q, Guo S, et al. High N₂O₅ Concentrations Observed in Urban Beijing: Implications of a Large Nitrate Formation Pathway. *Environmental Science & Technology Letters* 2017; doi:10.1021/acs.estlett.7b00341.
- Wang H, Lu K, Chen X, Zhu Q, Wu Z, Wu Y, et al. Large particulate nitrate formation from N₂O₅ uptake in a chemically reactive layer aloft during winter time in Beijing, *Atmos. Chem. Phys. Discuss.* 2018a; doi:10.5194/acp-2017-1217.

- Wang H, Lu K, Guo S, Wu Z, Shang D, Tan Z, et al. Efficient N_2O_5 Uptake and NO_3 Oxidation in the Outflow of Urban Beijing, *Atmos. Chem. Phys. Discuss.* 2018b; doi:10.5194/acp-2018-88.
- Wang X, Wang H, Xue L, Wang T, Wang L, Gu R, et al. Observations of N_2O_5 and ClNO_2 at a polluted urban surface site in North China: High N_2O_5 uptake coefficients and low ClNO_2 product yields. *Atmospheric Environment* 2017; 156: 125-134.
- Wang Z, Wang W, Tham YJ, Li Q, Wang H, Wen L, et al. Fast heterogeneous N_2O_5 uptake and ClNO_2 production in power plant and industrial plumes observed in the nocturnal residual layer over the North China Plain. *Atmos. Chem. Phys.* 2017; 17: 12361-12378.
- Yun H, Wang T, Wang W, Tham YJ, Li Q, Wang Z, et al. Nighttime NO_x loss and ClNO_2 formation in the residual layer of a polluted region: Insights from field measurements and an iterative box model. *Science of The Total Environment* 2018; 622-623: 727-734.
- Zhou W, Zhao J, Ouyang B, Mehra A, Xu W, Wang Y, et al. Production of N_2O_5 and ClNO_2 in summer in urban Beijing, China. *Atmos. Chem. Phys. Discuss.* 2018; 2018: 1-39.

Chapter 9. Summary and future work

9.1 Summary of this thesis

This thesis emphasizes the importance of reactive nitrogen chemistry in different ambient environments in China with a chemical box model constrained with the measurement data from four separate field campaigns. HONO played an important role in the daytime photochemistry in the ambient air near ground surface, especially in street canyon microenvironment and in regional pollution episode, whereas ClNO₂ was more important to the atmospheric oxidation capacity in the upper boundary layer than near ground surface. The N₂O₅ chemistry presented significant contribution to the formation of aerosol nitrate in regional pollution episode near ground surface.

9.1.1 HONO concentrations, formation and the impact

In this thesis, high daytime concentrations of HONO were found in a street canyon microenvironment (Mong Kok in Hong Kong) and in a regional severe pollution episode in the PRD (Hua Guo Shan in the city of Heshan, Jiangmen). In the street canyon, HONO concentrations in the day (3.9 ppbv as average) were significantly higher than those at night, suggesting a predominant source from vehicles, including direct emission of HONO and conversion of NO₂ to HONO. HONO photolysis was the dominant primary source of radicals, contributing 86.5% of the total production rates of radicals. HONO may enhance the production of NO₂ and O₃ under calm conditions or with low O₃ in background air. The high levels of HONO accelerated the removal of NO_x through

the formation of HNO_3 and increased the secondary formation of OVOCs, especially HCHO. The deposition or adsorption of HNO_3 on surfaces may cause damage to building materials, and more HCHO will result in a higher health risk to pedestrians and surrounding residents.

In the Heshan campaign, high HONO concentration of 1.1 ppbv around noon time was observed together with high HONO/ NO_2 ratio of 6.5%. HONO was the dominant source (43.7%-64.1%) of radicals, and governed the in-situ production of ozone. A large unknown daytime source of HONO with production rate of 4.3 ± 3.6 (0.3-17.4, range) ppbv h^{-1} was derived which correlated to a NO_2 related source in the morning, and a possible photosensitive source on aerosol surface (e.g. photo-enhanced reactions on BC or nitrate photolysis) in the afternoon. Further studies should focus on the quantification of reaction coefficients for reactions which lead to HONO formation, and apply these parameters into a model to identify their relative importance.

9.1.2 $\text{N}_2\text{O}_5/\text{ClNO}_2$ concentrations, formation and the impact

In this thesis, the impacts of high concentrations of N_2O_5 and ClNO_2 in the upper boundary layer (Tai Mo Shan in Hong Kong) and at two near-ground semi-rural sites in NCP (Wangdu) and PRD (Hua Guo Shan in the city of Heshan, Jiangmen) were investigated. In this follow-up study of TMS 2013 campaign, four $\text{N}_2\text{O}_5/\text{ClNO}_2$ -laden air masses captured just after sunset were investigated with an iterative box model which tracked the chemical evolution in the air masses from sunset to sunrise. As the ageing of “young” air masses, the predicted ClNO_2 increased up to 6 ppbv at sunrise

which resulted in ~34.3% increase of peak O₃ concentration. Cl chemistry in the upper boundary layer contributed to ~56% of the total produced O₃ with 6.0 ppbv of ClNO₂ at sunrise. Therefore, the high ClNO₂ was predicted to have significant effects on the atmospheric oxidation capacity in the upper boundary layer.

At Wangdu, Cl reactions with VOCs contributed to 3% and 9% of the average daytime RO_x budget (10% and 30% in the early morning) with ClNO₂ of 0.5 ppbv and 2.1 ppbv, respectively. Integrated ozone concentrations also increased 3.3% (4 ppbv) and 13.3% (10 ppbv), respectively. At Heshan, ClNO₂ of up to 3.5 ppbv in the morning led to 7% increase of the integrated O₃ production. Compared to the HONO impact on radical and O₃ formation at these two sites, the impact of ClNO₂ was considerable but not that significant. At Heshan, nitrate formed through N₂O₅ heterogeneous reactions at night was comparable to the daytime formation potential of nitrate through OH+NO₂. Overall, N₂O₅ heterogeneous reaction was a significant source of aerosol nitrate in this regional highly-polluted episode.

9.2 Future work

(1) The Master Chemical Mechanism mainly aims at representing the chemical reactions in gas phase. There is only limited work focusing on expanding the mechanism to represent the heterogeneous reactions on surfaces. The current mechanism cannot reproduce the measured nighttime and daytime HONO concentrations in the box model. New HONO formation mechanisms with proper reaction coefficients should be added into the box model to better reveal the HONO level in different environments. For the

N_2O_5 heterogeneous reactions, the uptake coefficients of N_2O_5 and yields of ClNO_2 changed with aerosol composition and meteorological conditions. Even though a Cl mechanism was added into the box model, it still could not reproduce the measured N_2O_5 and ClNO_2 well in the box model without proper parameters. Current parameterization solution should be considered to add into the box model to better reproduce the formation processes of N_2O_5 and ClNO_2 .

(2) Specially-designed lab or field studies are needed to explain the source of HONO and to give out better reaction coefficients on HONO sources. It is difficult to identify the specific HONO sources based on current field studies which aim at HONO level in the ambient air. Only some primary indicators were found out for the possible HONO sources. Lab studies can further verify the mechanism and give out proper reaction coefficients which can be used in the model simulation. Previous studies on HONO formation on BC surfaces always treated NO_2 as the precursor. But from the results in the Hua Guo Shan campaign, NO_2 was probably not the direct precursor in the afternoon. At the same time, the photo-enhanced reaction on BC had obvious correlation with the unknown HONO source. So new mechanisms should be guessed and verified in the lab studies. From the field campaign, it is hard to establish relationship with soil emissions. More field studies on soil emission of HONO should be conducted in the real environments, not just using the soil samples in the lab.

(3) Considering the significant contribution of Cl chemistry to the atmospheric oxidation capacity in the upper boundary layer, more studies about the vertical distribution of $\text{N}_2\text{O}_5/\text{ClNO}_2$ and their impacts should be conducted. The current observation of

$\text{N}_2\text{O}_5/\text{ClNO}_2$ in the upper boundary layer in China was only conducted at TMS in Hong Kong and at Mt. Tai in NCP by our group. The impact of ClNO_2 at Mt. Tai has not been further investigated. It is expected that there should be a layer with high ClNO_2 in the middle boundary layer to explain the observed morning peaks of ClNO_2 at Wangdu or at Heshan. It is urgent to know more about the characteristics and impacts of $\text{N}_2\text{O}_5/\text{ClNO}_2$ in the middle boundary layer to depict a clearer picture of $\text{N}_2\text{O}_5/\text{ClNO}_2$ within the whole boundary layer.